Design of Copper-Based Adsorbents for Gas Separation and Purification: Exploring Novel Materials and Optimization Strategies

by

Farshad Feyzbar-Khalkhali-Nejad

A dissertation submitted to the Graduate Faculty of
Auburn University
in partial fulfillment of the
requirements for the Degree of
Doctor of Philosophy

Auburn, Alabama
August 5, 2023

Keywords: Adsorbent, Adsorption mechanism, Surface modification, Selectivity, Thermodynamics of adsorption

Approved by

Dr. Tae-Sik Oh, Chair, Assistant Professor Department of Chemical Engineering
Dr. Andrew Adamczyk, Assistant Professor Department of Chemical Engineering
Dr. Bryan Beckingham, Associate Professor Department of Chemical Engineering
Dr. Lauren Beckingham, Associate Professor Department of Civil and Environmental Engineering

Abstract

This dissertation provides a comprehensive overview of the design, synthesis, and performance optimization of copper-based adsorbents for gas separation and purification. Adsorption, a cost-effective separation technique known for its high capacity and selectivity, has garnered significant attention in various gas separation applications. The dissertation is structured into four distinct chapters, each exploring different aspects of copper-based adsorbents and their effectiveness in capturing specific gases.

In the first chapter, the current state of the field of adsorption is presented, along with identified research gaps. Emphasis is placed on the importance of investigating the adsorbent-adsorbate interaction to design new materials and explore their performance under realistic conditions. Various chemical modification methods for various supports, including activated carbon, zeolites, mesoporous silica, alumina, and metal-organic frameworks, are discussed. Specifically, the focus is on enhancing the adsorption capacity and selectivity for carbon monoxide (CO) as a representative system.

The second chapter delves into the modification of copper surface to form CuCl as an active material for interaction with CO. The study examines the effect of solvent-regulated CuCl morphologies on CO adsorption capacity, selectivity, and kinetics. It is revealed that CuCl with triangular and granule morphologies show the highest adsorption capacity, while the cubic morphology provides the highest selectivity for CO adsorption. The significance of surface morphology and crystalline plane in achieving desired adsorption performance is emphasized.

In the third chapter, a dual-active site adsorbent based on Cu(I) ions is synthesized through a two-step synthesis route. This chapter addresses the challenges associated with stability and selectivity of CuCl-modified copper and explores the aspect of surface energetic heterogeneity and

the performance of the sample under realistic condition for CO separation from CO-CO_2 mixture as a representative system for hydrogen purification. The study highlights the superior CO selectivity achieved by the dual-active site adsorbent, which makes it a promising candidate for CO separation for gas purification purposes. The stability of the adsorbent under atmospheric air and the impact of surface modifications on the adsorbent performance are thoroughly investigated.

In the fourth chapter a facile synthesis method for zeolite@MOF composites at room temperature is presented. This chapter focuses on pre- and post-synthesis surface modification techniques and their influence on structural and chemical properties of the composites. The CO and CO_2 adsorption performance of composite is evaluated, revealing the influence of copper salt choice, solvent selection, and modification of the zeolite and MOF components on adsorption capacity and selectivity. The role of surface chemistry in enhancing the interaction with CO is highlighted, and the overall performance of the designed composite is discussed.

These studies showcase the advancements in design and performance of copper-based adsorbents for gas separation and purification. The investigations highlight the importance of designing novel materials, optimizing their structure and properties, and exploring various strategies to enhance adsorption performance and stability. The findings in this dissertation offers promising avenues for further development of efficient adsorbents for gas separation applications.

Acknowledgments

I would like to extend my heartfelt appreciation to my advisor, Dr. Tae-Sik Oh, for his remarkable guidance, infinite patience, and mentorship throughout the entire PhD journey. Your unwavering support, invaluable insights, and friendly approach have not only shaped me into the researcher I am today but also created countless fond memories. I am immensely grateful for his mentorship and opportunities he has provided me.

To the real superheroes of my life—my beloved mom and dad. Thank you from the depth of my heart for being my unwavering source of encouragement, especially when I doubted my abilities. Your belief in me, even when I attempted to cook experimental dishes that defied all the basics of cooking, has kept me going. And let's not forget our family quote, "WE CAN!"—a constant reminder of our collective strength and determination. The hardest thing during these years was not being able to see you, but your love transcended the distance and made every challenge surmountable. I am eternally grateful for your love and support.

To my extraordinary sister, you are a superhero in disguise! While I was away pursuing my dreams, you stepped up and filled the void, supporting mom and dad with unwavering strength and love. Thank you for being their rock and for being mine as well. Your unwavering support, endless encouragement, and hilarious memes sent during my toughest moments were like a lifeline. I couldn't have asked for a better sister, and I am forever grateful for your presence in our lives.

To my incredible friends, thank you for being the source of laughter and sanity during this wild ride. Your unwavering support, whether it was the late-night studies or impromptu parties, has kept me motivated and uplifted. Your friendship has been the perfect balance to the academic intensity, and I am grateful for each and every one of you.

Table of Contents

List of Tables

List of Figures

Table of parameters, acronyms, and abbreviations

Parameters/Acronyms	Description	Unit
A	Clark's model constant	
C_0	Initial concentration	mg L^{-1}
C_p	Heat capacity	J K^{-1}
C_t	Adsorbate concentration at time t	mg L^{-1}
E	Heat of adsorption	kJ mol^{-1}
k_1	Pseudo-first-order kinetic constant	min^{-1}
k_2	pseudo-second-order kinetic constant	g mg^{-1} min^{-1}
k_{AB}	Bohar-Adams kinetic constant	L $mg^{-1}min^{-1}$
k_d	Intraparticle diffusion rate constant	mg g^{-1} $s^{-0.5}$
K_e	Equilibrium constant	
K_{EL}	Adsorption coefficient	kPa^{-1}
K_F	Freundlich empirical constant	kPa^{-1}
K_L	Langmuir constant	L mg^{-1}
K_s	Sips affinity coefficient	kPa^{-1}
K_T	Temkin affinity coefficient	kPa^{-1}
k_{Th}	Thomas constant	mg g^{-1}
k_{YN}	Yoon-Nelson rate constant	min^{-1}
m	Mass of adsorbent	g
N	Number of binding site	mol kg^{-1}
N_0	Saturation concentration	mg L^{-1}
N_a	Adsorbed amount	molecules/nm^2
n_F	Freundlich empirical constant	
N_m	Monolayer capacity	molecules/nm^2
n_s	Sips dimensionless number	
n_T	Toth isotherm exponent	
Q	Flow rate	mL min^{-1}
q	Adsorbed amount	mmol g^{-1}
q^{diff}	Differential heat of adsorption	kJ mol^{-1}
q_e	Equilibrium adsorbed amount	mg g^{-1}
Q^{int}	Integral heat of adsorption	kJ
q_{st}	Isosteric heat of adsorption	kJ mol^{-1}
q_t	Adsorbed amount at time t	mg g^{-1}
q_{Th}	Equilibrium uptake	mg g^{-1}
r	Clark's model constant	min^{-1}
t	Time	min
u	Molar surface energy	kJ mol^{-1}
u^g	Molar energy of gas	kJ mol^{-1}
X	Adsorption energy	J mol^{-1}
Z	Bed height	cm
α	Elovich model initial adsorption rate	mmol g^{-1} min^{-1}
β	Elovich model desorption constant	g $mmol^{-1}$
$\Delta\bar{h}_a$	Differential molar enthalpy of adsorption	kJ mol^{-1}
$\Delta\bar{u}_a$	Differential molar energy of adsorption	kJ mol^{-1}
θ	Surface coverage	
ν	Linear velocity	cm min^{-1}
τ	Time required for 50% adsorbate breakthrough	min

DSL	Dual Site Langmuir
DSLF	Dual Site Langmuir-Freundlich (Dual Site Sips)
Dyn	Dynamic
Eq	Equilibrium
ESA	Electrical Swing Adsorption
F	Freundlich
LF	Langmuir-Freundlich
MCEL	Multi-Component Extended Langmuir
PSA	Pressure Swing Adsorption
SSL	Single Site Langmuir
TSA	Temperature Swing Adsorption
TSL	Triple Site Langmuir
VPSA	Vacuum Pressure Swing Adsorption
VTIR	Variable Temperature InfraRed

Chapter 1: Principles and Materials for Adsorption-based separation of carbon monoxide

Abstracta

Adsorption is a cost and energy-effective method of separation that can provide high adsorption capacity and selectivity towards a target gas with correct selection of adsorbent. In this chapter, an overview of equilibrium and dynamic adsorption setups with equilibrium and kinetic models of adsorption are presented. Adsorption data collection using equilibrium and dynamic setups, FTIR, mass spectroscopy, and microcalorimetry, are presented. We emphasized the need to explore the performance of new adsorbents in realistic conditions and a better understanding of adsorbent-adsorbate interaction. We gave a detailed overview of CO adsorption technology discussing CO adsorbents and the respective challenges. Chemical modification methods were reviewed for various porous supports such as activated carbon, zeolites, mesoporous silica, alumina, and metal-organic frameworks. We highlighted novel chemical modification techniques and how they affect the performance of adsorbents (i.e., adsorption capacity and selectivity). Finally, we presented the required future direction for research in the field of CO adsorption.

Keywords: Carbon monoxide; Adsorbent; Copper (I) ion; adsorption isotherms; adsorption kinetics

1.1 Introduction

Separation is a laborious process as the second law of thermodynamics does not favor it. Almost all processes in industries such as chemical, pharmaceutical, environmental, and petrochemical industries require separation processes. They contribute about 40-70% of the total production cost. The examples include hydrogen recovery from ammonia plants, removal of hazardous and polluting gases such as hydrogen sulfide and carbon dioxide from natural gas, and separation of color impurities from active pharmaceutical ingredients [1-4]. Due to the high impact of the

separation process on the production cost, there have been many ongoing investments and research in this area.

Carbon monoxide (CO) is a toxic gas that has brought up climate change, ozone depletion, acid rain, and other environmental concerns [5]. Many chemical products such as acetic acid, formic acid, methanol, liquid hydrocarbon fuels, plastics, and fibers are produced using CO as the raw material [6-8]. Reforming of natural gas or biomass, partial oxidation, and coal gasification are the main methods of CO production [9-12]. Coke oven gas (COG), Linz-Donawitz gas (LDG), and blast furnace gas (BFG) in steel and metallurgical plants are other sources of CO production [13]. CO is considered as a waste product in these processes, and it is a common practice to burn CO to form CO_2 for disposal and simultaneous energy recovery [13, 14]. Consequently, for both environmental and economical benefits, it is required to separate CO from a stream of gases such as CO_2, CH_4, H_2, and N_2.

The processes that have been applied to separate CO rely on absorption, cryogenic distillation, or adsorption. The two commonly used separation methods in industry are cryogenic distillation and absorption. Two absorption methods are by ammoniacal copper liquor and by CuCl-$AlCl_4$-toluene complex solution (COSORB). Each method has its advantages over the other that makes one more suitable in a specific application [1, 14-16]. For instance, absorption of CO using the COSORB system does not require pretreatment of a feed gas containing nitrogen and carbon dioxide, while cryogenic separation requires complete removal of CO_2 and N_2 from the feed gas due to the prevention of solid freeze-up of CO_2 at very low temperature and similar boiling points of N_2 and CO [15]. In COSORB process, the main problem is the stability of Cu^+ ion and its reaction to produce Cu^{2+} and Cu^0 [14]. Besides, there is also the disadvantage of required high pressure for the absorption process. Also, the presence of H_2O and H_2S results in harmful side reactions and

the formation of hydrochloric acid [1, 14]. Other challenges facing COSORB is the frequent solvent renewal leading to high operation costs [14, 15].

1.1.1 Adsorption

Adsorption is an important separation method that is used in industry for separation of compounds from gas mixtures. Adsorption plays an important role in future energy and environmental technologies such as hydrogen purification and storage, carbon capture, desulfurization of transportation fuels, and other technologies [17].

Adsorption is a surface phenomenon in which the molecules, atoms, or ions adhere to a solid surface due to the excess of the surface free energy caused by bond deficiency [18]. Basically, surface determines the thermodynamic phase boundary where physical and chemical properties of the adjacent phase change abruptly. Based on the strength of interaction between the adsorbate and adsorbent, it is possible to classify adsorption as physisorption characterized by van der Waals forces, and chemisorption, characterized by covalent bonds [19]. The strength of interaction is measured through calculation of isosteric heat of adsorption. It should be mentioned that in order to investigate the heat of adsorption it is required to measure the adsorption isotherm at different temperatures. The topic of heat of adsorption will be discussed more in detail further in this chapter.

1.1.2 Activated and non-activated adsorption

The adsorbate, either physically or chemically adsorbed on a solid, in thermal equilibrium resides at the bottom of the potential well (**Figure 1-1**) [20]. In order to desorb the adsorbate, one must supply it with energy thermally or electronically to return to the gas phase. On classical theory of adsorption (non-activated adsorption), the activation energy is zero and the required energy for desorption (λ) is equal to magnitude of heat of adsorption. On the other hand, the modification of

classical adsorption theory (activated adsorption) states that an activation energy, E, is required for adsorption and, consequently, the desorption process requires an activation energy of E+λ [21]. In case there is activation barrier involved, the activation barrier should be overcome in addition to adsorption energy.

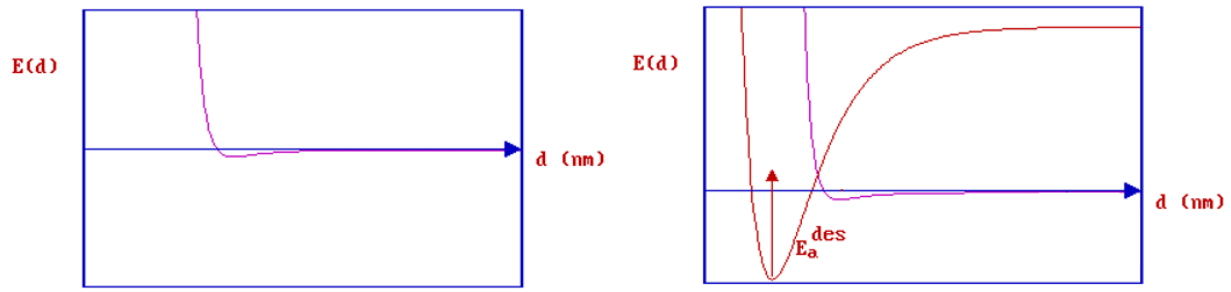

Figure 1-1 a) Physisorption, b) Chemisorption (activated adsorption)[20]

Adsorption is a spontaneous accumulation of a gas or vapor (i.e., adsorbate) at a solid surface (i.e., adsorbent) as compared to the bulk phase (i.e., adsorptive). The four commercially dominant adsorbents include activated carbon, zeolites, silica gel, and activated alumina. According to Humphrey and Keller, in 1997, the accumulative worldwide sale of these four main commercial adsorbents were below 2 billion dollars **Table 1-1**[17, 22].

Table 1-1 Adsorbent materials worldwide sale in 1997 [17]

Adsorbent	Worldwide sale
Activated carbon	$1 billion
Zeolites	$100 million
Silica gel	$27 million
Activated Alumina	$26 million

Adsorption occurs when the interaction potential energy ϕ is equal to the work done to bring a molecule from gas phase to the adsorbed state [17]. The potential energy for physical adsorption is

$$\phi = \phi_D + \phi_R + \phi_{Ind} + \phi_{F\mu} + \phi_{\dot{F}Q} \qquad 1\text{-}1$$

where ϕ_D is dispersion energy, ϕ_R is repulsive energy, ϕ_{Ind} is the induction energy (interaction between electric field and an induced dipole), $\phi_{F\mu}$ is interaction between electric field (F) and a permanent dipole (μ), and $\phi_{\dot{F}Q}$is the interaction between field gradient ($\dot{F}$) and a quadrupole (with quadrupole moment). These energies can be divided into two groups of nonelectrostatic ($\phi_D + \phi_R + \phi_{Ind}$) and the electrostatic ($\phi_{F\mu} + \phi_{\dot{F}Q}$) energies [17]. For activated carbon, the first group dominates and for the metal oxides, zeolites, and ionic solids, the second group dominates. For example, the nonelectrostatic energies directly depend on the polarizability of the sorbate molecule; therefore, a surface such as activated carbon tends to adsorb CO_2 due to its higher polarizability in comparison to N_2 or CO.

This chapter, as shown in **Figure 1-2**, is divided into two parts. The first part (section 1.2-1.5) overviews experimental setups and adsorption models. The second part (section 1.6) overviews adsorbent materials and chemical modification techniques. We first discuss different experimental gas adsorption setups followed by a more detailed discussion on various mathematical equilibrium and kinetic models for in-depth analysis with an emphasis on the performance of adsorbents in dynamic conditions. Later on, we discuss different adsorbents with a focus on chemical modification of their surfaces for interaction with CO as a representative adsorbate. Furthermore, various challenges regarding the application of different supports and a review of the conventional and newly emerging techniques of chemical modification are provided. The performance of pristine and modified adsorbents provides insight for new adsorbent designs.

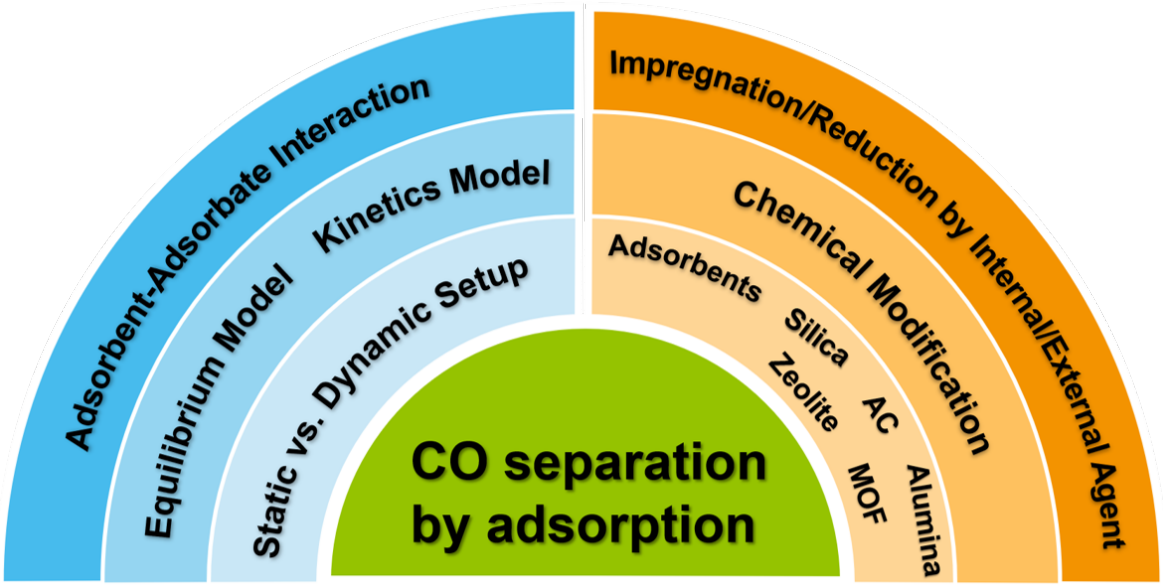

Figure 1-2 Schematic of the review outline.

1.2 General setups

Generally, adsorption setups can be classified as equilibrium and dynamic flow adsorption, in which the former is used to evaluate adsorbents for their adsorption capability at equilibrium. The latter reflects realistic phenomena such as adsorption kinetics and dynamic flow through packed beds. The details of these two setups are discussed in the following sections.

1.2.1 Equilibrium adsorption setup

The equilibrium adsorption setup is an integral part of adsorption research that has been used in almost every adsorption research. **Figure 1-3** shows the schematic of equilibrium adsorption setup [23, 24] that is also applied to commercial adsorption analysis devices. This setup includes two cells of specific volume, one for loading of the adsorbate and the other for adsorption, two pressure indicators connected to the two cells, a temperature-controlled oven to control the ambient adsorption temperature, and a vacuum pump. The adsorbate is loaded to the loading cell, and the pressure and the temperature are recorded, then the valve to the adsorption cell is opened, and the adsorbate gets into contact with the adsorbent material loaded in the cell at a determined ambient

temperature. The vital point in this step is that enough time should be given for the adsorption to reach equilibrium. After reaching the equilibrium, the pressure is recorded, and the connecting valve of loading and adsorption cell is closed, and an additional amount of adsorbate is introduced to the loading cell to obtain another equilibrium point at higher pressure. This process is repeated at the same ambient temperature to cover the whole pressure range. The adsorption amount is calculated using the generalized equation of state derived mole balance before and after adsorption equilibrium [23, 24]

$$\left.\frac{PV}{ZRT}\right|_{AC}^{b} + \left.\frac{PV}{ZRT}\right|_{LC}^{b} = \left.\frac{PV}{ZRT}\right|_{AC}^{a} + \left.\frac{PV}{ZRT}\right|_{LC}^{a} + qm \qquad 1\text{-}2$$

where q (mmol g^{-1}) is the adsorbed amount per adsorbent mass, m (g) is the mass of adsorbent, R (J mol^{-1} K^{-1}) is the universal gas constant. T (K), P (kPa), V (cm^3), and Z are ambient temperature, pressure, volume, and compressibility factor, respectively (b: before adsorption equilibrium; a: after adsorption equilibrium). The equilibrium adsorption setup provides the adsorption isotherm from which valuable information such as adsorbent-adsorbate interaction, surface properties, and adsorbate affinities can be determined by fitting data to the equilibrium adsorption models.

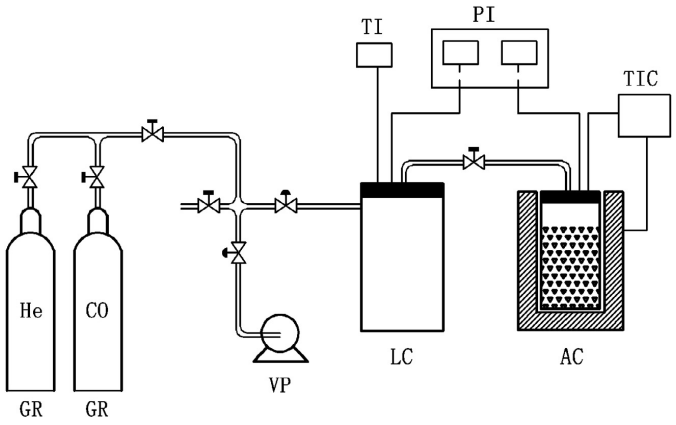

Figure 1-3 Schematics of equilibrium adsorption setup: (TI) temperature indicator, (PI) pressure indicator, (TIC) temperature indicator and controller, (VP) vacuum pump, (LC) loading cell, (AC) adsorption cell, (GR) gas reservoir. Reproduced from Ref [23] with permission from The Royal Society of Chemistry. Copyright 2016 The Royal Society of Chemistry.

1.2.2 Dynamic flow adsorption setup

Figure 1-4 shows the schematic of the typical setup used to investigate the kinetics of adsorption for many gases [25-33]. The setup consists of an adsorption column packed with the adsorbent, flow controllers, pressure controller since adsorption highly depends on pressure, and a continuous gas analyzer device such as a mass spectrometer, and other analyzers equipped with thermal conductivity detector (TCD) or infra-red detector connected to the outlet of the column to measure the gas concentration. The provided data from this setup can be presented as the breakthrough curve, a graph of relative concentration (C/C_0, where C_0 is the initial concentration) versus time. For this setup, it is crucial to have the feed gases well mixed and the column length short enough. This prevents errors in concentration measurements and breakthrough time. Typical bed length and diameter ranges about 15-25 cm, and 1-10 cm, respectively [27, 28, 30, 31, 34].

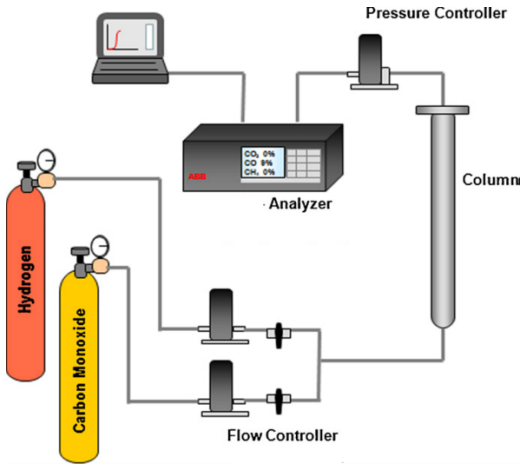

Figure 1-4 Schematic of one-column dynamic flow adsorption setup. Reprinted with permission from Ref [25]. Copyright 2010 Elsevier.

Ideal adsorption solution theory (IAST), a similar concept to the ideal solution model, was first proposed by Myers and Prausnitz in 1965. According to this theory, we can predict the adsorption of one component in a mixed gas from pure gas adsorption isotherms [3, 35]. Adsorption selectivity is calculated for two-component gas mixtures according to the following equation

$$S_{ij} = \frac{x_i/x_j}{y_i/y_j} \quad 1\text{-}3$$

where i and j represent the gas components, x_i and x_j are equilibrium adsorption capacities of gas i and j, and y_i and y_j are molar fractions of gas i and j in the gas phase, respectively [12].

Experimentally a mixture of gases can be analyzed in a dynamic adsorption setup to investigate the adsorption capacity and kinetics. The dynamic adsorption setup is usually used to complement the equilibrium adsorption study to confirm the IAST-estimated selective adsorption of a gas component from a mixture. From a breakthrough curve, a plot of normalized off-gas concentrations against time, shown in **Figure 1-5**, Kim et al. confirmed that CO adsorption capacity of Cu(I)/MIL-100(Fe) under CO-CO_2 mixture flow agrees well with the IAST-predicted value [9]. Furthermore, the regeneration of adsorbent that is usually done under vacuum was performed using the dynamic setup over three adsorption/desorption cycles under He flow at room temperature. The breakthrough curves for all the cycles are identical, which confirms the complete regeneration of the adsorbent. In another dynamic adsorption study, the selective adsorption of CO on Cu(I)/MIL-101(Cr) in CO-N_2 mixture was confirmed [36]. **Figure 1-5** clearly shows the selective adsorption of CO since CO_2 and N_2 are the first detected gases after the packed bed. It takes a longer time for CO to show up at the detector. The concentration ratio C/C_o (C_o, concentration in the feed gas) can temporarily go higher than 1 for the weakly bound molecules. When this takes place, it is called a roll-up. The roll-ups in breakthrough curves in **Figure 1-5** show the competitive adsorption among the involved gases. This phenomenon takes place due to the fast movement of weakly adsorbed molecules such as CO_2 or N_2 that will later be replaced by more strongly adsorbed CO molecules.

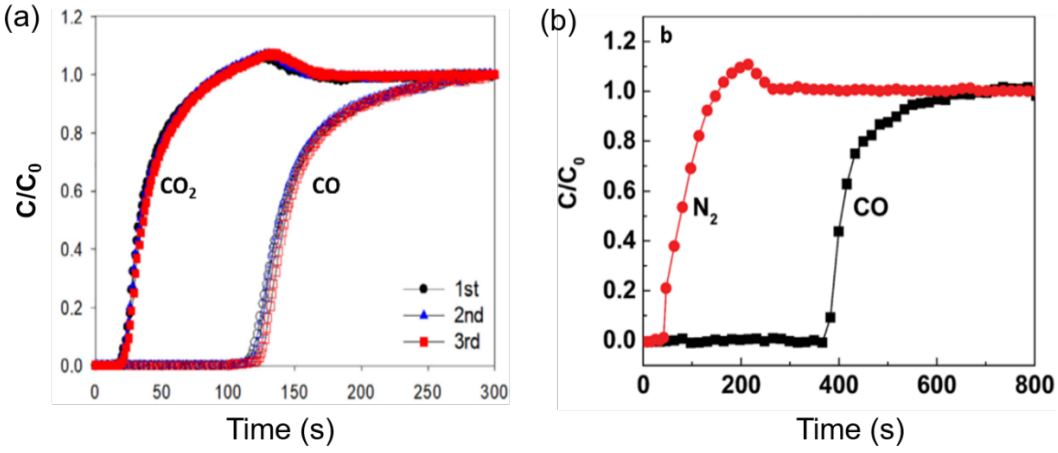

Figure 1-5 Dynamic breakthrough curves of (a) CO/CO_2 over Cu(I)@MIL-100(Fe). Reprinted with permission from Ref 9. Copyright 2018 Elsevier. (b) CO/N_2 over Cu(I)/MIL-101(Cr). Reproduced from Ref [36] with permission from The Royal Society of Chemistry. Copyright 2018 The Royal Society of Chemistry.

The single roll-up phenomena are common in pure sorbent beds, and double and multiple roll-ups are frequent in layered sorbent columns. Layered adsorbent beds are used in gas separation, particularly in Pressure Swing Adsorption (PSA), with the basic principle of using a weak sorbent at the inlet followed by a stronger sorbent to maximize the adsorbent efficiency and minimize the adsorbent size [29]. Park et al.[29] used a double-layered adsorbent column of activated carbon followed by a 5A zeolite to investigate the dynamics and optimal design of layered beds for hydrogen separation from a gas mixture. It was shown that the use of a double-layered adsorbent column of AC and ZMS 5A could reduce the size of the adsorbent layer in comparison to a column packed with a bed of AC. The conditions and models used (i.e., dynamic condition, non-isothermal, and non-equilibrium model) are comparable to industrial conditions, and there are many adsorbents of CO such as Cu(I)V(IV)/MIL-101 and CuCl/bayerite that are required to be tested in these conditions to explore their potential application.

1.2.3 Pressure Swing Adsorption (PSA)

It is required for adsorption processes to be cyclic since, for most industrial processes, it is required to regenerate the adsorbents. Temperature swing adsorption (TSA), and pressure swing adsorption (PSA), are two of the cyclic adsorption processes that use different methods of regeneration of adsorbents. The choice of method is based on the targeted type of separation [3, 37]. TSA and PSA are usually selected for purification and bulk separation purposes, respectively.

In the TSA process, the adsorbent is regenerated by passing a hot gas through the bed. In the case of CO_2 adsorption using TSA, the disadvantage of using hot gases such as N_2 is the low heat capacity that leads to the use of a large volume of gas to heat the adsorbent bed that results in a lower concentration of recovered adsorbate [38]. Long cycles of heating and cooling the adsorbent in TSA lead to high energy consumption and increased investment in adsorbent [37, 38]. Induction heating [39, 40], microwave heating [41], and direct electrical heating (Joule heating)[42] have been proposed to enhance the performance of TSA. The first two methods suffer from inefficient thermal energy transfer to the adsorbent materials. Direct electrical heating takes place when an electric voltage is applied to electrically conductive adsorbents. This process is called Electric Swing Adsorption (ESA) [42]. The in-situ heating of the adsorbent overcomes the limitations of the low heat capacity of heating gas. The rate of heat transfer to adsorbents is high, and the heating cycle time can be shortened. ESA has been used for volatile organic compounds (VOCs) abatement [43, 44], and CO_2 capture [42]. ESA-suitable CO_2 adsorbents include zeolites [45], amine impregnated solid sorbents [44], carbon fibers [46], carbon monoliths [47], carbon-zeolite monoliths [48], and graphene [49]. The main disadvantage of ESA process is the use of electric power to increase the temperature since electric power has a higher exergetic value than heat used in TSA process [50].

Pressure swing adsorption is a flexible method for separation and purification of gas mixtures that are used in major industrial applications such as CO-H_2 separation [51, 52], separation of CO_2 and CH_4 from landfill gas [53, 54], H_2 production using steam methane reformer [55, 56], gas drying, and air fractionation (a process to produce nitrogen or oxygen-enriched gas streams) [57, 58]. PSA includes multiple columns packed with microporous or mesoporous solid adsorbents. The height of the columns depends on the crush strength of the adsorbent particles while the diameter is limited to about 4 meters [59]. A mixture of gases at super-ambient pressure flows through the columns, and the outlet stream is enriched with less strongly adsorbed gas from the feed mixture. The adsorbed gas is then desorbed by reducing the column pressure to about ambient pressure, and no external heat is used in the desorption process. Afterward, the desorbed gases are enriched in the more strongly adsorbed species of the feed gas. **Figure 1-6a** shows the typical pressure history of one adsorption column. **Figure 1-6b** illustrates the elementary steps in a lab-scale PSA setup [60]. The performance of PSA is evaluated based on product purity, productivity (gas produced per adsorbent mass per time), and recovery (ratio of the amount of gas in product to the amount of gas in feed). Higher purity and recovery of the target component can be achieved by increasing the number of columns; however, the capital cost is directly related to the number of columns. Factors affecting the yield and separation efficiency of PSA include the choice of adsorbent material, the length ratio of the adsorbent layers in the column, the composition of the feed gas, and adsorbate-adsorbent interaction [25, 61, 62].

Multi-sorbent layered beds have been used in industrial practices to separate multicomponent gas by PSA for decades [29]. The layered beds are used to minimize the bed size and maximize the utilization of sorbents. The PSA separation unit for the off-gas of steam reforming uses a multi-sorbent layered bed to separate hydrogen from CO, CO_2, CH_4, and moisture. The process includes

a guard bed of silica gel or alumina to remove the moisture, followed by two layered sorbents of activated carbon and zeolite in which the former is used to adsorb CO_2, and the latter adsorbs CO and CH_4. The productivity and recovery of multi-sorbent layered PSA depend on the relative length of layers. The design of a multi-sorbent bed and its bed length optimization can be done by investigating the adsorption dynamics of the multicomponent mixture in a layered bed.

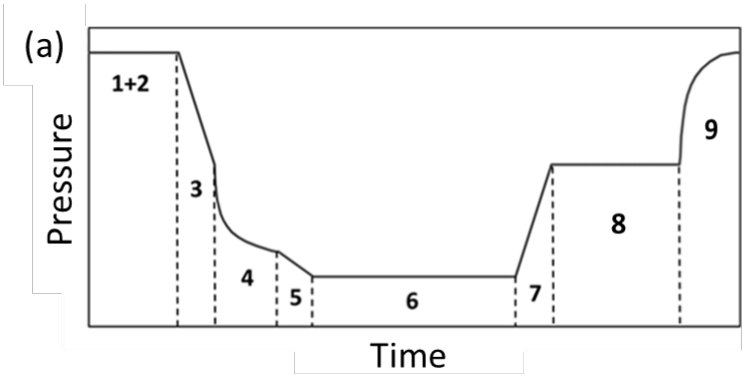

(b)

Steps		Process
1	Adsorption	Feed goes through the first column
2	Adsorption/Providing backfill	Produced stream divided into two streams one goes to storage column and the other goes to another column
3	Depressurization pressure equalization	After producing phase, the first column is depressurized by equalizing pressure with another column
4	Providing purge	The remaining gas in the first column is used to purge another column and reduce the pressure to a specific amount
5	Blowdown	Depressurization from the bottom end of the column
6	Purge	The column is purged with purging gas to regenerate the adsorbent
7	Pressurization pressure equalization	The first column is pressurized by equalization of pressure with another column
8	idle	In this step, all the valves connected to the column are closed
9	Backfill	The first column is backfilled with purified hydrogen from another column to reach the maximum operating pressure

Figure 1-6 (a) Pressure history of one adsorption column in a cycle. (b) PSA steps for a column in one cycle. Reprinted with permission from Ref [60]. Copyright 2018 American Chemical Society.

Vacuum pressure swing adsorption (VPSA) is operated at a wide range of temperatures and has the same operation principle as PSA [63]. However, in this scheme, adsorption occurs at ambient pressure, whereas desorption happens under vacuum between adsorption periods. The regeneration step (desorption step) determines the power consumption of VPSA. **Figure 1-7a** shows a five-bed VPSA setup used for the separation of CO from syngas. In this setup, each bed goes through the

seven-step process of adsorption, pressure equalization for depressurization, replacement, blowdown, vacuum, pressure equalization for pressurization, and feed re-pressurization. These steps are evident in the pressure history curve for one adsorption bed (**Figure 1-7b**). The compressed syngas is introduced to the first column for the adsorption process. Afterward, the column is depressurized by delivering the gas to pressurize another column. This is followed by the replacement step using part of CO product gas. The blowdown is then conducted before pulling vacuum. This saves energy compared to a direct vacuum without the blowdown step.

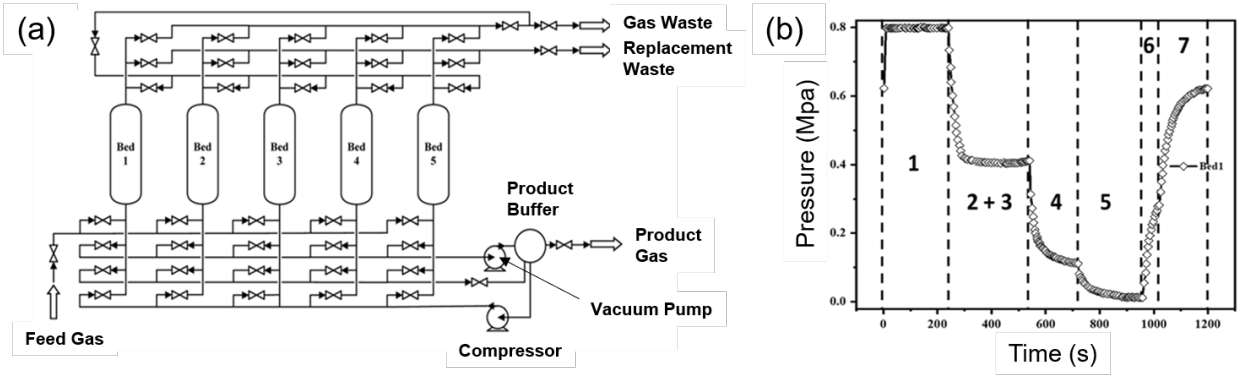

(c)

	Steps	Process
1	Adsorption	Feed gas passes through the column after compression
2	Pressure equalization for depressurization	The column is depressurized by pressurizing another column
3	Replacement	Introducing part of CO product to the column at a specific pressure to increase the concentration of CO and remove the exhaust gas in the column
4	Blowdown	Performed to vent the inside pressure of the column and desorb the loosely adsorbed components
5	Vacuum	Desorption of CO from adsorption bed to produce high purity CO and regenerate the adsorbent
6	Pressure equalization for pressurization	Pressurization of the column by pressure equalization with another column at high pressure
7	Feed repressurization	Pressurization of column using the outlet gases of a column at adsorption step

Figure 1-7 (a) Schematic flow diagram of five-bed VPSA. (b) Pressure history curve of one adsorption bed in a cycle. (c) VPSA steps for a column in one cycle. Reproduced from Ref [64] with permission from The Royal Society of Chemistry. Copyright 2018 The Royal Society of Chemistry.

1.3 Measurement of the heats of adsorption

Adsorption calorimetry is a surface technique that provides the measurement of a molecule's interaction energy with a surface as a function of coverage. This, in turn, provides information on

the state of a surface and the thermodynamic characteristics of the adsorption process [65]. Calorimetry has been applied widely used to characterize adsorbate-adsorbent interaction and solid adsorbents.

1.3.1 Heat of Adsorption

Based on different experimental procedures, meaning to keep variables such as gas volume (V^g), interfacial layer volume (V^s), and pressure constant during the experiment, various types of heats of adsorption are defined which differ by order of RT. This value is negligible for chemisorption and as high as 10% of the heat of physisorption; therefore, it is important to state the type of heat of adsorption for physisorption [66].

1.3.2 Integral heat of adsorption

Integral heat of adsorption is the produced amount of heat by the system upon adsorption amount at constant temperature and volume. Since the volume is constant, the volume-related work is zero, the integral heat of adsorption (Q^{int}) is calculated according to the first law of thermodynamics [67].

$$-Q^{int} = n\,(u - u^g) = n\,\Delta u_a \qquad 1\text{-}4$$

where n (mol) and u (kJ mol^{-1}) are the adsorbed amount and molar surface energy, respectively that can be defined based on either Gibbs dividing surface or interfacial layer models, u^g (kJ mol^{-1}) is the molar energy of the gas, and Δu_a is the molar change in internal energy upon adsorption.

1.3.3 Differential heat of adsorption

The differential molar heat of adsorption can be measured using a closed isothermal calorimeter. This calorimeter consists of two cells in a closed isothermal calorimeter. One cell is loaded with a known amount of sample and initially goes under vacuum while the other cell contains a known amount of gas at pressure p. Then the two cells are connected, and adsorbate get into contact with

the adsorbent until an equilibrium pressure is reached [67]. The differential heat of adsorption is related to the differential molar energy of adsorption ($\Delta\overline{u}_a$) according to

$$q^{diff} = -\Delta\overline{u}_a = \left(\frac{\partial Q^{int}}{\partial n}\right)_{T,m,V^g} \quad 1\text{-}5$$

where m (g) is the adsorbent mass and V^g (cm^3) is the volume of the gas phase. One can determine the differential heat of adsorption by calculating the slope of the plot of integral heat of adsorption as a function of the adsorbed amount. This plot can be obtained by repeating the aforementioned experimental procedure at different pressures [67].

1.3.4 Isosteric heat of adsorption

If the adsorption process occurs at constant pressure and temperature, the differential molar enthalpy of adsorption ($\Delta\overline{h}_a$), also called isosteric heat of adsorption (q_{st}), is defined as

$$\Delta\overline{h}_a = -q_{st} = -\left(\frac{\partial Q^{int}}{\partial n}\right)_{T,P,V^g} \quad 1\text{-}6$$

Since isosteric heat of adsorption is a differential quantity, it is more sensitive to adsorption potential than integral heat of adsorption as the adsorbed amount is changed [68]. Using a set of adsorption isotherms collected for a adsorptive-adsorbent system, isosteric heat of adsorption can be calculated according to the Clapeyron equation [66]

$$-\frac{q_{st}}{R} = \left(\frac{\partial \ln f}{\partial\left(\frac{1}{T}\right)}\right)_{\theta} - h^R \quad 1\text{-}7$$

Where θ is the surface coverage (adsorbed amount/monolayer capacity). For an ideal gas, the fugacity $f = P$ and the residual enthalpy $h^R = 0$. At the limit of zero coverage, the isosteric heat q_{st}^0 is calculated as

$$q_{st}^{0} = R\left(\frac{d \ln H}{d\left(\frac{1}{T}\right)}\right) \quad 1\text{-}8$$

$$H = \lim_{P \to 0}(d\theta/dP) \quad 1\text{-}9$$

where H is the Henry's constant. Since the difference between differential molar energy and differential molar enthalpy is the pressure times the molar volume of gas phase, the following holds for an ideal gas

$$q^{diff} - q_{st} \approx RT \quad 1\text{-}10$$

The value of isosteric heat of adsorption at specific pressure and temperature depends on the number of active sites on the surface and their corresponding binding energy. Usually, the calculated heat of adsorption for CO adsorbents with transition metal as binding site varies in the range of physisorption and chemisorption, i.e., 10-80 kJ/mol [69, 70].

Piper et al. studied the adsorption of CO on exfoliated graphite [68]. The integral heat of adsorption has been measured using an adiabatic calorimeter in which the changes of temperature (ΔT) and pressure (ΔP) are measured when an increment of gas is adsorbed in the calorimeter. The change in the integral heat was computed according to the following

$$\Delta Q^{int} = \left[C_{P,cal} + C_{P,ads} + C_{P,gas}\right]\Delta T - V_{cal}\Delta P \quad 1\text{-}11$$

where $C_{P,cal}$, $C_{P,ads}$, and $C_{P,gas}$ are the heat capacities of the calorimeter vessel and adsorbent combined, the adsorbed film, and the vapor phase in the calorimeter vessel. V_{cal} is the free volume of the calorimeter and $V_{cal}\Delta P$ is the heat of compression. The value of Q^{int} was obtained by summing the increments of ΔQ^{int} and the isosteric heat of adsorption was calorimetrically measured based on **Eq. 1-6** [71]. Using the classical Monte Carlo methods, the integral heat of adsorption at different coverages was calculated. It was confirmed that calculated Q^{int} was in good agreement with the experimental data.

Using the temperature dependence of q_{st}^{0} (or Q_{0}^{int}) it is possible to estimate the CO-graphite interaction potential and the nature of adsorbed phase [68]. Accordingly, it was found that the adsorbed layer is mobile. This; however, contradicted the deductions from the calculated entropy of adsorption that indicated the molecules are neither completely mobile nor completely localized on the surface [68].

Garrone et al. calculated isosteric heat of adsorption for adsorption of CO on TiO_2 by substituting generalized Temkin isotherm in Clausius-Clapeyron (**Eq. 1-7**). The integral heat of adsorption confirmed the nonideality of the adsorption by deviation from the ideal heat of adsorption (Q^{id}). Ideal heat of adsorption is the heat evolved in an ideal assembly of non-interacting particles. This is calculated through the summation of integral heat of adsorption and the repulsion energy [72, 73].

1.4 Adsorption model

1.4.1 Equilibrium isotherms

Adsorption isotherms describe the adsorption capacity of adsorbents by correlating the quantity of adsorbate to pressure or concentration of an adsorptive at a constant temperature.

1.4.1.1 Freundlich isotherm

The first empirical equation of adsorption isotherm was proposed by Freundlich in 1894 to describe the isothermal adsorption of a gas on a solid surface [74]

$$q = K_F P^{1/n_F} \qquad 1\text{-}12$$

q (ml g^{-1}) is the adsorbed amount, and K_F and n_F are the empirical constants dependent on the adsorbate-adsorbent system at a specific temperature. The value of K_F indicates the affinity of the adsorbate molecule to the surface of the adsorbent [75]. In other words, higher values of K_F mean more affinity towards a specific adsorbate at a specific temperature. The constant "n_F" indicates

the lateral interaction between the adsorbed molecules and the energetic surface heterogeneity, with higher values of n showing higher energetic heterogeneity of the surface [76]. The value of $1/n_F$ is almost always between 0 and 1. The lower the value of $1/n_F$, the lower the adsorption amount with increasing gas pressure [77]. When 1/n = 0, adsorption is independent of pressure, while $1/n_F = 1$ gives adsorption that is directly proportional to pressure. Freundlich isotherm can describe both monolayer and multilayer adsorption (i.e., chemisorption and physisorption, respectively) [78]. Freundlich isotherm has successfully been applied to many adsorption equilibrium data, including the adsorption of CO on in-situ brass formed on Cu/ZnO [79].

1.4.1.2 Langmuir isotherm

1.4.1.2.1 Single site Langmuir

In 1916, a model for adsorption of gases on solid surfaces was proposed by Irving Langmuir by considering the adsorption-desorption equilibrium (dynamic equilibrium). Langmuir adsorption isotherm is widely used to describe the equilibrium adsorption of molecules in liquid or gas phase to solid surfaces [80]. Some of the assumptions in this model include: 1-All the adsorption sites have the same binding energy, 2-There are no interactions between the adsorbed molecules, and 3-Adsorptive adsorbs only on the vacant sites; in other words, the adsorption capacity is limited to only a monolayer. The following is the Langmuir isotherm equation [80, 81]

$$q = \frac{NK_L C_e}{1 + K_L C_e} \quad \text{1-13}$$

where C_e (mg L^{-1}) is the concentration of adsorbate at equilibrium, N (mol kg^{-1}) is the number of binding sites, and K_L (L mg^{-1}) is the Langmuir constant and is related to the binding energy. Traditionally, the value of the equilibrium constant is calculated as the following [81]

$$\frac{1}{q} = \frac{1}{K_L N C_e} + \frac{1}{N} \quad \text{1-14}$$

The parameters N and K_L can be calculated from linear regression by plotting 1/q versus $1/C_e$ [80-82]. The Langmuir isotherm equations can be written for pressure by merely replacing the C_e with P.

Langmuir adsorption isotherm has been used in many studies of CO adsorption on different adsorbents to investigate the interaction of CO with the surface of adsorbent material. In a study of selective adsorption of CO on CuCl/AC [7, 23], the equilibrium adsorption data was successfully fitted to the Langmuir isotherm equation. There are, however, other studies such as the adsorption of CO on CuCl/bayerite [6] and CO binding on metal-organic framework (MOF-74) [83] that this model does not apply well to the equilibrium data since the model neglects heterogeneity in adsorption sites.

1.4.1.2.2 Multiple site Langmuir

Linear combination of multiple Langmuir isotherms can model a homotattic surface. This homotattic surface is made of multiple patches. Within one patch, all the binding sites have the same binding energy (**Figure 1-8**) [80, 84]. Considering gas adsorption on a crystal, the adsorbate surface binding energy on one crystallographic termination will differ from those of other crystallographic terminations. For an adsorbent with homotattic surface composed of n different patches, the Langmuir equation can be written as [85]

$$q = \sum_{i=1}^{n} q_n = \sum_{i=1}^{n} \frac{N_i K_{L,i} C_e}{1 + K_{L,i} C_e} \qquad 1\text{-}15$$

where q_n (mol kg^{-1}) is the adsorbed amount on one specific set of adsorption sites on a patch. **Figure 1-8** compares single-site and multiple site Langmuir isotherms. The values of N_i and $K_{L,i}$ can be calculated using regression analysis. Some examples of homotattic surfaces include carbon structures and metal-organic frameworks with bimodal or trimodal pore size distribution [80].

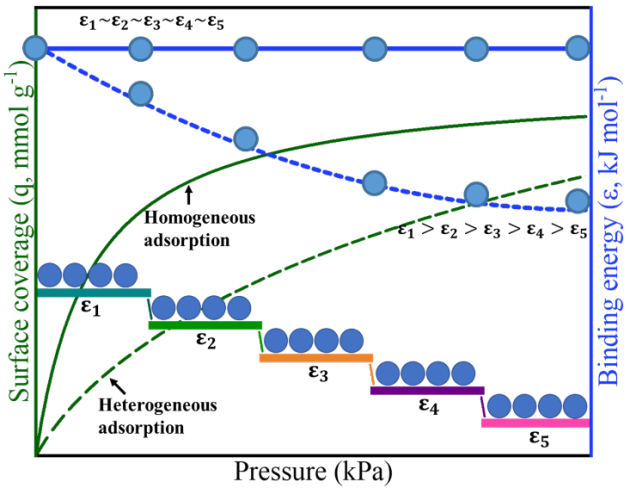

Figure 1-8 Homogeneous vs. homotattic (heterogeneous) adsorption. Reproduced/adopted from Ref [80] with permission from The Royal Society of Chemistry. Copyright 2019 The Royal Society of Chemistry.

For MOFs, disregarding the surface chemistry, each pore size can be considered as a homotattic surface patch with the assumption that the interaction potential inside the pores is uniform. The dual-site Langmuir has been applied to describe the adsorption of CO on Cu(I) and vanadium modified MIL-101(Cr) (**Figure 1-9a**) [12]. Bloch et al. fitted the CO adsorption data of M_2(dobdc) MOF with metal cores of Mg, Mn, Fe, Co, Ni, and Zn to a triple-site Langmuir model. The adsorption isotherms plotted in a logarithmic pressure scale emphasize the capability of multiple site Langmuir isotherm in describing the CO adsorption on M_2(dobdc) at the low-pressure end (**Figure 1-9b**) [83].

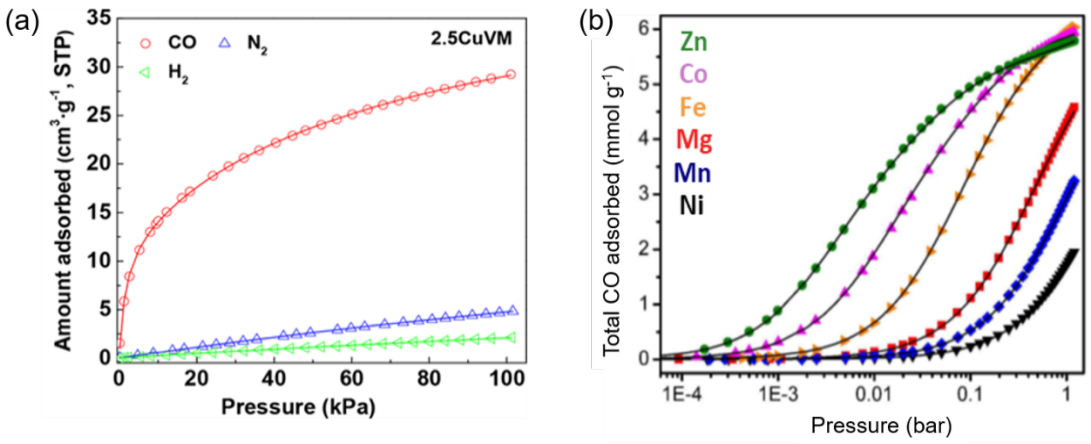

Figure 1-9 Pure gas adsorption isotherms of (a) Cu(I)V(IV)/MIL-101(Cr) fitted to dual-site Langmuir and (b) MOF-74(M) fitted to triple-site Langmuir. Reprinted with permission from Ref [12]. Copyright 2019 American Chemical Society. Reprinted with permission from Ref [83]. Copyright 2014 American Chemical Society.

1.4.1.3 Temkin isotherm

Temkin isotherm assumes structural heterogeneity for a given surface with non-interacting adsorption sites with constant distribution of adsorption energies between a maximum value, X_M (J mol^{-1}) and zero. For any kind of non-interacting sites, a local Langmuir isotherm holds. Temkin isotherm is applicable only in an intermediate range of pressure and assumes a linear decrease in heat of adsorption with surface coverage. The general form of Temkin isotherm is as follows

$$\theta = \frac{N_a}{N_m} = \left(1 - \frac{RT}{X_M} \ln a\right) + \frac{RT}{X_M} \ln P \qquad 1\text{-}16$$

where θ is the surface coverage, N_a is the adsorbed amount (molecules/nm^2), N_m is the monolayer capacity (molecules/nm^2), and "a" is a parameter related to standard entropy change upon adsorption (ΔS^0, J mol^{-1} K^{-1}) and is the same for all kinds of sites [72, 73].

$$\Delta S^0 = R - R \ln a \qquad 1\text{-}17$$

By assuming a constant distribution of adsorption energies in a narrow energy range rather than between a maximum value, X_M (J mol^{-1}) and zero, Garrone et al. proposed a generalization of Temkin isotherm that is applicable when heterogeneity is both structural (i.e., surface

functionalities such as hydroxyls) and induced (the interaction among adsorbed species). **Eq. 1-18** is the generalization of the Temkin isotherm.

$$N_a = K_1 \ln(1 + K_2 P) \quad \text{1-18}$$

$$K_1 = \frac{N_M RT}{X_2 - X_1};\ K_2 = \frac{\exp\left(\frac{X_2}{RT}\right)}{a} \quad \text{1-19}$$

where X_2 and X_1 (J mol^{-1}) are adsorption energies ($X_2 > X_1$). The generalized Temkin isotherm has been successfully applied to describe the adsorption of CO on group IV transition metal dioxides [72, 73].

1.4.1.4 Sips isotherm

1.4.1.4.1 Single site Sips isotherm

Sips isotherm is the combined form of Langmuir and Freundlich (LF) isotherm that was proposed by Sips as an empirical expression [86]. In this model, the non-dissociative adsorption of molecules is assumed [80]. Its mathematical form can be written as

$$q = \frac{q_m k_S p^{n_S}}{1 + k_S p^{n_S}} \quad \text{1-20}$$

q_m (mol kg^{-1}) is the maximum adsorption amount, k_S (kPa^{-1}) is the adsorption affinity, and n_s is a dimensionless number related to the heterogeneity of the adsorbate-adsorbent system. This model is suitable for predicting adsorption on heterogeneous systems. Unlike Freundlich isotherm, the adsorption amount does not increase indefinitely as gas pressure goes up [86, 87]. As one can see from the Sips isotherm equation, Sips isotherm reduces to Freundlich isotherm at very low pressures, whereas it predicts the Langmuir monolayer adsorption characteristic at higher pressures; therefore, it shall be used only to describe the monolayer adsorption systems [86, 88].

1.4.1.4.2 Dual site Sips

Dual-site Sips (also called dual-site Langmuir-Freundlich (DSLF)) is an extension of Sips isotherm for heterogeneous adsorption on two different adsorption sites. Naturally, two terms are involved [10, 89-93]

$$q = q_{m_1} \frac{k_{S1} p^{n_{S1}}}{1 + k_{S1} p^{n_{S1}}} + q_{m_2} \frac{k_{S2} p^{n_{S2}}}{1 + k_{S2} p^{n_{S2}}} \quad 1\text{-}21$$

where q_{m1} and q_{m2} are the saturation capacities of sites 1 and 2. k_{S1} and k_{S2} are the affinity coefficients of site 1 and 2, respectively. $n_{s,1}$ and $n_{s,2}$ represent the heterogeneity of the surface. p is the pressure of bulk gas equilibrated with the adsorbed phase. Dual-site Sips, unlike multiple-site Langmuir, considers the continuous exponential decay in binding energy with increasing surface coverage. This model has been applied in many studies to describe the adsorption of different gases (i.e., CO, CO_2, CH_4, C_3H_6, and C_3H_8) onto the surface of porous adsorbents [9, 10, 89-94]. It should be mentioned that the application of dual-site Sips isotherm is not restricted by pore size distribution. Using this dual-site Sips model, Chen et al. fitted the CO_2 adsorption data of MOF-505@GO with unimodal distribution [95]. Likewise, Al-Naddaf et al. used this model to fit adsorption of both CO_2 and CO on zeolite-5A@MOF-74 (**Figure 1-10a**) [55]. Vo et al. applied the same model to CO adsorption on Cu(I)-doped MIL-100(Fe) with a tri-modal distribution [10] (**Figure 1-10b**). Other studies of adsorption of CO on MIL-100(Fe) reported a good fitting to dual-site Sips isotherm (R^2 >0.9995) [9, 92].

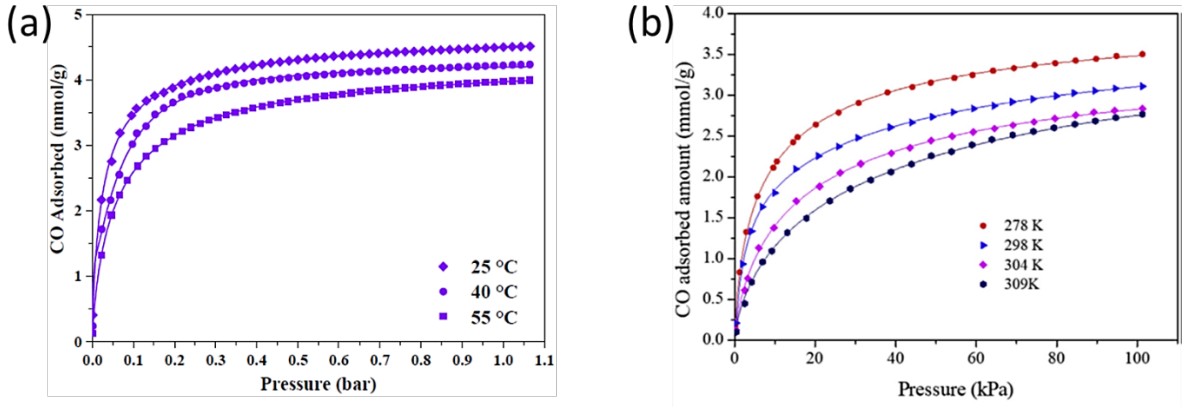

Figure 1-10 Pure CO gas adsorption isotherms of (a) Zeolite-5A@MOF-74 and (b) Cu(I)/MIL-100(Fe) fitted to dual-site Sips isotherm. Reprinted with permission from Ref [55]. Copyright 2018 American Chemical Society. Reprinted with permission from Ref [10]. Copyright 2018 Elsevier.

1.4.1.5 Toth isotherm

The Toth equation is a three-parameter empirical modification of the Langmuir equation used to describe adsorption on heterogeneous surfaces with sub-monolayer coverage [96-98]. Freundlich isotherm is invalid at low and high ends of pressure, and Sips isotherm is not valid at the low end since they do not have the correct Henry-Law-Type behavior [87, 96]. Henry-Law-Type behavior is a linear relationship between partial pressure and the adsorbed amount since adsorbed molecules are isolated from their neighbors at low gas pressures. Toth empirical isotherm overcomes the high and low ends pressure limitations of Freundlich and Sips isotherm. Toth isotherm is expressed as follows [97]

$$q = \frac{q_m K_T P}{(1 + (K_T P)^{n_T})^{\frac{1}{n_T}}} \qquad 1\text{-}22$$

where q_m (mol kg^{-1}) is the maximum adsorption capacity, K_T (kPa^{-1}) is a constant for the binding affinity between adsorbate-binding site pairs, and n_T is the Toth isotherm exponent. When $n_T = 1$, the Toth isotherm reduces to Langmuir isotherm that shows adsorption on a homogeneous surface; therefore, n characterizes the heterogeneity of the adsorption system, and deviations from unity imply the heterogeneity of the system.

In conclusion, there are many candidate adsorption models, and the critical step is to find a suitable model that fits the data over the pressure range of interest. Therefore, it is necessary to consider various adsorption models with the knowledge of their assumptions. Pre-determined characteristics of the adsorbent will help researchers narrow down the choices for realistic application [98].

1.4.2 Competitive coadsorption

In real conditions, usually, there are several adsorbates present in the adsorption systems. The adsorbates generally compete for adsorption sites with a high heat of adsorption. The selectivity of adsorbents, efficiency of separation, and heterogeneous catalysis highly depend on competitive adsorption; therefore, the understanding of competitive or multicomponent adsorption is of great importance. It should be noted that the effect of adsorption conditions such as temperature and pressure in both equilibrium and dynamic conditions are more significant in competitive adsorption. This is due to the difference in adsorbates diffusion rates, kinetics and free energy of adsorption, and their nature of interaction with the surface and medium [99].

The competitive adsorption can be described using different mathematical models such as the extensions of Langmuir and Temkin models (Langmuir and Temkin formalisms) for the co-adsorption of gas mixtures. The extended Langmuir model for competitive adsorption was developed by Butler and Ockrent (1930). This model assumes homogeneity of adsorption sites with respect to adsorption energy, no interaction between the adsorbed species, and equal availability of adsorption sites for all adsorbed species. Multi-component Extended Langmuir (MCEL) equation can be written as [100, 101]

$$\theta_i = \frac{K_{EL,i}(E_i)P_i}{1 + \sum_{j=1}^{n} K_{EL,j}(E_j)P_j} \qquad 1\text{-}23$$

Where i and j represent adsorbate species, θ_i is the surface coverage of adsorbed species i, K_{EL} (kpa^{-1}) is the adsorption coefficient of adsorbates with the heat of adsorption E (kJ/mol), and P_i and P_j are the adsorption pressure of species i and j, respectively. Competitive Langmuir model for a binary mixture of gases with dissociative adsorption of species A and dissociative or non-dissociative adsorption of species B, is according to [102]

$$\theta_A = \frac{K_{EL,A}(E_A)P_A}{1 + K_{EL,A}(E_A)P_A + \left(K_{EL,B}(E_B)P_B\right)^{1/\xi}} \quad 1\text{-}24$$

And

$$\theta_B = \frac{\left(K_{EL,B}(E_B)P_B\right)^{1/\xi}}{1 + K_{EL,A}(E_A)P_A + \left(K_{EL,B}(E_B)P_B\right)^{1/\xi}} \quad 1\text{-}25$$

Where ξ = 1 or 2 for non-dissociative or dissociative adsorption of species B, respectively.

Temkin model formalism considers: (a) competitive Langmuir (**Eq. 1-24**, and **Eq 1-25**) holds for each group of sites with the same adsorption properties and (b) a uniform distribution of the sites with the assumption that heat of adsorption of each species follows the Temkin model in the absence of competitive adsorption. Accordingly, different mathematical expressions are proposed for competitive chemisorption, considering the non-dissociative adsorption of species. Couble et al. [102] developed a mathematical formalism of the Temkin model for competitive adsorption of binary gas mixtures on a heterogeneous surface in the absence of reaction (i.e., non-dissociative adsorption of CO and dissociative adsorption of H_2 on the Pt sites of 2.9%Pt/Al_2O_3 catalyst; see equations 24 and 25 in Ref [102]). Experimental data of surface coverage by linear CO adsorbed species competitive chemisorption with dissociated hydrogen species in CO/H_2 gas mixture was used to support the development of the Temkin model for competitive chemisorption. Comparing the developed Temkin model with models based on the Langmuir formalism showed its advantage for large ranges of adsorption temperature and partial pressure [102]. The developed model has

further been extended by considering the presence of chemical reaction in which linear adsorbed CO species are intermediate species in the formation of CH_4 from CO/H_2 reaction at temperatures higher than 500 °C [103].

1.4.3 Dynamic models

Successful column design and description of adsorption mechanism in a dynamic process require prediction of the breakthrough curve and kinetics of adsorption.

1.4.3.1 Breakthrough models

1.4.3.1.1 Thomas model

Thomas model is the most commonly used model to establish the breakthrough curve and determine the maximum adsorption capacity of an adsorbent. This model is proposed based on assumptions of no axial dispersion and Langmuir kinetics of reversible adsorption that rate-driving forces follow pseudo-second-order kinetics [104, 105]. The linear form of the Thomas model is expressed as

$$\ln\left(\frac{C_0}{C_t} - 1\right) = \frac{k_{Th} q_{Th} m}{Q} - k_{Th} C_0 t \qquad 1\text{-}26$$

where C_0 is the initial concentration of the adsorbate (mg L^{-1}), C_t is the adsorbate concentration at time t, k_{Th} is the Thomas constant (L min^{-1} mg^{-1}), q_{Th} is the equilibrium uptake (mg g^{-1}), m is the mass of the adsorbent (g), and Q is the flow rate (mL min^{-1}).

1.4.3.1.2 Adams-Bohart model

Bohart and Adams proposed a model establishing the relationship between concentration ratio (C_t/C_0) and time for a continuous adsorption system. This model assumes that the adsorption bed is homogeneous and equilibrium is not instantaneous; therefore, the rate of adsorption depends on the concentration of adsorptive and residual capacity of adsorbent [104-106]. The Bohart-Adams model is used to describe the initial part of the breakthrough curve and is expressed as

$$\frac{C_0}{C_t} = \exp(k_{AB}C_0 t - k_{AB}N_0\frac{Z}{\nu}) \quad 1\text{-}27$$

where k_{AB} is the kinetic constant of the Bohart-Adams model (L mg^{-1} min^{-1}), ν is the linear velocity (cm min^{-1}), N_0 is the saturation concentration (mg L^{-1}), and Z is the bed height (cm).

1.4.3.1.3 Yoon-Nelson model

Yoon-Nelson model assumes that the rate of decrease in the probability of adsorption for each adsorbate molecule is proportional to the probability of adsorbate adsorption and the probability of adsorbate breakthrough on the adsorbent [105, 107, 108]. This model is simple in comparison to other models and does not require details such as adsorbate characteristics, type of adsorbent, and physical properties of the adsorption bed. Yoon-Nelson model is given below

$$\ln\left(\frac{C_t}{C_0 - C_t}\right) = k_{YN}t - \tau k_{YN} \quad 1\text{-}28$$

where k_{YN} is the rate constant (min^{-1}), and τ is the time required for 50% adsorbate breakthrough (min).

1.4.3.1.4 Clark model

The Clark model assumes that the process follows a Freundlich isotherm for equilibrium and the shape of the mass transfer zone is constant. However, this model also holds for systems with a variable mass transfer zone [108]. Equation 25 shows the Clark model.

$$\frac{C_t}{C_0} = \left(\frac{1}{1 + Ae^{-rt}}\right)^{1/(n-1)} \quad 1\text{-}29$$

where A and r (min^{-1}) are the Clark's model constants, and n is the Freundlich constant. The value of n can be calculated experimentally according to adsorption isotherm.

1.4.3.2 Kinetic models

1.4.3.2.1 Pseudo-first-order model

The pseudo-first-order or Lagergren's kinetic model assumes a reversible interaction with an established equilibrium between adsorbate and the surface of the adsorbent. Based on the adsorption capacity and the number of available adsorption sites, this model describes the rate of adsorbate amount change. It assumes the physisorption of gas molecules onto the surface. The pseudo-first-order equation is reproduced here [26, 109, 110]

$$\ln(q_e - q_t) = \ln(q_e) - k_1 t \qquad 1\text{-}30$$

where q_e and q_t (mg g^{-1}) are equilibrium adsorption amount and adsorption amount at time t (min), respectively. k_1 (min^{-1}) is the pseudo-first-order kinetic constant. The values of q_e and k_1 can be calculated by determining the intercept and slope of the linear plot of $\ln(q_e\text{-}q_t)$ versus t.

1.4.3.2.2 Pseudo-second-order model

In the pseudo-second-order model, one adsorbate molecule takes up two adsorption sites [111-113]. The adsorption rate is related to the number of available adsorption sites, and chemisorption is assumed to be the rate-limiting step [110]. It is also assumed that adsorption is influenced by the chemical potentials of both the adsorbent surface and the adsorptive [24]. The pseudo-second-order equation is given as [25, 26, 110]

$$\frac{t}{q_t} = \frac{1}{k_2 q_e^2} + \frac{t}{q_e} \qquad 1\text{-}31$$

where k_2 (g mg^{-1} min^{-1}) is the pseudo-second-order rate constant for the adsorption process. q_e and q_t (mg g^{-1}) are the adsorption amounts at equilibrium and time t (min). The values of k_2 and q_e can be determined from a linear plot of t/q_t versus t. **Figure 1-11ab** shows the fitting of kinetic data of CO on Ni/Al_2O_3 composite to the pseudo-first-order and pseudo-second-order model at 305 K. The calculated coefficient of determination (R^2) of the pseudo-second-order model is greater than

that of the pseudo-first-order model. Furthermore, the calculated value of equilibrium adsorption amount, q_e, from the pseudo-second-order model showed a better agreement with experimental equilibrium capacity, as illustrated in **figure 1-11c**. Accordingly, it is considered that the pseudo-second-order model explains the adsorption of CO on Ni/Al_2O_3 better than the pseudo-first-order model. However, this conclusion can be misleading and require more investigation to be confirmed.

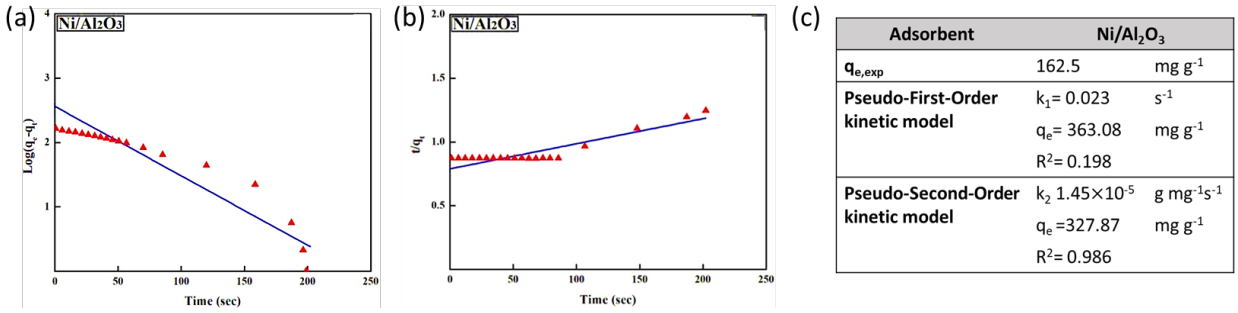

(c)

Adsorbent	Ni/Al_2O_3	
$q_{e,exp}$	162.5	mg g^{-1}
Pseudo-First-Order kinetic model	k_1= 0.023	s^{-1}
	q_e= 363.08	mg g^{-1}
	R^2= 0.198	
Pseudo-Second-Order kinetic model	k_2 1.45×10^{-5}	g $mg^{-1}s^{-1}$
	q_e =327.87	mg g^{-1}
	R^2= 0.986	

Figure 1-11 Adsorption kinetics of CO on Ni/Al_2O_3. (a) Pseudo-first-order model analysis, (b) Pseudo-second-order model analysis, and (c) Experimental adsorption amounts and kinetic model predictions. Reprinted with permission from Ref [5]. Copyright 2020 American Chemical Society.

It is crucial to understand the assumptions of the pseudo-second-order model before starting data fitting. The assumptions are (i) reaction-controlled adsorption, (ii) constant adsorptive concentration, and (iii) no desorption [114]. The analysis can often mislead if one looks only at the determination coefficient of data fitting to equation 27. This is because the linear plot of t/q_t against t often results in a very high determination coefficient regardless of the true working model [114]. In a typical adsorption experiment, with time, the adsorption rate decreases due to the occupation of vacant sites. If the experimental data is collected over a long time, the variation of time is much larger than that of adsorption capacity (q_t), which results in a high value of determination coefficient. To prevent the erroneous application of this model, Xiao et al. recommended three steps: verification of assumptions of a model, fitting of the experimental data

to the nonlinear form of the model, inspection of the residual plot to assess the goodness of fit according to the following equation [114].

$$\text{standardized residual} = \frac{q_t - q'_t}{s} \quad 1\text{-}32$$

where q'_t (mg g^{-1}) is the adsorbed amount at time t calculated by the model, and s (mg g^{-1}) is the standard deviation of residuals.

1.4.3.2.3 Elovich model

In reactions that involve the adsorption of species on the surface of a solid without desorption of products, the adsorption rate decreases with time due to an increase of surface coverage [115]. Elovich model is suitable for such a case. Zeldowitsch established the kinetic law of chemisorption by describing the rate of adsorption of CO on MnO_2 [116]. The proposed model by Zeldowitsch, commonly called the Elovich model, assumes chemisorption of species on an energetically heterogeneous surface [109, 110, 116]. The model can explain reaction mechanisms, including bulk and surface diffusion and activation-deactivation of catalytic surfaces [117]. The adsorption amount changes over time according to the following equation

$$\frac{dq}{dt} = \alpha \exp(-\beta q) \quad 1\text{-}33$$

where q is the adsorbed amount at time t, α (mmol g^{-1} min^{-1}) is the initial adsorption rate, and β (g $mmol^{-1}$) is the desorption constant which depends on temperature and pressure. Assuming no adsorption at t=0, the integrated form of the equation is

$$q = \frac{1}{\beta}\ln(t + t_0) - \frac{1}{\beta}\ln t_0 \quad 1\text{-}34$$

where $t_0=1/\alpha\beta$. In case of instantaneous adsorption of a gas volume, q_0, Elovich equation is modified to

$$q = \frac{1}{\beta}\ln(t + k) - \frac{1}{\beta}\ln t_0 \qquad 1\text{-}35$$

where $k = t_0 \exp(\beta q_0)$. Usually, k is considered an adjustable parameter and varies to get the best fit of q versus ln(t+k). Gamboa et al. [118]analyzed the adsorption kinetics of CO on Co_3O_4 using the Elovich model at different initial pressures and temperatures. The calculated values of α and β expressed a very fast initial adsorption rate due to physisorption followed by a slow adsorption rate that is independent of pressure but dependent on temperature and time [118]. **Figure 1-12a** shows the Elovich plots at different temperatures for adsorption of CO on alumina [119]. According to the calculated Elovich parameters, the rate of CO adsorption mainly depends on the value of β. It can be seen from the figure that the adsorption rate at 151 °C is slower than other temperatures. The fitting of Elovich model indicates two distinct adsorption processes that involve two types of surface sites [119].

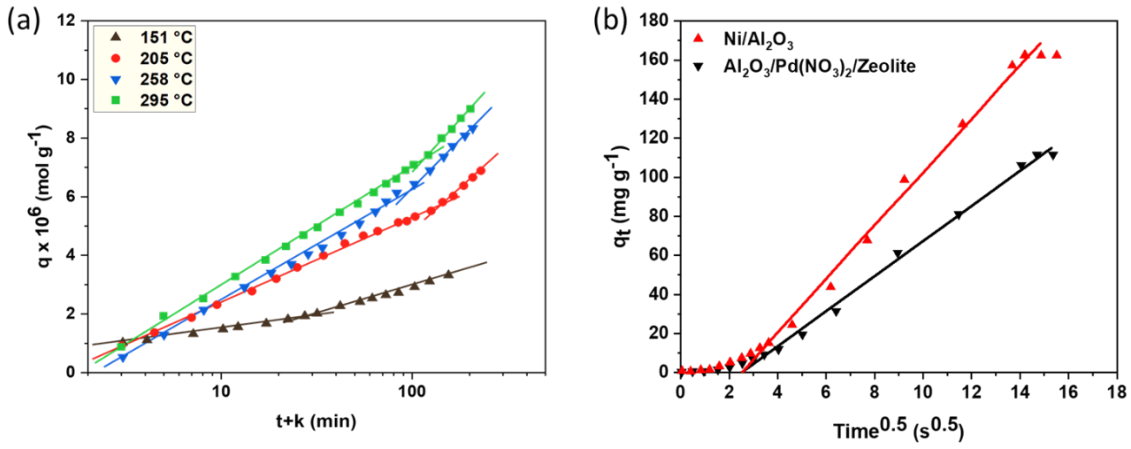

Figure 1-12 (a) Elovich plot of CO adsorption kinetics on Al_2O_3 at different temperatures. Reprinted with permission from Ref [119]. Copyright 1972 American Chemical Society. (b) Intraparticle diffusion kinetic model for CO adsorption on Ni/Al_2O_3 [5], and $Al_2O_3/Pd(NO_3)_2$/Zeolite [26]. Reprinted with permission from Ref [5]. Copyright 2020 American Chemical Society.

1.4.3.2.4 Intraparticle diffusion

The intraparticle diffusion model, or Morris-Weber kinetic model, is used when adsorption kinetics is influenced by diffusion from the surface of the adsorbent into the pores. The influence of mass transfer resistance on the binding of species onto the adsorbent surface can be investigated by this model [5, 110, 120]. This model can describe the adsorption process that includes external surface adsorption (instantaneous adsorption), diffusion inside the pores (gradual adsorption), and equilibration step that is the slow movement of adsorbates from larger pores to micropores. This model states that

$$q_t = k_d t^{0.5} + C \qquad 1\text{-}36$$

q_t (mg g^{-1}) is the adsorbed amount at time t, k_d (mg g^{-1} $s^{-0.5}$) is the intraparticle diffusion rate constant, and the value of C (mg g^{-1}) corresponds to the thickness of the boundary layer. The linearity or multi-linearity in the plot of q_t versus $t^{0.5}$ indicates the involvement of intraparticle diffusion in the mechanism of the adsorption process. Moreover, if the graph passes through the origin, there will be no external diffusion resistance for adsorptive molecules making intraparticle (internal) diffusion the rate-limiting step [121].

As in the case of equilibrium adsorption isotherms, to describe the kinetics of adsorption with high accuracy, different models should be tested. In many adsorption studies, including adsorption of CO, these models have been used as a complement to one another to describe the adsorption process. Since both pseudo-first-order and pseudo-second-order models do not consider diffusion, the intraparticle diffusion model is used to estimate the contribution of diffusion. There are only a few kinetic studies on CO adsorption. Mozaffari et al. [5, 26] investigated the CO adsorption kinetics on alumina support by fitting the adsorption data to pseudo-first-order, pseudo-second-order, and intraparticle diffusion kinetic model. **Figure 1-12b** shows the involvement of

intraparticle diffusion as the main mechanism of adsorption of CO on Ni/Al_2O_3 and $Al_2O_3/Pd(NO_3)_2$/Zeolite. Since all the plots begin from the origin, the intraparticle diffusion is considered to be the rate-limiting step in the adsorption process [5, 26]. Generally, the multilinearity in the fitting of the intraparticle diffusion model indicates different stages of adsorption, such as external mass transfer and intraparticle diffusion into the pores [110]. It should be mentioned that in many cases, the dynamic adsorption measurements have been performed mainly to confirm the results obtained from equilibrium adsorption data [9, 64, 122].

1.5 Mechanism of adsorption of CO

Many metals have been studied for the adsorption of carbon monoxide since it provides an adsorption system with the complete non-dissociative chemisorption of a diatomic molecule on a metal surface. The high stability of carbon monoxide, with bond-dissociation energy of 1074 kJ mol^{-1}, leads to non-dissociative chemisorption of this molecule on a metal surface [123]. In many cases, infrared absorption of metal carbonyls and adsorbed CO shows stretching of the CO bond that is due to the weakening of CO bond as a result of electron donation into antibonding orbitals of the CO molecule. The bonding ability of CO to metal atom depends on the relative availability of vacant and filled d orbitals of metals with correct symmetry [123]. For the bridged carbonyl complex such as $Fe_2(CO)_9$, the overlapping of the CO orbitals with d orbitals of two Fe atoms fulfills these conditions easily. Adsorption of CO has been investigated on transition metals such as groups VIb, VIII, and Ib. Adsorption of CO on transition metals starts by lone pair electron donation from the carbon atom into the vacant d orbital of the metal atom (**Figure 1-13a**). Lewis basicity of CO is low, and stabilization of the metal-carbon bond is obtained through pi-backdonation of d orbitals of metal to the CO molecule (**Figure 1-13b**). **Figure 13** shows a schematic of pi-complexation between the group Ib element, copper, and CO molecule (Blyholder

model) [124]. It should be mentioned that the anion electronegativity (e.g., Cl^- and O^- in CuCl and Cu_2O, respectively) is important for the pi-complexation mechanism since high electronegativity of the anion leads to cations with high positive charges that are better acceptors in pi-complexation [125].

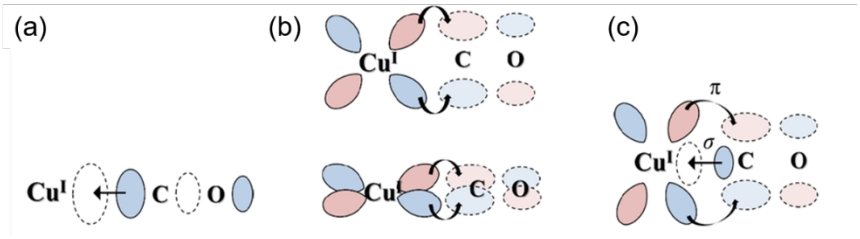

Figure 1-13 Schematic of pi-complexation between Cu(I) and CO molecule. (a) CO lone pair electron donation, (b) pi-backdonation of metal to CO, and (c) overall interaction. Reprinted with permission from Ref [9]. Copyright 2018 Elsevier.

One of the most studied cases of metals is tungsten. Rideal et al. did the first systematic study of adsorption of carbon monoxide on Tungsten in 1950 [123]. In this study, they measured the isosteric heat of adsorption of CO using the adsorption isotherm data obtained at multiple temperatures with the lowest at -195 °C and the highest 20 °C. The value of isosteric heat of adsorption varied with increasing coverage of surface from 61.9 to 15 kJ mol^{-1}. These values suggest the process of transition from chemisorption into physisorption. By comparing adsorption isotherms of oxygen, hydrogen, and CO at low temperatures, it was revealed that there are two types of adsorption sites (α sites and β sites, **Figure 1-14**). It is suggested that the multiplicity of β state of adsorption could be due to adsorption on different crystalline planes with varying energies of adsorption and interatomic spacing. α adsorption could arise from adsorption on less preferred crystal planes. Accordingly, β adsorption occurs first with preferred sites, followed by α adsorption [126].

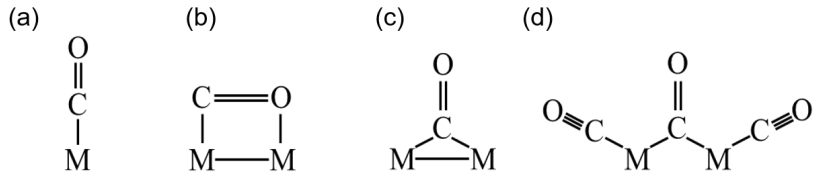

Figure 1-14 (a) Possible single site (α site) adsorption complex. (b), (c), and (d) Possible two-site (β site) adsorption complex. Reprinted with permission from Ref [123]. Copyright 1970 Elsevier.

According to the proposed model of CO adsorption on transition metal surfaces by Fohlisch et al., for systems of bonding to transition metals through π orbital interaction and metal d states, there is a delicate balance between the π bonding interaction and the σ repulsion within the bond that determines the strength and nature of bonding and geometric structure [124, 127]. In case of having a weak π interaction, the repulsion dominates for sites with higher coordination which favors adsorption on atop site. However, Pd is an exception which, according to DFT calculations, the hollow site is the preferred adsorption site.

In a study of CO adsorption on Pt (111) surface using Density Functional Theory (DFT), Lakshmikanth et al. [124] investigated the adsorption sites, energy, and the effect of van der Waals interaction on CO/Pt (111) system. The DFT results showed that atop site was the preferred adsorption site for CO. The predicted adsorption energy values and site-preference order was in agreement with experimental results.

Based on the DFT study on the trends of CO adsorption on transition metals (Ni, Cu, Ru, Rh, Pd, Ag, Ir, Pt, and Au), the number of available d electrons and the principal quantum number of the valence shell has a direct positive relation with the vibrational stretching frequency of the C-O bond [128]. This is inconsistent with the classical Blyholder model and in agreement with the interpretation that σ-repulsion and π-backbonding occur [129]. According to Constantinos et al., the DFT calculated CO adsorption energies on transition metal clusters were in good agreement

with experimental data except for Au, which was overestimated but in agreement with other computational studies [128].

Investigation of Lewis acidity of surface provides an understanding of the behavior of surface with respect to adsorbate. Metal oxides can interact with the carbon end of CO through coordinatively unsaturated cations that act as strong electron-withdrawing centers. For non-d metal oxides where back donation does not exist, a strong σ-dative bond is formed as a result of partial emptying of the weakly antibonding 5σ lone pair orbital [130]. The type of coordinatively unsaturated cations depends on crystalline modification, preparation method, and heat treatment of the surface.

Garrone et al. investigated the type of σ-coordinated CO adsorbed on TiO_2 using IR spectroscopy and adsorption microcalorimetry [72]. The spectroscopic and energetic results and adsorption isotherms reveal the formation of up to two σ-coordinated species, one of which shows ideal behavior and the other showing non-ideality. According to Bolis et al. [131], group 4 metal oxides exhibit structural and induced heterogeneity towards CO adsorption. These depend on the geometrical structure of the site, presence of charge donating (e.g., hydroxyl group), or charge withdrawing (e.g., SO_4^{2-}) species, and surface coverage by CO molecules. The heterogeneity causes shifts in CO peak positions in vibrational spectroscopy, makes adsorption partial molar enthalpy decrease with coverage, and has isotherms follow the generalized Tempkin model [72].

Figure 1-15 shows the IR spectra of adsorbed CO on sulfate-free (**Figure 1-15a**) and sulfate-doped TiO_2 (**Figure 1-15b**) heat-treated at 673 K at high to low pressures. The comparison shows two peaks versus one peak behavior for adsorbed CO on sulfate-free and sulfate-doped TiO_2, respectively. Furthermore, Garrone et al. reported only one band in IR spectra from sulfate-free TiO_2 that was heat-treated at temperatures below 420 K. The frequency at zero coverage (ν_0, cm^{-1}) also changes due to adsorbent thermal pretreatment.

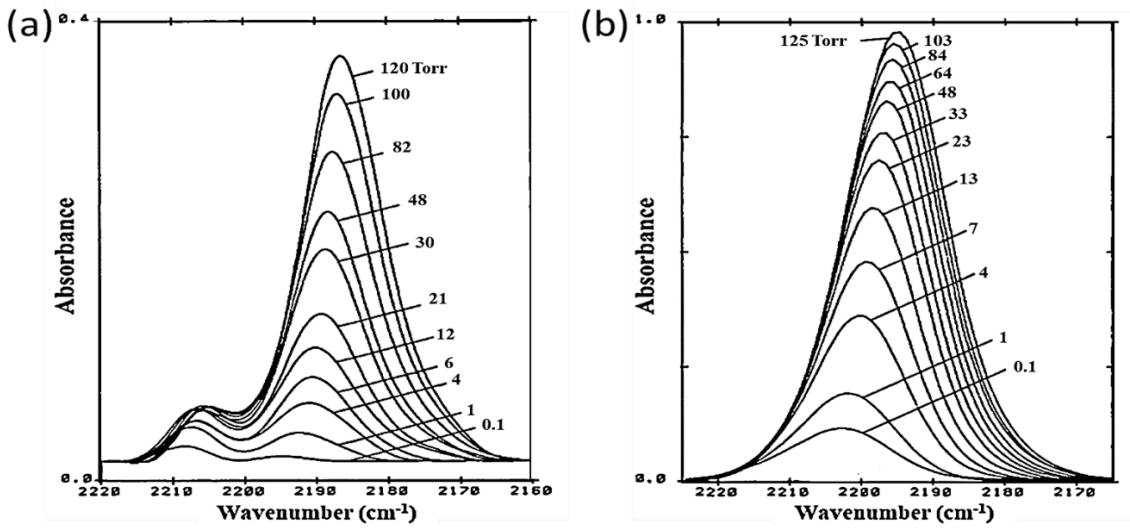

Figure 1-15 Infrared spectra of CO adsorbed on (a) sulfate-free TiO_2, (b) sulfate-doped TiO_2 at decreasing pressures. Reprinted with permission from Ref [72]. Copyright 1989 American Chemical Society.

Volumetric adsorption isotherms can be obtained using the intensity of IR spectra. In the case of a single band in IR spectra (**Figure 1-15b**), volumetric adsorption isotherm is equivalent to optical isotherm (i.e., the integrated absorbance versus equilibrium pressure). The integrated absorbance (A) relates to the adsorbed amount according to Beer-Lambert law (for homogeneous systems) or a posteriori Beer-Lambert (for heterogeneous systems) [130]. The contribution of each adsorbed species in overall uptake can be distinguished by the decomposition of volumetric isotherm using the molar extinction coefficient (ε, cm mol^{-1}). The molar extinction coefficient is an intrinsic property of chemical species and is obtained by comparing optical and volumetric isotherms [132]. Accordingly, Bolis et al. calculated the molar extinction coefficients of different CO adsorbed species on zirconia to distinguish the contribution of each adsorbed species in overall uptake. It should be mentioned that the calculation of molar extinction coefficients was based on the assumptions that the frequencies and pre-heat treatment of samples do not change with surface coverage [132]. In their more recent works, Bolis et al. confirmed a linear dependence of molar

extinction coefficient with the frequency of CO adsorbed on HfO_2, ZrO_2, and TiO_2 [73] and accordingly calculated the contribution of each species in total CO ad-amounts [131].

A combined DFT and FTIR study of CO adsorption on Anatase nanocrystals enabled assignment of the features of IR spectra of adsorbed CO through the calculation of vibrational properties of CO adsorbed on (101), (100), (001), and (112), and surface energies [133]. **Figure 1-16** shows the FTIR spectra of CO adsorbed on anatase nanocrystals recorded at 60K. The peak at the lowest wavenumber is assigned to the formation of a multilayer of physisorbed CO followed by a broad band related to CO interaction with the residual OH group on the surface. According to the DFT calculations, the weak band at 2165 cm^{-1} is assigned to the CO adsorbed on Ti Lewis center located at (001) surface, strongly bound to two O(2f) anions resulting in a reduced acidity. Three components overlapped at 2179 cm^{-1}. The main component is assigned to the interaction of CO with Ti sites on (100) surface, while the shoulder centered at 2184 cm^{-1} is assigned to Ti Lewis sites on flat (101) and (112) surfaces. The weak band at the highest wavenumber is related to Ti Lewis sites located on edges, steps, and corners.

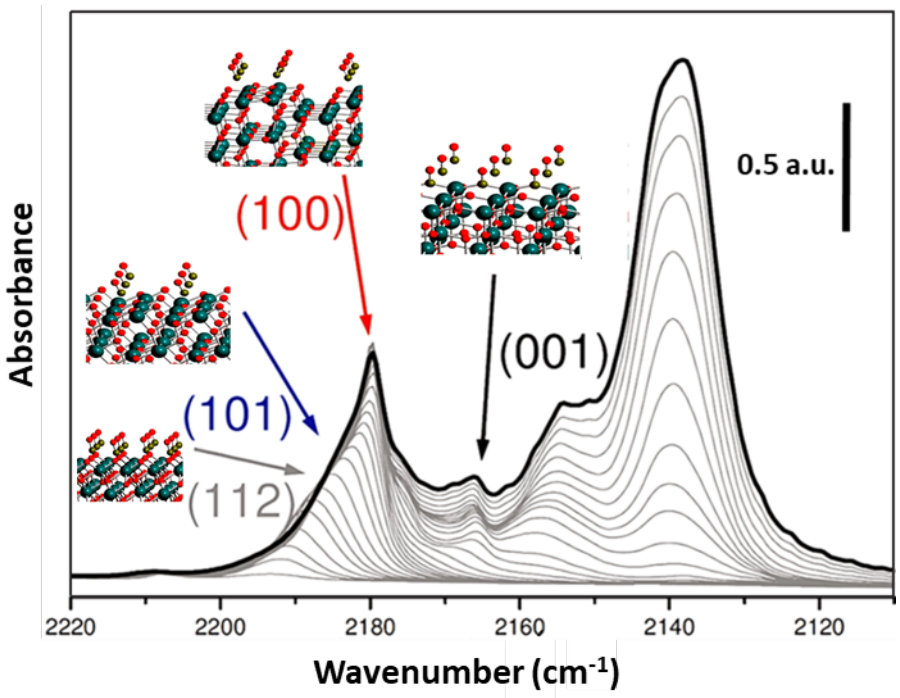

Figure 1-16 FTIR spectra of CO adsorbed at increasing coverages on anatase nanocrystals. The insets show the optimized geometry of CO adsorbed on anatase (112), (101), (100), and (001) surfaces at full coverage. Reprinted with permission from Ref [133]. Copyright 2011 American Chemical Society.

Understanding the structural and physicochemical properties of the inner surface of the porous materials such as zeolites and MOFs is essential to the development of adsorbents, catalysts, and porous materials for other purposes such as semiconductors [134]. FTIR spectroscopy of adsorbed probe molecule along with calorimetry provides the structural detail and calculation of thermodynamic parameters to understand physicochemical interaction between the porous material and adsorbed molecule. IR spectroscopic studies of alkaline zeolites using CO as the probe molecule show the formation C-bonded carbonyl species with alkali metal cation.

Garrone et al. comprehensively investigated the adsorption of CO on Na-ZSM-5 zeolite using FTIR spectroscopy and microcalorimetry accompanied with simultaneous volumetric measurement of adsorption isotherm. The IR spectra of the zeolite featured three peaks, from highest to lowest wavenumber; they relate to the interaction of CO with extra-framework Al^{3+}

species, C-bonded, and O-bonded adduct formed between CO and Na^+ ions. The simultaneous presence of the two latter adducts is a consequence of the isomerization equilibrium described by the following equation.

$$ZNa^+\cdots CO \rightleftarrows ZNa^+\cdots OC \qquad 1\text{-}37$$

The proportionality of the integrated intensities of C-bonded and O-bonded adducts at different pressures shows the existence of an equilibrium between the two modes of adsorption (**Figure 1-17**). Using the variable temperature IR (VTIR) spectra of CO, the isomerization enthalpy of CO adsorbed on Na-ZSM-5 was measured. The calculated equilibrium constant ($K_e = \theta_{OC}/\theta_{CO} = 0.23$), shows the percentage of C-bonded (~ 80%) and O-bonded (~ 20%) adducts to Na^+ ions. Furthermore, the measured heat of adsorption was portioned between the two adducts accordingly. The adsorption enthalpy of the C-bonded CO on Na-ZSM-5 was in excellent agreement with those reported in the literature [134].

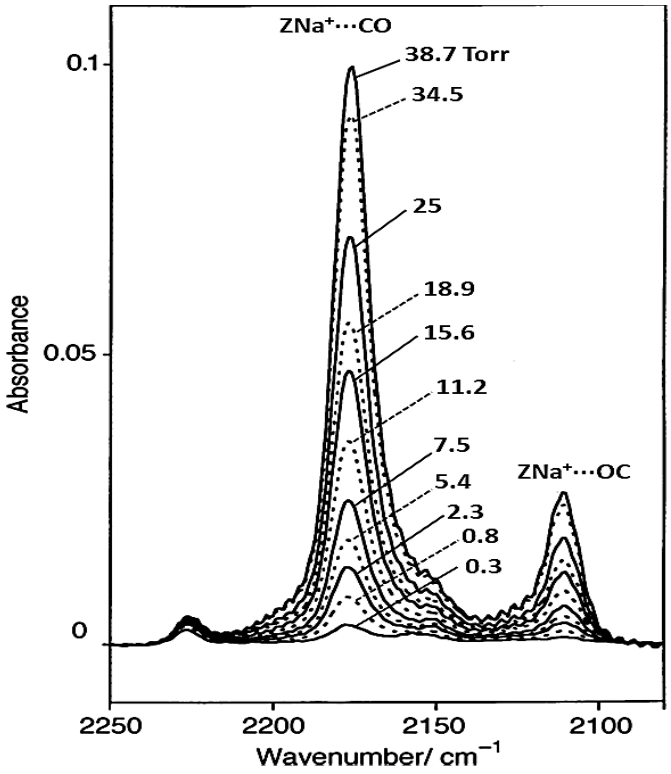

Figure 1-17 IR spectra of CO adsorbed on Na-ZSM-5 at room temperature. Respective equilibrium pressures are included in the graph in the Torr unit. Reproduced from Ref [134]. With permission from The Royal Society of Chemistry. Copyright 2014 The Royal Society of Chemistry.

Using VTIR and periodic DFT, Nachtigall et al. [135] investigated adsorption CO on High-silica protonic ferrite (H-FER) zeolite. They characterized different hydrogen-bonded OH···CO complexes formed by the interaction between adsorbed molecules and Brønsted acid sites of the zeolite (i.e., OH groups). According to the periodic DFT calculations, the highest enthalpy of adsorption was in the range of -25 to -29 kJ mol^{-1} related to the formation of the linear OH···CO complex pointing towards a sufficiently ample free space. Less stable complexes are formed when void space is insufficient, and the Brønsted acid OH group is involved in intra-zeolite hydrogen bonding [135]. It should be mentioned that the calculated value of enthalpy of adsorption was in agreement with VTIR measured value (28.4(±1) kJ mol^{-1}, the average value for coverages in the range of 3-70%).

Miroslav et al. [136] investigated the temperature dependence of the isosteric heat of adsorption of CO on an H-FER zeolite using microcalorimetry and DFT/Coupled-Cluster (DFT/CC). They observed a difference in the measured heat of adsorption at zero coverage at two different temperatures (i.e., 32.2 kJ mol^{-1} and 25.4 kJ mol^{-1} at 200 K and 300 K, respectively). This was justified using the ab initio molecular dynamic simulation stating that the CO molecule is localized at 200 K while at 300 K, the CO molecule jumps between the Brønsted sites except for a specific site being enclosed by a curved ferrite wall. Furthermore, the calculated heat of adsorption calculated using DFT/CC was in agreement with the previous report by Nachtigall et al. [135].

1.6 Preparation of materials

1.6.1 Porous supports

For the adsorption-based application of porous materials, properties such as pore structure, surface, and framework chemical composition, and mechanical strength need detailed characterization. Studies on porous adsorbents have been focused on the investigation of synthesis steps that lead to pore structure formation and reactivity at the surface [137]. The importance of pore structure is because adsorption and desorption processes occur at active sites on the pore walls, while the width of the pore dictates the diffusion rate of adsorptive molecules. The pore structure is characterized by specific surface area ($m^2\ g^{-1}$), total pore volume ($cm^3\ g^{-1}$), average pore diameter $\bar{d}_p$ (Å), and pore size distribution.

These parameters can be obtained using the adsorption isotherm of probe molecules. Nitrogen and Krypton are the most widely used probe molecules. Average pore diameter and adsorptive molecule size are the most critical parameters in adsorption on porous materials. For adsorbents with large pore diameters, pore walls are readily accessible to adsorptive, and the surface of the pore wall can be considered a flat surface. In the case of small pore diameter, the adsorptive

requires more energy to diffuse and adsorb on pore walls. Also, in this case, adsorptive molecules interact with opposite surfaces of the pore wall. These different mechanisms of adsorption lead to variations in adsorption isotherms. Due to the different adsorbent-adsorbate interaction, the adsorbents are classified into three different types: microporous, mesoporous, and macroporous adsorbents with approximate ranges $\bar{d}_p < 2$ nm, $2 < \bar{d}_p < 200$ nm, and $\bar{d}_p > 200$ nm, respectively [137, 138]. Mostly, synthetic adsorbents have non-homogeneous pore size distribution, meaning that they often have all three pore size types. The synthesis of adsorbents with uniform pore structure is challenging [137]. A summary of the performance of various porous adsorbents for CO adsorption is provided in **tables 1-2 to 1-5, 1-7**, and **1-8**.

1.6.2 Alumina

Various phases of alumina (i.e., alpha, gamma, delta, eta, and theta) can be prepared by heat treatment of precursors such as boehmite, pseudo-boehmite, bayerite, and nordstrandite [138]. Commercial alumina is produced through heat treatment of gibbsite, $Al(OH)_3$. This heat treatment is performed in air at about 400 °C / 700 °C to form the η/γ phases of alumina, respectively, with a trace amount of boehmite with the surface area of ~250 $m^2\ g^{-1}$. Performing the rapid heat treatment at higher temperatures, 400-800 °C, leads to the formation of amorphous alumina with a surface area of 300-350 $m^2\ g^{-1}$. The activation temperature, pressure, air composition, and heating rate are among the determining factors in the formation of various phases of alumina. **Figure 1-18** shows the conditions for the formation of different alumina phases, in which the gamma phase is usually used for adsorption due to thermal stability, porosity, surface area, and surface chemistry (presence of both Lewis and Brønsted acid sites depending on hydration degree).

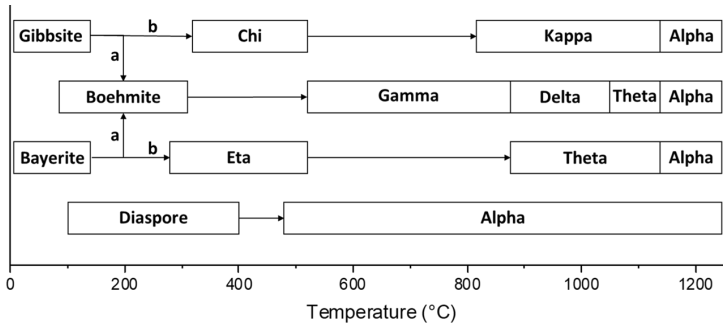

Figure 1-18 Decomposition of aluminum hydroxide to form crystalline phases of alumina. Path a: >1atm, moist air, heating rate> 1°C min^{-1}, >100 μm size. Path b: 1 atm dry air, < 1°C min^{-1}, < 10 μm. Reproduced from Ref [3] with permission from John Wiley and Sons. Copyright 2003 John Wiley and Sons.

The process of heat treatment involves dehydration, phase transformation, and sintering that affect the pore structure of alumina. Two critical factors in the application of alumina in adsorption are the pore structure and surface chemistry (i.e., acidity), in which the former is systematically investigated by Rouquerol [139]. Gamma and eta phases of alumina can have both Lewis and Brønsted acid sites, which are acceptors of electrons and donors of the proton. The presence of Brønsted acid sites (i.e., OH group) depends on the hydration degree of alumina. Furthermore, the acidity of the surface of alumina can be manipulated by treatment with acids such as HCl and HF [3, 140].

Due to controllable pore structure and surface chemistry, thermal and mechanical stability, and low cost, alumina has been used as adsorbents, catalyst support, and ion exchangers [3, 141, 142]. Industrial applications require alumina support with uniform pore structure and high pore volume. Uncontrolled pore structure may lead to deactivation. The deactivation often occurs by the plugging of micropores due to coke formation. Deposited solid carbon blocks the diffusion of reactants [143, 144].

Table 1-2 CO adsorption summary for alumina-based adsorbents. The adsorption amounts are for gases at 100 kPa.

Adsorbent	SA_{BET}/ $m^2\ g^{-1}$	Eq model	T/ K	q_{CO}/ mmol g^{-1}	q_{CO_2}/ mmol g^{-1}	S_{CO/CO_2}	S_{CO/N_2}	q_{H_2}/ mmol g^{-1}	S_{CO/H_2}	q_{CH_4}/ mmol g^{-1}	S_{CO/CH_4}	Ref
CuCl(0.3)/bayerite	**302**	**LF[a]**	**293**	**1.97**	**0.13**	**16.8**	**542**	**0.045**	**48.9**	**0.011**	**187**	**[6]**
CuCl/(γ-Al_2O_3)*	**311**			**0.45**	**0.13**	**3.5**						**[145]**
CuCl/boehmite	**203**			**1.56**	**0.13**	**12.4**						

***** Commercial sample, [a] Langmuir-Freundlich

1.6.3 Activated Carbon (AC)

Activated carbon has gained much attention due to its large micropore and mesopore volumes and, in turn, high surface area. The production of activated carbon includes three steps of raw material preparation, low-temperature carbonization, and activation [3]. Raw materials such as wood, coals, coconut shell, petroleum coke, and fruit nuts are used for the preparation of activated carbon. Activated carbon, in contrast to many other adsorbents, is non-polar or slightly polar with a very high surface area, which gives it the advantage of adsorbing non-polar or weakly polar organic molecules. Consequently, AC can be used for CO adsorption/separation purposes only with further chemical modification where active metal sites are introduced to on the surface of the adsorbents using a solution containing precursor metal (wet impregnation) or dispersion of metal salts by heating (solid dispersion) [3]. **Table 1-3** shows investigations of CO interaction with AC-based adsorbents at different conditions along with CO selectivity in a mixture of gases. It can be seen that modification of AC with CuCl results in a decrease of the surface area while the adsorption capacity increases. This shows that the Cu^+ ions are the active sites of adsorption of CO. However, increasing the CuCl loading does not necessarily mean increasing the adsorption capacity since excess loading can cause the blockage of pores.

Table 1-3 CO adsorption summary for AC-based adsorbents. The adsorption amounts are for gases at 100 kPa. The values of heat of adsorption are measured at low coverage.

Adsorbent	SA_{BET} / $m^2\ g^{-1}$	Setup	Eq model	T/ K	q_{CO}/ mmol g^{-1}	CO ΔH_{ads}/ kJ mol^{-1}	q_{CO_2}/ mmol g^{-1}	S_{CO/CO_2}	q_{N_2}/ mmol g^{-1}	S_{CO/N_2}	q_{H_2}/ mmol g^{-1}	q_{CH_4}/ mmol g^{-1}	S_{CO/CH_4}	Ref
AC		Eq +Dyn		299	~0.1	16.68								[29]
AC	1170	Eq	LF[a]/SSL[b]	298	0.2									[7]
CuCl/AC	652				2.28	25		3.2	0.07	35		0.41	9	
BPL AC	859	Eq +Dyn (PSA)	LF	298	0.35	16	1.8				0.03	0.8		[52]
AC	1784	Eq	SSL/LF	303	0.25									[23]
CuCl(0.7)/ AC	478				2.95		0.47	9	0.07	70		0.18	25	
AC D55/2 C PSA*	765.4	Eq +Dyn	Toth	298	0.75	14.6								[25]
CuCl/AC	477	Eq	MCEL[d]	303	~2.5	31.4	~0.45		~0.12		~0.1	~0.18		[64]
Kuraray 2GA-H2*		Eq +Dyn	DSL[c]	303	~0.45		~2.15				~0.03	~0.95		[60]
CuCl(2)/A C					~1.4		~1.4				~0.02	~0.5		
Carbon Xerogel	441	Eq			0.33									[146]
CuCl(2.5)/ Carbon Xerogel	97				0.49									
AC	1082	Eq +Dyn	LF	298	0.28	30								[147]
CuCl/AC	505				1.85	50	1.13	2.6	0.094	34.3		0.34	3	

***** Commercial sample, [a] Langmuir-Freundlich, [b] Single-Site Langmuir, [c] Dual-Site Langmuir, [d] Multi-Component Extended Langmuir

1.6.4 Zeolite

Zeolites are also one of the most widely used adsorbents for wide range of applications such as CO_2 removal from natural gas, CO removal from reforming gas, and air drying among many others [148]. Zeolites are crystalline aluminosilicates of alkali or alkali earth elements with the following chemical composition $M_{x/n}[(AlO_2)_x(SiO_2)_y].zH_2O$, where x and y are integers with y/x equal to or greater than 1, n is the valence of cation M, and z is the number of water molecules in each unite

cell. Zeolites are highly porous materials with molecular pore dimension that in turn provide high surface area and adsorption capacity.

1.6.5 MOF

Metal-organic frameworks (MOFs) are coordinated polymers in which the organic ligands are coordinated with metal ions or clusters [149]. The organic linkers, which are imidazolate-based or carboxylate-based, self-assemble on the metal ions during synthesis and form cage-like structures. Each metal ion is fixed by linkers to produce rigid entities with a specific geometry that is called the secondary building units (SBUs), and these SUBs are joints, and organic linkers are the struts of the MOFs [150, 151]. Due to their large internal surface area, tunable porosity, and chemical functionality, MOFs have gained much interest in different fields such as adsorption, catalysis, batteries, fuel cells, and supercapacitors [152-157]. A promising area of MOF application is adsorption or separation, including the adsorption of carbon monoxide.

Based on their interaction with CO, MOFs can be used without further chemical modification since they have active metal sites capable of forming the pi-complexation. Different MOFs are synthesized to have (i) pi-complex active metalcore, (ii) metal oxides or halides of desired valencies within the framework, or (iii) cation exchanged functionalized groups. In the synthesis of MOFs, carboxylate or imidazolate based ligands, called organic linkers, assemble with metal ions or clusters to form a 1-, 2-, or 3-dimensional structure. MOF-74 or CPO-27, MIL-100, and MIL-101 are among the MOFs with active metal cores for adsorption of CO. In a comprehensive study, six MOF-74s, which contain one-dimensional hexagonal pores with different metal cores of Mg, Mn, Fe, Co, Ni, and Zn, were synthesized through a hydrothermal method [83]. MOF-74 is synthesized using the precursor solution containing a mixture of metalcore salt and 2,5-dioxido-1,4-benzenedicarboxylate. Among these six cations, Mg^{2+} and Zn^{2+} cannot form pi-complexation

to CO while all the rest can. Mg^{2+} does not possess d electrons, and the 3d orbital is full for Zn^{2+} making σ-donation impossible. Using these six cations, the effect of different metal cores on adsorption capacity and CO binding strength was investigated. The CO uptake follows the order of Fe > Co > Ni > Mg > Mn > Zn. The strongest interaction with CO was found for Ni (**Table 1-4**). The isosteric heat of adsorption and selectivity of the MOF-74 with different metal cores are presented in **table 1-4**. Up to now, the highest CO adsorption capacity reported at atmospheric pressure and temperature are recorded for MOF-74(Fe), MOF-74(Co), and MOF-74(Ni) (i.e., 6, 5.8, and 5.7 mmol g^{-1}) that is higher than CO adsorption capacity of benchmark CuCl/zeolite Y [7] or CuCl/zeolite NaY [158]. However, MOFs with open metal sites such as MOF-74 mentioned above and HKUST-1 have a strong affinity toward the water, and the dissociative adsorption of water on metal sites causes the collapse of the structure or hydrolysis of these MOFs, which in turn leads to a decline in performance. Therefore, chemical modification of MOFs such as MIL-101(Cr), with high hydrothermal stability has been favored over MOFs with open metal sites [159].

Table 1-4 CO adsorption summary for open metal site MOFs adsorbents. The adsorption amounts are for gases at 100 kPa. The values of heat of adsorption are measured at low coverage.

Adsorbent	SA_{BET} / $m^2\ g^{-1}$	Setup	Eq model	T/ K	q_{CO}/ mmol g^{-1}	CO ΔH_{ads}/ kJ mol^{-1}	q_{CO_2}/ mmol g^{-1}	S_{CO/CO_2}	q_{N_2}/ mmol g^{-1}	S_{CO/N_2}	q_{H_2}/ mmol g^{-1}	S_{CO/H_2}	q_{CH_4}/ mmol g^{-1}	S_{CO/CH_4}	Ref
MOF-74(Mg)	1957[a]	Eq	SSL/DSL/TSL	298	4.3	35.4			~0.9	10.3		170			[83]
MOF-74(Mn)	1797[a]				2.9	29.7			~0.5	10.3	~0.1	86			
MOF-74(Fe)	1535[a]				6	43.6			~0.55	68	~0.1	507			
MOF-74(Co)	1433[a]				5.8	48.8				163	~0.05	1040			
MOF-74(Ni)	1574[a]				5.7	52.7			~0.6	216		1705			
MOF-74(Zn)	1105[a]				1.7	27.2			~0.3	7.5	~0.1	47			
MIL-101(Cr)	2471	Eq +Dyn		303	1[b]	41.92	2.9[b]	0.34	0.23[b]	4.35			0.51[b]	1.96	[160]
MIL-101(Cr) [granules]	1642				0.58[b]	41.16	2.6[b]	0.34	0.14[b]	4.14			0.32[b]	1.81	

Adsorbent	SA_{BET} / $m^2\ g^{-1}$	Setup	Eq model	T/ K	q_{CO}/ mmol g^{-1}	CO ΔH_{ads}/ kJ mol^{-1}	q_{CO_2}/ mmol g^{-1}	S_{CO/CO_2}	q_{N_2}/ mmol g^{-1}	S_{CO/N_2}	q_{H_2}/ mmol g^{-1}	S_{CO/H_2}	q_{CH_4}/ mmol g^{-1}	S_{CO/CH_4}	Ref
MOF-5		**Eq +Dyn**	**SSL[c]/F[d]**	**298**	**~0.1**	**16**									**[161]**
MOF-177						**~21.7**									
MIL-125(Ti)_NH$_2$*		**Eq +Dyn (PSA)**	**MCEL[e]**	**303**	**~0.22**	**13.4**	**~2**		**~0.15**		**~0.12**		**~0.55**		**[34]**
UTSA-16	**805**	**Eq +Dyn**	**DSL[f]**	**298**	**~0.23**		**~4.2**		**~0.3**		**~0.01**		**~0.55**		**[56]**

[a] Langmuir surface area**; *** Commercial sample**;** [b] 110 kPa, [c] Single-Site Langmuir, [d] Freundlich, [e] Multi-Component Extended Langmuir, [f] Dual-Site Langmuir

1.6.6 Chemical modification

For many porous materials such as activated carbon, mesoporous silica, alumina, and even some of MOFs, selective adsorption is not possible unless preferential adsorption sites are introduced on their surfaces. Chemical modification is the addition of preferential adsorption sites, usually pi-complex-active transition metals, to the surface of porous material by metal impregnation [34]. Researchers have been continuously exploring methods to introduce active sites on the surface of adsorbents for different purposes [162-170]. The methods used to introduce the metallic sites onto the surface of porous materials include ion exchange, metal dispersion, and functionalization.

1.6.6.1 Conventional methods

The dispersion of metal salts on the surface of porous materials is a common practice for selective adsorption of CO. Porous materials without exchangeable cation are usually chemically modified through the dispersion of metal salts [7, 23, 70, 158, 171-173]. The metal sites are formed on the pore surfaces from dissolved metal precursors containing in aqueous solution or directly from the solid-state precursors [173]. Depending on the oxidation state of the metal, calcination or reduction might be required to achieve the desired oxidation state of active metal site. The reduction step directly affects the adsorption capacity since it controls the amount of active site on the surface of the adsorbent. Among the metallic impregnants, copper has been widely used due to its abundance

and low cost. Copper salts such as $Cu(NO_3)_2$, $CuCl_2$, $Cu(HCOO)_2$, and CuCl have been used to impregnate mesoporous silica SBA-15, AC, γ-Al_2O_3, a porous organic polymer (POP) [174], and aluminosilicate or pillared interlayered clays (PILC) [172] for separation purpose. Many instances of copper-based adsorbents and their CO adsorption capacities can be found in tables throughout this article. Solid-state spontaneous monolayer dispersion is a conventional method to make adsorbents for selective CO adsorption [7, 175]. In a study by Wang, pi-complexation active metal halides of CuCl and $PdCl_2$ were dispersed on SBA-15 and MCM-41 using this method in which CuCl and $PdCl_2$ salts are physically mixed with the supports and heated in an inert gas flow to form a chloride monolayer [175]. Since the main focus of this study is the desulfurization of jet fuel, CO adsorption was used to characterize the chemical properties of the adsorbent. A comparison between SBA-15 and MCM-41 modified with $PdCl_2$ and CuCl (**Table 1-5**) shows a higher adsorption capacity (saturation amount) for the former that is due to the stronger binding of CO on $PdCl_2$.

Table 1-5 CO adsorption summary for silica-based adsorbents. The adsorption amounts are for gases at 100 kPa.

Adsorbent	SA_{BET} / $m^2\ g^{-1}$	Eq model	T/ K	q_{CO}/ mmol g^{-1}	q_{N_2}/ mmol g^{-1}	S_{CO/N_2}	Ref.
MCM-41	**1225**		**308**	**0**			**[175]**
CuCl/MCM-41	**456**			**0.57**			
$PdCl_2$/MCM-41	**502**			**1.47**			
SBA-15	**901**			**0.01**			
CuCl/SBA-15	**411**			**0.5**			
$PdCl_2$/SBA-15	**358**			**1.06**			
Si-Cu/SBA-15	**457**	**DSL[a]**	**298**	**0.7**	**~0.11**	**~47**	**[146]**
Cu/SBA-15	**573**			**0.44**	**0.07**	**~6**	

[a] Dual-Site Langmuir

Ion exchange is another process used to introduce active metal sites onto the surface zeolites or resins [3, 7]. In this process, the cation of porous support is exchanged with the desired metal cation through the reaction with an aqueous solution of metal salt. To generate Cu(I) sites, the ion exchange process is followed by a reduction step to achieve the desired oxidation state of copper. Direct exchange of Cu(I) is not possible due to the insolubility of Cu(I) salts in the water. Such separate reduction step is not required for other metals with desired oxidation states–Ni(II), Pd(II), Pt(II), Ag(I), and Zn(II)–since water-soluble salts are available for them [7, 125]. Hernandez et al. modified zeolite Y through ion exchange; however, due to limited reduction from Cu(II) to Cu(I) and insufficient cation exchange capacity of the support the adsorption capacity was low. By vacuum-assisted reduction at 450 °C, it was possible to reduce only 40-50% of Cu(II) to Cu(I) for the zeolite adsorbent [176].

In a study to synthesize a CO adsorbent quickly from low-cost materials [23], Cu(I) was loaded onto activated carbon through monolayer dispersion by mixing a specific amount of AC with cupric chloride hydrate followed by 270 °C nitrogen reduction for Cu(II) to Cu(I) conversion. The activation process was controlled to avoid metallic copper formation on the surface of AC. This method does not guarantee a good distribution of active sites in the pores of the support since reduction at high temperatures causes the aggregation of active species. The prepared adsorbent was tested for CO separation from syngas using the static equilibrium setup, and the performance of the adsorbent in the VPSA process was investigated through mathematical modeling. The Cu(I)/AC prepared by monolayer dispersion could extract 98 vol% purity CO from syngas containing 32 vol% CO. The recovery was at 92% [64].

Cu(I) doped carbon xerogel (CXs) is another CO adsorbent synthesized through the impregnation of CuCl precursor solution [147]. Since CuCl is not soluble in water, it was dissolved in a mixture

of HCl and H_2O, followed by immersion of CXs in the precursor solution at 50 °C to evaporate the solvent, which was repeated multiple times. The presence of CuCl on the surface of CXs was confirmed using XRD and XPS; however, this method did not lead to monolayer formation CuCl. Furthermore, the XPS result shows the presence of Cu (II) that is incapable of forming pi-complex with CO molecule, and the use of HCl, besides being hazardous, reduces the crushing strength of the support.

Active metal sites can also be synthesized within MOFs through impregnation with precursor solutions. In a recent study, palladium nanoparticles were embedded within MIL-101 through the incipient wetting procedure using a $Pd(acac)_2$ precursor solution, followed by reduction under hydrogen flow to obtain Pd/MOF-101 [177].

The conventional chemical modification methods face challenges such as the low surface concentration of active sites and high reduction temperature. High-temperature processes tend to result in low adsorption capacity of the adsorbents. Different techniques applied to impregnation/reduction steps to address these challenges are systematically discussed in the following sections.

1.6.6.2 Internal-agent-assisted impregnation

For CO adsorption, the chemical modification of porous supports using Cu(II) ion requires a reduction step to form the Cu(I). The reduction is usually performed under the flow of a reducing gas (i.e., H_2, CO) or inert gas at high temperatures. These methods of reduction have disadvantages such as aggregation of copper species and destruction of active sites. In addition to lowered CO adsorption capacity and selectivity, reduction at high temperatures limits the choice of porous supports.

Figure 1-19 shows three different routes of loading Cu_2O on mesoporous silica SBA-15. The conventional method (**Figure 1-19a**) includes calcination of pristine SBA-15 to burn off the template followed by the introduction of copper precursor $Cu(NO_3)_2$, a second calcination step to form CuO, and finally, a high-temperature reduction to form Cu_2O [178]. This method leads to a low Cu(I) surface concentration on SBA-15, which is not favorable. A more facile method to form Cu_2O sites with better yield and dispersion was achieved by direct thermal treatment of $Cu(NO_3)_2$ to Cu_2O (**Figure 1-19b**).

Kou et al. employed solid-state dispersion by grinding $Cu(NO_3)_2$ and as-synthesized SBA-15 together to get a homogeneous powder mixture first. The nitrate then decomposes into Cu_2O by annealing at 700 °C under N_2 flow (**Figure 1-19c**) [179]. In their method, the copper precursor is introduced between the silica walls and template, and the following calcination is a multi-purpose step for template removal and Cu_2O formation. Due to the required high temperature to obtain Cu_2O, this technique is only applicable to porous material with high thermal stability such as alumina, AC, and silica.

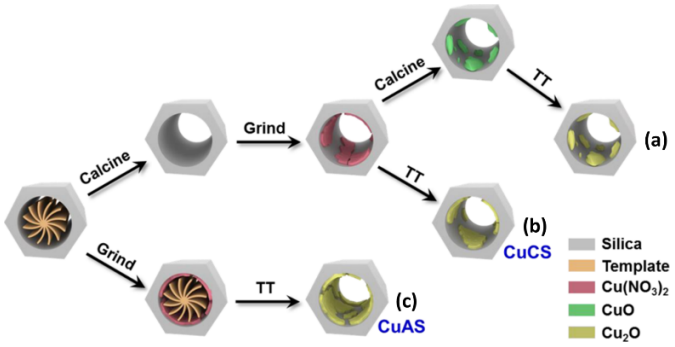

Figure 1-19 Chemical modification of mesoporous silica. (a) Conventional method. (b) Direct thermal treatment (TT). (c) Multipurpose direct thermal treatment. Reprinted with permission from Ref [179]. Copyright 2015 American Chemical Society.

Cho et al. used boehmite, decomposed aluminum hydroxide (**Figure 1-18**), as a new and suitable supporting material for Cu(I) sites [145]. The chemical modification method applied in their study was thermal monolayer dispersion of CuCl that is simply mechanical mixing of CuCl with

boehmite followed by heat treatment under vacuum condition. Before introducing any copper species, compared to the gamma phase of alumina, boehmite shows a larger surface area and a lower CO_2 affinity due to high mesoporosity but low microporosity. Interestingly, it was found that the CO adsorption capacity of Cu(I)/boehmite is higher than Cu(I)/γ-alumina. This is claimed to be due to higher hydrophilicity of boehmite surface with more hydroxyl groups inducing stronger affinity of CuCl to the adsorbent surface hence better dispersion of CuCl in mesopores.

Following up on their study, Cho et al.[6] used bayerite, a decomposed aluminum hydroxide with more content of hydroxyl group, as the supporting material for dispersion of CuCl. The activation of bayerite was performed before loading of CuCl at an optimum temperature to maintain the crystalline structure of bayerite while increasing its surface area. Owing to the high content of the hydroxyl group, a large amount of CuCl was impregnated into bayerite using the thermal monolayer dispersion method. The CO uptake and CO/CO_2 selectivity factor measured for Cu(I)/bayerite at 293 K under 100 kPa of CO are 1.97 mmol g^{-1} and 16.8, respectively, that are higher than measured values for Cu(I)/boehmite (i.e., 1.56 mmol g^{-1}, and 12.4).

1.6.6.3 External-agent-assisted impregnation

Recently, high dispersion and yield of Cu(I) sites in SBA-15 have been achieved by introducing confined spaces in silica nanopores [146]. This method introduces the second impregnation phase, a structural promoter, in addition to the active impregnation phase. Before the final high-temperature reduction process, the CuO-modified SBA-15 is coated with a layer of porous silica (**Figure 1-20**). The introduced porous silica provides a confined space for CuO that prevents the aggregation of copper during the reduction process. Interestingly, uniform pores were formed on the silica layer that resulted in highly accessible sites. The adsorbent exhibited outstanding performance concerning both CO adsorption capacity and selectivity (**Table 1-5**).

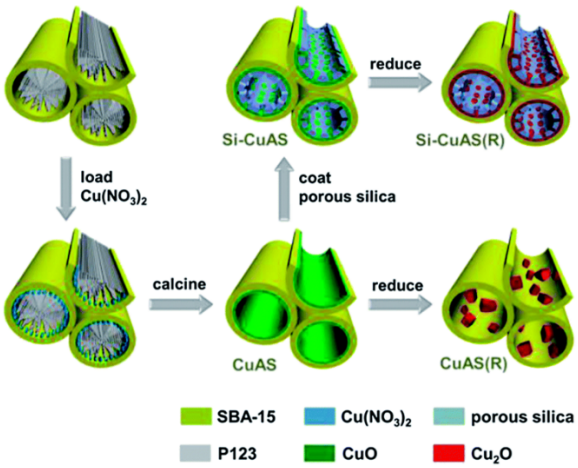

Figure 1-20 Chemical modification of mesoporous silica. Reduction of CuO to Cu_2O in a confined space. Reproduced from Ref [146] with permission from The Royal Society of Chemistry. Copyright 2014 The Royal Society of Chemistry.

Ammonium citrate is a promising dispersing agent for AC and alumina supports. Relvas et al. applied the conventional method, wet impregnation, to synthesize Cu(I)/AC and investigated its performance in a single-stage PSA to produce fuel cell grade hydrogen [60]. Aqueous $CuCl_2$ solution was used as a precursor mixed with ammonium citrate. To achieve the maximum dispersion of copper species, AC was heated up in air before impregnation to increase its hydrophilicity. For mesoporous alumina, another popular support material for Cu(I) sites, Wang et al. investigated the equilibrium and dynamic adsorption of ethylene and CO on CuCl/γ-alumina which was prepared using the wet-impregnation of CuCl [180]. The cuprous precursor solution was prepared using the mixture of ammonia hydroxide, ammonia citrate as a dispersing agent, and water. To prevent the oxidation of Cu(I) to Cu(II), the impregnation process was performed under nitrogen.

Aijaz et al. successfully immobilized ultrafine platinum nanoparticles inside the pores of MIL-101 using a double solvent method that prevents the aggregation of Pt nanoparticles on the external surface of the framework [181]. Firstly, MIL-101 particles were suspended in hexane, a

hydrophobic solvent. In the following step, aqueous solution containing chloroplatinic acid was added to it dropwise. Given the large inner surface area of MIL-101 compared to the outer surface area, this double solvent technique utilizes capillary pressure to let aqueous Pt precursor solution diffuse into the hydrophilic pores to reduce Pt deposition on the outer surface significantly. A predetermined precursor amount should be used–equal or less than pore volume–for the success of this strategy. Conventional single solvent impregnation by contrast results in deposition and aggregation of metal nanoparticles on the external surface. The double solvent method has also been applied to load Cu(I) sites on MIL-101, which has been used for separation of olefin-paraffin mixtures [182]. The main reason for the choice of loading method in this work was to avoid the aggregation of copper nanoparticles on the external surface of MOF-101. The loading amount should also be considered carefully in chemical modification as a high amount of loading can cause the aggregation of metal species and even blockage of the pores that, in turn, results in lower adsorption capacity [158, 182, 183]. XRD and XPS are the commonly used techniques in combination to confirm the formation of active metal chloride monolayer on the substrate. **Figure 1-21a** shows the XRD characterization of Cu(I)/MIL-101 with different loadings of Cu(I). It is shown that for loadings of CuCl below 50 weight percent the characteristic peaks of CuCl is not showing; however, the XPS result (**Figure 1-21b**) confirms the presence of CuCl and conversion of Cu(II) to Cu(I) since the corresponding Cu $2p_{3/2}$ satellite peak in the region of 940-950 eV is not showing up. The characteristic peaks of CuCl for loadings of higher than 50 wt% show the aggregation of Cu(I) on the surface of MIL-101 [182].

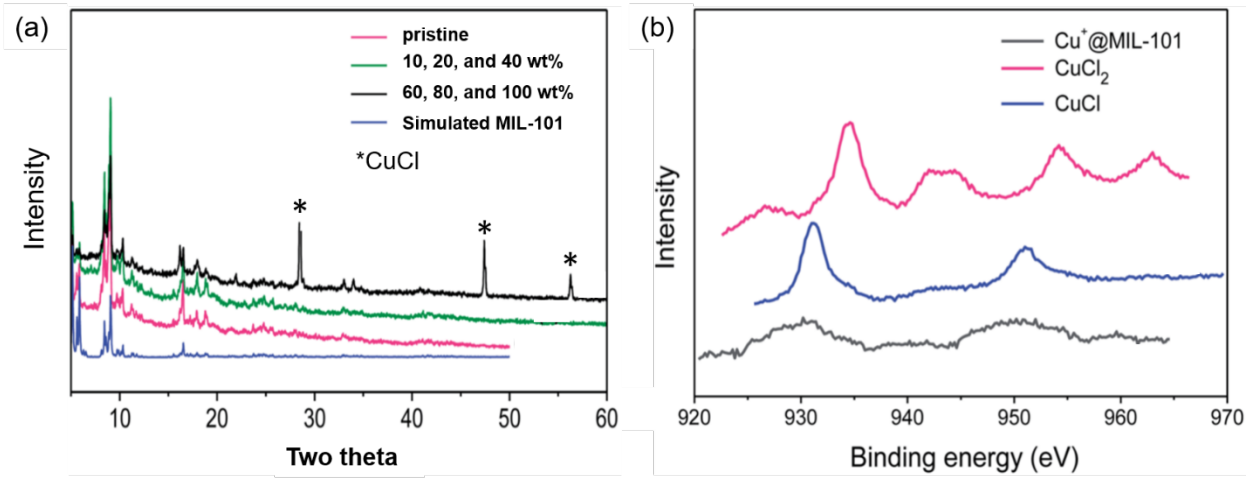

Figure 1-21 Confirmation of monolayer dispersion of Cu(I) using the combination of (a) X-ray diffraction and (b) X-ray photoelectron spectroscopy. Reproduced from Ref [182] with permission from The Royal Society of Chemistry. Copyright 2014 The Royal Society of Chemistry.

1.6.6.4 Internal-agent-assisted reduction

Khan et al. investigated the adsorption capacity of $CuCl_2$ loaded MIL-47 that contains vanadium. Interestingly, after drying at room temperature and vacuum at 100 °C, XPS and XRD analyses already confirmed the presence of CuCl on MIL-47 without calcination and high-temperature reduction. The observed binding energy shift of vanadium in MIL-47 framework suggested that the reduction of Cu(II) to Cu(I) originates from the following redox process [184].

$$V^{III} + Cu^{II}Cl_2 \rightarrow V^{IV}{-}Cl + Cu^{I}Cl \qquad 1\text{-}38$$

The internal agent facilitated reduction method was utilized by Kim et al.[9] to reduce Cu(II) to Cu(I) on MIL-100(Fe) that has high densities of Fe(II) and Fe(III) sites [185]. Kim investigated the role of Fe in the reduction of Cu(II) to Cu(I) using FTIR and XPS techniques and proposed the following possible mechanism of reduction that is similar to the mechanism proposed by Khan et al.

$$Fe(II) + Cu(II)Cl_2 \rightarrow Fe(III){-}Cl + Cu(I)Cl \qquad 1\text{-}39$$

The authors reported a high CO/CO_2 selectivity (29 at 100 kPa) and working capacity (1.61 mmol g^{-1} at 10-100 kPa) for 0.9Cu(I)/MIL-100(Fe) where the 0.9 is $CuCl_2$/MIL-100(Fe) weight ratio [9]. Furthermore, the dynamic performance and cyclic adsorption/desorption of the adsorbent in CO-CO_2 mixture showed a consistent CO adsorption capacity from the breakthrough experiment with IAST predicted CO adsorption capacity and complete regeneration of adsorbent under He flow at 250 °C.

Polydopamine can serve as the reducing agent to reduce noble metallic salts into metallic particles [186]. Xie et al. showed the potential of core-shell Fe_3O_4@polydopamine (PDA) microspheres as an adsorbent for methylene blue removal. In preparation of Fe_3O_4@PDA-Ag, PDA is the internal reducing agent by reducing $AgNO_3$ to metallic Ag [186]. Liu et al. used PDA in Fe_3O_4@PDA to reduce chloroauric acid to Au nanoparticles that served as an adsorbent of Rhodamine B [187].

1.6.6.5 External-agent-assisted reduction

Vapor-induced reduction (VIR) of CuO is another strategy to synthesize Cu_2O on mesoporous silica SBA-15 that has addressed the issues of high-temperature calcination, the formation of Cu(0), and low yield of Cu(I). In this method (**Figure 1-22a**), CuO is dispersed in as-prepared SBA-15 to obtain a high degree of dispersion of CuO and prevent aggregation that also has led to lower reduction temperature for CuO. The use of formaldehyde/water vapor mixture as an external reducing agent led to a nearly 100% conversion of Cu(II) to Cu(I). **Figure 1-22b** shows the high-temperature autoreduction (HTA) process. As the figure shows, HTA does not lead to the complete reduction of CuO to Cu_2O. In **figure 1-22c**, we see that conventional impregnation where CuO is dispersed after SBA-15 calcination (template burn-off) resulted in aggregation of CuO and low yield of Cu_2O even when the VIR route was taken afterward [188].

In general, MOFs cannot be used as support materials when high-temperature calcination is involved in the synthesis process due to their low thermal and chemical stability; therefore, the loading of active sites on MOFs requires using mild conditions. A method used to address the issue of high-temperature reduction is introducing a mild reducing agent. Peng et al. applied the mild reducing agent ($Cu(HCOO)_2$) to form Cu(I) active sites according to the following chemical reaction [10, 92].

$$CuCl_2 + Cu(HCOO)_2 \rightarrow 2CuCl + H_2O + CO_2 + CO \quad 1\text{-}40$$

Khan et al. used a low-temperature method of Cu_2O synthesis to form Cu(I) sites on MIL-100 (Fe) for adsorptive desulfurization [183]. The method works based on the reduction of the copper-citrate complex solution with glucose at 80 °C according to the following chemical reaction [185].

$$Cu(Citrate) + C_6H_{12}O_6 \rightarrow Cu_2O + C_5H_{11}O_5COOH \quad 1\text{-}41$$

Ma et al. [7] introduced Cu(I) sites on AC and Zeolite Y using $CuCl_2$, $CuCl_2$-$Cu(HCOO)_2$ mixture, $CuCl_2$-$Cu(CH_3COO)_2$ mixture, and CuCl to investigate and address this limitation. Water-insoluble cuprous chloride layer was formed on the surface of AC by heating the solid mixture to a temperature between Tamman (213 °C) and melting temperature (426 °C) of CuCl in an inert gas or under vacuum. Other copper sources dissolve well in water. The aqueous solution wets the support surface for dispersion. $Cu(HCOO)_2$ helps to overcome the incomplete reduction problem by reacting with $CuCl_2$. The CO adsorption capacity of AC and zeolite impregnated by $CuCl_2$-$Cu(HCOO)_2$ mixture is as high as that of AC with CuCl monolayer on it. This suggested a complete reduction of Cu(II) to Cu(I). Comparison of isosteric heat of adsorption for CuCl/Y (**Table 1-7**, Ref [7]) and CuCl/AC (**Table 1-3**, Ref [7]) shows that the stronger interaction between the zeolite support and CO leads to 30% reduction in adsorption-desorption reversibility of CO.

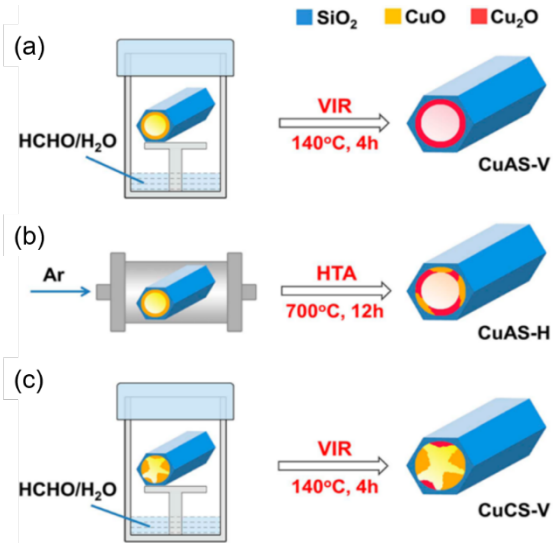

Figure 1-22 Chemical modification of (a) as-prepared mesoporous silica by VIR, (b) as-prepared mesoporous silica by HTA, and (c) calcined mesoporous silica by VIR. Reprinted with permission from Ref [188]. Copyright 2015 American Chemical Society.

Another external reducing agent, Na_2SO_3, was used to load CuCl into MIL-100(Cr) following the redox process shown below [189].

$$2CuCl_2\,(aq) + Na_2SO_3\,(aq) + H_2O \rightarrow 2CuCl\,(s) + Na_2SO_4\,(aq) + 2HCl\,(aq) \qquad 1\text{-}42$$

Recently, Cu(I)V(IV)/MIL-101(Cr), a selective CO adsorbent with good stability, was synthesized using VCl_3 for facilitated Cu(II) to Cu(I) reduction. The synthesis procedure includes grounding of copper precursors and vanadium simultaneously with MIL-101, followed by a calcination step. The presence of vanadium enabled reduction at 250 °C. This lowered reduction temperature guaranteed the structural integrity of MIL-101(Cr).

The Cu(I) adsorbents suffer from phase instability due to the inactivation by oxidation or disproportionation of the Cu(I) ion, the active site of CO adsorption. Although it remains a challenge to synthesize oxidation-resistant Cu(I) modified adsorbent, a method to improve the stability of these adsorbents is the addition of sacrificial metal sites to delay the oxidation of Cu(I). Interestingly, the vanadium used in the preparation of Cu(I)V(IV)/MIL-101(Cr) enhanced the

stability of this adsorbent such that 91.8% of the initial CO adsorption capacity was maintained after two weeks. XPS results confirmed the oxidation of vanadium before Cu(I) ions [12].

Li et al. synthesized Cu(I)/MIL-101(Cr) by a two-step strategy. The first step, external agent facilitated impregnation, is to introduce Cu(II) on the surface of MIL-101(Cr). The second step is the reduction of Cu(II) to Cu(I). When both hydrophobic n-hexane and hydrophilic water are used in sequence in each step, proper distribution of copper precursor inside the pores was ensured to prevent the aggregation of copper outside the pores. Complete reduction of Cu(II) to Cu(I) in the liquid phase was achieved using the reducing aqueous solution of Na_2SO_3 (**Figure 1-23**) [36]. was possible to get Cu(I) sites without thermal stability of MIL-101(Cr) To investigate the effect of two-step double-solvent strategy, each step was separately treated with a double-solvent method. **Figure 1-23a** shows the use of the double-solvent strategy for loading of Cu(II) precursor into MIL-101(Cr) (step 1) followed by liquid reduction (Cu(I)/MIL-101(Cr)(DL)), and **figure 1.23b** shows the use of wet impregnation for the first step and double solvent strategy in the liquid phase reduction step (Cu(I)/MIL-101(Cr)(ID)).

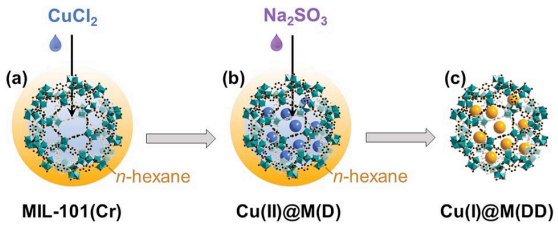

Figure 1-23 Schematic of Cu(I)/MIL-101(Cr) preparation using the two-step double solvent (DD) method. (a) Dispersion of MIL-101(Cr) in hydrophobic n-hexane followed by the addition of hydrophilic aqueous $CuCl_2$ solution; (b) dispersion of Cu(II)/MIL-101(Cr) in n-hexane followed by the addition of hydrophilic aqueous reducing agent; (c) formation of Cu(I)/MIL-101. Reproduced from Ref [36] with permission from The Royal Society of Chemistry. Copyright 2018 The Royal Society of Chemistry.

A comparison between the three routes presented in **figure 1-23** showed that the adsorption capacity and CO/N_2 and CO/CH_4 selectivity of Cu(I)/MIL-101(Cr)(DD) at room condition was higher than the other two routes, which are due to less aggregated copper species (**Table 1-8**).

Furthermore, the adsorbent was tested under dynamic conditions with a mixture of N_2 and CO, and the dynamic breakthrough curves are in agreement with the single-component equilibrium CO adsorption data.

Table 1-6 summarizes the chemical modification techniques covered in section 1.6.6.

Table 1-6 Unconventional adsorbent preparation routes.

Adsorbent	Agent	Ref
Internal-agent-assisted Impregnation		
SBA-15	Template	[179]
Boehmite	-OH group	[145]
Bayerite	-OH group	[6]
External-agent-assisted Impregnation		
SBA-15	Structural promoter (porous silica)	[146]
AC	Ammonium Citrate	[60]
γ-Alumina	Ammonia citrate + Ammonium hydroxide	[180]
MIL-101	Hexane	[181]
Internal-agent-assisted Reduction		
MIL-47	Vanadium (V(III))	[184]
MIL-100	Iron (Fe(II))	[94]
Fe_3O_4@PDA	Polydopamine (PDA)	[186]
Fe_3O_4@PDA	Polydopamine (PDA)	[187]
External-agent-assisted Reduction		
SBA-15	Formaldehyde + Water	[188]
MIL-100	Copper formate ($Cu(HCOO)_2$)	[92]
MIL-100	Glucose ($C_6H_{12}O_6$)	[183]
AC	Copper formate ($Cu(HCOO)_2$)	[7]
Zeolite Y	Copper formate ($Cu(HCOO)_2$)	[7]
MIL-100	Sodium Sulfate (Na_2SO_4)	[189]
MIL-101	Vanadium chloride (VCl_3)	[12]

Table 1-7 CO adsorption summary for zeolite-based adsorbents. The adsorption amounts are for gases at 100 kPa. The values of heat of adsorption are measured at low coverage.

Adsorbent	SA_{BET}/ $m^2\ g^{-1}$	Setup	Eq model	T/ K	q_{CO}/ mmol g^{-1}	CO ΔH_{ads}/ kJ mol^{-1}	q_{CO_2}/ mmol g^{-1}	S_{CO/CO_2}	q_{N_2}/ mmol g^{-1}	S_{CO/N_2}	Ref
ZMS 5A		Eq + Dyn		298	0.2	29					[29]
CuCl/Y		Eq	LF/SSL	298	2.24	63.5					[7]
13X	392	Eq + Dyn	LF	298	0.72	23.3	4.2				[52]
NaY		Eq		303	~0.65[c]		~5.4[c]				[158]
CuCl/NaY					~3.42[c]		~2[c]		~0.09[d]		
13X					~0.49[c]		~4.6[c]				
CuCl/13X					~3.42[c]		~2.34[c]				
Zeolite A5[b]	669.9	Eq + Dyn	Toth	298	1.25	30.5					[25]
Zeolite B[b]	669.9				1.25	31.6					
KOSTROLITH 5ABF[b]	680			293	1.3	26.7					
Zeolite Y	694	Eq	SSL/LF	303	~0.25						[190]
CuCl/Y	329				2.72	43	0.96	2.83[a]	0.11	68[a]	
Zeolite 5A		Eq + Dyn	SSL/F	298	~1.25	~69					[161]
Zeolite 13X					~0.5	70					
Zeolite 13X [pelletized]	742.98	Eq+ Dyn	SSL/LF	293	0.93		4.6		0.349		[191]
Cu(1.5)ZSM-5	310			303	0.11[e]	~122					[192]
Fe(0.3)ZSM-5	335				0.007[e]	~55					
Co(0.37)ZSM-5	284				0.0045[e]	~81					
Fe(0.78),Cu(0.48)ZSM-5	340				0.053[e]	~150					
Cu(1.25),Fe(0.2)ZSM-5	342				0.12[e]	~139					
Cu(1.22),Co(0.1)ZSM-5	345				0.06[e]						

a Selectivity factor**; b** Commercial adsorbent**; c** 70 kPa**; d** 64 kPa**; e** 60 Pa

Table 1-8 CO adsorption summary for modified MOF-based adsorbents. The adsorption amounts are for gases at 100 kPa. The values of heat of adsorption are measured at low coverage.

Adsorbent	SA_{BET} / $m^2\ g^{-1}$	Setup	Eq model	T/ K	q_{CO}/ mmol g^{-1}	CO ΔH_{ads}/ kJ mol^{-1}	q_{CO_2}/ mmol g^{-1}	S_{CO/CO_2}	q_{N_2}/ mmol g^{-1}	S_{CO/N_2}	q_{H_2}/ mmol g^{-1}	S_{CO/H_2}	q_{CH_4}/ mmol g^{-1}	S_{CO/CH_4}	Ref
HKUST-1	1070	Eq	DSL	298	0.28				~0.23	~1.3	~0.04	~9			[193]
Cu/HKUST-1	855				0.53	~65			~0.22	~9.3	~0.04	~65			
MIL-100(Fe)	2458	Eq + Dyn	DSLF	303	1.2		~3.5								[9]
Cu(I)/MIL-100	898				3.52		0.49	42	0.02	~950			0.15	~200	
MIL-100(Fe)	2200	Eq	DSLF	298	0.15	40	1.3								[10]
Cu(I)/MIL-100(Fe)	790				3.1	53	0.44	420							
MIL-100(Fe)	2042	Eq	DSLF	298	0.38	38			0.3	3					[92]
Cu(I)/MIL-100(Fe)	762				2.78	50			0.15	220					
MIL-101(Cr)	3189	Eq	DSL	298	0.5	44			0.24	6.3	0.12	16			[12]
CuV/MIL-101(Cr)	1697				1.23	52			0.21	70.1	0.09	641.7			
MIL-101(Cr)	3615	Eq + Dyn	DSL	298	1.33	44			0.27	7.4			0.41	4.3	[36]
Cu(I)/MIL-101(Cr)-3(DD)	1843				2.42	46			0.12	1233			0.34	26	
Cu(I)/MIL-101(Cr)-3(ID)					2.25	43			~0.15				~0.3		
Cu(I)/MIL-101(Cr)-3(DL)					2.15	43			~0.15				~0.3		
Zeo-5A (A)	689	Eq	DSLF	298	1.4[a]		5.3[a]		0.52[&]		0.004[a]	796	0.72[a]		[55]
Zeo-5A-COOH (B)	564				1.2[a]		5[a]		0.52[&]		0.022[a]	65	0.77[a]		
MOF-74 (Ni)	1180				4.1[a]		5.5[a]		0.8[&]		0.032[a]	3903	1.1[a]		
Zeo-A@MOF-74 (Ni)-1	1504				5.2[a]	48	7.1[a]		0.87[&]		0.046[a]	24375	1.2[a]		

Adsorbent	SA_{BET} / $m^2\ g^{-1}$	Setup	Eq model	T/ K	q_{CO}/ mmol g^{-1}	CO ΔH_{ads}/ kJ mol^{-1}	q_{CO_2}/ mmol g^{-1}	S_{CO/CO_2}	q_{N_2}/ mmol g^{-1}	S_{CO/N_2}	q_{H_2}/ mmol g^{-1}	S_{CO/H_2}	q_{CH_4}/ mmol g^{-1}	S_{CO/CH_4}	Ref
Zeo-B@MOF-74 (Ni)-1	1216				4.5[a]	43.7	7.1[a]		1.5[&]		0.048[a]	4624	1.26[a]		
POP SNW-1	719	Eq + Dyn		293	0.34				2.25	-					[174]
Cu(I)/SNW-1	136				0.98				0.24	23					

a 110 kPa

1.7 Conclusions and final remarks

In this review, we have presented equilibrium and dynamic adsorption setups, equilibrium and kinetic models, and complied methods of porous support chemical modification for pi-complexation-based adsorption/separation of various chemicals, mainly carbon monoxide. The industrial techniques of CO separation are mainly absorption (i.e., COSORB) and cryogenic separation that face particular challenges of low stability (i.e., the reaction of Cu^{+} to Cu^{2+}, and Cu^{0}) and high-energy consumption, which has led to research on adsorption technology, and preparation of efficient CO adsorbents.

Activated carbon, silica, alumina, zeolites, and metal-organic frameworks are among porous CO adsorbents and support materials. Open metal site MOFs have shown the highest CO adsorption capacity exceeding the performance of Cu-exchanged zeolite Y; however, they lack the stability leading to the choice of adsorbents with higher stability, mainly chemically modified porous adsorbents. Wet impregnation and solid dispersion are two conventional methods of chemical modification used to prepare CO adsorbents that offered limited adsorption capacity and the choice of potential porous supports.

One of the main objectives of this review was to present methods of introducing pi-complex active metal ion, especially Cu(I), to the surface of porous supports using different chemical modification

techniques that address the challenges facing conventional chemical modification methods such as complete reduction and distribution of active species while preserving the porous support.

The introduced internal and external agent facilitated impregnation and reduction were the successful strategies that were employed recently to address these challenges. Moreover, among the chemical modification methods, the external agent facilitated reduction method showed potential in increasing the stability of Cu(I) modified adsorbent against oxidation. However, the issue of Cu(I) stability against oxidation remains a challenge that requires to be addressed in the future.

The typical setup used so far to test the adsorption capacity of different CO adsorbents throughout the literature is the equilibrium adsorption setup providing single-component adsorption isotherm. Single column dynamic adsorption setup, if used, usually serves as a confirmatory technique to equilibrium adsorption. Detailed kinetics of adsorption is often neglected along with the adsorbate-adsorbent interaction at the molecular level. Moving forward, it is necessary to employ various equilibrium adsorption models and adsorption kinetics models simultaneously to fully understand the adsorbent behavior. This will allow the identification of efficient adsorbents under the constraints of process temperature, gas concentration, and adsorbent mass. In many cases, the failed equilibrium/kinetics models are not reported; however, they provide insights and confirmation of the best model.

Throughout the literature, many adsorbents passed the initial testing under equilibrium conditions showing good adsorption capacity and selectivity towards CO based on the IAST calculation. Although promising, the performance of these samples should be investigated under realistic conditions where the separation is performed in a mixture of gases in realistic setups such as PSA, VPSA, and TSA.

Chapter 2: Controlled Formation of CuCl Modified Copper with Solvent-Mediated Morphologies and Their Impact on CO Adsorption Performance

Abstract

Cu^+ ion has been used for the purpose of CO adsorption in many adsorbent materials. In this work, CuCl with different morphologies has been synthesized to investigate the effect of different crystalline planes such as 111 (triangular morphology), and 100 (cubic morphology) on CO adsorption capacity, selectivity, and kinetics. The prepared samples were synthesized on the surface of copper support to form the different morphologies of CuCl and to effectively increase CO adsorption. The CuCl modified samples were characterized using XRD, Rietveld analysis, N_2 adsorption, and SEM. It was confirmed that Cu^+ selectively adsorbed CO through π-complexation and CuCl with triangular and granule morphology has the highest CO adsorption capacity while the cubic morphology of CuCl provides the highest selectivity towards adsorption of CO.

Keywords: morphology, adsorption isotherm, adsorption capacity, selectivity, surface modification

2.1 Introduction

Carbon monoxide is a colorless, odorless, and flammable gas manly produced by reforming of natural gas, partial oxidation, and coal gasification [9-11, 194]. It is also the raw material for production of many chemicals such as acetic acid, formic acid, methanol, liquid hydrocarbon fuels [10, 161]. Carbon monoxide is also present in the effluent gas mixture of steel and metallurgical plants. These effluent gas mixtures include carbon monoxide, carbon dioxide, nitrogen, hydrogen, and methane [9, 195, 196]. Besides, carbon monoxide is highly toxic to the human body as it binds rapidly with the hemoglobin and causes tissue hypoxia [9, 197]. Therefore, selective adsorption of carbon monoxide is crucial both from industrial and environmental health point of view.

There are many methods of CO separation available such as cryogenic separation, absorption, and adsorption. All the mentioned methods, like many others, face specific challenges of separation. For instance, the cryogenic separation is highly energy intensive and ineffective when nitrogen and carbon monoxide are present in the gas mixture since the boiling points of nitrogen and carbon monoxide are the same. Absorption, while effective in separation, has the disadvantage of corrosion of equipment and solvent degradation [9, 14]. Adsorption has gained a lot of attention due to their effective operation and low cost. Synthesis of new materials for adsorption of different pollutants or target gases is the key for the success of adsorption technology. The challenges for adsorption of carbon monoxide using the developed adsorbents are selectivity, working capacity, and stability. For example, in mixture of gases containing carbon dioxide and carbon monoxide, the adsorbents tend to adsorb carbon dioxide due to its higher polarizability [9]. To address these challenges, it is required the adsorbent to be capable of forming a specific type of bonding with carbon monoxide that is stronger than van der Waals bonding, and weaker than chemical bond, as formation of chemical bond increases the cost of regeneration and lowers the carbon monoxide working capacity. Working capacity is defined as the difference of adsorption capacity between the adsorption pressure and the desorption pressure [9, 198].

Transition metal ions, such as Cu^{+}, Ag^{+}, Pt^{2+}, and Pd^{2+}, can form a π-complexation with the π orbital of gas molecule [125]. The π-complexation is a weak dual bond between the transition metal ion and electron cloud of adsorbate in which the s orbital of the metal ion makes a σ bond with the adsorbate and the d orbital of the metal forms a π back-donation with the adsorbate. Usually, Cu^{+} is dispersed on the surface of the adsorbents to adsorb carbon monoxide as it is cheap and readily available. The conventional method of preparing the adsorbents is using copper salt solutions such as CuCl in acids, or $CuCl_2$ in aqueous solution and disperse the solution on the

surface support such as activated carbon, zeolites, metal organic frameworks (MOF). However, it should be mentioned that using the acid solution reduces the crushing strength of the support and impregnation using aqueous solution of cupric chloride does not end up with a high loading of copper. Furthermore, after impregnation the formed cupric chloride should be reduced in a reducing agent such as carbon monoxide or hydrogen to cuprous chloride.

An important aspect that has been neglected in the dispersion/formation of CuCl is the cuprous chloride crystalline plane orientation on the surface of adsorbents. The growth of CuCl on different crystalline planes leads to the formation of crystals with distinct morphologies. For example, the growth of CuCl on the 111 and 100 planes lead to formation of triangular and cubic morphologies respectively. In this study, the effect of CuCl morphology on selective adsorption of carbon monoxide has been investigated.

2.2 Experimental

2.2.1 Materials

Copper(II) chloride dihydrate ($CuCl_2.2H_2O$), ACS, 99+% was purchased from Alfa Aesar, pure ethanol (C_2H_5OH) 200 proof was purchased from KOPTEC, copper powder (99%) was purchased from STREM Chemicals, INC, and deionized water.

2.2.2 Synthesis of CuCl/Cu

0.17 grams of $CuCl_2.2H_2O$ was added to 10 ml pure water, or ethanol, or water-ethanol (v:v, 1:1) solution. After stirring, 1 gram of copper powder was added to the prepared solutions. After 90 seconds, using a vacuum filter, the solution and powder were separated. The collected powder was dried up in oven at 60 °C. Upon drying of the thin liquid layer of cupric chloride formed on copper surface, the surface color was changed which shows the formation of cuprous chloride on the surface of copper powder. Throughout this research the term “copper support” is used for copper

powder since the formed CuCl is supported on the surface of the copper powder. The synthesized samples were stored in a vacuum oven at 50 °C to prevent the oxidation/hydration of CuCl. All prepared samples have the same copper loading (~ 15 wt%) and will be denoted as (X)-CuCl/Cu, where X is the abbreviation for the solutions used (i.e., water:W, ethanol:E, water-ethanol:WE).

2.2.3 Characterization

Powder X-ray diffraction patterns were obtained from Proto Manufacturing AXRD powder diffraction system with a scanning rate of 10 ° min^{-1} in 2θ ranges from 25° to 50°. The copper loadings of the samples were calculated using the obtained XRD pattern and Rietveld analysis. Nitrogen adsorption-desorption equilibrium isotherms were measured at 77 K (liquid nitrogen temperature) using Quantachrome NOVA 2200e surface area, and pore size analyzer. Prior to adsorption equilibrium isotherm analysis, samples were degassed under vacuum at 393 K for 1 hour. The specific surface areas were calculated using Brunauer-Emmet-Teller (BET) method. The total pore volumes were measured at the relative pressure (p/p_0) of about 0.99. The X-CuCl/Cu were characterized using ZEISS EVO 50 scanning electron microscope (SEM) operating at 20 kV.

2.2.4 Gas adsorption measurement

The adsorption isotherms of CO and CO_2 gases were obtained using a static volumetric method. A schematic of the employed apparatus (NOVA 2200e) is shown in **Figure 2-1**.

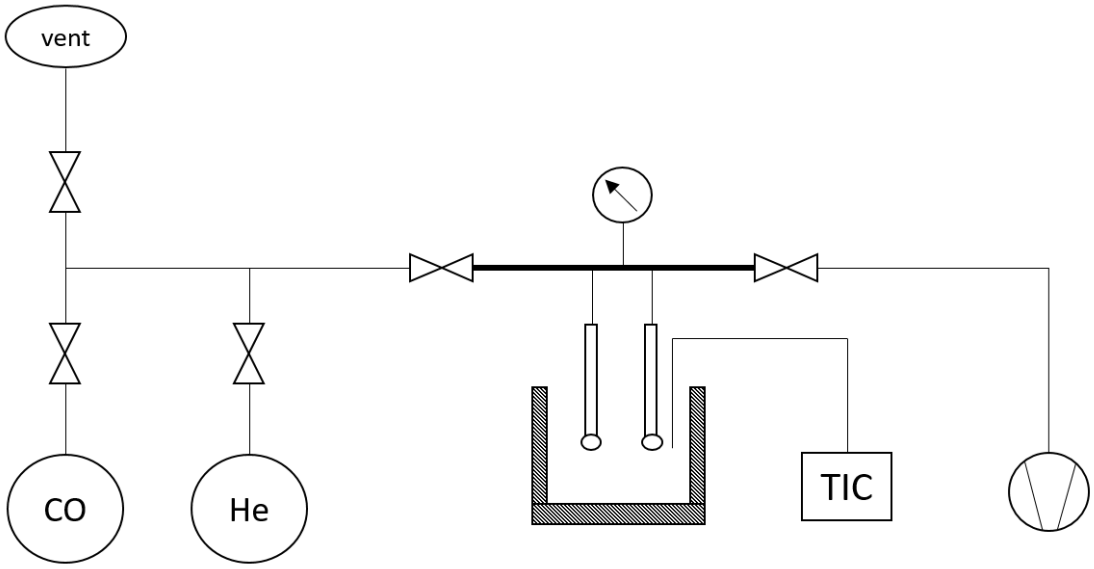

Figure 2-1 Schematic of equilibrium adsorption setup

The setup includes a loading manifold, an adsorption cell, a vacuum pump, and a heating bath equipped with a temperature indicating controller (TIC). The adsorption cells were calibrated by a blank measurement to account for amount of adsorbate gas occupying the cell void volume during adsorption measurement. Before measurements, the samples were loaded into the adsorption cell and degassed under vacuum at 120 °C for one hour to remove any impurities reserved. After degassing, the temperature of the sample was decreased to the desired adsorption temperature. Both loading manifold and adsorption cell are in vacuum condition at the beginning of the adsorption test. Then, the adsorbate, CO or CO_2 is introduced into the loading manifold. After reaching a stable pressure, the valve connecting adsorption cell and loading manifold was opened and the adsorbate gets into contact with the adsorbent. It should be mentioned that the pressure points are introduced to the system prior to running the experiments in the range of 0-100 kPa. Although the equilibrium was reached in 10 minutes, the adsorption time was set to 20 minutes to guarantee that equilibrium was achieved. The value of pressure tolerance to consider a point as equilibrium is 0.1 mmHg, meaning that in the defined amount of time, if the pressure does

not change more than 0.1 mmHg, that point is considered as equilibrium pressure. After reaching the equilibrium, the pressure was recorded and the valve to the adsorption cell was closed. An additional amount of adsorbate was introduced to the loading manifold to obtain another equilibrium point at a higher pressure. **Table 2-1** shows the pressure points introduced to NOVA 2200e prior to the adsorption experiment. This process was repeated for multiple points up to 100 kPa at constant temperatures of 20, 30, 45, and 60 °C. The CO_2 adsorption measurements were performed at 45 °C up to 100 kPa.

Table 2-1 Pressure set points introduced to NOVA 2200e

Pressure (kPa)										
P_1	P_2	P_3	P_4	P_5	P_6	P_7	P_8	P_9	P_{10}	P_{11}
2.5	10.6	18.75	26.87	35	45.66	56.33	67	77.67	88.33	99

2.2.5 Fixed-Bed adsorption experiment

The dynamic breakthrough experiment of CO adsorption on X-CuCl/Cu was performed using a custom-made setup. A schematic of the dynamic flow adsorption is provided in **Figure 2-2**. A column of quartz furnace tube 0.4 m in length and 0.01 m in internal diameter was packed with X-CuCl/Cu. The flows of He and CO were regulated using three digital mass flow controllers (MKS GE50, 0-100 mL/min) with accuracy of 1%. Two of the mass flow controllers were used to mix pure CO and He flow. To achieve the constant inlet concentration of CO (9% CO/He, v/v) before the packed bed, CO and He were mixed with a constant flow of 16.5 mL min^{-1} and vented out. The third mass flow controller was used to control the flow of pure He for the purpose of degassing of prepared X-CuCl/Cu. Helium is used as it is an inert gas and does not undergo chemical reaction with the prepared samples. The degassing was performed under He flow of 100 mL min^{-1} at 393

K for one hour to remove all the impurities adsorbed. Subsequently, the temperature of the bed was reduced to the desired temperature, and He flow was switched to the premixed flow of CO-He. The concentration of CO at the outlet of bed was measured using a thermal conductivity detector (TCD) and the temperature of the bed was monitored using a thermocouple (TC).

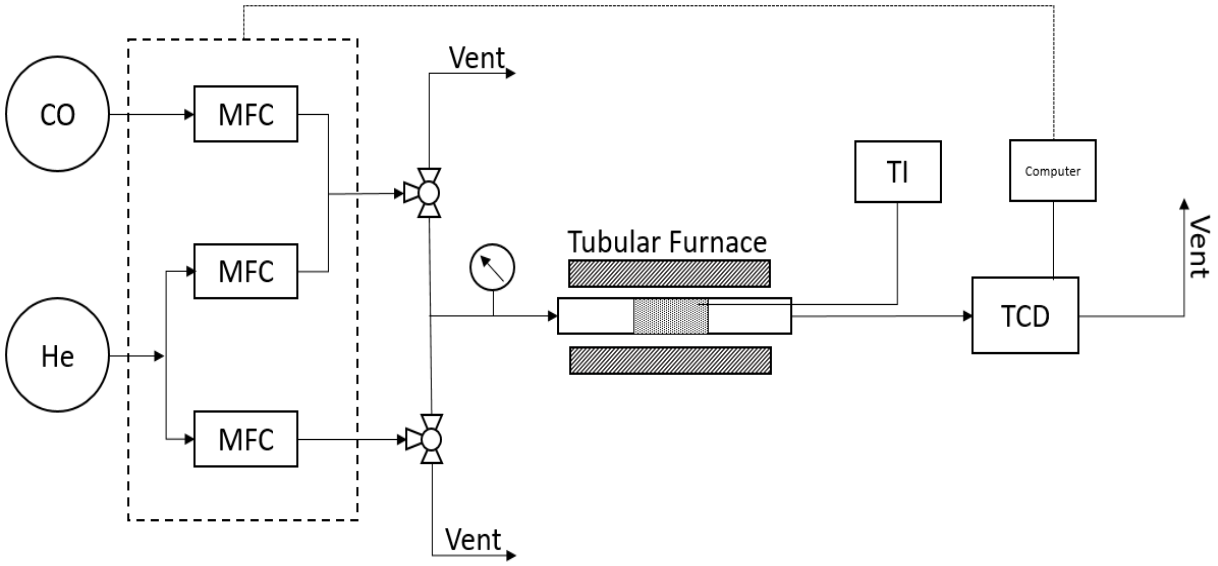

Figure 2-2 Schematic of dynamic adsorption setup

Approximately 10 grams of the as-synthesized samples were loaded into the column. The pressure change in the adsorption column is measured using a pressure gauge at the inlet of the column. Due to large particles of commercial copper powder, there was no pressure drop in the bed. It should be mentioned that in a separate test while the column was packed with much finer copper powder, a pressure drop was observed using the pressure gauge. According to Ergun equation, the particle size has reciprocal relationship with the pressure drop [199]. The experiments were carried out at 318 K and 100 kPa. At t=0, the flow of He was switched to the mixture of CO-He and the experiment continued until the concentration of CO at the outlet of bed reached to initial concentration (i.e., $C/C_0=1$). It should be mentioned that the initial concentration of CO was

regulated using mass flow controllers and the outlet concentration of the carbon monoxide was measured using a Thermal Conductivity Detector (TCD).

2.2.6 Adsorption equilibrium isotherm

Adsorption equilibrium isotherms show information about the adsorption capacity at a given set of state variables, adsorbent-adsorbate interactions, surface properties and affinities of adsorbents. Therefore, it is of importance to establish a mathematical model for adsorption equilibrium isotherms. There are many models proposed to describe the equilibrium adsorption isotherms such as Langmuir, Langmuir-Freundlich (also called Sips), Dual-Site Langmuir [89], and Toth [23]. In this study, the Langmuir model has been employed due to its capability for describing the chemisorption process when ionic or covalent chemical bonds are formed between the adsorbent and the adsorbate [200], to correlate adsorption isotherms of CO at 20, 30, 45, and 60 °C. Langmuir isotherm states a monolayer adsorption on a structurally homogeneous adsorbent in which adsorption occurs at fixed number of surface sites present and all adsorption sites have the same binding energy, and as a result, there is no coverage dependence of heat of adsorption. Langmuir equation is given by:

$$q = q_m \frac{kp}{1 + kp} \qquad 2\text{-}1$$

where q is the adsorbed amount at equilibrium with adsorbate pressure ($\mathrm{mmol\ g^{-1}_{adsorbent}}$), q_m is the maximum amount of adsorption ($\mathrm{mmol\ g^{-1}_{adsorbent}}$), k is adsorption equilibrium constant ($\mathrm{kPa^{-1}}$), and p (kPa) is the equilibrium pressure of the adsorbate in the gas phase.

In contrast to the Langmuir adsorption isotherm in which there is no coverage dependence of heat of adsorption, Sips considers an exponential decay of site density with respect to heat of adsorption. This model predicts the behavior of heterogeneous adsorbents and is written as:

$$q = q_m \frac{kp^n}{1 + kp^n} \quad \text{2-2}$$

where n is a dimensionless isotherm parameter expressing the heterogeneity of the adsorption. To estimate the equilibrium adsorption parameters, a nonlinear regression analysis was performed using Levenberg Marquardt algorithm in OriginPro software version 9.4. It should be noted that the fitting accuracy of both models is estimated using the nonlinear coefficient of determination (R^2) value.

To investigate the interaction between the adsorbate and adsorbent, isosteric heat of adsorption (ΔH) was calculated using the Clausius-Clapeyron equation which is represented as

$$-\Delta H_{adsorption} = R\left[\frac{\partial \ln p}{\partial\left(\frac{1}{T}\right)}\right]_\theta \quad \text{2-3}$$

where θ ($ml\, g^{-1}_{adsorbent}$) is the surface coverage or in other words, the adsorbed amount of adsorbate and R is the gas constant. The integrated form of **Eq. 2-3** is as follows

$$\Delta H_{adsorption} = \frac{RT_1T_2}{T_2 - T_1} \ln\left(\frac{p_2}{p_1}\right) \quad \text{2-4}$$

Selectivity of the samples toward adsorption of carbon monoxide in a mixture of gases (CO-CO_2) was calculated using Ideal Adsorption Solution Theory (IAST) and the Langmuir fitting data according to the following equation

$$S = \frac{x_i/x_j}{y_i/y_j} \quad \text{2-5}$$

where i, and j represent the components in the gas mixture, x and y represent the molar fraction of the species in the adsorbed phase and gas phase, respectively.

Natural heterogeneity of the adsorbents surface hosting the carbon monoxide molecules and binding site affinity spectra are exposed using the Scatchard equation as follows [80]

$$\frac{q}{p} = KN - Kq \quad (2\text{-}6)$$

where K (kPa^{-1}) is the adsorption constant and N ($ml\ g^{-1}_{adsorbent}$) is the number of adsorption sites. It should be mentioned that the adsorption constant is related to binding energy.

2.2.7 Adsorption kinetic

Adsorption kinetic data is an integral part of design, simulation, and development of gas separation, and removal system as it determines the residence time for completion of adsorption, the size of adsorption bed, and hence, unit capital cost [201, 202]. Many kinetic models have been developed to describe the adsorption processes such as the pseudo-first-order kinetic model, pseudo-second-order kinetic model, and Avrami model. Pseudo-first-order kinetic model assumes equilibrium is established between sorbate and sorbent through physisorption, and states that the adsorption rate has a linear relationship with the number of unoccupied adsorption sites. The model is presented by:

$$\frac{dq}{dt} = k_F(q_e - q) \quad (2\text{-}7)$$

where q ($mmol\ g^{-1}$) is uptake amount with respect to time t (s), k_F (s^{-1}) is pseudo-first-order kinetic rate constant, and q_e represents the equilibrium uptake ($mmol\ g^{-1}$). Integrating 2-7 with the boundary conditions q=0 at t=0, and q=q_e at t=t_∞ ends up with the following equation.

$$q = q_e(1 - \exp(-k_F t)) \quad (2\text{-}8)$$

The assumption is pseudo-second-order kinetic model is that chemical interaction between adsorbate and adsorbent control the overall adsorption kinetic. This model is expressed as

$$\frac{dq}{dt} = k_S(q_e - q)^2 \quad (2\text{-}9)$$

where k_s (mmol g^{-1} s^{-1}) is pseudo-second-order kinetic constant. As it can be seen from 2-9, the uptake rate is proportional to the square unoccupied adsorption sites. Integrating equation 2-9 and applying the boundary conditions as q=0 at t=0, and $q=q_e$ at $t=t_\infty$ ends up with the following equation:

$$q = \frac{q_e^2 k_s t}{1 + q_e k_s t} \qquad 2\text{-}10$$

Recently, Avrami model has been used for prediction of carbon dioxide adsorption kinetics on amine-modified adsorbents [203-205]. The Avrami model is expressed as

$$\frac{dq}{dt} = k_A^n t^{n-1}(q_e - q) \qquad 2\text{-}11$$

where k_A (s^{-1}) is Avrami kinetic constant, and n is the Avrami exponent. Integrating the Avrami model ends up with

$$\frac{q}{q_e} = 1 - e^{-(k_A t)^n} \qquad 2\text{-}12$$

The fitting of adsorption kinetic data, as in the case of equilibrium adsorption, was performed by a nonlinear regression using the Levenberg Marquardt algorithm and the goodness of fit was investigated using the nonlinear coefficient of determination (R^2).

2.3 Results and discussion

2.3.1 Sample characterization

SEM images of the copper support and the prepared samples were obtained to investigate the morphology of cuprous chloride on the surface of copper support. **Figure 2-3a** shows the surface of copper support. Typically, after the comproportionation reaction between copper powder and 0.1 M ethanol solution of cupric chloride, cuprous chloride crystals with granule and triangular morphology of the size of 1-2 microns were formed on the surface of copper support (**Figure 2-3b**). This is while the comproportionation reaction using the 0.1 M water solution of cupric

chloride resulted in formation of irregular morphology of CuCl on the surface of copper support (**Figure 2-3c**). Using the 0.1 M ethanol-water (v:v, 1:1) solution of $CuCl_2$ resulted in the formation of CuCl with cubic morphology on the surface of copper support (**Figure 2-3d**). The results are in agreement with the reported CuCl morphology in the literature [206].

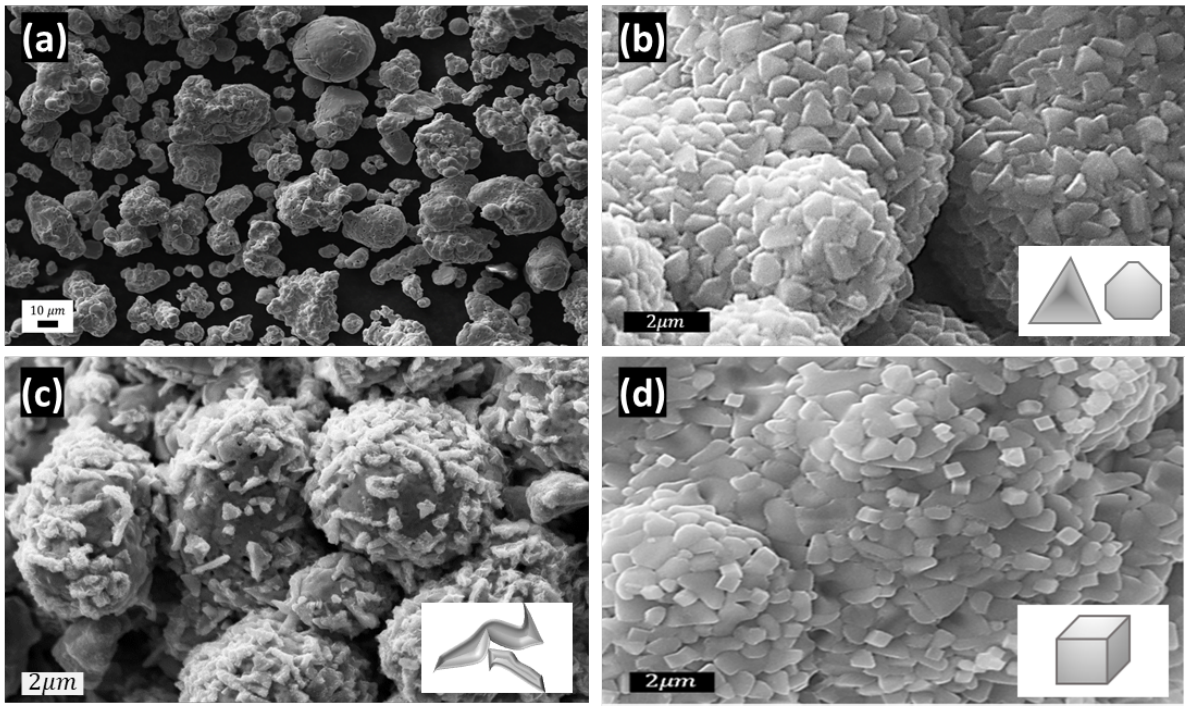

Figure 2-3 SEM image of a) copper powder, b) E-CuCl/Cu, c) W-CuCl/Cu, and d) WE-CuCl/Cu

Figure 2-4 shows the X-ray diffraction of (X)-CuCl/Cu. Peaks at 28 ° and 47 ° confirm the presence of cuprous chloride on the surface of copper support. Furthermore, the peak with the highest intensity at 43 ° confirms the presence of copper support. These peaks are available for all three samples with different morphologies which confirms the presence of CuCl for all the prepared samples. However, to investigate the effect of different morphologies of CuCl on adsorption of carbon monoxide, one must be sure that the loading of CuCl is the same for all the prepared samples. Therefore, the loadings of different samples were calculated using Rietveld analysis, using the XRD patterns of the samples.

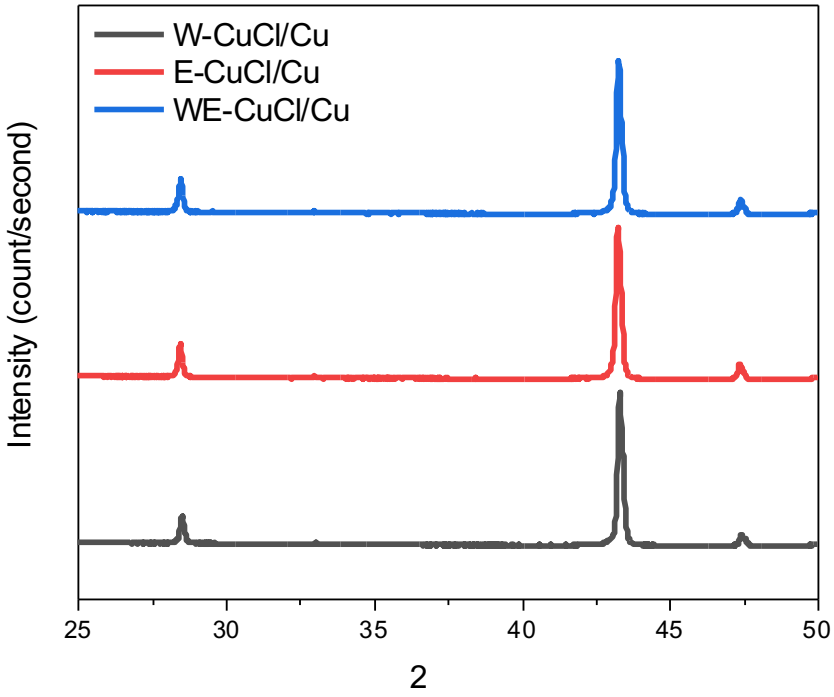

Figure 2-4 XRD patterns of X-CuCl/Cu

Table 2-2 shows the calculated average weight percent loadings of CuCl on different samples. It has been confirmed that all the samples have the same weight percent loadings about 14 %. The accuracy of the calculations was confirmed using the weight profile R factor. An acceptable value of the R factor is below 10% [207]. Throughout this research, Rietveld analysis has been done for all the prepared samples to guarantee the consistency of samples.

Table 2-2 CuCl loading of X-CuCl/Cu base on Rietveld analysis

Sample	Loading average (wt%)	Weight profile R-factor, Rwp average(%)
W-CuCl/Cu	13.7 (± 1)	4.11
E-CuCl/Cu	13.7 (± 1)	4.04
WE-CuCl/Cu	14.0 (± 1)	3.48

As mentioned before, two of the important factors affecting adsorption capacity of different adsorbents are surface area and pore volume. Accordingly, the nitrogen adsorption isotherm and surface area were measured. **Figure 2-5** shows a characteristic type II nitrogen adsorption isotherm for copper powder and (X)-CuCl/Cu. The linearity of the isotherms shows the presence of non-porous material, since for porous materials the amount of adsorbed nitrogen at low pressures is characterized by a sharp increase due to adsorption in pores. It should be mentioned that E-CuCl/Cu (triangular and granule morphology) adsorbed the highest amount of N_2 (i.e., 7.5 ml g^{-1} at $p/p_0 = 1$) and W-CuCl/Cu (irregular morphology) had the lowest amount of nitrogen adsorption (i.e., 3 ml g^{-1} at $p/p_0 = 1$). **Table 2-3** shows the BET analysis results of copper powder and (X)-CuCl/Cu. As it can be seen from this table, the measured surface area for copper powder and all the samples were about 2 m^2 g^{-1}. The pore volume of the samples was calculated from the amount of vapor adsorbed at a relative pressure close to unity, by assuming that the pores are filled with liquid adsorbate. The volume of nitrogen adsorbed (V_{ads}) can be converted to the volume of liquid nitrogen (V_{liq}) contained in the pores using the following equation [208]

$$V_{liq} = \frac{P_a V_{ads} V_m}{RT} \qquad 2\text{-}13$$

where T and P_a are ambient temperature and pressure, respectively, V_m is the molar volume of the liquid adsorbate (34.7cm^3 mol^{-1} for nitrogen), and R is the gas constant. The measured pore volume for all the samples (i.e., ~ 0.003 ml g^{-1}) confirm that our samples are non-porous.

Table 2-3 BET results of copper substrate and X-CuCl/Cu

Sample	Surface area (m^2 g^{-1})	Pore volume (ml g^{-1})
Cu	2.3 (± 0.03)	0.002
E-CuCl/Cu	2.5 (± 0.03)	0.005
W-CuCl/Cu	1.9 (± 0.06)	0.002
WE-CuCl/Cu	1.8 (± 0.05)	0.003

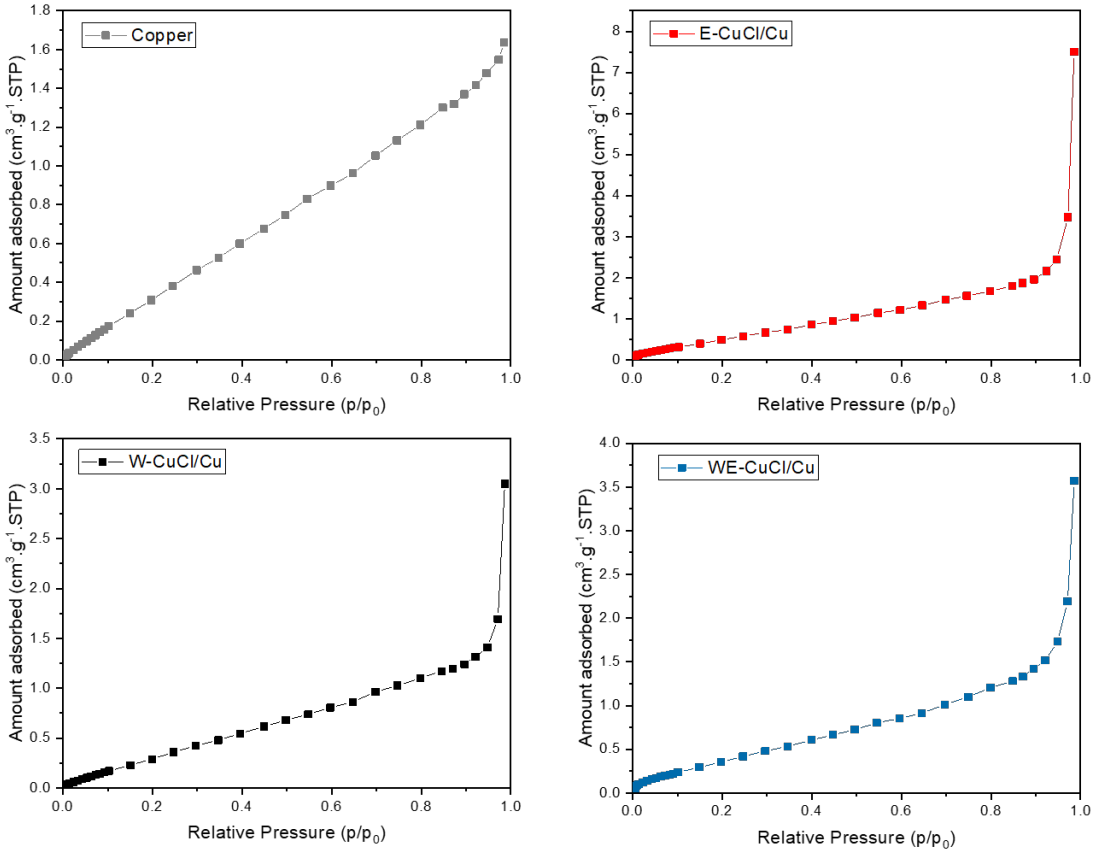

Figure 2-5 Nitrogen isotherm of copper substrate and X-CuCl/Cu

2.3.2 Effect of temperature on adsorption of carbon monoxide

The effect of temperature on adsorption of carbon monoxide has been investigated for the prepared samples.

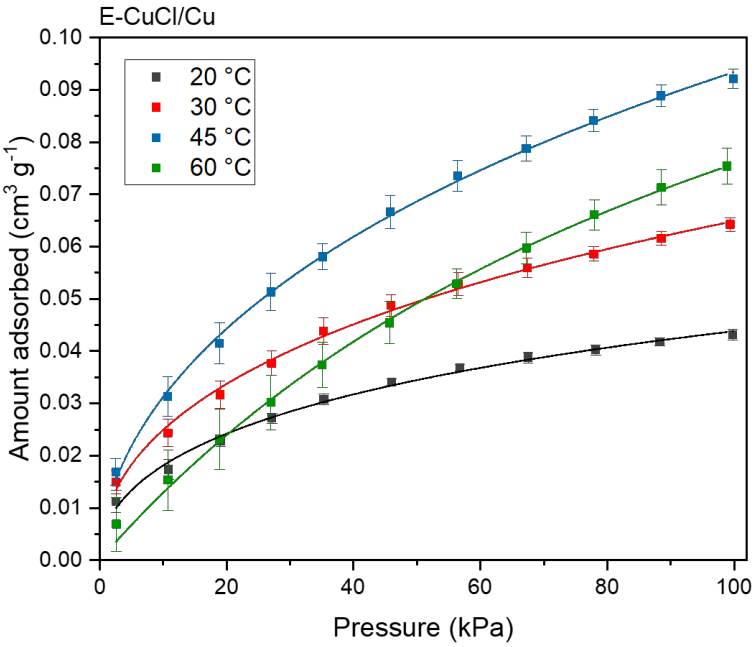

Figure 2-6 shows the CO equilibrium adsorption isotherm of E-CuCl/Cu at 20 °C, 30 °C, 45 °C, and 60 °C. Each point in the graph represents the acquired data using the static adsorption setup and the line shows the fitted data using Langmuir isotherm equation (**Eq. 2-1**). Interestingly, it was found that there is an optimal temperature for adsorption of carbon monoxide on E-CuCl/Cu. With increase of temperature from 20 °C to 45 °C, the uptake has increased significantly; however, increasing temperature from 45 °C to 60 °C resulted in a decrease in the amount of CO adsorbed on E-CuCl/Cu. This behavior is showing that there is a minimum energy is required to bring the CO molecule from the gas phase to adsorbed state, as a result more energy will be required to completely desorb the molecule from the surface of E-CuCl/Cu. Furthermore, at all the experimental temperatures, the amount of adsorption has increased with the increase of pressure up to 100 kPa, which is due to the increase in interaction of CO molecules with the surface.

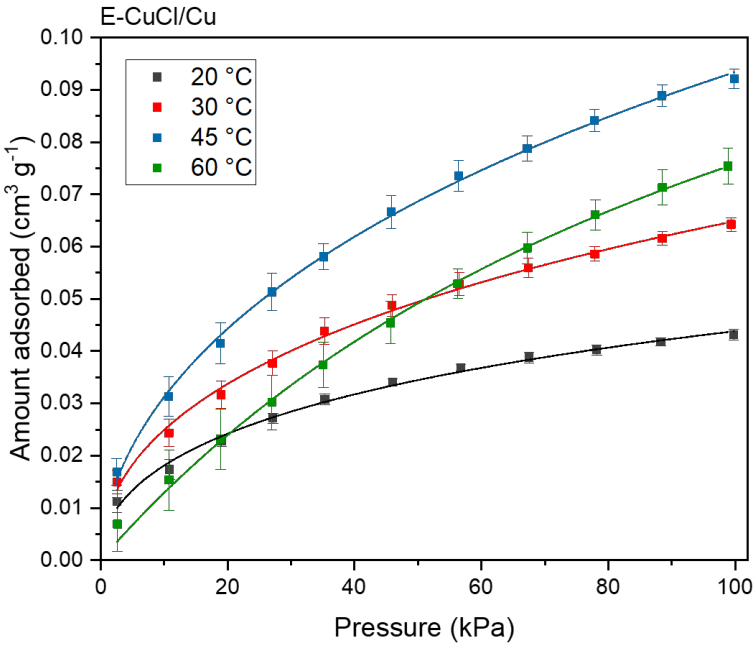

Figure 2-6 CO adsorption isotherms of E-CuCl/Cu at different temperatures

The acceptable Langmuir fit (**Table 2-4**) shows that monolayer adsorption of carbon monoxide is predominant for adsorption of carbon monoxide on the surface of E-CuCl/Cu.

Table 2-4 Langmuir and Langmuir-Freundlich fitting parameters for CO

Model		Langmuir			Langmuir-Freundlich			
Sample	T (°C)	q_m ($cm^3\ g^{-1}$)	k_L (kPa^{-1})	R^2	q_m ($cm^3\ g^{-1}$)	k_S (kPa^{-1})	n_S	R^2
E-CuCl/Cu	20	0.05146	0.04516	0.965	0.12658	0.05259	0.50137	0.994
	30	0.0789	0.03733	0.968	0.30459	0.02931	0.48268	0.996
	45	0.12306	0.02743	0.982	0.40148	0.02345	0.55577	0.998
	60	0.16576	0.00843	0.997	0.374	0.00641	0.80312	0.999

Figure 2-7 shows the equilibrium adsorption isotherm of W-CuCl/Cu at 20 °C, 30 °C, 45 °C, and 60 °C. The points are the actual data obtained from static adsorption setup and the lines show the fittings of the data according to Langmuir equation and **Table 2-5** shows the Langmuir fitting parameters. The R^2 values express the goodness of fitting of the data to Langmuir equation which in turn shows the monolayer adsorption of carbon monoxide on the surface of W-CuCl/Cu.

Interestingly, W-CuCl/Cu is showing the same behavior as E-CuCl/Cu in adsorption of carbon monoxide at different temperatures. As can be seen in the pure adsorption isotherm of carbon monoxide at different temperatures (**Figure 2-7**) with the increase in temperature from 20 °C to 45 °C the uptake has increased significantly and by increasing the temperature from 45 °C to 60 °C, there is a drop in the CO adsorbed amount. It should be stated that in all experimental temperatures the adsorption amount has increased with the increase of pressure to 100 kPa.

Table 2-5 W-CuCl/Cu Langmuir and Langmuir-Freundlich fitting parameters for CO

Model		Langmuir			Langmuir-Freundlich			
Sample	T (°C)	q_m ($cm^3\ g^{-1}$)	k_L (kPa^{-1})	R^2	q_m ($cm^3\ g^{-1}$)	k_S (kPa^{-1})	n_S	R^2
W-CuCl/Cu	20	0.025	0.00938	0.996	0.03281	0.0096	0.89468	0.996
	30	0.03889	0.00876	0.997	0.07999	0.00718	0.80971	0.999
	45	0.15934	0.00342	0.999	0.15933	0.00342	1	0.999
	60	0.29315	0.00142	0.998	0.10206	0.00228	1.18983	0.999

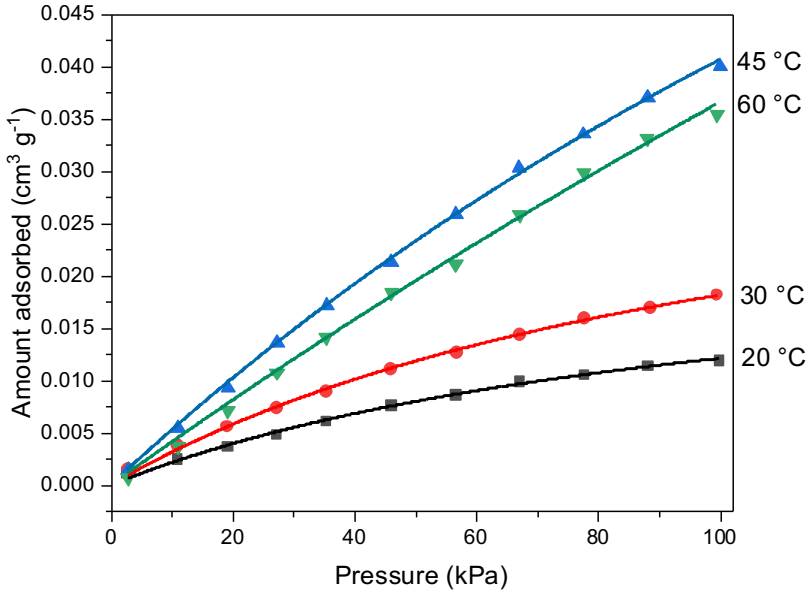

Figure 2-7 CO adsorption isotherm of W-CuCl/Cu at different temperatures

Figure 2-8Error! Reference source not found. shows the adsorption isotherm of pure carbon monoxide on WE-CuCl/Cu. Using this sample, the adsorption capacity of CO has increased with increase of pressure to 100 kPa at all the experimental temperatures. In addition, this cubic morphology of CuCl, is showing the same adsorption behavior as the other morphologies, meaning that with the increase of temperature up to 45 °C, there is a significant increase in the adsorption while the increase of temperature up to 60 °C resulted in a decrease in adsorption amount. The R^2 values express (

Table 2-6) a good fit of data to Langmuir equation that shows the monolayer adsorption of carbon monoxide on the surface of WE-CuCl/Cu.

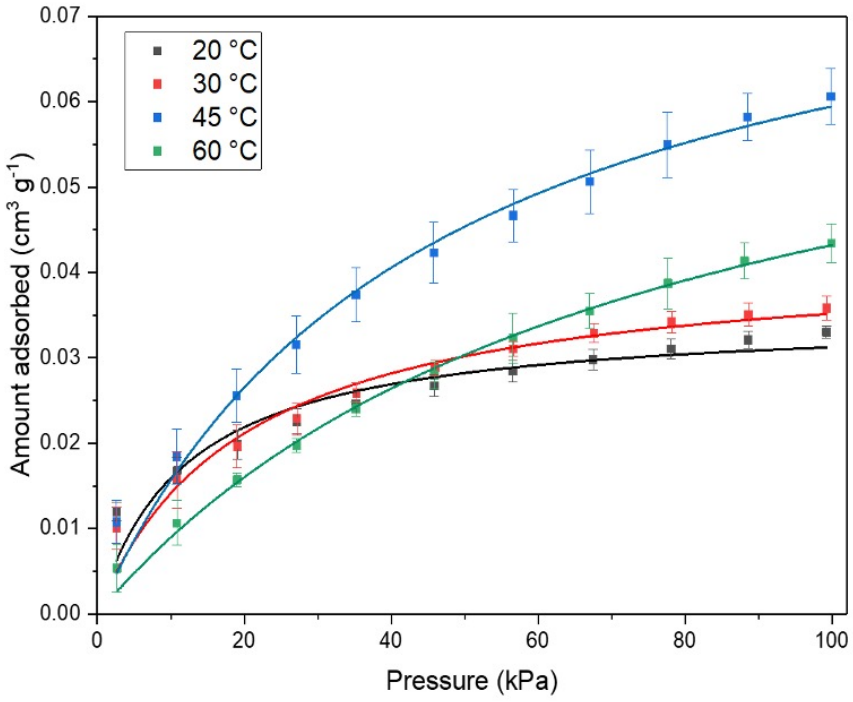

Figure 2-8 CO adsorption isotherm of WE-CuCl/Cu at different temperatures

Table 2-6 WE-CuCl/Cu Langmuir and Langmuir-Freundlich fitting parameters for CO

Model		Langmuir			Langmuir-Freundlich			
Sample	T	q_m	k_L	R^2	q_m	k_S	n_S	R^2

	(°C)	($cm^3\ g^{-1}$)	(kPa^{-1})		($cm^3\ g^{-1}$)	(kPa^{-1})		
WE-CuCl/Cu	20	0.03498	0.08345	0.895	0.41749	0.02046	0.31299	0.997
	30	0.04217	0.05033	0.955	0.12858	0.04951	0.45389	0.995
	45	0.08624	0.0222	0.983	0.45942	0.0119	0.55693	0.997
	60	0.0751	0.01355	0.994	0.19045	0.01129	0.7133	0.998

Figure 2-9 shows the comparison between different prepared samples and the copper substrate for adsorption of carbon monoxide at 45 °C. As can be seen in the graph, copper support is not an adsorbent of carbon monoxide and the decorating CuCl with different morphologies on the surface of copper support are causing the increase in the adsorption of carbon monoxide. Furthermore, the E-CuCl/Cu, with triangular and granule shape, shows the highest adsorption amount of carbon monoxide (i.e., 0.09 cm^3g^{-1}), while WE-CuCl/Cu, with cubic shape, has higher adsorption amount (i.e., 0.06 cm^3g^{-1}) in comparison to W-CuCl/Cu with irregular morphology (i.e., 0.035 cm^3g^{-1}).

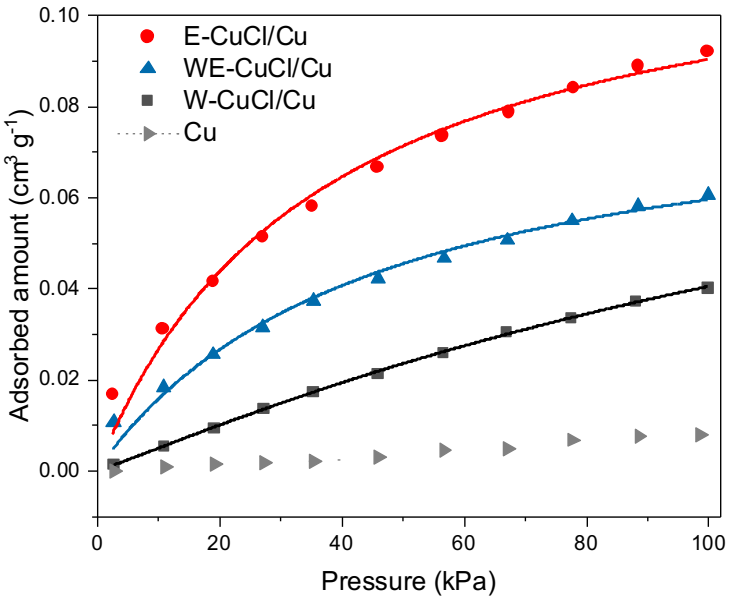

Figure 2-9 CO adsorption isotherm of copper powder and X-CuCl/Cu at 45°C

As it was shown, for all the samples, the increase of temperature up to 45 °C resulted in the increase in the adsorption capacity. This behavior indicates that activated adsorption is the mechanism

adsorption of carbon monoxide on X-CuCl/Cu. This means that for carbon monoxide to adsorb on the surface of sample it requires some energy which has been provided by increasing the temperature to 45 °C; however, by increasing the temperature to 60 °C, the repulsion forces overcome the attraction forces between CO and the surface of the sample leading to lower adsorption capacity.

2.3.3 Selectivity of X-CuCl/Cu towards adsorption of carbon monoxide

The adsorption capacity of samples towards adsorption of carbon dioxide were investigated using the pure adsorption isotherm of CO_2 at 45 °C and the acquired data were fitted to both Langmuir and LF equations and the fitting parameters are provided in **Table 2-7**. **Figure 2-10** shows the comparison between the pure component adsorption of carbon monoxide and carbon dioxide on E-CuCl/Cu. For both carbon monoxide and carbon dioxide, with increase of pressure to 100 kPa, the adsorption amount has increased; however, the adsorption of carbon dioxide is showing an unfavorable isotherm that has a concave shape and requires a relatively high pressure to achieve an economic adsorption. Besides, the favorable isotherm of adsorption of carbon monoxide, with the convex shape, is due to presence of CuCl on the surface of copper support. Therefore, the pure adsorption isotherm of E-CuCl/Cu is showing a higher adsorption of CO than CO_2.

Table 2-7 Langmuir and LF fitting parameters of adsorbents for CO_2 at 45 °C

Models	Langmuir			Langmuir-Freundlich			
Sample	q_m ($cm^3\ g^{-1}$)	k_L (kPa^{-1})	R^2	q_m ($cm^3\ g^{-1}$)	k_S (kPa^{-1})	n_S	R^2
E-CuCl/Cu	1.14817	0.000249	0.976	0.09243	0.000365	1.55651	0.999
W-CuCl/Cu	1.23058	0.000310	0.989	0.06974	0.000624	1.62792	0.999
WE-CuCl/Cu	0.80326	0.000159	0.927	0.07273	0.00007	1.7779	0.997

Figure 2-11 shows the pure component isotherms of CO and CO_2 achieved from W-CuCl/Cu at 45 °C. From the graph, it can be seen that for both gases, W-CuCl/Cu, which has the irregular morphology, shows a very close uptake of adsorbates. Therefore, it can be said that the irregular

morphology of CuCl is not a good candidate for selective separation of carbon monoxide and, as mentioned before, the irregular morphology has the lowest adsorption capacity of CO in comparison to other morphologies.

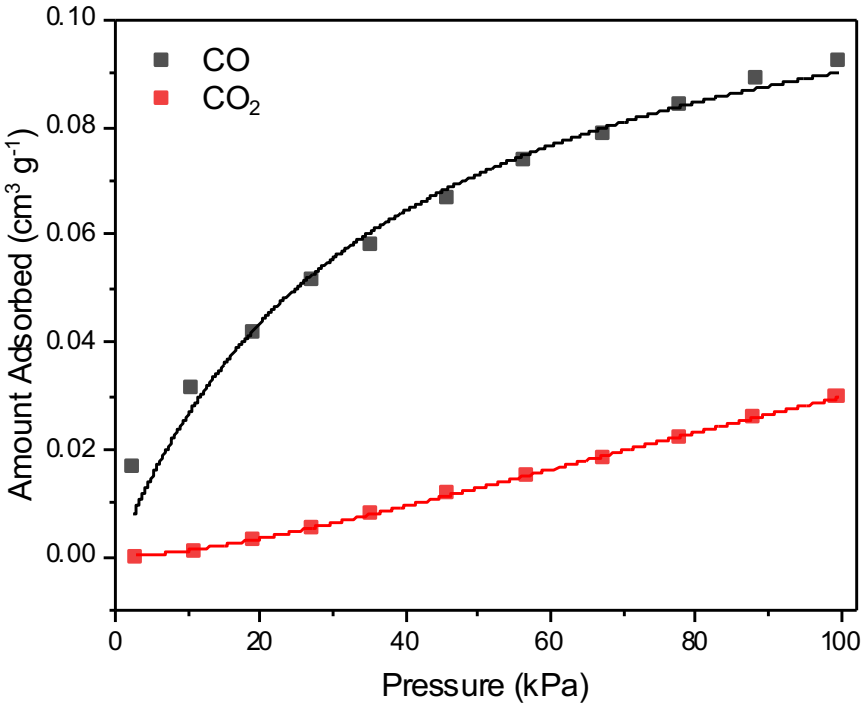

Figure 2-10 Pure component adsorption isotherms of E-CuCl/Cu

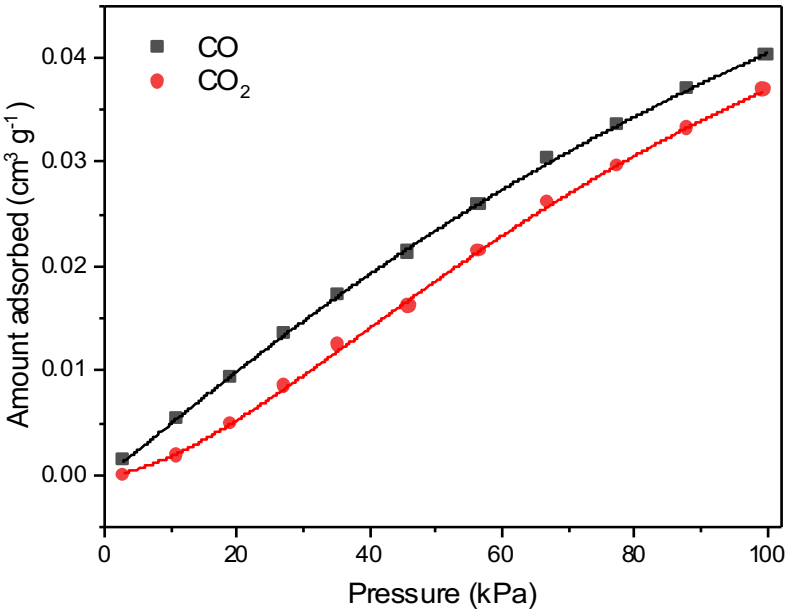

Figure 2-11Pure component adsorption isotherms of W-CuCl/Cu

The pure component adsorption isotherms of WE-CuCl/Cu at 45 °C for both carbon monoxide and carbon dioxide are shown in **Figure 2-12**. The adsorption isotherm of carbon dioxide has a concave form while that of carbon monoxide is convex. This shows a favorable adsorption of carbon monoxide and unfavorable adsorption of carbon dioxide, which in turn shows that cubic morphology of CuCl, is a very good adsorbent of CO in comparison to CO_2.

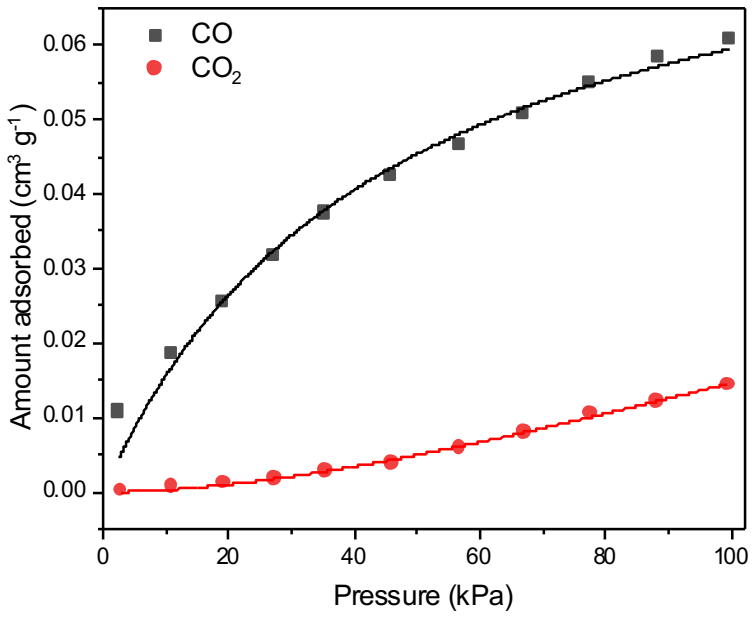

Figure 2-12 Pure component adsorption isotherms of WE-CuCl/Cu

The selectivity of samples towards adsorption of carbon monoxide in a mixture of gases containing CO_2 and CO were investigated using the fitted data and IAST according to the **Eq. 2-5** and the results are presented in **Figure 2-13**. The graph states the selectivity towards adsorption of carbon monoxide in a gas mixture containing different volumetric concentrations (i.e., molar ratio) of carbon monoxide. With the increase of CO concentration in the gas mixture, the selectivity values of CO/CO_2 have increased. Interestingly, one can see that the cubic morphology of CuCl (i.e., WE-CuCl/Cu) has the highest selectivity value at all concentrations of CO, while CuCl with irregular morphology has the lowest selectivity value. In detail, at a CO molar fraction of 0.5, cubic CuCl shows a selectivity of 9 for CO/CO_2 whereas the selectivity of triangular-granule morphology and irregular morphology at a CO molar fraction of 0.5 is 5.55 and 1.25 for CO/CO_2 respectively. Further calculations show that the selectivity of CO/CO_2 on WE-CuCl/Cu is about 3 and 9 times that of E-CuCl/Cu and W-CuCl/Cu, respectively.

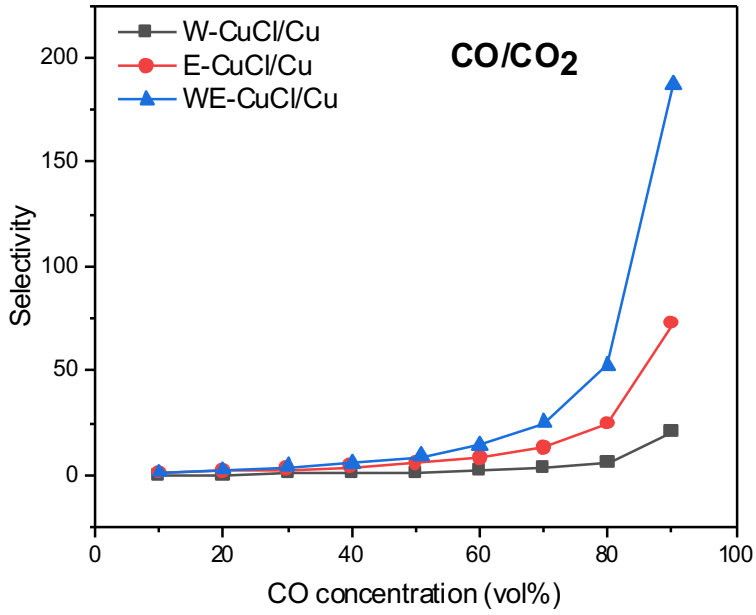

Figure 2-13 Selectivity of X-CuCl/Cu toward adsorption of CO

2.3.4 Type of interaction between X-CuCl/Cu and carbon monoxide

The isosteric heat of adsorption was calculated to investigate the interaction between the adsorbate and adsorbent. The Langmuir fitting parameters for E-CuCl/Cu and WE-CuCl/Cu (**Table 2-4** and **Table 2-6)Error! Reference source not found.** at 45 °C and 60 °C were used to conduct the calculations. **Figure 2-14** describes the result of isosteric heat of adsorption for E-CuCl/Cu, and WE-CuCl/Cu. It is shown that the initial heat of adsorption at zero coverage of the surface is 79.67 and 51.75 kJ mol^{-1} for E-CuCl/Cu and WE-CuCl/Cu respectively. Afterwards, with the increase in both adsorption capacities, the value of heat of adsorption drops to 50 and 43 kJ mol^{-1} for E-CuCl/Cu and WE-CuCl/Cu respectively. These values are lower than the reported value for chemical bond forces and higher than the value reported for van der Waals force, therefore, these values confirm the formation of π-complexation bond between CuCl and carbon monoxide. The decline in isosteric heat of adsorption after is attributed to the occupation of active sites of Cu^{+} by

carbon monoxide. It should also be noted that in all the pressure range, the values of isosteric heat of adsorption for E-CuCl/Cu is higher than that of WE-CuCl/Cu, which shows a stronger reaction between triangular-granule shape CuCl with carbon monoxide.

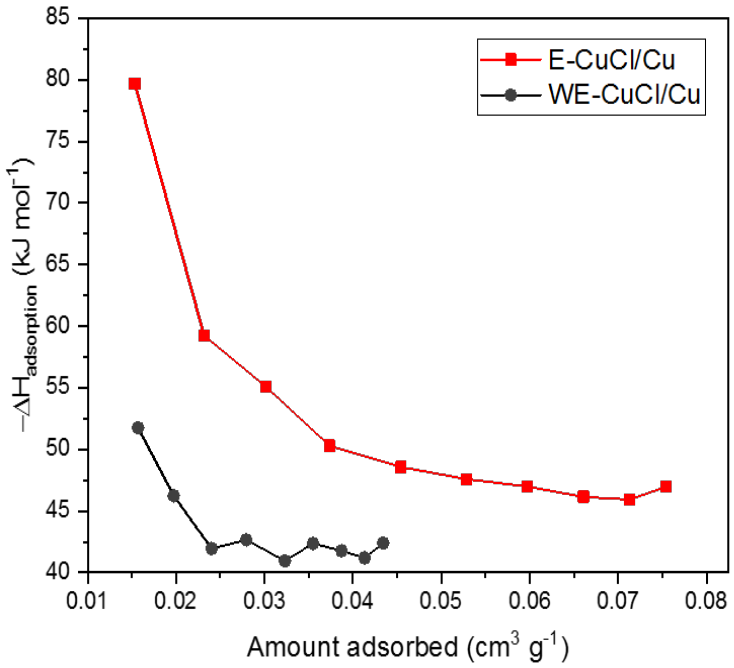

Figure 2-14 Isosteric heat of adsorption

2.3.5 Heterogeneity of X-CuCl/Cu

Since it is less likely for crystalline materials to have a homogeneous adsorption of adsorbate molecule on the surface, the heterogeneity of the samples was investigated using the Scatchard equation (**Eq. 2-6**). **Figure 2-15** shows the Scatchard plot, the plot of q/p versus q, which provides the information about the energetic heterogeneity of the prepared samples. According to the equilibrium data fitted with the Scatchard equation, three different regions can be seen. This indicates that E-CuCl/Cu has at least three distinct types of adsorption sites with the corresponding binding energies of K_1, K_2, and K_3 (see **Figure 2-15a**). Heterogeneity of WE-CuCl/Cu was also investigated using the Scatchard equation (see **Figure 2-15**). According to data fitted with the

Scatchard equation, as for the case of E-CuCl/Cu, there are at least three distinct adsorption sites with corresponding energies of K_1, K_2, and K_3.

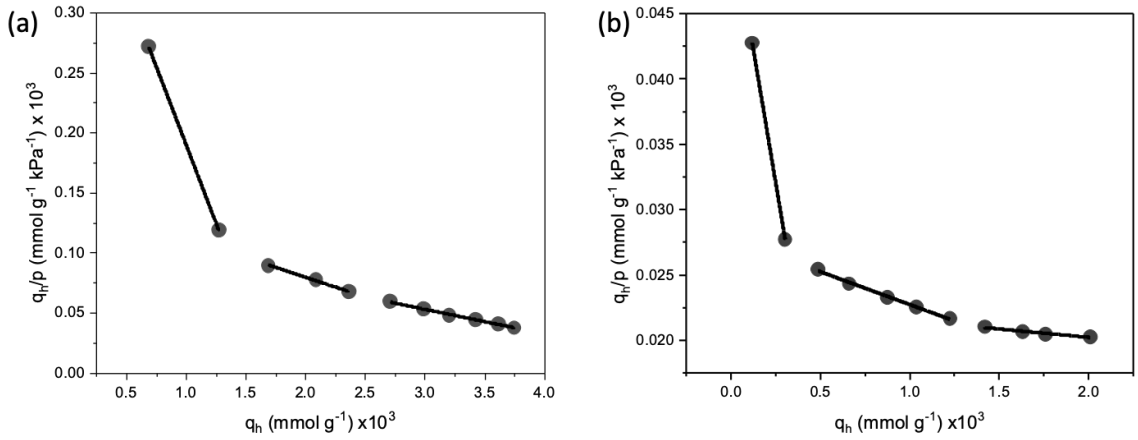

Figure 2-15 Experimental data and fitted Langmuir isotherm according to Scatchard equation for (a) E-CuCl/Cu, and (b) WE-CuCl/Cu

2.3.6 Kinetics of adsorption

Although equilibrium adsorption is being widely used to perform the initial screening of the adsorbents. In order to capture the adsorption behavior in a realistic condition, the samples were tested in the dynamic adsorption setups and kinetics of adsorption were investigated. The breakthrough experiment was performed at room temperature and the result is shown in **Figure 2-16**.

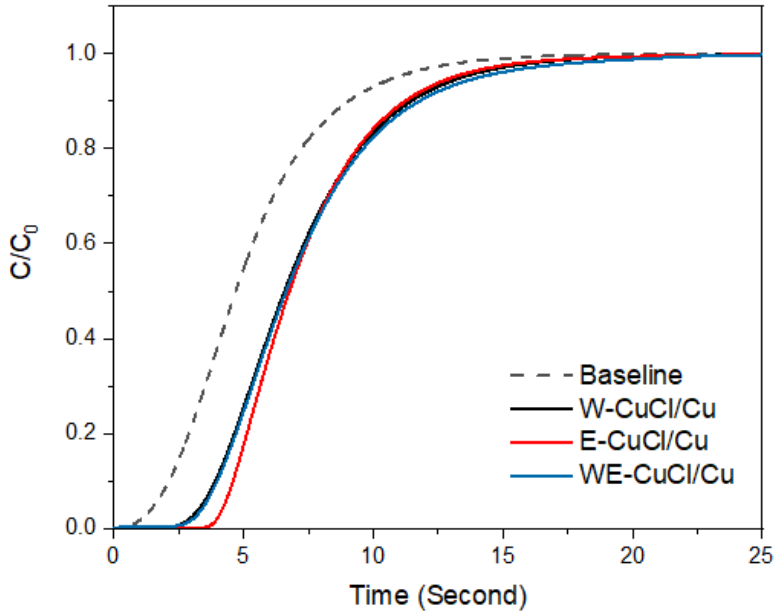

Figure 2-16 Breakthrough curve obtained from dynamic setup using X-CuCl/Cu

Using the breakthrough curve, the kinetic of adsorption on different samples were calculated. **Figure 2-17** presents the adsorption amount versus time for three prepared samples in which the points represent the experimental data collected from the TCD (Thermal Conductivity Detector) and the lines show the fitting to discussed kinetic models. The results reveal that E-CuCl/Cu, characterized by the triangular-granule shape, achieved the highest adsorption uptake of 0.0028 mmol g^{-1}, while W-CuCl/Cu with the irregular morphology exhibited the lowest CO uptake of 0.0017 mmol g^{-1}, and WE-CuCl/Cu had the intermediate CO uptake of 0.0026 mmol g^{-1}. The fitting parameters and the goodness of fit (R^2) are provided in **Table 2-8**. Compared to Avrami model, both PFO and PSO models overpredicted the CO adsorption capacity comparing to the experimental value. Furthermore, the fitted curves **Figure 2-17** and R^2 values show a better fit to Avrami model. These observations suggest that CO adsorption involves a combination of physisorption and chemisorption, which Avrami model accounts for effectively by considering

both interactions. Additionally, the equilibrium adsorption isotherm data supports the chemical interaction of CO with the adsorbent, as evidenced by the increase in adsorption capacity with temperature. The fractional order of n_A reflects the complexity of the reaction mechanism or the presence multiple reaction pathways [209]. Furthermore, the calculated k_A values demonstrate a faster adsorption kinetics in the order of E-CuCl/Cu>WE-CuCl/Cu>W-CuCl/Cu.

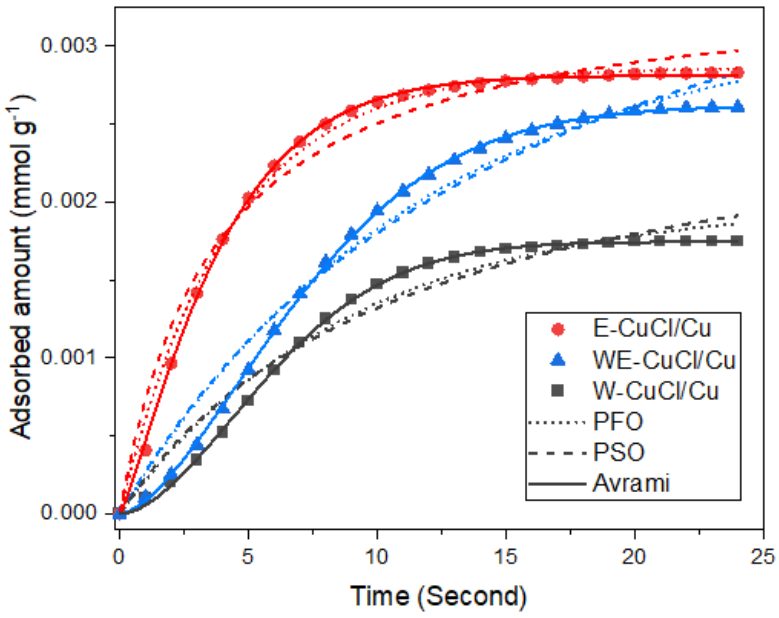

Figure 2-17 Adsorption kinetic of X-CuCl/Cu

Table 2-8 Pseudo-first order model fitting parameteres

Models	Parameters	E-CuCl/Cu	W-CuCl/Cu	WE-CuCl/Cu
	$q_{experiment}$ (mmol g^{-1})	0.0028	0.0017	0.0026
Pseudo-First-Order (PFO)	k_F (s^{-1})	0.24	0.11	0.085
	$q_{calculated}$ (mmol g^{-1})	0.0029	0.0020	0.0032
	R^2	0.995	0.966	0.977
Pseudo-Second-Order (PSO)	k_S (mmol g^{-1} s^{-1})	78.95	31.42	12.66
	$q_{calculated}$ (mmol g^{-1})	0.0034	0.0028	0.0048
	R^2	0.975	0.953	0.970

Avrami	K_A (s^{-1})	0.243	0.142	0.120
	$q_{calculated}$ (mmol g^{-1})	0.0028	0.0017	0.0026
	n_A	1.20	1.75	1.61
	R^2	0.999	0.999	0.999

2.4 Conclusion

Here, surface of copper was decorated with different morphologies of CuCl through comproportionation reaction. It was shown that the solvents act as morphology-regulating agents. The use of pure ethanol, pure water, and ethanol-water mixture formed CuCl with triangular/granule, irregular, and cubic morphologies. investigated the adsorption capacity of different prepared morphologies of CuCl crystals for adsorption of carbon monoxide using different solutions of 0.1 M cupric chloride solution. We found that the highest CO adsorption capacity is achieved by a triangular-granule morphology of CuCl that was prepared using an ethanol-based solution. Based on the result from dynamic setup, this morphology also has the highest adsorption kinetics. The cubic morphology showed a higher selectivity towards adsorption of carbon monoxide whereas irregular morphology has the worst selectivity and adsorption capacity towards adsorption of carbon monoxide. Furthermore, according to isosteric heat of adsorption it is confirmed that CuCl made a π-complexation with carbon monoxide.

Chapter 3: A Highly Stable CuO-Derived Adsorbent with Dual Cu(I) Sites for Selective CO Adsorption

Abstract

Cu(I)-based adsorbents with high stability and adsorption capacity enable effective carbon monoxide separation. Starting from CuO nanoparticles, we synthesized a CO adsorbent with Cu_2O and CuCl on the surface by a two-step synthesis route. The first step was a fast thermal reduction under 5 vol% flow of H_2 at 673 K. CuCl was then introduced by a room temperature liquid-phase reaction between surface metallic copper and $CuCl_2$. X-ray diffraction was used to investigate the stability of the dual-active site adsorbent under atmospheric air. Compared to single Cu(I) site counterparts, the dual-active site adsorbent has a superior adsorption capacity and selectivity for CO, making itself a promising candidate for CO-CO_2 mixture separation. Site energy distribution was used to describe the heterogeneity of the adsorbent surface based on equilibrium adsorption isotherm models. Each synthesis step resulted in the formation of sites at both high and low ends of the site energy spectrum. Adsorption kinetics of CO and CO_2 to the adsorbent was also investigated by fitting kinetics results to various adsorption kinetic models. We found that adventitious metallic copper reaction with air forms new active Cu_2O sites. Further reaction with ambient air formed a protective layer of copper oxide and carbonate on the surface. These surface moieties enhanced adsorbent stability under atmospheric air for up to 10 days while retaining the adsorption capacity once activated. The oxygen-resistant layer can be easily removed by heating under a vacuum. This study provides a path for the design and synthesis of Cu(I)-based adsorbents with high CO adsorption capacity and stability.

KEYWORDS: Heterogeneous surface, Site energy distribution (SED), Adsorption mechanism, Ideal adsorbed solution theory, Stability

3.1 Introduction

Carbon monoxide is the raw material for production of varieties of chemicals such as acetic acid, formic acid, methanol, liquid hydrocarbon fuels, fibers, and plastics [9]. Moreover, it has brought about environmental issues such as climate change, ozone depletion, and acid rain [210]. The main methods of CO production are steam reforming of natural gas, partial oxidation, and coal gasification. CO is also present in gas mixtures containing CO, CO_2, H_2, N_2, and CH_4 in metallurgical plants [5, 9, 210]. Therefore, selective capture and recovery of CO from gas mixtures is highly important due to its environmental effects and industrial benefits.

There are many CO separation methods such as cryogenic distillation, absorption, and adsorption. Cryogenic separation is an energy-intensive process, and not suitable for mixtures containing N_2 since the boiling points of CO and N_2 are very close [211]. The disadvantages of absorption include solvent degradation and corrosion of equipment [14, 211]. Adsorption has received a lot of attention due to its low energy cost and efficient operation; however, the synthesis of materials with high selectivity towards adsorption of a specific gas in a mixture is challenging. The surface of porous materials is usually modified for selective adsorption. Amine functionalization of mesoporous silica (SBA-15) using poly(glycidyl amine) and poly(ethylenimine) has been reported for selective adsorption of CO_2 from ambient air and flue gas [212, 213]. Surface modification of metal organic framework (MOFs) with Pt group metals has been reported for H_2 adsorption [214]. Likewise, selective adsorption of CO, especially in CO_2-containing mixtures, requires modification of porous materials with transition metals such as Ag(I), Cu(I), Pt(II), and Pd(II). Due to the high polarizability of CO_2 in comparison to CO, the CO_2 adsorption capacity of normal adsorbent materials is higher. Modification with the mentioned transition metal ions highly increases the CO adsorption capacity by formation of π-complexes [9, 125, 174, 210]. However,

among them, Cu(I) is often used for selective adsorption of CO as it is cheap and readily available [9, 174, 190].

Adsorbents are typically modified by dispersion of copper salts into the pores of various supports such as activated carbon, mesoporous silica, alumina, zeolites, and MOFs [6, 7, 9, 10, 145, 179, 188, 190, 210, 215]. Basically, copper precursors are dissolved in an aqueous or acidic solution depending on the oxidation state of copper or used in a solid state (copper salt) and dispersed on adsorbent supports. Yoon et al. incorporated Cu(I) in a porous organic polymer (SNW-1) using a solution of CuCl and investigated the CO adsorption capacity and selectivity. They reported the increase of adsorption capacity with the loading of Cu(I) on SNW-1 and a CO/CO_2 selectivity of 23 for the adsorbent [174]. Ma et al. investigated the adsorption capacity of Cu(I) modified activated carbon (CuCl/Cu) prepared by impregnation of copper salt precursors and reported the highest CO adsorption capacity for AC modified using the precursor solution containing two copper salts. They have further reported a CO/CO_2 selectivity of 19 for the sample with the highest adsorption capacity [7]. Gao et al. modified zeolite Y support by CuCl for CO adsorption using solid dispersion of $CuCl_2$ followed by reduction under CO. They investigated the optimal loading of CuCl to achieve the highest CO adsorption capacity. Moreover, they reported a CO/CO_2 selectivity of 2.83 for CuCl/Y [190]. Zhu et al. modified carbon xerogels through doping of cuprous chloride for CO adsorption [147]. The modification was performed using an acidic solution containing CuCl that has been reported to adversely affect the crushing strength of the adsorbents [7, 9]. Previously, we reported numerous other reports of modification of supports with Cu(I) ion exist in which the focus is on addressing the challenges of conventional chemical modification methods such as distribution of active species and complete reduction of Cu(II) to Cu(I) [210]. To our knowledge, modification of supports with single active material is dominantly

investigated in the literature; however, modification of supports by multiple active sites for adsorption purposes has scarcely been done. Xiang et al. reported an elevated phosphate adsorption capacity for bimetallic La/Zr hydroxide adsorbent [216]. They showed that incorporation of both La and Zr cations can, due to the electronegativity difference of La and Zr, induce an internal electron transfer which leads to strengthened the $[MO_6]$-PO_4 bonding [216]. Mostly, modification with two active sites is observed for synthesis catalysts for higher catalytic activity [217-221].

One of the challenges regarding the use of Cu(I) modified adsorbents is their fast oxidation in air. Therefore, synthesis of adsorbents with resistivity towards oxidation remains a challenge [11, 23, 69, 222]. Moreover, oxidation and hydrolysis have also been a challenge regarding the use of MOFs such as MOF-74 for adsorption purposes. Substitution of strongly reducing metal ions (e.g., Mg^{+}) with metal ions of higher resistance to oxidation and hydrolysis (e.g., Ni and Co) is proposed to enhance the stability of MOF-74 [1]. Yin et al. incorporated Cu(I) into MIL-101 using solid state dispersion of copper nitrate which was selectively reduced by vanadium to form the Cu(I) ions on the surface of MIL-101. It was shown that vanadium has increased the oxidation resistivity of the adsorbent by acting as a sacrificial metal [12].

The selection for impregnant to achieve the highest adsorption is based on frontier orbital theory which states that adsorptive interaction is attributed to the mixing of the highest occupied molecular orbital (HOMO) and the lowest unoccupied molecular orbital (LUMO) [223, 224]. It has been reported that the ligand (anion) of metals has an influence of adsorption of carbon monoxide, for instance, the adsorption capacity for CuCl, CuBr, and CuI is with the following order of CuCl>CuBr>CuI. The higher the HOMO energy of anions than that of CO, the more metal ion perturbs with the anion rather than CO, which results into lower adsorption of CO. Therefore, different anions affect the adsorption capacity of carbon monoxide. Cu(I) with the anion of oxygen

is one of the materials that has been used for the purposes of CO oxidation and adsorption [225, 226]. The interaction between Cu_2O and CO is chemisorption which leads to high CO adsorption capacity. Unlike the adsorption of CO on CuCl, CO adsorption on Cu_2O has the disadvantage of recyclability, meaning that desorption of CO from Cu_2O is a hard process.

Herein, we modified the surface of an adsorbent with Cu_2O and CuCl using a facile two-step method and investigated the effect of introducing energetic heterogeneity to the surface of adsorbent on adsorption of CO. The dual-active site adsorbent shows an elevated CO adsorption capacity and very high efficiency for the separation of CO from CO-CO_2 mixture in terms of adsorption capacity and selectivity. To deeply probe the interaction of CO with dual-active site adsorbent (mechanism of adsorption), site energy distribution (SED) analysis through the adsorption isotherms coupled with the kinetics of adsorption obtained by adsorption under dynamic conditions were conducted. The findings of this investigation provide information for the understanding of CO adsorption on heterogeneous surfaces. Moreover, the dual Cu(I) active site adsorbent shows a high oxygen resistivity for 10 days of storage in atmospheric air. The proposed strategy in our work provides a path for the design and synthesis of new adsorbents and catalysts with high reactivity and oxygen resistivity.

3.2 Site energy distribution (SED) analysis of adsorbent

Equilibrium adsorption isotherms are related to the site energy distribution (SED) of the adsorbent. For a heterogeneous surface, the total amount of adsorption (q_e) can be obtained according to the following integral equation [80, 227]

$$q_e(p) = \int_{E_{min}}^{E_{max}} q_h(p, E)\, F(E) dE \qquad 3\text{-}1$$

where the total amount of adsorption on a heterogeneous surface (q_e; $cm^3\ g^{-1}$) is the integral of adsorption on a homogeneous surface that is represented by an energetically homogenous isotherm

(q_h) with adsorption energy E multiplied by the site energy frequency distribution (F(E); cm^3 mol g^{-1} kJ^{-1}) over a range of sites with homogeneous energies. The limits of the integral are assigned based on the minimum and maximum adsorption energies which are not known in a priori [80, 228]. Therefore, it is assumed that the limits of the adsorption energy range from zero to infinity. Since the adsorption of CO on the solid surface can be described by heterogeneous isotherms such as Generalized Freundlich, and Langmuir-Freundlich isotherms, using **Eq. 3-1** it is possible to calculate the exact site energy distribution. Here, the site energy distribution is determined using the Cerofolini approximation which involves generating approximate energy distribution function from isotherm equations. Under the assumption of Cerofolini approximation, the equilibrium fluid phase concentration is related to the energy of adsorption according to the following [80, 97, 228-230].

$$p = p_s \exp\left(-\frac{E^*}{RT}\right) = p_s \exp\left(-\frac{E-E_s}{RT}\right) \quad 3\text{-}2$$

where p_s (kPa) is the saturation pressure of the adsorbate molecule, E (kJ mol^{-1}) is the lowest physically realizable energy, and E_s (kJ mol^{-1}) is the adsorption energy corresponding to p_s of the gas, E* (kJ mol^{-1}) is the net energy, R is the universal gas constant (kJ mol^{-1} K^{-1}), and T (K) is the absolute temperature. Since the saturation pressure, p_s, cannot be physically explained at supercritical conditions with any available theories, the following empirical expression, proposed by Ozawa et al. [231], was used to calculate the saturation pressure [97, 232].

$$p_s = p_c \left(\frac{T}{T_C}\right)^2 \quad 3\text{-}3$$

where p_c (34.529 atm) and T_c (132.91 K) are critical pressure and temperature of CO, respectively [233]. Approximate SED function can be calculated by incorporating **Eq. 3-2** into Generalized Freundlich (GF) and Langmuir-Freundlich (LF) models, followed by differentiating the isotherm

with respect to E*. The Generalized Freundlich and Langmuir-Freundlich isotherms and their respective SED function are shown in **Table 3-1**.

Table 3-1 Adsorption isotherm models and their respective SED functions.

Model	Equation	SED function
Generalized Freundlich (GF) [234]	$\mathbf{q_e = q_m \left(\frac{k_F p}{1 + k_F p}\right)^{n_F}}$	$\mathbf{F(E^*) = \frac{q_m n_F (k_F p_s)^{n_F}}{RT} \exp\left(-\frac{n_F E^*}{RT}\right)\left[1 + k_F p_s \exp\left(-\frac{E^*}{RT}\right)\right]^{-(n_F+1)}}$
Langmuir-Freundlich (LF) [234]	$\mathbf{q_e = q_m \frac{k_s p^n}{1 + k_s p^n}}$	$\mathbf{F(E^*) = \frac{q_m n_S k_s p_s^{n_S}}{RT} \exp\left(-\frac{n_S E^*}{RT}\right)\left[1 + k_s p_s^{n_S} \exp\left(-\frac{n_S E^*}{RT}\right)\right]^{-2}}$

Here, q_m ($cm^3\ g^{-1}$) is the maximum adsorption capacity, n_F and n_s are heterogeneity parameters, k_F and k_S (kPa^{-1}) are constants determined by the maximum site frequency energy [234].

3.3 Experimental

3.3.1 Materials

Copper oxide nanoparticles (CuO, 99%, grain size 30 ± 2 nm) were purchased from US research nanomaterials incorporation. Copper(II) chloride dihydrate ($CuCl_2$•$2H_2O$, ACS, 99+%) was obtained from Alfa Aesar. Ethanol was used as a liquid-phase reaction medium (KOPTEC, 200 proof).

3.3.2 Preparation of adsorbents

Dual Cu(I) active site adsorbent was prepared in a two-step process. The first process is the synthesis of Cu_2O by following the reported procedure [235]. CuO nanoparticles were reduced to Cu_2O at 673 K with a heating rate of 50 °C/min under a 5% H_2 in an H_2-He gas mixture with a flow rate of 50 cm^3/min for 30 minutes. This high heating rate was to prevent the complete

reduction of CuO to Cu. After that, the powder was cooled down to room temperature under the same flow conditions to form metallic copper. The resulting powder is labeled as R-CuO (Reduced CuO). The further modification includes the liquid-phase reaction of R-CuO to form CuCl following the reported process [206, 236]. In detail, one gram of R-CuO is dispersed in 10 ml of 0.1 M ethanol-based $CuCl_2$ solution for 90 seconds. The resulting powder is then collected using a vacuum filter and dried at 333 K in the air to form CuCl. The resulting powder is labeled as CR-CuO (Chemically modified R-CuO). The as-synthesized CR-CuO was then either sealed and transferred into a desiccator or stored in ambient air for later adsorption study.

In addition, CuCl modified copper adsorbents (C-Cu) were synthesized. To minimize Cu_2O content in the final product, complete reduction of CuO to Cu was achieved under pure hydrogen flow at 673 K for 2 hours. The same liquid-phase reaction as in CR-CuO preparation was carried out.

3.3.3 Adsorbent characterizations

Nitrogen adsorption/desorption isotherms were measured at 77 K using a Quantachrome NOVA 2200e surface and pore analyzer. The surface area was measured according to the Brunauer-Emmett-Teller (BET) equation in the relative pressure range of $0.05 < p/p_0 < 0.3$. The total pore volume was calculated by N_2 adsorbed amount at a relative pressure of 0.99. The thermal activation/degassing temperature of samples is indicated by "–X" at the end of sample labels (i.e., R-CuO-X, C-Cu-X, and CR-CuO-X). Any sample label without temperature at the end stands for specific cases where thermal activation was not carried out. X-ray diffraction (XRD) patterns of the materials were obtained using a Proto manufacturing AXRD powder diffraction system with Cu K_α radiation (λ=1.5418 Å). The samples were scanned at a rate of 2.2°/min at 30 mA and 40 kV. Rietveld analysis was performed on the XRD data by MAUD software to identify the loading

of materials in the samples [4, 237, 238]. The phase quantification was performed for 3 separate samples, and the average weight percentage was reported in figures and tables with standard deviations.

3.3.4 Equilibrium adsorption measurement

Single component adsorption equilibrium isotherms of carbon monoxide and carbon dioxide were measured at 298 K using Quantachrome NOVA 2200e surface and pore analyzer. Before adsorption measurement, samples were activated/degassed for 2 hours under a continuous vacuum at temperature X specified at the end of each label (i.e., CR-CuO-X). The adsorption equilibrium isotherms were obtained at pressures up to 100 kPa. The equilibrium was usually achieved about 10 minutes; however, to guarantee the adsorption equilibrium was achieved, 30 minutes of adsorption time was used for each adsorption point. The single component adsorption isotherms were fitted into multiple adsorption models such as Langmuir, Generalized Freundlich, and Langmuir-Freundlich model to understand the adsorbate-adsorbent interaction [80, 234].

3.3.5 Adsorption selectivity calculation

The ideal adsorbed solution theory (IAST) proposed by Myers and Prausnitz [35, 239] has been widely used to investigate the adsorption selectivity based on the pure component adsorption isotherms. IAST has been successfully used to calculate the selectivity of various adsorbents such as activated carbon, zeolites, MOFs, and other adsorbents [11, 83, 92, 240-243]. To apply the IAST, single component adsorption isotherms should be fitted precisely to an adsorption model [70]. In this work, the fitting parameters of the Generalized Freundlich model were combined with IAST to calculate the selectivity of CR-CuO-453 for CO/CO_2 adsorption. For a binary mixture, the CO adsorption selectivity S is calculated by the following equation [70].

$$S = (x_{CO}/x_{CO_2})/(y_{CO}/y_{CO_2}) \quad 3\text{-}4$$

where x_{CO} and x_{CO2} are the mole fractions of CO and CO_2 in the adsorbed phase, and y_{CO} and y_{CO2} are the molar fraction of gas CO and CO_2 in the gas phases, respectively.

3.3.6 Dynamic adsorption measurement

The dynamic breakthrough test was performed under pure CO and 25 vol% CO in a custom-built packed bed column system at room temperature. The flow rates of the gases were regulated using four MKS 0-100 mL/min mass flow controllers. Three of them were used to control the streams of CO, CO_2, and He. These flows were well mixed before entering the adsorption column. The last one was used for pure He stream to regenerate the adsorbent loaded in the column. The adsorption column was placed in a furnace for degassing and keeping the adsorption temperature constant. The gas composition at the outlet was measured using a Cirrus 2 MKS mass spectrometer. Before loading to the column, the samples were activated under vacuum at 453 K. The activated powder was then loaded into a stainless-steel column (45 cm length, 0.88 cm inner diameter) to house a packed bed of 10 cm length. The dead volume was filled with glass beads. Due to the agglomeration during adsorbent particle processing, the adsorbent particle size reached 40 μm on average. This led to almost no pressure drop in the column such that we did not need adsorbent pelletization. Prior to collecting breakthrough curves, the column was degassed at 453 K under 50 mL/min flow of pure He for 1 hour to remove all the adsorbed impurities during the loading process. The dynamic adsorption was performed at 298 K and 100 kPa. At t = 0, the pure He flow was switched to the He flow containing a CO/CO_2 mixture with a total flow of 50 ml/min ($He:CO:CO_2$ = 25:12.5:12.5).

3.3.7 Adsorption kinetics measurement

The kinetics of the adsorption was investigated for pure CO and CO_2. To investigate the kinetics of CO and CO_2 adsorption onto CR-CuO-453 at 298 K and 100 kPa, the collected data were fitted to pseudo-first-order, pseudo-second-order, and Avrami models.

Lagergen's Pseudo-first-order (PFO) kinetic model assumes physisorption of gas molecules on the surface. This model describes the adsorption rate based on the available sites and adsorption capacity. It is represented by equation [210]

$$q_t = q_e(1 - e^{-k_1 t}) \quad 3\text{-}5$$

where q_t and q_e ($cm^3\ g^{-1}$) are the adsorption capacity at time t (sec) and equilibrium, respectively. k_1 (sec^{-1}) is the PFO adsorption rate constant.

Pseudo-second-order (PSO) kinetic model assumes the chemisorption of adsorptive on the adsorbent surface while the rate of adsorption is related to the number of available active sites [210]. It is represented by equation

$$q_t = \frac{q_e}{\frac{1}{k_2 q_e} + t} \quad 3\text{-}6$$

where k_2 ($g\ cm^3\ sec^{-1}$) is the PSO adsorption rate constant.

Avrami's fractional-order kinetic model was developed to simulate the phase transition and crystal growth of materials. It has also been used to describe CO_2 adsorption on amine-functionalized sorbents. This model accounts for both physical and chemical interactions [244-246]. The model is represented by **Eq. 3-7**.

$$q_t = q_e(1 - e^{-(k_A t)^{n_A}}) \quad 3\text{-}7$$

where k_A (sec^{-1}) is the Avrami's kinetic constant and n_A is the Avrami exponent. Avrami exponent represents the growth dimensionality of the adsorbate on adsorption sites [246]. The value of n_A=1 shows homogenous adsorption, stating an equal probability of adsorption for available zones at a

fixed time interval [247]. One-, two-, and three-dimensional growths of adsorbed species at the adsorption sites are represented by n_A values of 2, 3, and 4, respectively. Furthermore, n_A exhibits the changes of mechanisms that may occur during the adsorption process [246, 248]. The fractional order states the complexity of the reaction mechanism or presence of more than one reaction pathways [209].

3.4 Results and discussion

3.4.1 Characterization of materials

Figure 3-1a shows the XRD pattern of adsorbents at different stages of synthesis. The peaks at 36.5° and 43.5° show the presence of Cu_2O and Cu after reduction of CuO at 673 K, respectively. The CuCl characteristic peaks at 28.6° and 47.5° show the successful chemical modification of the reduced CuO sample. **Figure 3-1b** shows the nitrogen adsorption-desorption isotherm of the samples. The isotherms of commercial CuO-453, R-CuO-453, and chemically modified R-CuO (CR-CuO-373 and CR-CuO-453) exhibit the typical type II isotherm that is obtained on non-porous materials, where mono- and then multi-layers are formed on the surface [249].

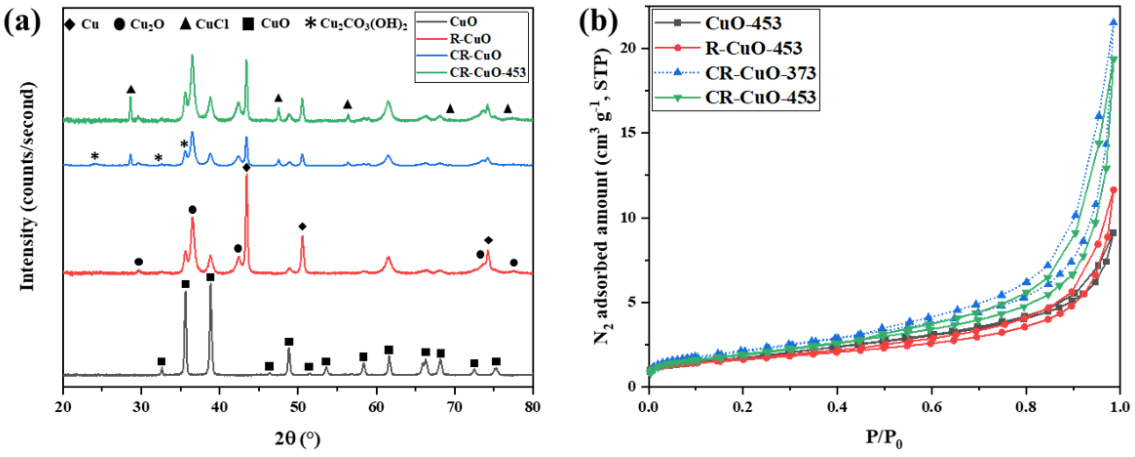

Figure 3-1 (a) XRD pattern of the commercial CuO, R-CuO, CR-CuO, and activated CR-CuO at 453 K (CR-CuO-453). (b) N_2 adsorption isotherms for samples.

Table 3-2 shows the microstructure and composition change of the samples at different stages of synthesis. The thermal reduction and liquid-phase reaction led to a minor decrease and increase of the surface area of the sorbent, respectively. This slight loss of the surface area is due to particle coalescence and densification by the formation of the copper phase in the reduction step. The formation of new oxide and chloride sites resulted in a small increase in the surface area after the modification step. These changes can be confirmed by changing copper phase content obtained by XRD analysis. It should be mentioned that the measured pore volumes of samples at any step of synthesis were ≤ 0.03 cm^3 g^{-1}; therefore, we consider the samples non-porous. This low porosity makes the CO adsorption analysis more straightforward.

Table 3-2 Physicochemical properties of samples at different stages of synthesis.

Sample	S_{BET} (m^2 g^{-1})	V_P (cm^3 g^{-1})	Phase content (wt%)			
			CuCl	Cu_2O	CuO	Cu
CuO#	6.3 (± 0.3)	0.0149 (± $7.57x10^{-4}$)	0	0	100	0
R-CuO	5.5 (± 0.3)	0.0179 (± $5.22x10^{-4}$)	0	41.6 (± 1.5)	26.1 (± 1.9)	32.3 (± 1.5)
CR-CuO	7.9 (± 0.4)	0.0211 (± $1.923x10^{-3}$)	4.9 (± 0.94)	46.3 (± 1.0)	30.9 (± 2.3)	15.6 (± 1.7)
CR-CuO-453	7.1 (± 0.4)	0.0304 (± $2.731x10^{-3}$)	11.3 (± 0.42)	45.0 (± 1.1)	33.6 (± 2.4)	10.1 (± 1.4)

A commercial product without any modification.

The effect of storage time on CR-CuO before and after activation is shown in **Figure 3-2**. The increase of storage time changes the composition of CR-CuO by increasing the CuO content and decreasing Cu and CuCl content. Comparing the samples after 72 hours of storage before and after activation at 453 K (**Figure 3-2a** and **Figure 3-2b**), we can see that CuCl has always been present

and both CuCl and Cu_2O have been protected from oxidation and hydrolysis. The elemental mapping of the adsorbent after 72 hours of storage shows the presence of chlorine before and after activation (**Figure 3-2c** and **Figure 3-2d**). This confirms that the active sites were protected from oxidation.

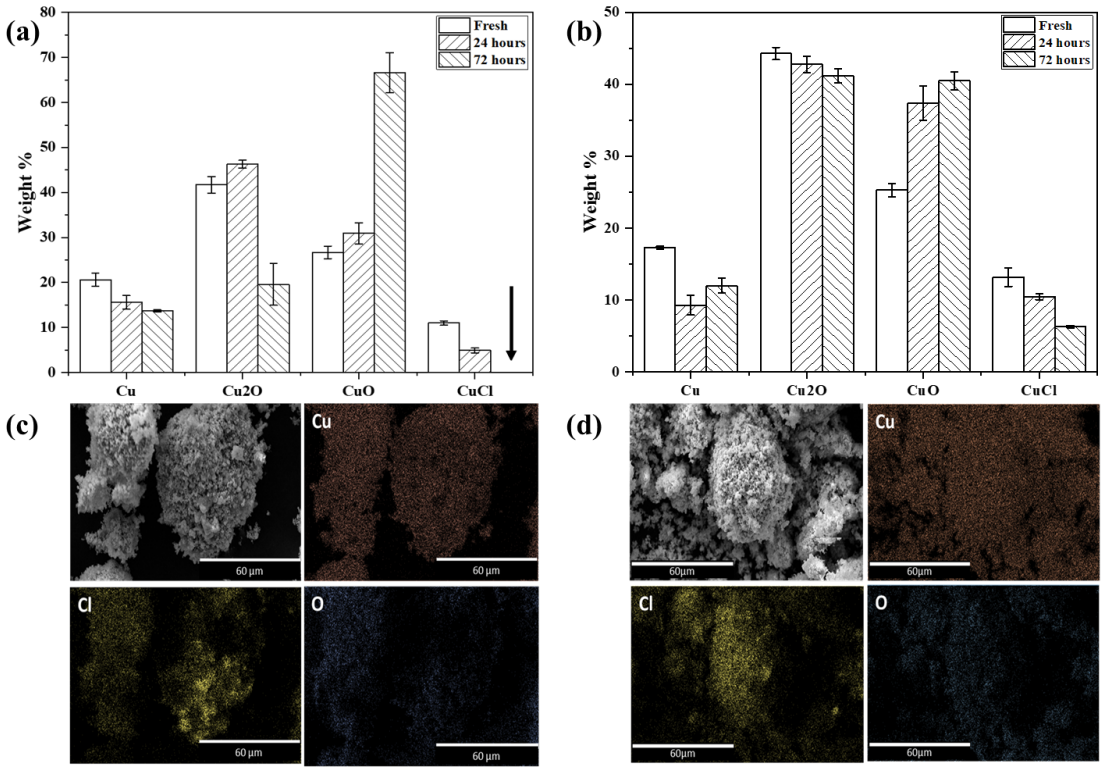

Figure 3-2 The effect of storage on the composition of CR-CuO (a) before activation, (b) after activation at 453 K, and EDS elemental mapping of CR-CuO (c) before activation, and (d) after activation at 453 K. Error bars represent the standard deviation.

The formation of a protective layer is characterized by collecting XRD patterns from samples stored for varied time lengths at room conditions. A new peak at 24° was detected (**Figure 3-3**). This peak is attributed to $Cu_2CO_3(OH)_2$. According to **Figure 3-2ab** and **Figure 3-3**, the following can be the mechanism for the changes in the adsorbent with storage in room condition.

$$2Cu\ (s) + O_2(g) \rightarrow Cu_2O\ (s) \qquad 3\text{-}8$$

$$2Cu_2O\ (s) + O_2\ (g) \rightarrow 4CuO\ (s) \qquad 3\text{-}9$$

$$2CuO\ (s) + CO_2\ (g)\ +\ H_2O\ (g) \rightarrow Cu_2(OH)_2CO_3\ (s) \qquad 3\text{-}10$$

The formed metallic copper phase after reduction interacts with oxygen at room temperature to form surface Cu_2O (**Eq. 3-8**) [250]. The Cu_2O on the surface further reacts with oxygen to form CuO (**Eq. 3-9**). Moreover, it has been reported that at room or low temperatures, copper naturally forms a protective CuO layer on top of Cu_2O [250-253]. The topmost CuO then reacts with carbon dioxide and moisture in ambient conditions and for the protective carbonate phase (**Eq. 3-10**) [254, 255].

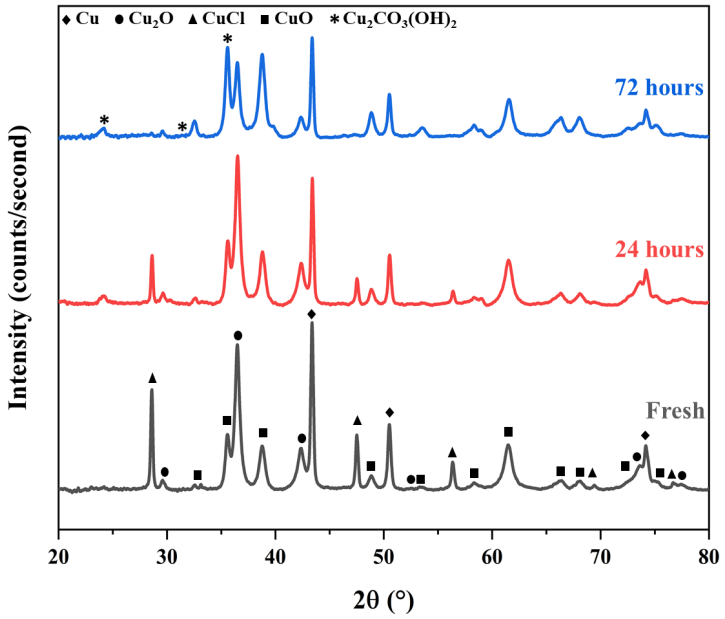

Figure 3-3 CR-CuO XRD pattern change over storage time.

The effect of activation temperature on the composition of the prepared samples (CR-CuO) and their respective adsorption capacities are presented in **Figure 3-6**. Activation of the adsorbents was done under continuous vacuum at 373, 453, and 486 K. Activation at 373 K show a moderate impact on the change of composition. In other words, the protective layer covering the active sites will not be completely removed, leading to a low adsorption capacity. The activation at 486 K

resulted in detachment of CuCl formed on the surface leading to the lower adsorption capacity of the adsorbent (**Figure 3-4**). This can be due to the expansion of supporting copper at high temperatures. However, activation at 453 K removes the protective layer exposing the active sites for adsorption of CO molecules.

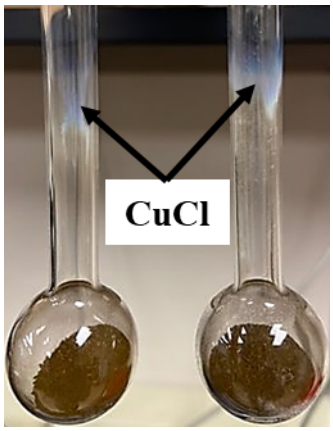

Figure 3-4 Detachment of CuCl from the surface of adsorbent after activation at 486 K.

Figure 3-5 shows the XRD pattern of CR-CuO before and after activation at 453 K. The absence of carbonate peak along with the decrease in the content of CuO after activation at 453 K states the mechanism of activation. Heating under vacuum at 453 K decomposes the carbonate and CuO protective layer to form CuO, Cu_2O, CO_2, and O_2 in which the gases are desorbed into vacuum. The reduction of CuO to Cu_2O under vacuum condition at temperatures ≥ 380 K has been reported in the literature [256]. The highest adsorption capacity of the adsorbent was achieved by activation at 453 K (**Figure 3-6b**). It was shown that CR-CuO-453 after 10 days of exposure to room conditions retained its adsorption capacity (**Figure 3-7**).

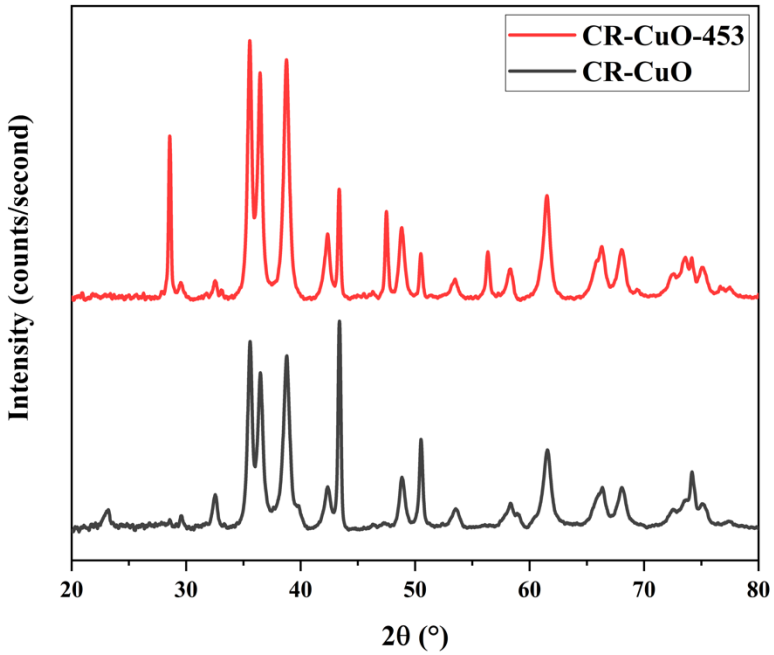

Figure 3-5 XRD patterns of CR-CuO before and after activation at 453 K

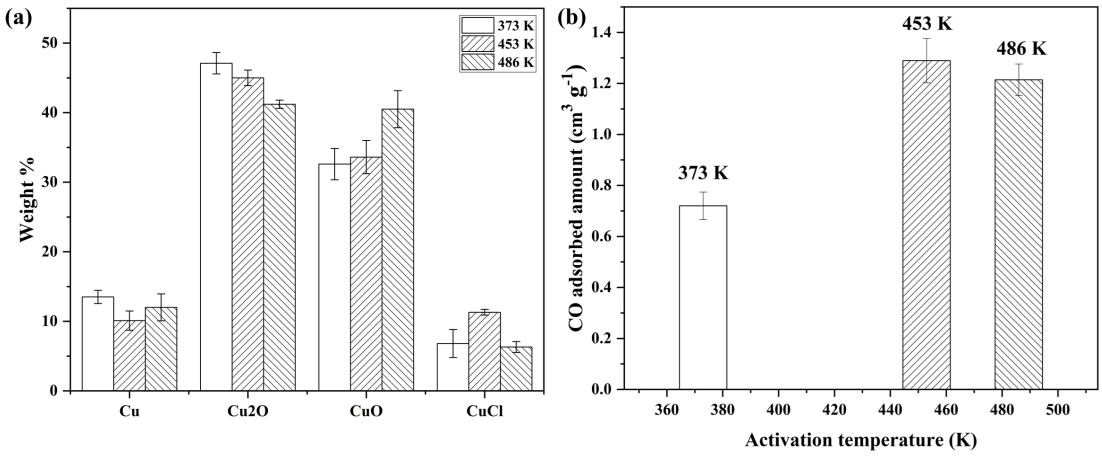

Figure 3-6 Effect of activation temperature on CR-CuO. (a) Composition, and (b) adsorption capacity at 100 kPa and 298 K. Error bars represent the standard deviation.

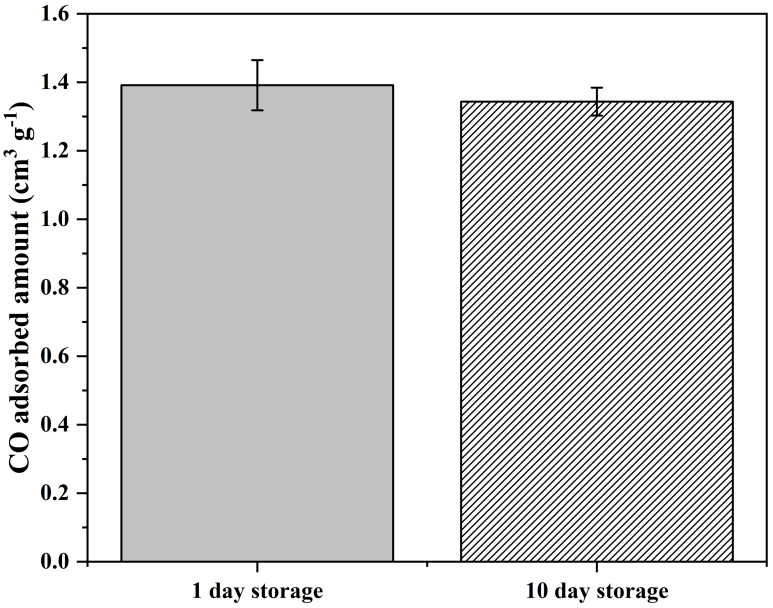

Figure 3-7 Adsorption capacity of CR-CuO-453 at room temperature after long-term storage.

To investigate the contribution of present components in CO adsorption capacity of the dual-active site adsorbent (CR-CuO-453), the adsorption capacity of different present components was measured separately. The XRD pattern and Rietveld analysis of synthesized metallic copper and chemically modified copper (C-Cu) are presented in **Figure 3-8** and **Table 3-3**, respectively. **Figure 3-9** shows the CO adsorption isotherm of prepared sorbents at room temperature (298 K). Pure copper and copper oxide show insignificant CO adsorption capacity because of the absence of Cu(I) sites that can form the π-complexation bonding with CO molecules. The R-CuO-453 and C-Cu-453 samples show a higher amount of CO adsorption capacity (i.e., 0.34 and 0.66 $cm^3\ g^{-1}$, respectively) due to the presence of active sites. The adsorption capacity of CR-CuO-453 is larger than the combined CO adsorption capacities of R-CuO-453 and C-Cu-453 demonstrating the effectiveness of the two-step modification.

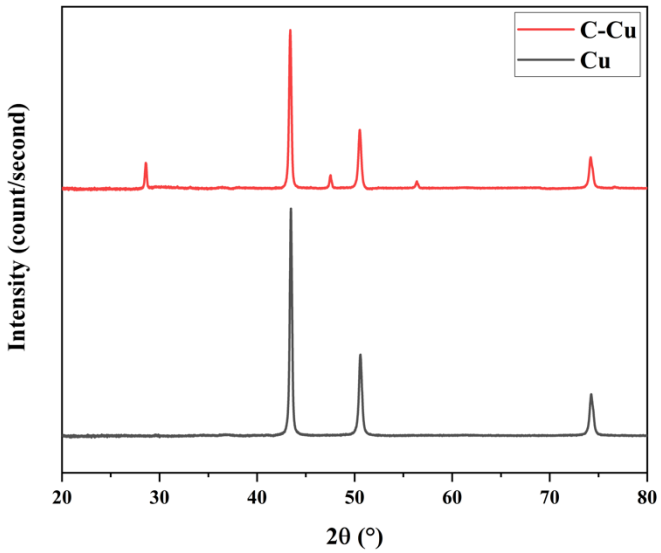

Figure 3-8 XRD patterns of synthesized copper and chemically modified copper.

Table 3-3 Adsorbent analysis using X-ray diffraction data.

Sample	Phase content (wt%)			
	CuCl	Cu_2O	CuO	Cu
Cu-453	0	0.67	0	99.33
C-Cu-453	14.03	2.55	0	83.42

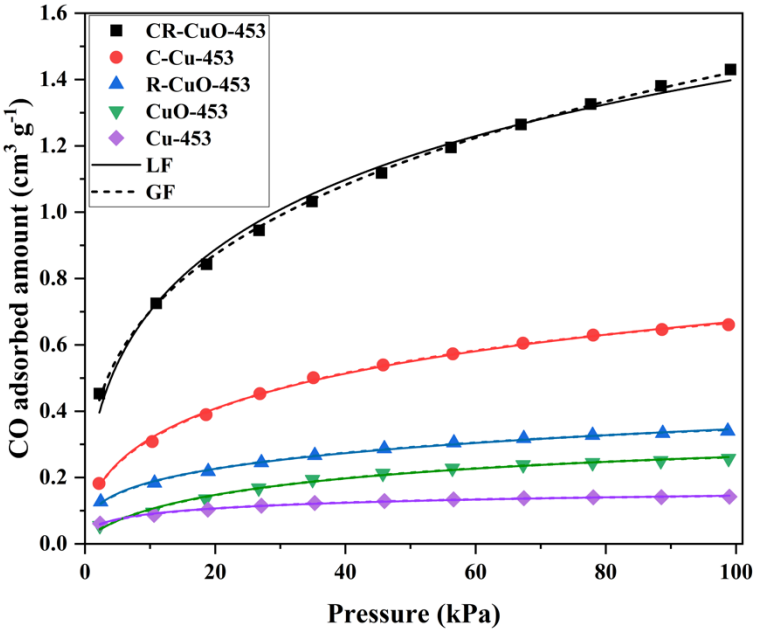

Figure 3-9 CO adsorption isotherms of activated adsorbents. The points are the experimental data. The dashed and solid lines show the fitting to Generalized Freundlich and Langmuir-Freundlich models, respectively.

To further understand the elevated CO adsorption capacity of the CR-CuO-453, the experimental equilibrium adsorption isotherms were fitted to GF and LF models and the SEDs of the adsorbents were investigated according to the SED function of the respective model presented in **Table 3-1**. The calculated isotherm fitting parameters of GF and LF models and the values of R^2 are presented in **Table 3-4**. The high values of R^2 (**Table 3-4**) and the fitting curves (**Figure 3-9**) show that both GF and LF models may explain the equilibrium adsorption of CO on the prepared adsorbents at room temperature. Therefore, the calculated isotherm constants from both models were used to develop the SED spectra. Substituting the determined isotherm parameters for all adsorbents (**Table 3-4**) in SED function (**Table 3-1**) the binding energies were calculated. It should be mentioned that there is no mathematical restriction for SED functions. The negative value for site energy is an artifact that does not have physical meaning [80]. Therefore, the calculated SED

curves from the equations in **Table 3-1**, are only valid in the range of pressures presented in the CO adsorption isotherm (shaded area in **Figure 3-10**). The site energy (E*) as a function of CO equilibrium adsorption capacity of adsorbents is presented in **Figure 3-11**. The site energy decreases sharply with the adsorption of CO. This proved the presence of a limited number of high-energy adsorption sites and that adsorption of CO molecules starts by the occupation of high-energy sites and then spreading to sites with lower energy [229].

It can be observed from **Figure 3-10a** that Cu-453 and CuO-453 show a site energy distribution of two regions: (i) a unimodal peak corresponding to the low-energy binding sites and (ii) an asymptotically decaying tail at the high energy side. The wide spreading of site energy for R-CuO-453, C-Cu-453, and CR-CuO-453 shows the induced heterogeneity of these processed sorbents. Calculated values of n_F and n_S also confirmed the heterogeneity of these three adsorbents. The n value sequence from both GF and LF models indicated that the reduction step sharply increased the energetic heterogeneity of the adsorbent while the following liquid-phase reaction reduced the heterogeneity to a lesser degree.

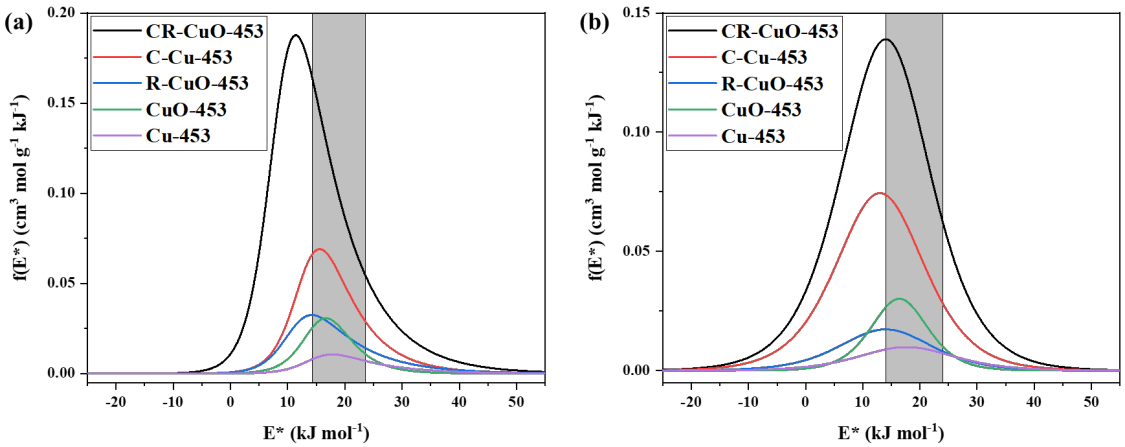

Figure 3-10 SED of adsorbents based on (a) Generalized Freundlich, and (b) Langmuir-Freundlich model.

The SED variation in **Figure 3-10** suggests differences in the active sites and surface microstructure among the adsorbent materials [80, 230]. GF and LF-based SED both indicated that C-Cu-453 and CR-CuO-453 have higher site frequency in all energy ranges compared to Cu-453 and R-CuO-453, respectively. The increased surface area after liquid-phase reaction of R-CuO (**Table 3-2**) was only 44% while the number of active sites increased with a greater degree.

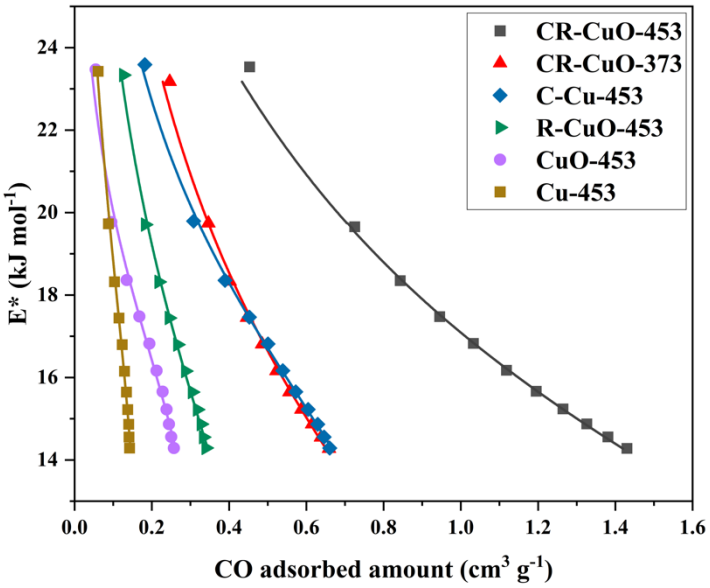

Figure 3-11 Dependence of site energy to CO adsorption capacity for different adsorbents.

Thermal reduction, compared to liquid-phase reaction, did not bring as much change in the number of active sites in the GF-based SED. The LF-based SED shows a decrease in the number of sites for R-CuO-453 compared to CuO-453. Since thermal reduction should increase the number of active adsorption sites, we excluded LF-based SED and considered GF-based SED for further investigation of CO interaction with the adsorbent. **Figure 3-10a** shows an emergence of low-energy sites after thermal reduction of CuO in addition to the expected high-energy sites of Cu_2O [12, 92, 229].

To further investigate the differences in the distribution of binding energies, CO adsorption isotherms were measured for CR-CuO-373 (not sufficiently activated) and CR-CuO-453 (fully activated). The corresponding SED based on GF was calculated. **Figure 3-12a** shows the higher CO adsorption capacity for CR-CuO-453 at room temperature. The higher adsorption capacity of CR-CuO-453 can be solely related to the difference in phase composition after activation since the surface area of both CR-CuO-373 and CR-CuO-453 are in the same range. **Figure 3-12b** shows the similar shapes of the SED for both. Thermal activation increased adsorption site numbers throughout the energy spectrum.

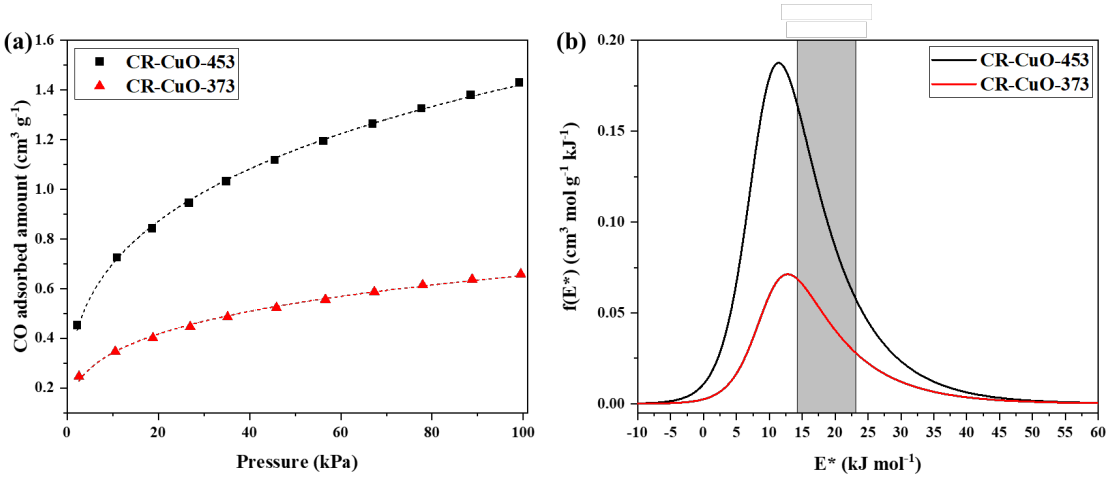

Figure 3-12 (a) Adsorption isotherms and (b) SED of CR-CuO-373 and CR-CuO-453 based on Generalized Freundlich model.

The average site energy (ASE) represents the adsorbent-adsorbate interaction strength [228]. The value of ASE (μ, kJ mol^{-1}) for the sorbents was determined based on GF-based SED according to the following equation [228].

$$\mu(E^*) = \frac{\int_0^{+\infty} E^* F(E^*) dE^*}{\int_0^{+\infty} F(E^*) dE^*} \qquad 3\text{-}11$$

The denominator represents the area under SED that is equal to maximum adsorption capacity. The ASE values of adsorbents are presented in **Table 3-4**. Metallic copper (completely reduced

CuO) shows the highest ASE value (21.79 kJ mol^{-1}) while having the lowest adsorption capacity. This is due to the fast formation of oxide (Cu_2O) on copper when exposed to air. This is confirmed according to the XRD diffraction pattern and Rietveld analysis of metallic copper (**Figure 3-8** and **Table 3-3**). The small amount of formed Cu_2O on the surface interacts with CO molecules; however, due to the very small amount of these sites, the adsorption capacity is very low. The ASE for chemically modified copper, C-Cu-453, is 18.16 kJ mol^{-1}, a significantly decreased value compared to 21.79 kJ mol^{-1} (Cu-453). The reduction of CuO to R-CuO led to an increase of the ASE to 18.32 kJ mol^{-1}. The following liquid-phase reaction of R-CuO again lowers ASE; however, both samples (C-Cu-453 and CR-CuO-453) show high adsorption capacities due to the increased total number of active sites. The decrease in the average surface energy of CR-CuO-453 can be attributed to the increase in the CuO content after liquid-phase reaction (**Table 3-2**).

Table 3-4 Langmuir-Freundlich and Generalized Freundlich isotherm parameters determined by non-linear regression.

Sample	Langmuir-Freundlich				Generalized Freundlich				
	q_m	k_s	n_s	R^2	q_m	k_F	n_F	R^2	$\mu(E^*)$
CuO-453	0.401	0.024	1.36	0.9930	0.351	0.0166	0.63	0.9942	17.68
Cu-453	0.224	0.04	2.29	0.9922	0.171	0.0134	0.31	0.9948	21.79
C-Cu-453	1.53	0.0059	2.11	0.9978	0.965	0.0067	0.41	0.9985	18.16
R-CuO-453	1.345	0.00042	2.20	0.9960	0.527	0.0033	0.30	0.9968	18.32
CR-CuO-373	2.035	0.0012	2.73	0.9933	1.1705	0.0016	0.30	0.996	17.04
CR-CuO-453	2.896	0.0087	2.14	0.9992	2.9632	0.0011	0.32	0.9994	15.32

3.4.2 Adsorption selectivity of CO/CO_2

Figure 3-13a shows the equilibrium adsorption of CO and CO_2 on CR-CuO-453 at room temperature. In comparison to CO pure adsorption equilibrium isotherm, CO_2 pure adsorption isotherm shows a low adsorption capacity for CR-CuO-453. This shows the potential efficacy of CR-CuO-453 for the separation of CO/CO_2. The adsorption equilibrium isotherms were well fitted by the GF model. The fitting isotherms are shown by dashed lines in **Figure 3-13a** and the fitting parameters of CO_2 adsorption isotherm are listed in **Table 3-5**. Ideal adsorbed solution theory (IAST) was used to further investigate the selectivity of CR-CuO-453 at various CO molar ratios.

Table 3-5 CO_2 GF isotherm parameters determined by non-linear regression.

Sample	Generalized Freundlich			
	q_m	k_F	n_F	R^2
CuO	1.10	0.0066	0.71	0.9999
R-CuO-453	1.65	0.0022	0.66	0.9996
C-Cu-453	1.99	0.0011	1	0.9999
CR-CuO-453	0.75	0.005	1	0.9993

Figure 3-13b shows that the CO/CO_2 selectivity gradually decreases with an increase in adsorption pressure. This shows that the adsorbent preferentially adsorbed CO over CO_2 which is ascribed to the strong interaction between CO and the Cu(I) sites. Moreover, the higher content of CO in the gas mixture CO selectivity decreases over the whole tested pressure range. The reason behind this behavior is the specific adsorption of CO to Cu(I) active sites. At low CO concentration in the 1:9 mixture, the number of available active sites to interact with CO is much higher than the present CO molecules at the adsorbent surface, leading to an increase in selectivity in comparison to mixtures with higher content of CO [257].

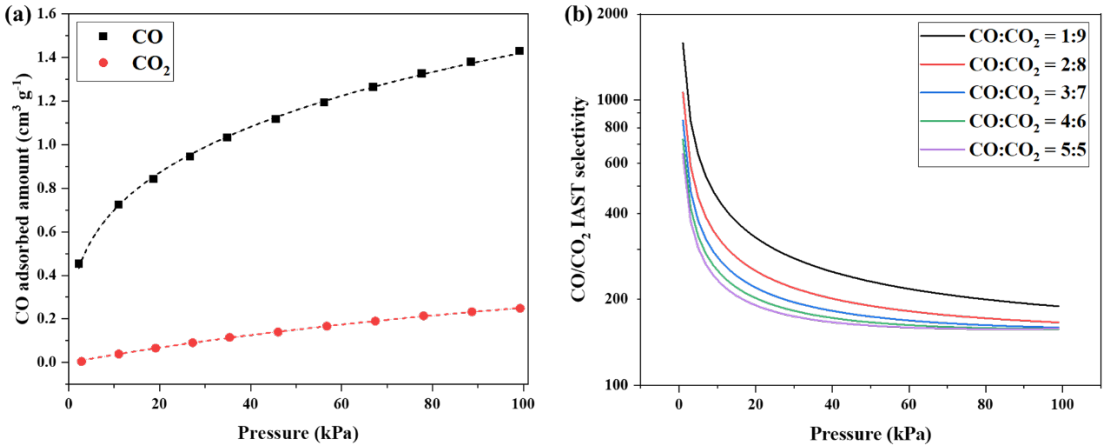

Figure 3-13 (a) CO and CO_2 pure adsorption isotherm for CR-CuO-453, and (b) IAST selectivity profile of CO/CO_2 on CR-CuO-453.

CO_2 adsorption isotherms at different stages of synthesis were measured at room temperature to investigate the contribution of various phases present on the sample to CO/CO_2 selectivity. **Figure 3-14** shows the pure CO_2 adsorption equilibrium isotherms of prepared samples at 298 K. The adsorption isotherm data were fitted to the GF model and the fitting parameters are presented in **Table 3-5**.

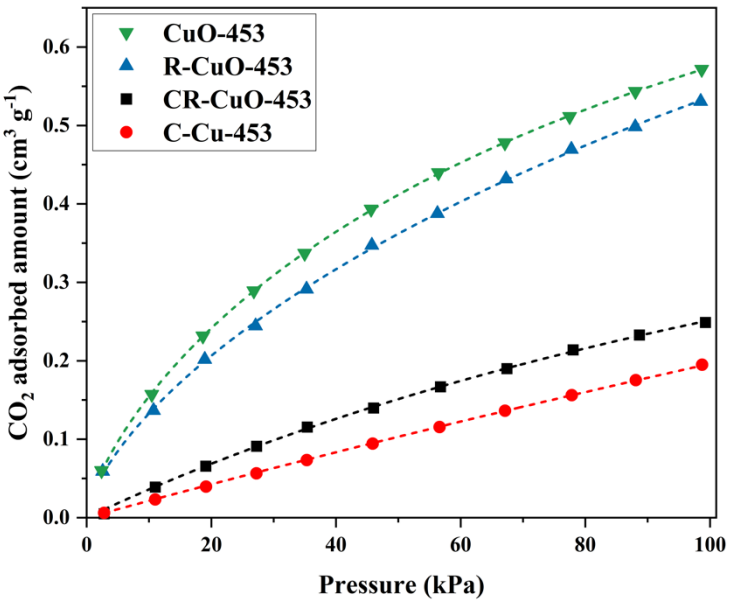

Figure 3-14 CO_2 single component adsorption isotherm of adsorbents at 298 K. The points are the measured data, and the dashed lines are fitting to the GF model.

Figure 3-15 shows the IAST calculated CO/CO_2 selectivity of adsorbents at different stages of synthesis in an equimolar mixture of CO/CO_2. The highest CO/CO_2 selectivity is related to the two Cu(I) active sites on CR-CuO-453. We see that CuO-453 is selective towards CO_2, and thermal reduction of CuO led to an increase in selectivity towards CO. Liquid-phase reaction of copper also enhanced CO/CO_2 selectivity for C-Cu-453; however, its selectivity is still lower than the CR-CuO-453.

The adsorption isotherms of CO and CO_2 as a function of the total bulk pressure were used to further understand the selectivity (**Figure 3-16**). In comparison to CO_2, CO is selectively adsorbed on CR-CuO-453, C-Cu-453, and R-CuO-453. However, CO_2 is preferentially adsorbed on CuO. This can be justified by the soft acidic nature of CO_2 molecules [258]. Accordingly, the presence of strong basic phases such as oxides (e.g., CuO and Cu_2O) can enhance the CO_2 adsorption capacity. This can also justify the comparable CO_2 and CO adsorption capacity at 100 kPa for R-

CuO-453. The high CO adsorption capacity at lower pressures for R-CuO-453 can be attributed to the strong interaction between Cu(I) and CO molecules forming the π-complexation on R-CuO-453.

We have compared CR-CuO-453 with Cu(I)-containing adsorbents in the literature considering the structural properties, adsorption capacity, and CO/CO_2 selectivity at 100 kPa. Remarkably, CR-CuO-453 shows superiority in CO/CO_2 selectivity over adsorbents reported in the literature, as presented in **Table 3-6**. The low adsorption capacity of CR-CuO-453 is due to the structural difference (i.e., low surface area and pore volume) in comparison to the reported Cu(I)-containing adsorbents in the literature.

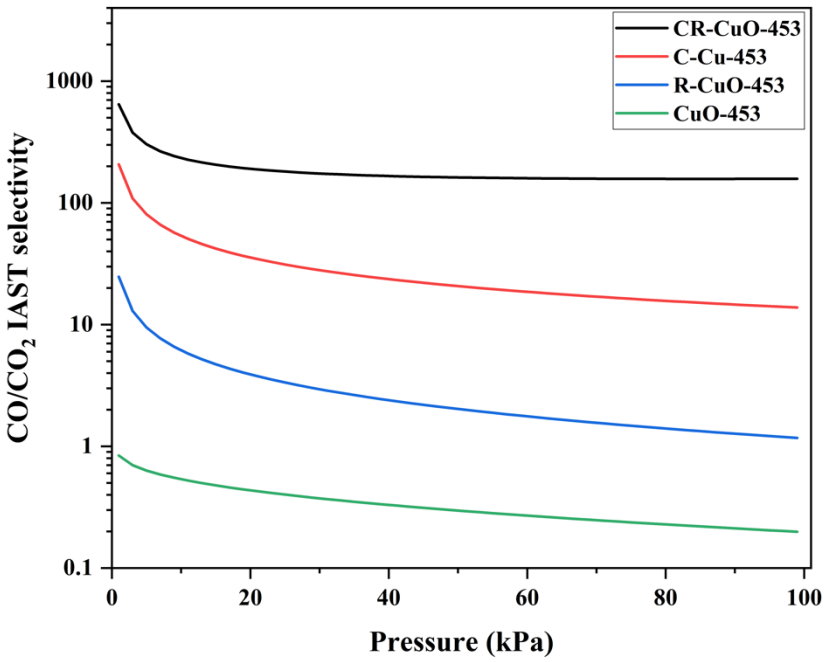

Figure 3-15 CO/CO_2 IAST selectivity of adsorbents at different stages of the synthesis in an equimolar mixture of CO/CO_2.

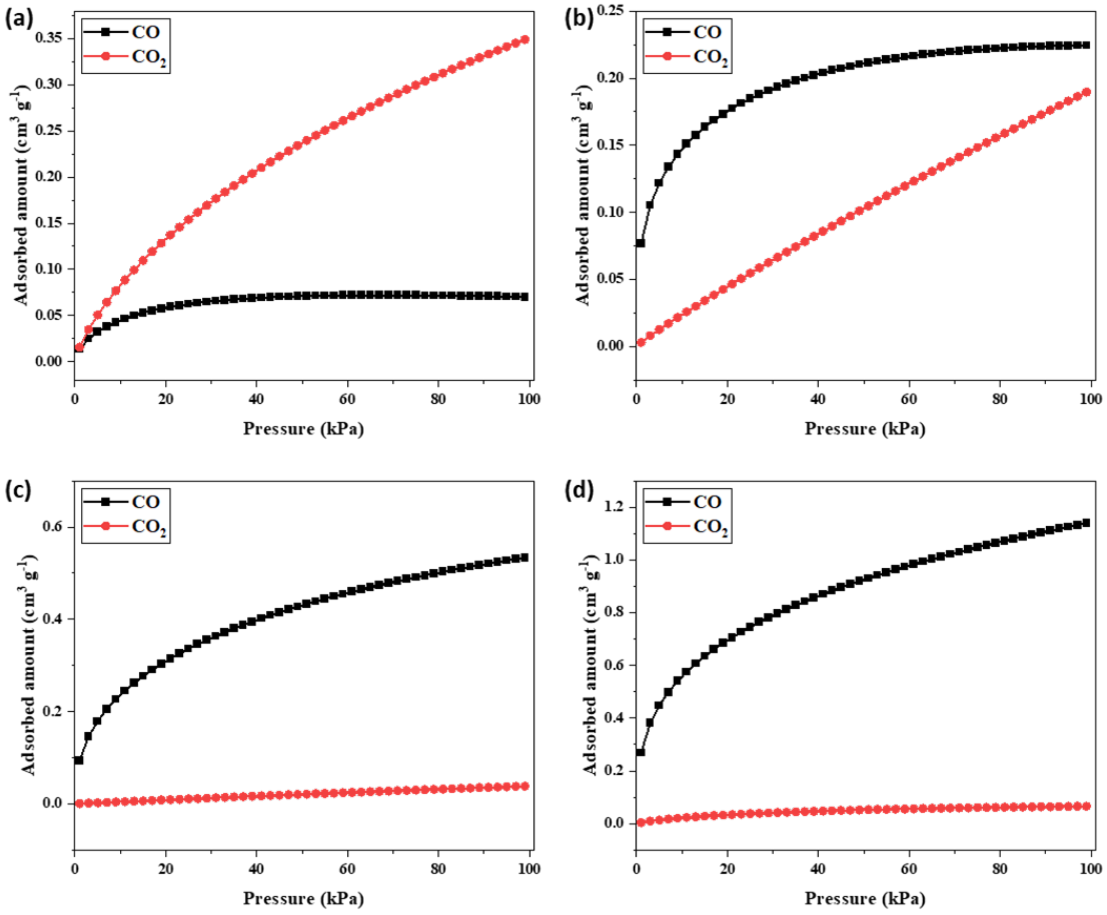

Figure 3-16 CO and CO_2 adsorption isotherms of (a) CuO, (b) R-CuO-453, (c) C-Cu-453, and (d) CR-CuO-453 as a function of total bulk pressure.

Table 3-6 Structure and adsorption behavior comparison of Cu(I)-containing adsorbents.

Adsorbent	BET surface area (m^2 g^{-1})	Total pore volume (cm^3 g^{-1})	CO adsorption capacity (cm^3 g^{-1})	CO/CO_2 selectivity	Ref.
0.9Cu(I)@MIL-100	898	0.37	86	29	[9]
1.3Cu(I)@SNW-1	136	0.36	23.8	23	[174]
40Cu(I)@MIL-101(Cr)-R	1030	0.69	69.3	34	[259]
Cu(I)@MIL-100(Fe)	436.2	0.263	63.9	63	[260]
Cu(I)Zn@MIL-100(Fe)	342.9	0.202	78.6	104	[260]
Cu(I)@MIL-101(Cr)-NH2-30	965	0.9	61.4	97	[261]

CR-CuO-453	7.1	0.02	1.4	158	This work

3.4.3 Breakthrough and cyclic adsorption experiment

Generally, IAST-predicted selectivity has been used for the initial screening of the adsorbents for their potential use to separate gases. However, it does not reflect realistic conditions such as adsorption kinetics and dynamic flow through a bed. Therefore, the adsorption kinetics and selectivity of the CR-CuO-453 for CO/CO_2 separation were investigated using dynamic flow through a packed bed. CR-CuO-453 was investigated in a dynamic setup since single component adsorption isotherms and IAST calculations both showed a good performance for CR-CuO-453. After introducing the $He/CO/CO_2$ mixture to the column packed with CR-CuO-453, CO_2 was first detected at the outlet of the column, while CO was retained (**Figure 3-17**). This shows that CO is selectively adsorbed to CR-CuO-453 even under mixed stream conditions. A peak is observed in the breakthrough curve of CO_2 with a maximum C/C_0 value of 1.5. This phenomenon is called a roll-up that originates from competitive adsorption between CO and CO_2 [9]. CO_2 molecules are weakly adsorbed in the column due to their fast movement that is then replaced with the strongly adsorbed CO molecules. The adsorption kinetics of mixture flow is presented in **Figure 3-18**. The CO adsorption capacity (0.91 $cm^3\ g^{-1}$ at a total pressure of 100 kPa) calculated from the breakthrough experiment under the mixture flow of $He/CO/CO_2$ (2:1:1 v:v:v) agreed with the IAST-predicted adsorption capacity under a CO/CO_2 mixture condition (0.92 $cm^3\ g^{-1}$ at a total pressure of 100 kPa).

Easy regeneration of adsorbents is a critical factor for the selection of potential materials for cyclic adsorption processes. The cyclic adsorption of the CR-CuO-453 was investigated in dynamic and equilibrium setups. He flow and vacuum are two methods usually used for the regeneration of adsorbents which are both reported to have similar regeneration performance [9, 262]. At the end

of a breakthrough run with CO/CO_2 mixture of gases, the column was purged with pure He at 303 K for 30 minutes. This mild regeneration condition reproduced identical breakthrough curves for 3 consecutive cycles (**Figure 3-17a**). The adsorption capacity of CR-CuO-453 was measured using pure CO equilibrium adsorption isotherm over 3 consecutive cycles (**Figure 3-17b**). The regeneration was performed at 303 K under continuous vacuum for 30 minutes. As illustrated in **Figure 3-17b**, the adsorption capacity of CR-CuO-453 was well maintained after 3 cycles. The formation of π-complexation interaction between Cu(I) adsorption sites and carbon monoxide provided a strong enough interaction for adsorption of CO molecules; however, the bonding is simultaneously weak enough so that we can regenerate the adsorbent under mild conditions[9, 17].

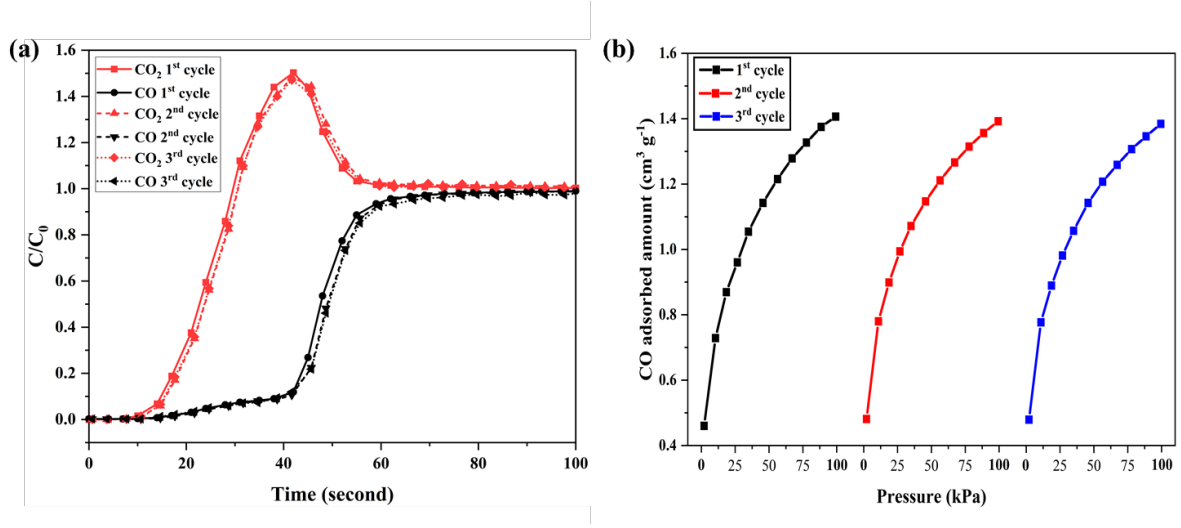

Figure 3-17 (a) Experimental breakthrough curves for CR-CuO-453 bed over three consecutive cycles with a gas mixture flow of $He/CO/CO_2$ ($He:CO:CO_2$ = 2:1:1, V:V:V) at 298 K and 100 kPa., (b) CO equilibrium adsorption profile for CR-CuO-453 over three consecutive cycles.

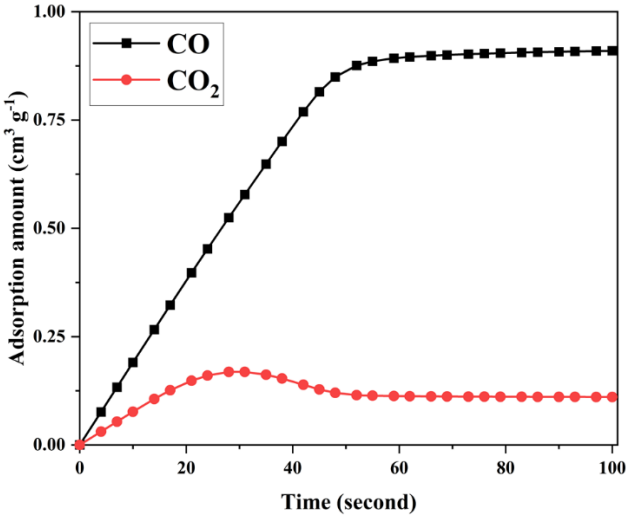

Figure 3-18 Adsorption kinetics of gas mixture (He:CO:CO_2=25:12.5:12.5; v:v:v) onto CR-CuO-453 adsorbent at 298 K.

3.4.4 Adsorption kinetics

The kinetic investigation of CO and CO_2 adsorption by CR-CuO-453 at 298 K and 1 bar is depicted in **Figure 3-19**. The plots of pure CO and CO_2 uptakes as a function of time over CR-CuO-453 show that the adsorption capacity of the pure component gases increased with time and reached a maximum value and then was retained at a constant value, indicating the saturation of the adsorbent with adsorbate molecules. The adsorption kinetic curves include two steps, an initial fast adsorption step where adsorbate molecules interact with the surface at a high rate due to the availability of vacant sites on the adsorbent. This step is followed by a slow adsorption step that is due to decreasing number of adsorption sites after adsorption of gas molecules leading to the constant adsorption for both CO and CO_2.

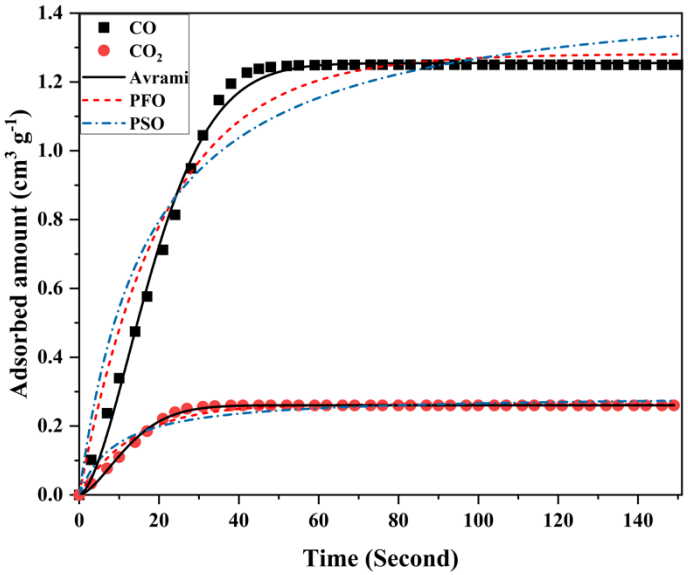

Figure 3-19 Experimental single component CO and CO_2 adsorption on CR-CuO-453 at 298 K along with the corresponding fitting to the kinetic models.

In comparison to CO_2, the CO adsorption time span is longer. This is due to the higher CO equilibrium adsorption capacity of CR-CuO-453 than that of CO_2. Therefore, it takes a longer time for CO to occupy the adsorption sites [240]. Furthermore, the higher affinity of CO to Cu(I) sites reduces the mobility of adsorbed CO molecules on the surface [240, 263] in comparison to CO_2 molecules. The adsorption kinetics were investigated using PFO, PSO, and Avrami models. The points in **Figure 3-19** represent the actual data points and the solid and dashed lines show the fitting curves of chosen kinetic models. The fitting parameters along with the calculated correlation coefficients (R^2) are shown in **Table 3-7**. The calculated values of q_e for CO and CO_2 using the Avrami model are very close to the experimental values. Furthermore, the calculated R^2 values for CO and CO_2 using the Avrami model are closer to unity than that of other kinetic models. Therefore, the kinetics of CO and CO_2 adsorption on CR-CuO-453 can be approximated using the Avrami model. The values of Avrami's kinetic constant ($k_{A,CO}$, and $k_{A,CO2}$) express the faster rate

of CO_2 adsorption on CR-CuO-453 than CO adsorption due to the aforementioned reason. The values of the Avrami exponent ($1 < n_A < 2$) show that the rate-controlling factors for CO and CO_2 adsorption on CR-CuO-453 are both physisorption and chemisorption [264]. The reaction between CuO and CO_2 is thermodynamically favorable under standard conditions (1 atm and 298 K). The value of n_A implies the chemical interaction of CO_2 with oxide sites (i.e., CuO) and additional physical interaction of CO_2 with other available sites (i.e., Cu_2O, CuCl, and Cu) [258]. Furthermore, the adsorbed amount of CO on CR-CuO-453 includes physisorption and the π-complexation adsorption through the interaction of CO molecules with Cu(I) sites [11]. Moreover, reactive adsorption of CO on CuO at room temperature has been reported to form surface carbonates [265]. Other studies indicate the adsorption of CO on copper surface and its subsequent engagement to reaction under continuous exposure to CO at room temperature [266]. Moreover, since the Avrami's exponent is larger than 1, it can be stated that adsorption of both CO and CO_2 on the surface is heterogeneous [209]. This result is consistent with GF and LF fitting parameters of CO and CO_2 (**Table 3-4** and **Table 3-5**). More specifically, since n_A values are close to 2, it can be stated that the adsorption rate decreases gradually as the adsorbed nuclei expand in one direction to cover more surface area [209].

Table 3-7 Calculated kinetic model parameters for single component CO adsorption and CO_2 adsorption on CR-CuO-453 at 298 K.

Model	CO adsorption			CO_2 adsorption		
PFO	k_1 (s^{-1})	q_e ($cm^3\ g^{-1}$)	R^2	k_1 (s^{-1})	q_e ($cm^3\ g^{-1}$)	R^2
	0.047	1.28	0.964	0.074	0.26	0.97
PSO	k_2($cm^3\ s\ g^{-1}$)	q_e ($cm^3\ g^{-1}$)	R^2	k_2($cm^3\ s\ g^{-1}$)	q_e ($cm^3\ g^{-1}$)	R^2
	0.038	1.49	0.917	0.372	0.29	0.914
Avrami	k_A (s^{-1}), n_A	q_e ($cm^3\ g^{-1}$)	R^2	k_A (s^{-1}), n_A	q_e ($cm^3\ g^{-1}$)	R^2
	0.046, 1.65	1.25	0.995	0.07, 1.59	0.26	0.998

3.4.5 Environmental impact assessment

We evaluated the sustainability of the adsorbent synthesis process using the mass-based sustainability and socioeconomic parameters (i.e., Mass Intensity (MI), Reaction Mass Efficiency (RME), Solvent Intensity (SI), Environmental factor (E-factor), Energy Intensity (EI)) [267, 268]. The equations used for this investigation are provided below and the results are presented in **Table 3-8**. CuO is the raw material used for thermal reduction, and $CuCl_2$ and R-CuO are the raw materials of the liquid-phase reaction where ethanol was used as a solvent. High values of RME have been reported for thermal reduction and liquid-phase reaction step (86.1 and 104.3). The reported RME >100 after liquid-phase reaction step accounts for CuO and Cu_2O formation from oxidation in air during the storage.

$$\text{Mass Intensity}\left(\frac{\text{kg}}{\text{kg product}}\right) = \frac{\text{mass of all reactants used excluding water}}{\text{mass of product}} \quad (3\text{-}12)$$

$$\text{Reaction Mass Efficiency (RME)} = \frac{\text{mass of product}}{\text{mass of all reactants}} \times 100\% \quad (3\text{-}13)$$

$$\text{Solvent Intensity}\left(\frac{\text{kg}}{\text{kg product}}\right) = \frac{\text{mass of all solvent used excluding water}}{\text{mass of product}} \quad (3\text{-}14)$$

$$\text{E factor} = \frac{\text{kg(raw materials)} - \text{kg(desired product)}}{\text{kg (total product including water)}} \quad (3\text{-}15)$$

$$\text{Energy Intensity (kWh/kg)} = \frac{\text{amount of non renewable energy used}}{\text{mass of product}} \quad (3\text{-}16)$$

Table 3-8 Mass-based sustainability metrics evaluation for the manufacturing process of the CR-CuO adsorbent

Materials	Mass Intensity (MI) (kg/kg)	Reaction Mass Efficiency (RME) %	Solvent Intensity (SI) (kg/kg)	E-factor	Energy Intensity (EI) (kWh/kg)
R-CuO	1.16	86.1	1.56	0.12	854.6
CR-CuO	1.1	104.3	6.58	0.86	1250

None of synthesis steps led to discharge of any harmful fume/solvents or side products. The E-factor of reduction and liquid-phase reaction (i.e., 0.12, and 0.86) show minimal emissions. It is easy to collect the copper salt after filtration and ethanol washing. Ethanol can also be recycled.

Electrical energy was used to operate furnace, stirrer, vacuum pump, and heating oven during synthesis. EIs of R-CuO and CR-CuO synthesis were calculated to be 854.6, and 1250 kWh/kg which can be effectively reduced by increasing the scale of production.

3.5 Conclusions

We synthesized a highly stable CO adsorbent, CR-CuO-453, with two co-existing Cu(I) sites through a facile two-step method (thermal reduction and liquid-phase reaction). Based on the XRD analyses, we confirmed the formation of the copper oxide and carbonate protective layer. Heat treatment could readily remove the protective layer to expose the active adsorption sites. The optimal thermal activation temperature was 453 K to ensure the removal of the protective layer and achieve the highest adsorption capacity. CR-CuO-453 adsorbent retained its adsorption capacity after 10 days of storage under ambient conditions. With dual Cu(I) active sites, CR-CuO-453 showed an elevated CO adsorption capacity due to the presence of two active adsorption sites. We investigated the impact of each step of the synthesis process on CO adsorption through adsorption site energy distribution approximation based on Generalized Freundlich and Langmuir-Freundlich models. It was shown that thermal reduction under hydrogen enhanced energetic heterogeneity resulting in a high value of the average surface energy and consequential high affinity to CO. The liquid-phase reaction decreased the overall energetic heterogeneity yet added many more adsorption sites in the low-energy range than in the high-energy range. CR-CuO-453 showed considerably high CO/CO_2 adsorption selectivity compared to single Cu(I) site adsorbents, R-CuO-453 and C-Cu-453.

Furthermore, CR-CuO-453 showed a good CO/CO_2 separation under dynamic mixed stream conditions. Under dynamic and static adsorption conditions, CR-CuO-453 maintained the adsorption capacity for 3 adsorption-desorption cycles. We analyzed CO and CO_2 adsorption

kinetics on CR-CuO-453 at room condition using the pseudo-first-order, pseudo-second-order, and Avrami kinetic models. Only the Avrami model gave a reasonable fit for the experimental kinetic data. CR-CuO-453 showed faster CO_2 adsorption kinetics than CO, while the eventual adsorption amount of CO exceeded that of CO_2 (1.25 $cm^3\ g^{-1}$ vs. 0.26 $cm^3\ g^{-1}$).

Chapter 4: Rapid Ambient Synthesis of ZSM-5@MOF-199 Composite Adsorbent with Tunable Core-Shell Structure

Abstract

Separation of carbon monoxide and carbon dioxide is crucial for various industrial applications with the aim of energy production and environmental sustainability. In this study, we have developed a ZSM-5@MOF-199 composite through a rapid room temperature method using a hydroxy double salt intermediate. The structural and chemical properties of the composite were fine-tuned through pre- and post-synthesis modification. Various characterization techniques were employed to investigate the formation of the composites along with their structural and chemical properties. Our result demonstrated that the choice of copper salt and solvent influenced the formation and growth of the metal—organic framework (MOF) shell with copper chloride and acetonitrile enhancing the growth of MOF layer. The composite exhibited a superior adsorption capacity for CO and CO_2 compared to parent adsorbents. Regulation of Cu(I) content in the MOF-199 through post-synthesis reduction resulted in improved CO adsorption performance. Modulating the zeolite core to protonic hierarchical ZSM-5 enhanced the composite's structure and increased the CO and CO_2 uptake by 20 and 28%, respectively. Analysis of the isosteric heat of adsorption revealed the nature of adsorbent-adsorbate interactions, indicating a stronger interaction between CO and modulated composites. The isosteric heat of adsorption revealed that the presence of HZSM-5 in the composite altered surface electronic properties and influenced the CO_2 adsorption performance through a synergistic effect. The overall adsorption behavior of the adsorbents was investigated through integral thermodynamic properties. Thermodynamic analysis indicated that the adsorption processes were spontaneous with an ordered arrangement of adsorbates, exothermic, and involved a combination of physisorption and electrostatic interactions.

Overall, this study provides valuable insights into the synthesis and characterization ZSM-5@MOF-199 composites with tunable structures for selective separation of CO and CO_2. The findings contribute to the development of efficient adsorbent materials applicable in industrial settings for environmental and energy production purposes.

KEYWORDS: Composite adsorbent, MOF-199, ZSM-5, Structural and chemical modification, Thermodynamics of adsorption, Adsorption mechanism

4.1 Introduction

The separation of carbon monoxide (CO) and carbon dioxide (CO_2) is essential for various industrial processes, particularly in energy production. Moreover, the environmental impact of these gases, such as global warming and ozone depletion, make their separation essential [4, 269-272]. In the production of hydrogen from natural gas through steam methane reforming (SMR) or coal gasification, CO and CO_2 removal is critical [55, 273]. Production of ultra-high-purity hydrogen from SMR off-gas is performed by a layered-bed pressure swing adsorption unit [55]. The hydrogen rich stream (70–80%) usually comes with impurities, such as traces of H_2S, water vapor (<1%), N_2 (<1%), CH_4 (3-6%), CO (1-3%), and CO_2 (15-25%), and passes through three adsorbent layers. The first layer is silica or alumina to separate the water. It is followed by an activated carbon layer to adsorb CO_2, CO, CH_4, and the traces of H_2S and a final layer of zeolites to improve adsorption of CO, N_2, and other trace components [25, 29]. Therefore, understanding the adsorbate-adsorbent interactions and development of suitable materials play a significant role in improving the overall efficiency of the separation process [25].

However, synthesis of adsorbent materials with tunable selectivity towards target gases in a mixture is challenging. Usually, the surface of adsorbents is modified through a variety of

techniques to selectively interact with target gases [269]. Sujan et al. reported significant enhancement in selective adsorption of CO_2 from ambient air and flue gas through amine functionalization of porous materials [212, 213]. Modification of porous materials with transition metals such as Ag(I), Cu(I), Pt(II), and Pd(II) have been reported to enhance selective adsorption of CO. In our previous work [273], we showed a highly selective separation of CO from a CO-CO_2 mixture using dual Cu(I) modification of adsorbent surface.

Metal—organic frameworks (MOFs) are a class of crystalline porous materials with high surface area and pore volume, rendering them useful in numerous applications, including separation, storage, and heterogeneous catalysis [274]. The combination of diverse metal clusters and organic ligands enables the development of MOFs with diverse structures, pore sizes, and shapes. Moreover, the functionalization of MOF frameworks through pre- and post-synthesis modifications of metal clusters and/or organic ligands extends the ability to fine-tune pore dimensions and the local environment within the pores [55, 274]. Recent studies demonstrate the potential of MOFs in selective separation of impurities for hydrogen purification applications. Several notable MOFs, including MOF-74, USTA-40, HKUST-1, IRMOF, MOF-177, UiO-66, and MIL-53, have been extensively investigated for their efficacy in this regard [55, 275-277].

Zeolites are crystalline microporous aluminosilicates that are widely used for adsorption and catalysis applications. Zeolites share the common characteristics as MOFs, including high surface area and uniform micropores. However, they offer a higher thermal, mechanical, and structural stability compared to MOFs [274].

Recently, hybrid materials such as MOF/zeolite, MOF/activated carbon, MOF/graphene, polymer/zeolite, and polymer/oxide have been synthesized to enhance the adsorption or catalytic performance efficiency through the synergistic effects offered by utilization of both material's

unique physical, chemical, and structural properties [95, 212, 213, 274, 278, 279]. Al-Naddaf et al. reported a 20-30% increase in the adsorption performance of zeolite-5A@MOF-74 compared to compared to MOF-74. They attributed this enhancement to the pore structure of the composite [55]. Kirby et al. developed a number of zeolite-5A@MOF composites with a HKUST-1 layer of different coordinating metals, such as copper (Cu), aluminum (Al), gallium (Ga), and cobalt (Co), and investigated the effect of coordinating metals on the CH_4 storage performance [279]. Zu et al. reported synthesis of ZSM-5@UiO-66 through a solvothermal method and showed its application as a bifunctional acid-base catalyst in cascade reactions [274]. Other composites such as MOF-505@graphene oxide and graphene oxide@Cu-BTC have been developed for selective adsorption of CO_2 in a mixture of CO_2-CH_4 [95, 278]. The synthesis of composites and MOFs are mainly through solvothermal method with typical synthesis conditions: temperature ~ 80-180 °C and synthesis time ~ 12-24 hours [95, 212, 213, 274-276, 278, 279]. These studies demonstrate the progress made in development of MOF-based composites into the potential materials for practical and industrials applications. While MOFs and MOF-based composites are promising materials for gas adsorption, separation, and catalysis, the low synthesis rate and harsh processing conditions (high temperature and pressure) of the traditional solvothermal methods remain an obstacle for industrial implementation of these materials [280].

In this study, we report a fast room temperature synthesis of ZSM-5@MOF-199 composites with tunable structure using a hydroxy double salt intermediate. HDSs are characterized as layered compounds featuring cationic sheets interconnected by inorganic/organic interlamellar anions [280, 281]. These materials are synthesized through reaction of a divalent metal oxide with another different divalent cation. Similar to layered double hydroxides, HDSs exhibit exceptional anion exchangeability, making them promising for diverse applications such as separation, catalysis, and

pharmaceutical processes [280, 281]. The use of HDS intermediate presents a significant advantage over alternative methods, as it eliminates he long reaction time, equipment cost, and energy-intensive heating steps [282]. Zeolite Socony Mobil-5 (ZSM-5) is employed as the zeolite core due to its well-structured pore systems, which consist of intersecting straight channels (5.1 x 5.3-5.6 Å) and a zig-zag 10-membered ring channel (5.3 x 5.6 Å). ZSM-5 offers intrinsic acidity and high hydrothermal stability and has been widely used in adsorption, catalysis, and ion-exchange processes [274, 283]. Notably, ZSM-5 cations offer a significant number of accessible coordinative vacancies, enabling simultaneous interaction with two or three molecules [283].

MOF-199, also known as Cu-BTC, HKUST-1, or commercially available as Basolite^{TM} C300, is a well-characterized metal-organic framework [284]. Based on the well-known copper paddle wheel, MOF-199 has a three-dimensional structure of large square channels (9 Å in diameter) connecting a system of octahedral cages of 5Å surrounded by small tetrahedral side-pockets (3.5 or 4.6 Å, hydrated and dehydrate) [285]. Studies have revealed the coexistence of Cu(I) and Cu(II) within the MOF-199 framework [286], contributing to its versatile functionality in catalysis, gas adsorption, and separation [284, 287-289]. Cu(I) and Cu(II) exhibit distinct coordination environments in mixed valence MOF-199. Cu(II) ions form the characteristic Cu_2-paddlewheel motif, while Cu(I) ions are part of tetrameric macrocycles containing four Cu(I) ions and four carboxylate groups [290].

The adsorption capacity of gases is predominantly influenced by the surface area and total pore volume of adsorbent materials. However, to enhance the effectiveness of adsorption, it is crucial to increase the number of sites that show strong interactions with target molecules. In this study, we first tuned the structural properties of the composite by altering the copper salt and organic solvent and subsequently employed a valence engineering approach to enhance the adsorption

performance of the composite. Through controlling the Cu(II)/Cu(I) ratio in MOF-199, we optimize the composite's adsorption capabilities. Moreover, the impact of structural and chemical properties of the zeolite core in adsorption performance of the composite is investigated by incorporating protonic hierarchical ZSM-5 (HZSM-5).

The adsorption performance of composites is evaluated in a CO and CO_2 mixture, chosen as a model system due to its practical relevance in the purification process of SMR off-gas [25, 29]. Furthermore, because of their distinct properties, the separation of CO and CO_2 offers insights into the electrostatic interactions with the composite surface. **Table 4-1** shows the molecular properties of CO and CO_2. To elucidate the binding strength and adsorption mechanism between the adsorbate molecules and the composites, we extracted the isosteric heat of adsorption and the thermodynamic properties of CO and CO_2 adsorption on the composites.

Table 4-1 Molecular properties of CO and CO_2 [196]

Property	**Unit**	**CO_2**	**CO**
Molecular Weight	amu	44.01	28.01
Boiling Point	K	194.7	81.5
Molecular Configuration		Linear	Linear
Molecular Length	Å	~2.326	~1.128
Kinetic Diameter	Å	3.3	3.69
Polarizability	X 10^{-25} cm^3	26.3	19.5
Dipole Moment	X 10^{18} esu cm	0	0.112
Quadrupole Moment	X 10^{-26} esu cm^2	4.1	2.5

4.2 Experimental

4.2.1 Materials

The chemicals used in the synthesis were all of ACS reagent grade. Commercial zeolite NH_4-ZSM-5 (SiO_2:Al_2O_3 23:1 mole ratio), copper(II) chloride dihydrate ($CuCl_2.2H_2O$, 99+%), and zinc nitrate hexahydrate ($Zn(NO_3)_2.6H_2O$, 99%) were purchased from Alfa Aesar. Copper(II) acetate

monohydrate ($Cu(CO_2CH_3)_2.H_2O$, ≥98%) and copper(II) nitrate trihydrate ($Cu(NO_3)_2.3H_2O$, 98%) were purchased from Sigma Aldrich. 1,3,5-benzenetricarboxylic acid (H_3BTC) and sodium thiosulfate anhydrous ($Na_2S_2O_3$, 99%) were purchased from TCI and Fisher Scientific, respectively. 200 proof pure ethanol anhydrous and acetonitrile HPLC grade (≥99.0%) were purchased from the commercial vendors and used without further purification. Ultrahigh-purity gases were obtained from Airgas.

4.2.2 Synthesis of hierarchical HZSM-5

HZSM-5 with hierarchical pore structure was synthesized following a reported method in the literature [291]. Commercial NH_4-ZSM-5 was first calcined at 550 °C for 2 hours at a heating rate of 20 °C/min to obtain HZSM-5. Next, a desilication process was carried out by dispersing 0.2 g of HZSM-5 in 300 ml of 0.1 M NaOH solution and heated at 65 °C with stirring for 30 minutes. The resulting suspension was cooled in an ice bath, collected using a vacuum filter, and washed with deionized water until a neutral pH was achieved. The obtained powder was dried at 80 °C for 1 hour, followed by an ion-exchange reaction where H^+ and Na^+ ions were exchanged NH_4^+ ions. This exchange reaction was carried out by stirring the powder in a 0.5 M NH_4Cl solution at 70 °C for 2 hours. The resulting suspension was cooled, filtered, and washed, and the sample was then dried at 80 °C and calcined at 550 °C for 2 hours to obtain protonic hierarchical HZSM-5.

4.2.3 Synthesis of zinc impregnated ZSM-5

ZSM-5 was modified by Zn using the wet-impregnation method [291, 292]. In a typical synthesis, 2, 4, and 8 ml of a saturated zinc nitrate aqueous solution was added dropwise into a beaker containing 1 g of ZSM-5. This mixture was then evaporated under stirring at 70 °C and stored in oven at 70 °C until completely dried up. The samples were then calcined at 550 °C for 2 hours to obtain (m)ZnO/ZSM-5, where m shows the weight % loading of ZnO on ZSM-5.

4.2.4 Synthesis of pure MOF-199

MOF-199 was synthesized according to the reported method in the literature [293]. 0.96 g of $Cu(NO_3)_2.3H_2O$ and 0.42 g of H_3BTC were dissolved in 20 ml of deionized water and 20 ml of ethanol, respectively. The obtained homogenous solutions were mixed under rigorous stirring and then transferred to 100 ml Teflon lined autoclave and reacted at 120 °C for 24 hours. After cooling down to the room temperature, the resulting powder was filtered and washed three times using ethanol and deionized water (40 mL) to remove the unreacted precursors. The bluish crystalline powder was dried in a vacuum oven at 60 °C overnight and was then labeled as MOF-199.

4.2.5 Synthesis of ZSM-5@MOF-199 composite using (Zn,Cu) hydroxy double salt intermediate

In a typical process, three Cu salts ($Cu(NO_3)_2.3H_2O$, $CuCl_2.2H_2O$, and $Cu(CO_2CH_3)_2.H_2O$) were separately dissolved in 5 ml deionized water to obtain a homogeneous solution containing 0.127 g copper. ZnO/ZSM-5 was dispersed in the Cu containing solution for 2 minutes to form the slurry under stirring. 0.2 g of H_3BTC was dissolved in 35 ml of EtOH or EtOH-MeCN. The BTC containing solution was then added to the slurry under stirring. After 15 minutes of reaction, the powder was filtered and washed with ethanol (40 mL, 3 times), and the product was dried in vacuum oven at 60 °C overnight. Throughout the paper, the core-shell structured adsorbent is referred to as H-X/Z@M or H-X/HZ@M, where X shows the anion of copper salt used to form the HDS in the synthesis process and HZ shows the protonic hierarchical ZSM-5.

4.2.6 Synthesis of mixed-valence ZSM-5@MOF-199

Cu(I)/Cu(II) mixed-valence of MOF-199 shell was systematically synthesized using $Na_2S_2O_3$ as the reducing agent [294]. In the synthesis process, 0.2 g of H-X/Z@M was dispersed in 60 ml of DI H_2O-EtOH solution (1:1 by volume, DI H_2O:EtOH) containing $Na_2S_2O_3$. The slurry was

transferred to a Teflon-lined autoclave and reacted at 85 °C for 24 hours. The final powder was filtered and washed with ethanol (40 mL, 3 times) and labeled as (n)R-H-X/Z@M, where n shows mass (g) of $Na_2S_2O_3$, and R denotes the reduced powder.

The overall synthesis route of composites is presented in **Figure 4-1**.

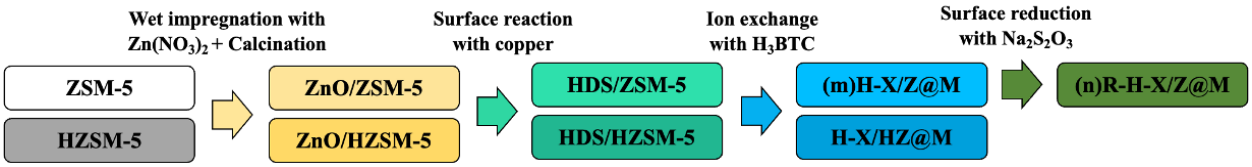

Figure 4-1 Overall synthesis process of ZSM-5@MOF-199 composites. X identifies the ligands of copper sources: nitrate (N), chloride (Cl), and acetate (A). m and n show loading of ZnO and mass of $Na_2S_2O_3$, respectively.

4.2.7 Adsorbents characterization

The X-ray diffraction (XRD) measurements were performed to investigate the crystallinity of the composites using a Proto manufacturing AXRD powder diffraction system with Cu K_α radiation (λ=1.5418 Å). The samples were scanned at a rate of 2.2°/min at 30 mA and 40 kV. Rietveld analysis was performed on the XRD data by MAUD software to identify the loading of materials on the composites [4, 270, 295]. The structural properties of the materials were evaluated by N_2 physisorption at 77 K using a Quantachrome NOVA 2200e surface and pore analyzer. The samples were degassed at 100 °C under vacuum for 6 hours prior to the measurements. The Brunauer-Emmett-Teller (BET) equation in the relative pressure range of $0.05 < p/p_0 < 0.3$ and density functional theory (DFT) methods were used to estimate the surface area and pore size distribution (PSD), respectively. The total pore volume was calculated by the adsorbed amount of N_2 at the relative pressure of 0.99. The structural morphology and elemental mapping of the materials were obtained by scanning electron microscopy (SEM) and energy-dispersive spectroscopy (EDS) using Zeiss EVO 50 Scanning Electron Microscope. The formation of HDS and composites was evaluated by Fourier transform infrared (FTIR) using a Nicolet-FTIR 6700 spectrometer. The

absorbance of the surface detector was plotted against the wavenumber (40-3800 cm^{-1}) in Attenuated Total Reflection (ATR) infrared mode, 64 scans, and resolution of 4 cm^{-1}. Thermogravimetric measurements were performed with a TA Instruments Q500 Thermogravimetric Analyzer (TGA) under N_2 flow at 100 mL/min from 25 to 900 °C at the rate of 20 °C/min to determine the thermal stability of the samples. X-ray photoelectron spectroscopy was performed on a PHI5000 VersaProbe II XPS equipment with a monochromatic Al Kα X-ray radiation source (1486.6 eV), using a focused spot size of 100 μm. The high-resolution scans were obtained with pass energy of 23.5 eV and a step size of 0.1 eV.

4.2.8 Adsorption isotherms measurements

The single component CO and CO_2 adsorption isotherms were measured at 20, 40, 60 °C using Quantachrome NOVA 2200e surface and pore analyzer. The isotherms were measured at the mentioned temperatures to estimate the heat of adsorption. Prior to adsorption measurements, samples were degassed for 6 hours under continuous vacuum at 100 °C to remove the preadsorbed gases and moisture. The adsorption equilibrium isotherms were obtained in the pressure range 0-100 kPa. The experimental adsorption isotherms were fitted with Langmuir-Freundlich (LF) and Dual-Site Langmuir-Freundlich (DSLF) models (**Eq. 4-1** and **Eq. 4-2**, respectively) to understand the adsorbate-adsorbent interaction [269, 273].

$$q = q_m \frac{k_S p^{n_S}}{1+k_S p^{n_S}} \quad 4\text{-}1$$

$$q = q_{m_1} \frac{k_{S1} p^{n_{S1}}}{1+k_{S1} p^{n_{S1}}} + q_{m_2} \frac{k_{S2} p^{n_{S2}}}{1+k_{S2} p^{n_{S2}}} \quad 4\text{-}2$$

where q_m (mmol g^{-1}) is the saturation capacity, k_S (kPa^{-1}) and n_S are the affinity coefficients and LF exponent, respectively. q_{m1}, q_{m2}, k_{S1}, k_{S2}, n_{S1}, and n_{S2} are analogous parameters on LF model for sites 1 and 2.

4.2.9 Ideal Adsorbed Solution Theory (IAST)

Ideal adsorption solution theory (IAST), proposed by Myers and Prausnitz, is widely used to predict the selectivity of binary gas mixtures based on the pure component adsorption isotherms [273]. IAST is a thermodynamic approach that draws an analogy between adsorption equilibria and Raoult's law for vapor-liquid equilibrium. It works on the assumption that adsorbed phase behaves as an ideal solution. The theory provides a framework to describe the equilibrium between the ideal gas and the adsorbed phase using **Eq. 4-3** [296, 297].

$$Py_i = P_i^0(\pi^*)x_i \qquad 4\text{-}3$$

where y_i and x_i are the molar fraction of component i in the gas phase and adsorbed phase, respectively. P is the total pressure of the mixture, and $P_i^0(\pi^*)$ denotes the equilibrium gas phase pressure of pure component i adsorbed at the same temperature and spreading pressure, π^*, as the mixture. When adsorption occurs, the amount of adsorption depends on the specific surface area of the adsorbent (A) [298]. Therefore, compared to vapor-liquid equilibrium, the presence of solid adsorbent introduces an additional degree of freedom for the equilibrium between the adsorbed phase and the gaseous phase which is represented by the spreading pressure. Spreading pressure is an intensive property associated with the extensive property A, which quantifies the reduction in the surface tension when an adsorbate spreads over the adsorbent surface [298]. For an ideal solution, there are no interactions between the adsorbed molecules in the adsorbed phase with equal spreading pressure of each component at a given temperature [296, 297]. Reduced spreading pressure (π^*) of component i in the standard state can be obtained from the integration of the Gibbs adsorption isotherm using **Eq. 4-4**.

$$\pi_i^* = \frac{\pi_i A}{RT} = \int_0^{P_i^0} \frac{q_i^*}{P_i} dP_i \qquad 4\text{-}4$$

where π_i^* and π_i are the reduced spreading pressure and spreading pressure of component i in the adsorbed phase, A is the specific surface area of the adsorbent, q_i^* is the pure component adsorption isotherm equation, and P_i^0 is the standard state pressure of pure component i corresponding to spreading pressure of the mixture. The standard state refers to the state where π^* of the mixture is the same as the π_i^* for each component.

$$\pi_i^* = \pi^* \qquad i=1, 2, 3 \ldots.N \tag{4-5}$$

In an ideal adsorbed mixture where there is no change in mixing area, the total adsorbed amount (q_T) can be calculated considering the loadings of individual components at standard state [296, 297].

$$\frac{1}{q_T} = \sum_{i=1}^{N} \frac{x_i}{q_i^0(P_i^0)} \tag{4-6}$$

where N represents the number of adsorbate species, $q_i^0(P_i^0)$ represents the amount of pure component i adsorbed at standard state pressure. The adsorbed amount of each component in the mixture can be determined using the following equation.

$$q_i = x_i q_T \tag{4-7}$$

The following constraints were considered for solving the IAST equations.

$$\sum_{i=1}^{N} x_i = \sum_{i=1}^{N} y_i = 1 \tag{4-8}$$

For each component, **Eq. 4-4** can be evaluated utilizing the pure component isotherm equation, which involves fitting a continuous function to a discrete set of adsorption data obtained across a specific range of pressure.

In this study, IAST approach was employed in combination with LF and DSLF isotherm equations. The equations for π_i^* of adsorbed mixture were derived by substituting the pure component LF and DSLF equations into **Eq. 4-4**, followed by integration with respect to P over the range from 0 to P_i^0. **Eq. 4-9** and **Eq. 4-10** yield the π_i^* for the LF and DSLF models, respectively.

$$\pi_i^* = \frac{q_{m,i}}{n_i} \ln\left(1 + k_i (P_i^0)^{n_i}\right) \quad 4\text{-}9$$

$$\pi_i^* = \frac{q_{m1,i}}{n_{1,i}} \ln\left(1 + k_{1,i} (P_i^0)^{n_{1,i}}\right) + \frac{q_{m2,i}}{n_{2,i}} \ln\left(1 + k_{2,i} (P_i^0)^{n_{2,i}}\right) \quad 4\text{-}10$$

Eq. 4-9 and **Eq. 4-10** were equated for each component, resulting in the following equations for LF and DSLF models, respectively.

$$\frac{q_{m,1}}{n_1} \ln\left(1 + k_1 \left(\frac{P_1}{x_1}\right)^{n_1}\right) = \frac{q_{m,2}}{n_2} \ln\left(1 + k_2 \left(\frac{P_2}{x_2}\right)^{n_2}\right) \quad 4\text{-}11$$

$$\frac{q_{m1,1}}{n_{1,1}} \ln\left(1 + k_{1,1} (P_1)^{n_{1,1}}\right) + \frac{q_{m2,1}}{n_{2,1}} \ln\left(1 + k_{2,1} (P_1)^{n_{2,1}}\right) = \frac{q_{m1,2}}{n_{1,2}} \ln\left(1 + k_{1,2} (P_2)^{n_{1,2}}\right) + \frac{q_{m2,2}}{n_{2,2}} \ln\left(1 + k_{2,2} (P_2)^{n_{2,2}}\right) \quad 4\text{-}12$$

The aforementioned equations were solved using MATLAB through an implicit approach to determine the values of x_i and adsorbed amount by each component. The CO/CO_2 selectivity of adsorbents was calculated using **Eq. 4-13**.

$$S = (x_{CO}/x_{CO_2})/(y_{CO}/y_{CO_2}) \quad 4\text{-}13$$

4.2.10 Thermodynamics of adsorption

4.2.10.1 Isosteric heat of adsorption

Isosteric heat of adsorption was used to evaluate the adsorbate-adsorbent interaction according to the Clausius-Clapeyron equation (**Eq. 4-14**) [55, 269].

$$Q_{st} = RT^2 \left(\frac{\partial \ln p}{\partial T}\right)_q = -R \left(\frac{\partial \ln p}{\partial \left(\frac{1}{T}\right)}\right)_q \quad 4\text{-}14$$

where p (kPa) is pressure, T (K) is the absolute temperature, and R is the ideal gas constant. Q_{st} (kJ mol^{-1}) can be calculated from the slope of ln(p) versus 1/T at constant loading of q (mmol g^{-1}). The partial pressure was calculated using the fitting parameters of LF and DSLF models for different temperatures at fixed loadings.

4.2.10.2 Integral thermodynamic properties

To explicate the behavior of the adsorption process, free of the limitations of the differential thermodynamic quantities, the integral thermodynamic parameters including Gibbs free energy, enthalpy, and entropy were calculated.

The change in the integral molar Gibbs' energy (**Δ**G) for adsorption process is the minimum amount of work required to load an adsorbent to a certain level under isothermal condition and can be evaluated according to following equation [297, 299].

$$\Delta G = \frac{\Omega}{q} = -\frac{RT\int_0^p q\ d\ln p}{q} \qquad 4\text{-}15$$

where **Ω** is the surface potential (kJ mol^{-1}), q is the adsorption amount (mmol g^{-1}), R is the universal gas constant (kJ mol^{-1} K^{-1}), and T is the absolute temperature (K).

The integral molar enthalpy change, **Δ**H (kJ mol^{-1}), indicates the heat effects of the adsorption process, and can be derived from fundamental thermodynamic relationships [297, 299].

$$\Delta H = \frac{\left[\frac{\partial\left(\frac{\Omega}{T}\right)}{\partial\left(\frac{1}{T}\right)}\right]_p}{q} \qquad 4\text{-}16$$

The integral entropy change, **Δ**S (kJ mol^{-1} K^{-1}), is a measure of the way in which a thermodynamic system may be rearranged and is considered as a measure of disorder. It also helps in comprehending the packing manner of the adsorbed molecules. It can be calculated using the following equation [297, 299].

$$\Delta S = \frac{-\left(\frac{\partial\Omega}{\partial T}\right)_p}{q} \qquad 4\text{-}17$$

These parameters are obtained by numerical analysis based on the isotherm models for pure component adsorption on adsorbents.

4.3 Result and discussion

4.3.1 Characterization of parent and zinc impregnated zeolite

Prior to MOF growth, XRD and FTIR analysis were performed on parent and ZnO-modified ZSM-5 to confirm the successful functionalization of ZSM-5 surface. **Figure 4-2a** shows the FTIR spectra of parent and ZnO/ZSM-5 in the lattice vibration region 400-3800 cm^{-1}. The five-membered pentasil unit of the ZSM-5 structure is represented by the bands at 430 and 550 cm^{-1}. Furthermore, the bands at 430, 550, and 790 cm^{-1} represent the bending vibration of SiO_4 and AlO_4 groups in ZSM-5 framework. The intensity of these bands, likewise the crystallinity of zeolite, is reduced by surface modification [291]. The decrease of XRD peak intensity after loading of ZnO on ZSM-5 (**Figure 4-2b**) can be supported by the lower intensity of FTIR bands. The external asymmetric stretching of Si—O—Si bridge is characterized by the adsorption bands at 1050 and 1214 cm^{-1}. The peak at 1627 cm^{-1} indicates the presence of hydroxy groups (OH^-) of adsorbed water on the surface of ZSM-5. **Figure 4-2b** shows the XRD patterns of the reference and (m)ZnO/ZSM-5 adsorbents. The characteristic peaks of ZSM-5 are located at 2θ equal to 13.59°, 14.19°, 15.14°, 15.91°, 23.38°, 24.16°, 25.63°, and 30.18° [291, 300]. These peaks correspond to (102), (112), (131), (022), (051), (313), (323), and (062) planes, respectively. Successful loading of ZnO on ZSM-5 is confirmed by the presence of ZnO diffraction peaks located at 31.61°, 34.26°, and 36.10° that are associated with (100), (002), and (101) planes, respectively [301]. The intensification of ZnO diffraction peaks indicates a higher loading of ZnO on ZSM-5, whereas the minor suppression of ZSM-5 peaks following ZnO modification suggests the preservation of ZSM-5 crystallinity. The ZnO content (wt%) of the adsorbents was determined using MAUD software. **Figure 4-2c** demonstrates that the nitrogen uptake of ZnO/ZSM-5 decreased with increasing ZnO loading. This reduction can be attributed to the blockage of pores caused by the loading of ZnO.

Nonetheless, there was no significant alteration in the pore size distribution of the samples (**Figure 4-2d**). **Table 4-2** shows the structural properties of reference and modified ZSM-5. **Figure 4-3** show the SEM and EDS elemental mapping of ZnO/ZSM-5. As it can be seen, the Zn is uniformly distributed on the surface of ZSM-5.

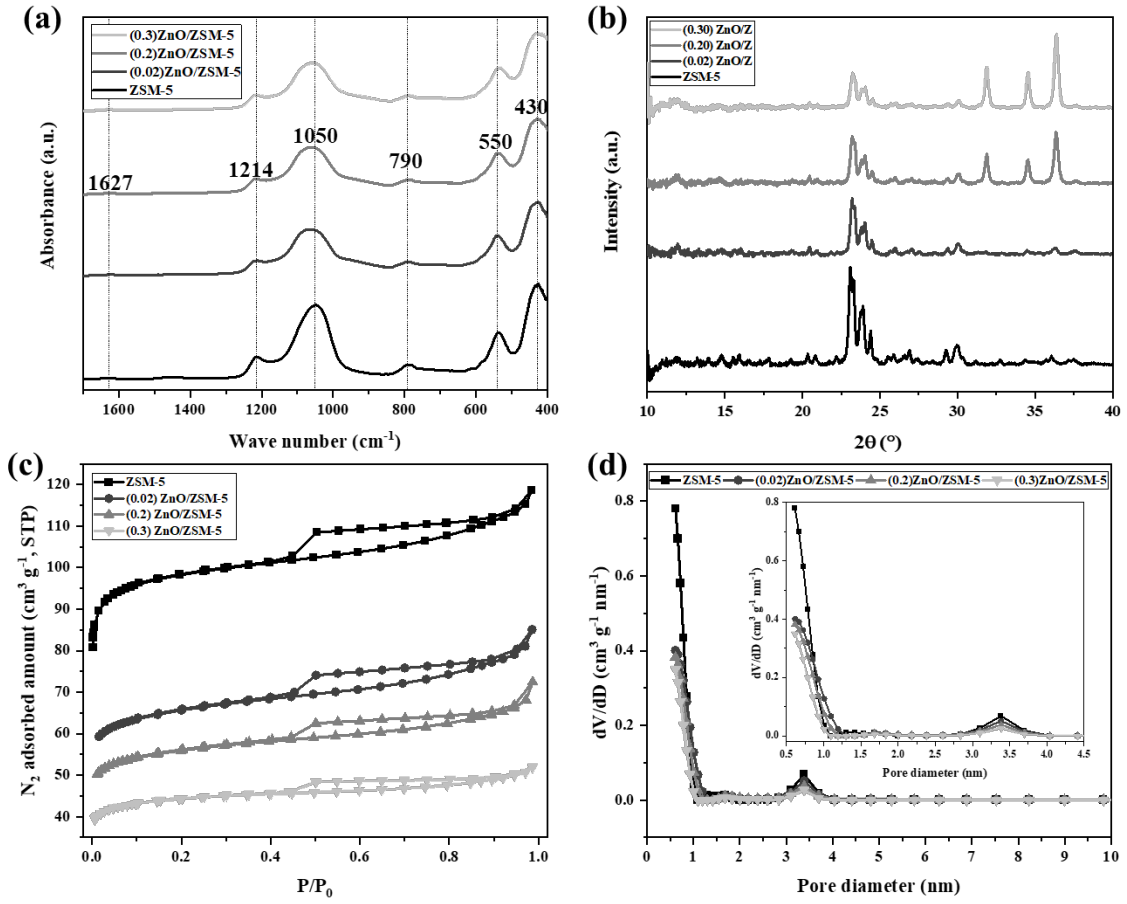

Figure 4-2(a) FTIR Spectra, (b) XRD patterns, (c) N_2 adsorption isotherms, and (d) pore size distribution of ZSM-5 before and after loading of ZnO

Table 4-2 Effect of ZnO loading on structural properties of ZSM-5

Sample	S_{BET} (m^2 g^{-1})	V_{micro} (cm^3 g^{-1})	V_{meso} (cm^3 g^{-1})	d_p (nm)
ZSM-5	304 (± 10)	0.15 (± 0.02)	0.04 (± 0.00)	2.4
(0.02)ZnO/ZSM-5	205 (± 7)	0.11 (± 0.01)	0.03 (± 0.00)	2.6

(0.2)ZnO/ZSM-5	174 (± 7)	0.09 (± 0.00)	0.02 (± 0.00)	2.6
(0.3)ZnO/ZSM-5	137 (± 8)	0.07 (± 0.00)	0.01 (± 0.00)	2.3

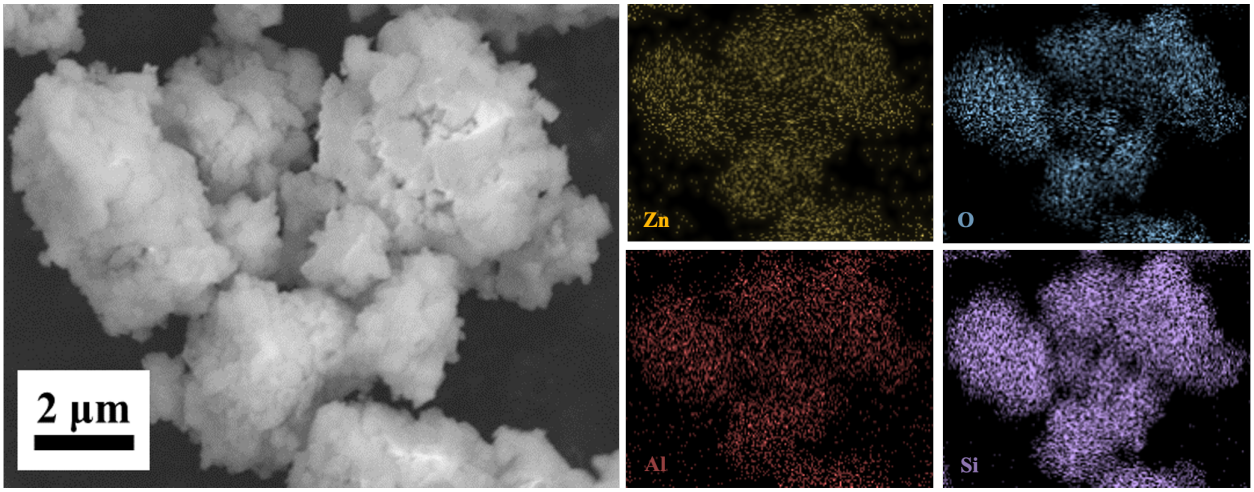

Figure 4-3 SEM and EDS elemental mapping of ZnO/ZSM-5.

4.3.2 Characterization of (Zn,Cu) Hydroxy Double Salt Intermediate

The SEM and EDS analysis (**Figure 4-4**) revealed the expected formation of highly dispersed structures on the surface of ZSM-5 after interaction with divalent copper salt. The SEM images showed the formation of 2D plate-like and needle-like crystals on the surface of ZSM-5 when exposed to $Cu(NO_3)_2$ and $CuCl_2$, respectively, consistent with the reported HDS structure in the literature [302].

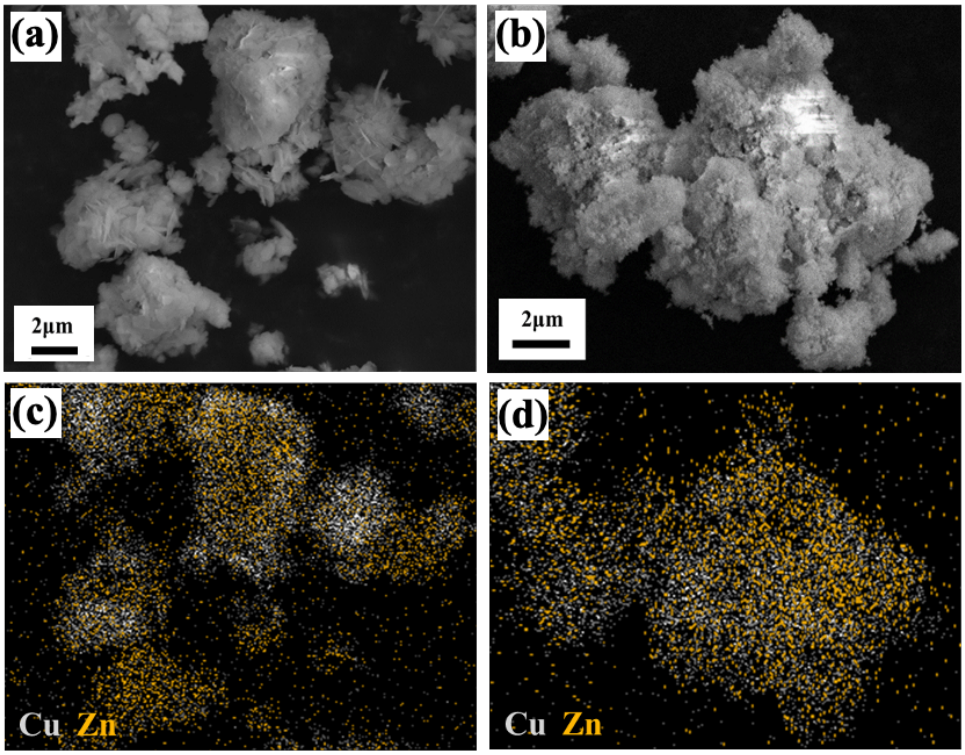

Figure 4-4 SEM images of (a) hydroxy nitrate, (b) hydroxy chloride, and EDS elemental mapping of (c) hydroxy nitrate, and (d) hydroxy chloride

Interestingly, no observable crystals were formed on the surface of ZSM-5 when copper acetate was used (**Figure 4-5**). This suggests that the anion of the copper salt plays a crucial role in determining the morphology of HDS and ultimately alters the structure of MOF-199.

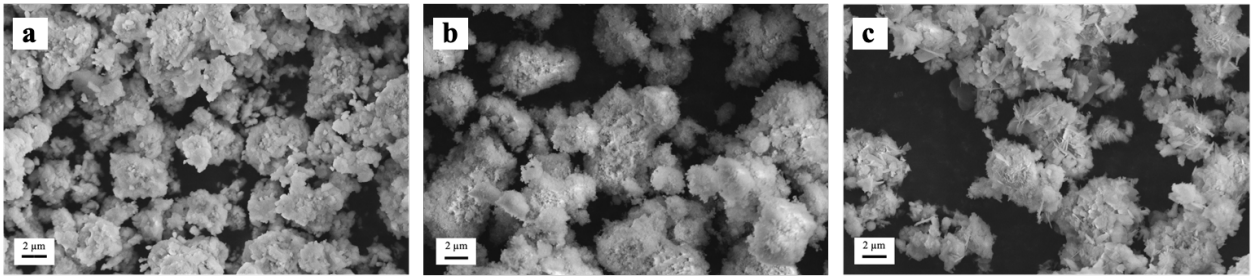

Figure 4-5 SEM images of (Zn, Cu) hydroxy (a) acetate, (b) chloride, and (c) nitrate.

The XRD analysis confirmed the formation of (Zn, Cu) hydroxy nitrate and (Zn, Cu) hydroxy chloride (**Figure 4-6a**). Additionally, the FTIR spectra showed characteristic bands at 1360 and 1420 cm^{-1} corresponding to NO_3^- and a peak at 847 cm^{-1} corresponding to Cl^-, respectively. The

O—H group modes in the range 3250-3600 cm^{-1} further confirmed the presence of hydroxy nitrate and hydroxy chloride (**Figure 4-6b**). A zoomed-in view of the O-H modes is presented in **Figure 4-7**. Notably, no characteristic HDS peaks were detected by XRD and FTIR when copper acetate was used.

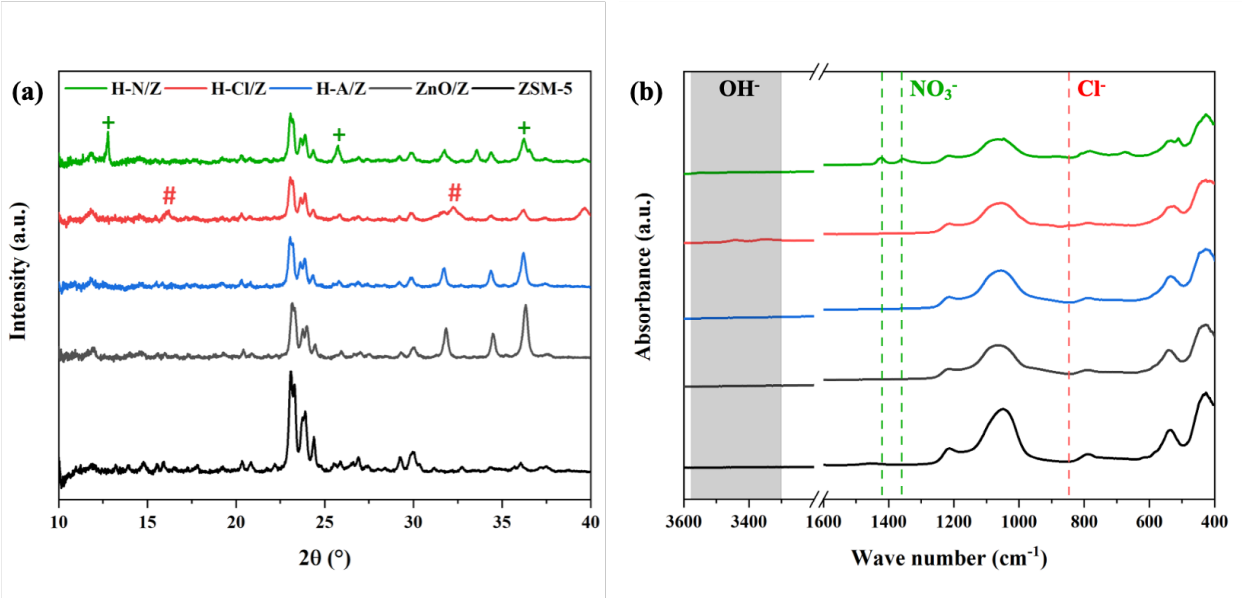

Figure 4-6 (a) XRD patterns and (b) FTIR adsorption spectra of parent and HDS-modified ZSM-5, the (+) and (#) signs show the presence of HDS crystals.

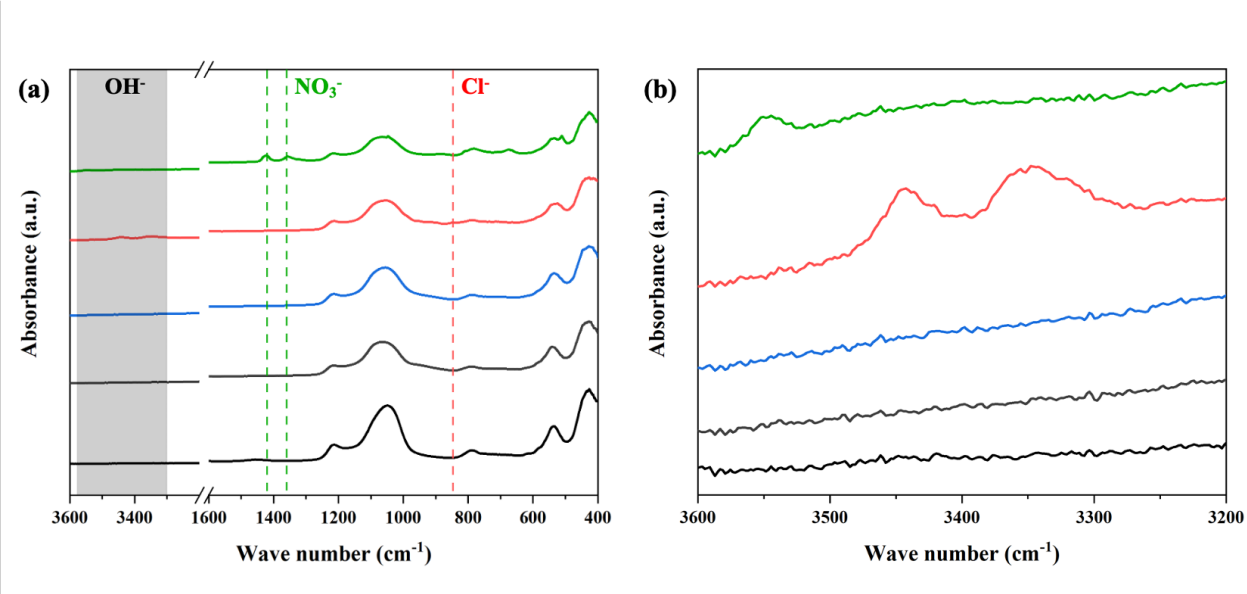

Figure 4-7 (a) full spectrum, and (b) zoomed-in view of the FTIR absorption spectra of parent and HDS-modified ZSM-5.

4.3.3 Characterization HDS assisted ZSM-5@MOF-199

4.3.3.1 Structural effects of ZnO loading and copper salt anion

The process of MOF-199 formation was confirmed by the disappearance of the HDS peaks and the appearance of corresponding XRD patterns (**Figure 4-8**) and octahedral crystals in the SEM image (**Figure 4-9**). Upon exposure to H_3BTC-containing solution, the FTIR spectrum revealed a decrease in the NO_3^-, Cl^-, and O—H group bands, while the asymmetric (1374 cm^{-1}) and symmetric (1651 cm^{-1}) stretching bands of the carboxyl group appeared. The bands at 729 and 1115 cm^{-1} indicate the out-of-plane and in-plane C-H bending vibrations. These changes in the FTIR spectrum indicate rapid anion exchange between NO_3^-, Cl^-, and OH^- with BTC^{3-}, leading to the formation of MOF-199. Additionally, the presented bands overlap with the characteristic absorption bands of parent MOF-199 synthesized via the solvothermal method.

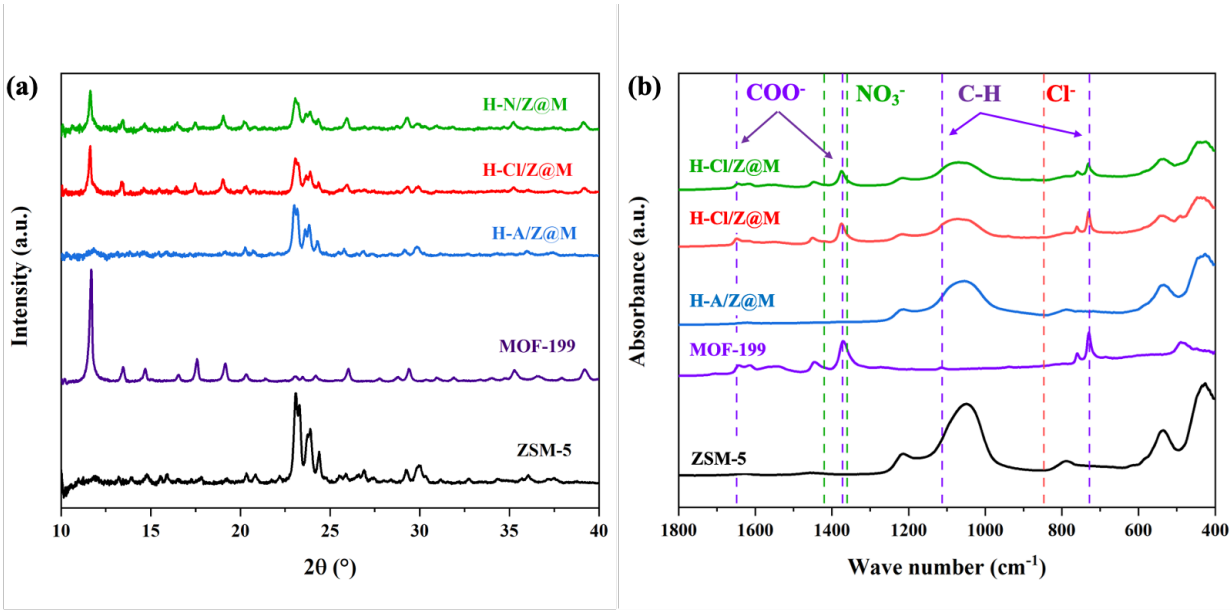

Figure 4-8(a) XRD patterns and (b) FTIR adsorption spectra of parent ZSM-5 and MOF-199, and composite adsorbent after exposure of HDS-modified ZSM-5 to H_3BTC solution.

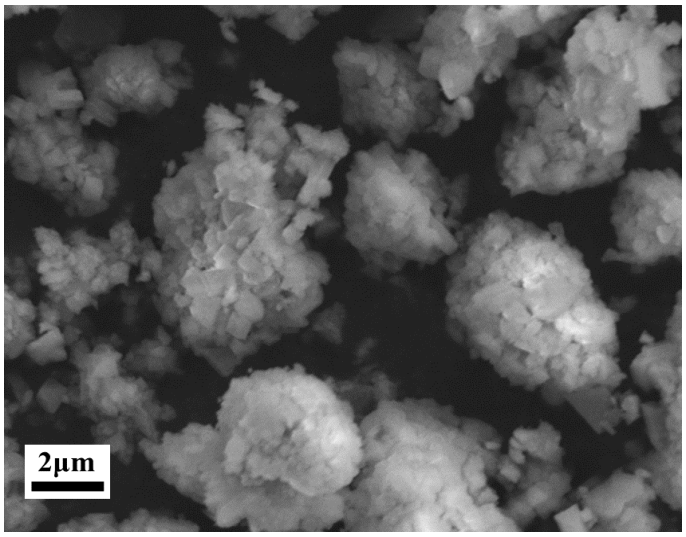

Figure 4-9 SEM image of ZSM-5@MOF-199.

The impact of ZnO loading on the formation and structural properties of the core-shell structure was investigated using XRD and N_2 adsorption isotherms (**Figure 4-10**). In the absence of ZnO, no MOF-199 shell was formed, indicating that the presence of zinc oxide is crucial to the formation of the MOF shell. When using nitrate anion, the intensity of MOF characteristic peaks increased with ZnO loading up to 20 wt%, while increasing ZnO to 30 wt% led to a decrease in the intensity

of MOF peaks. The decrease in XRD intensity can be attributed to the loss of surface area and pore blockage caused by ZnO loading and limited access to all available ZnO (**Figure 4-10**, **Table 4-3**). A comparison of **Figure 4-10b** and **Figure 4-10c** shows that the higher peak intensity of the MOF shell and therefore, the formation of a thicker layer of MOF-199 occurred when chlorine anion was used. This is due to the faster growth regime of the MOF shell when using $CuCl_2$ [282, 303, 304]. Interestingly, in case of using copper acetate, ZnO loading had no effect on the formation of the MOF shell (**Figure 4-10a**), which may be attributed to the size of the acetate anion compared to nitrate and chloride, as well as the higher stability factor of the Cu^{2+} complex with the anion [305].

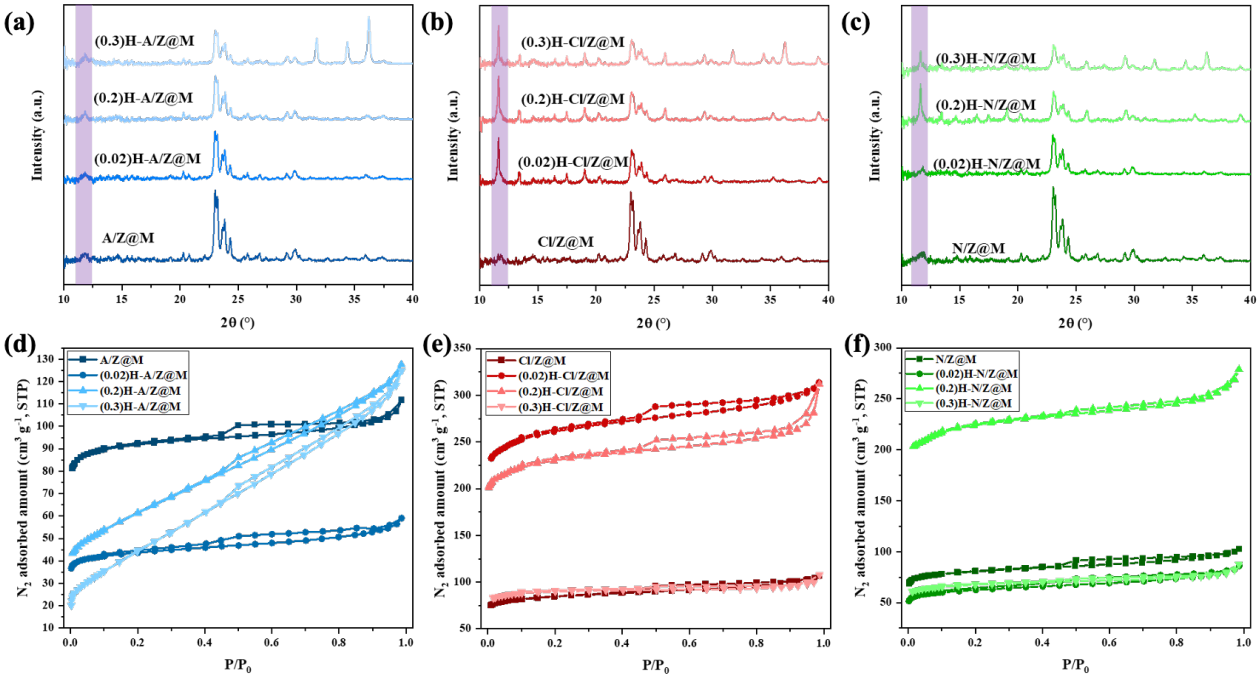

Figure 4-10 XRD patterns and N_2 adsorption isotherms of (a,d) acetate-, (b,e) chloride-, and (c,f) nitrate- HDS assisted ZSM-5@MOF-199 at different loadings of ZnO.

Table 4-3 Effect of ZnO loading on structural properties of HDS assisted ZSM-5@MOF-199

Sample	S_{BET} (m^2 g^{-1})	V_p (cm^3 g^{-1})	d_p (nm)
N/Z@M	262	0.17	2.5
(0.02)H-N/Z@M	195	0.13	2.7
(0.2) H-N/Z@M	697	0.43	2.5
(0.3) H-N/Z@M	208	0.14	2.6
A/Z@M	251	0.16	2.5
(0.02)H-A/Z@M	136	0.09	2.7
(0.2) H-A/Z@M	211	0.20	3.7
(0.3) H-A/Z@M	168	0.19	4.6
Cl/Z@M	283	0.17	2.4
(0.02)H-Cl/Z@M	813	0.49	2.4
(0.2) H-Cl/Z@M	716	0.48	2.7
(0.3) H-Cl/Z@M	354	0.22	2.4

The TGA data presented in **Figure 4-11** provides valuable insight into the thermal stability of both the parent adsorbents and the H-Cl/Z@M composite. It is observed that the composite's weight loss is intermediate to that of the parent adsorbents, indicating that the composite has higher stability compared to pure MOF-199. The initial weight loss observed up to 250 °C is attributed to the desorption of physically adsorbed water, while a higher weight loss is detected as the temperature increases, which is associated with the decomposition of MOF organic ligands.

To determine the weight percentage of MOF-199 shell in the composite, the temperature range between 300 – 900 °C is selected, where the decomposition of organic ligands occurs. The results obtained from TGA are in agreement with the MOF weight percentage calculated using Rietveld analysis of XRD patterns (**Figure 4-10b**, **Table 4-4**). However, it is important to note that when

using 20 wt% ZnO, some unreacted ZnO remains after MOF synthesis, resulting in lower surface area and pore volume of the composite compared to 2 wt% ZnO loading (**Table 4-3**). Therefore, it was decided to use the 2 wt% loading throughout the rest of this work.

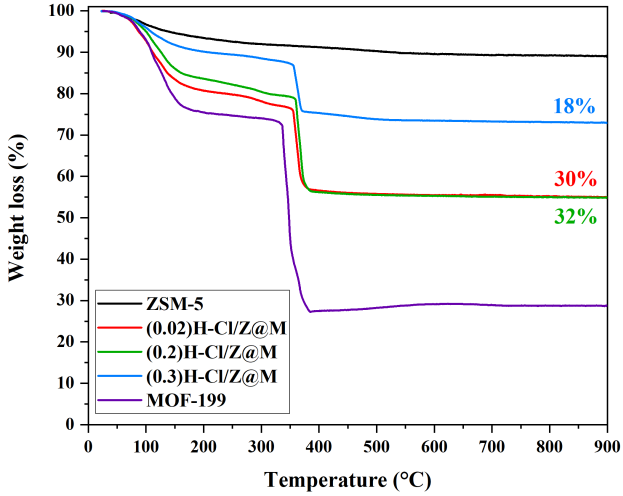

Figure 4-11 Thermogravimetric curves of parent adsorbents and (m)H-Cl/Z@M

Table 4-4 Quantification of (m)H-Cl/Z@M composite constituents using Rietveld analysis

	ZnO (wt%)	ZSM-5 (wt%)	MOF-199 (wt%)	Rwp %
(0.02)H-Cl/Z@M	0	68 (±4.2)	32 (± 2.1)	3.6
(0.2)H-Cl/Z@M	3	64 (±4.2)	33 (± 2.1)	3.7
(0.3)H-Cl/Z@M	10	73 (±4.3)	17 (± 3.1)	4.8

The structural properties of the synthesized adsorbents were characterized using N_2 adsorption isotherms, and the results are presented in **Figure 4-12** and **Table 4-5**. Parent and composites display a hybrid adsorption isotherm. A high adsorption volume followed by a plateau at low pressures that is typical of type I isotherm, followed by a type II isotherm character at higher relative pressures. This is associated with formation pores in the range of mesopores and small macropores [306]. A large hysteresis with gradual decrease in desorption up to low pressure ranges is observed for composites, which shows higher mesopore volumes with non-uniform pore

restrictions [307]. The highest N_2 uptake was observed for H-Cl/Z@M, which can be attributed to the high surface area and the formation of mesopores in the zeolite-MOF interface that enhanced the accessibility of zeolite micropores (**Figure 4-12b**, **Table 4-5**). The lower N_2 uptake of H-N/Z@M compared to MOF-199 and H-Cl/Z@M can be attributed to the slower growth of the MOF shell on the zeolite surface, which resulted in lower surface area for the composite adsorbent. Additionally, the use of copper acetate prevented the formation of the MOF shell and led to blockage of zeolite micropores (**Table 4-5**). These findings demonstrate the importance of careful selection of metal sources for the synthesis of zeolite-MOF composites to achieve optimal structural properties for desired applications.

Moving forward, our focus will be solely on (0.02)H-Cl/Z@M composite adsorbent synthesized through (Zn,Cu) hydroxy chloride intermediate. This composite was chosen because of its rapid MOF shell growth, superior surface area, and pore volume offered by using (Zn,Cu) hydroxy chloride.

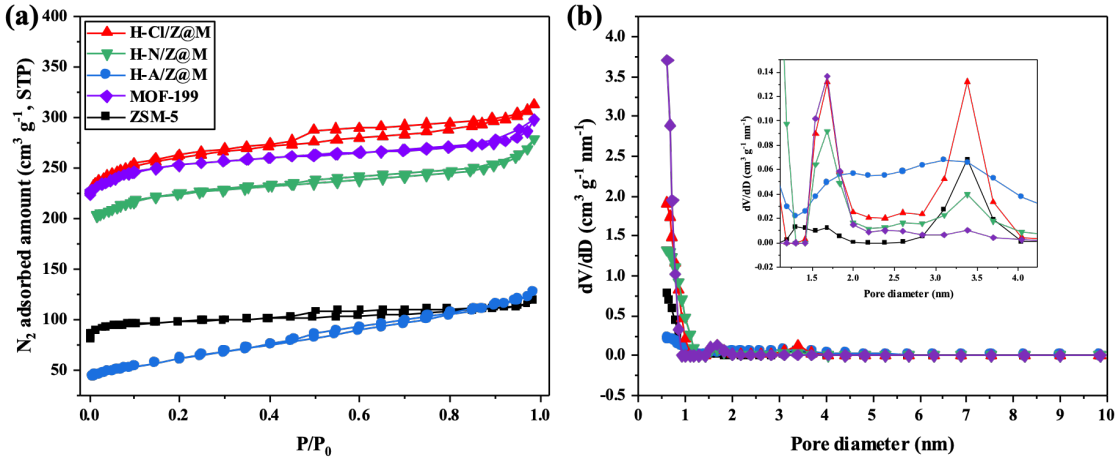

Figure 4-12(a) N_2 adsorption isotherms and (b) pore size distribution of parent and composite adsorbents.

Table 4-5 Structural properties of parent and composite adsorbents

Sample	S_{BET} (m^2 g^{-1})	V_{micro} (cm^3 g^{-1})	V_{meso} (cm^3 g^{-1})	d_p (nm)
ZSM-5	304 (± 10)	0.15 (± 0.02)	0.04 (± 0.00)	2.4
MOF-199	766 (± 16)	0.50 (± 0.03)	0.00 (± 0.00)	2.4
(0.2) H-A/Z@M	211(± 6)	0.07 (± 0.00)	0.13 (± 0.01)	3.7
(0.2) H-N/Z@M	697(± 18)	0.38 (± 0.02)	0.05 (± 0.01)	2.5
(0.02) H-Cl/Z@M	813 (± 22)	0.40 (± 0.01)	0.09 (± 0.01)	2.4

4.3.3.2 Solvent effect on structural properties of the ZSM-5@MOF-199 composite

Solvent properties such as polarity, acidity, basicity, and coordinating ability can influence the coordination of metal ions and organic ligands, resulting in different MOF crystalline structures and morphologies. Moreover, the choice of solvent is known to have a significant impact on the synthesis of MOFs, as it affects various aspects of the crystallization process such as nucleation kinetics, lattice parameters, and desolvation process leading to changes in surface area, pore size distribution, and gas adsorption properties [282, 308-313]. Therefore, careful consideration of solvent choice is crucial for the successful synthesis of MOFs with desired properties for various applications. For preparation of H-Cl/Z@M, two H_3BTC containing solvents were used: pure ethanol and an acetonitrile–ethanol mixture (MeCN:EtOH 1:3 by volume). By comparing the effect of these solvents on the structural properties of the H-Cl/Z@M, we can gain insight into their influence. Previous reports show the presence of MeCN can lead to secondary morphology formation in MOF-199, attributed to pH-dependent protonation state of BTC molecule during growth. Moreover, HDS is known to be sensitive to pH since it contains hydroxide ions [282, 310]. The presence of acetonitrile led to development higher volume of micropores, and higher surface area compared to when MeCN was absent (**Figure 4-13**, **Table 4-6**). The observed improvement

can be attributed to the stabilizing effect of the polar aprotic solvent, MeCN, which interacts favorably with the key components of the MOF-199, including Cu ions and ligand molecules [282, 308]. MeCN exhibits a stronger coordination tendency towards Cu(II) ions and forms a hydrogen-bonded solvate structure with the BTC ligand [282, 308]. This stronger interaction between the MeCN and the MOF-199 components promotes a stable and controlled growth environment, resulting in improved MOF formation compared to pure ethanol [282, 308]. Furthermore, previous studies have shown that an increase in the solution acidity can inhibit the growth of MOF-199 [282]. In this case, the higher acidity of pure ethanol compared to the solvent mixture resulted in the formation of MOF-199 layer with lower surface area and pore volume. Therefore, the solvent choice, specifically the presence of acetonitrile, has a significant impact on the structural properties of H-Cl/Z@M, influencing the volume of micropores, surface area, and overall performance of the composite material.

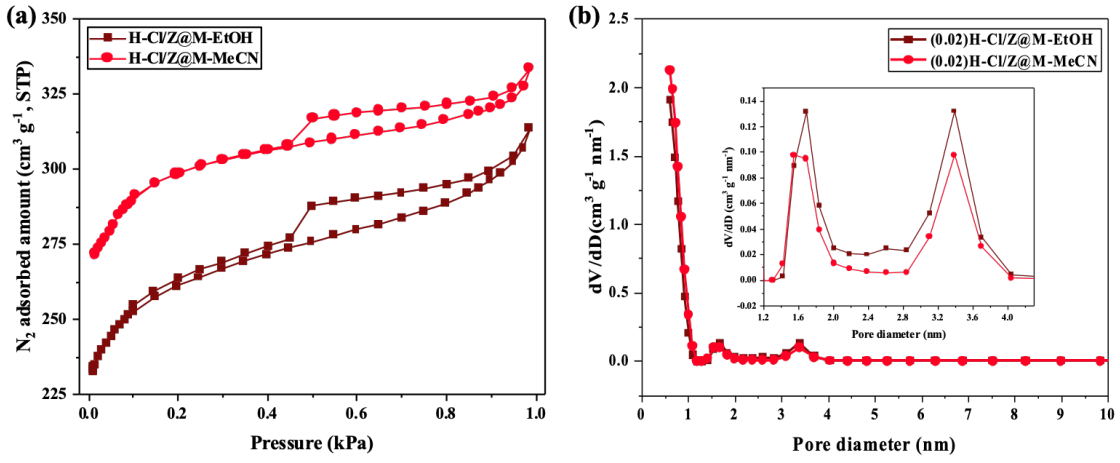

Figure 4-13 (a) N_2 adsorption isotherms and (b) pore size distributions of H-Cl/Z@M made with pure EtOH and EtOH:MeCN 1:3 solvents.

Table 4-6 Effect of solvent on the structural properties of H-Cl/Z@M

Sample	S_{BET} ($m^2\ g^{-1}$)	V_{micro} ($cm^3\ g^{-1}$)	V_{meso} ($cm^3\ g^{-1}$)	Average pore size (nm)
H-Cl/Z@M-EtOH	813 (± 22)	0.40 (± 0.01)	0.09 (± 0.01)	2.4
H-Cl/Z@M-MeCN	925 (± 31)	0.47 (± 0.04)	0.05(± 0.01)	2.2

4.3.3.3 Modulating structural properties of ZSM-5@MOF-199 composite through core and shell modification

Tuning the metal oxidation state of MOFs affects their structure, energetic stability, and overall performance [314, 315]. Here, the ratio Cu(I)/Cu(II) in H-Cl/Z@M was controlled by varying the concentration of the reducing agent. N_2 adsorption isotherms were used to assess the structural impacts of reduction. Increasing the concentration of the reducing agent caused progressive structural degradation, ultimately resulting in the collapse of MOF-199 framework (**Figure 4-14ab**). This degradation was evident from the disappearance of the hysteresis loop and a reduction in pore volume, as indicated by DFT pore size distribution (**Figure 4-14b, Table 4-7**). In MOF-199, Cu atoms are coordinated with 4 O atoms from the trimesic acid. The reducing agent breaks the Cu—O bond creating more uncoordinated Cu(I) sites to interact with CO. However, further increase of the $Na_2S_2O_3$ leads to extensive breaking of the Cu—O bond, resulting in structural degradation from a three-dimensional to a two-dimensional structure. This is done through degradation in long-range order and breakdown in the open framework topology of the MOF meaning the loss of surface area and pore volume which will be counterproductive in selective separation of CO [290, 294]. The XRD pattern depicted in **Figure 4-14c** illustrates that (0.1)R-H-Cl/Z@M retained its structure indicating minimal degradation of MOF structure following the copper reduction while pronounced degradation of MOF structure occurred for

(0.2)R-H-Cl/Z@M. Moreover, the presence of the peak at 31.9 ° for both reduced samples show the coordination of oxygen with Cu(I) upon reduction of Cu(II) [188, 294].

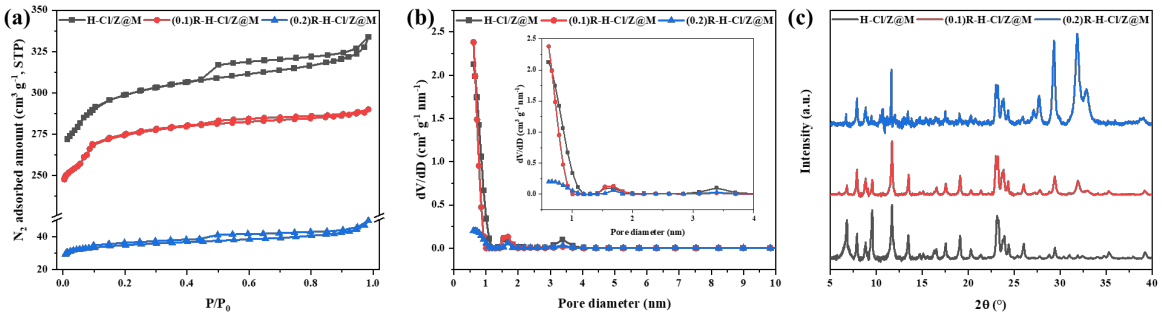

Figure 4-14 (a) N_2 adsorption isotherms, (b) pore size distribution, and (c) XRD patterns intact and mixed-valence composite adsorbents.

Table 4-7 Structural properties of intact and reduced H-Cl/Z@M

Sample	S_{BET} (m^2 g^{-1})	V_{micro} (cm^3 g^{-1})	V_{meso} (cm^3 g^{-1})	Average pore size (nm)
H-Cl/Z@M	925 (± 31)	0.47 (± 0.04)	0.05(± 0.01)	2.2
(0.1)R-H-Cl/Z@M	848 (± 26)	0.44 (± 0.03)	0.01(± 0.01)	2.1
(0.2)R-H-Cl/Z@M	109 (± 5)	0.06 (±0.00)	0.02 (±0.00)	2.8

The oxidation state of copper was examined through the XPS analysis (**Figure 4-15**). The binding energy was corrected using C 1s peak at 284.6 eV as a reference. In the Cu $2p_{3/2}$ region, four peaks were observed. The peak at 932.9 and 930.7 eV correspond to Cu(II) and Cu(I), indicating the presence of both oxidation states of copper in the reduced composites as well as the intact composite. The increase of reducing agent concentration was accompanied by a decrease in intensity of the Cu(II) peaks compared to the intact sample [316]. The presence of two peaks in the spectrum ranging from 938-946 eV indicate shake-up features associated with Cu(II) oxidation state. These features arise when Cu electronic configuration is unsaturated (d^9), thus allowing p →

d hybridization. Conversely, such feature are absent in the Cu(I) oxidation state, where the electronic configuration is saturated (d^{10}) [290, 294]. The presence of Cu(I) species in the intact composite is attributed to the autoreduction under vacuum at 100 °C [286]. The Cu(I) and Cu(II) ratios were calculated by fitting Cu $2p_{3/2}$ peaks and Cu(II) associated shake-up features.

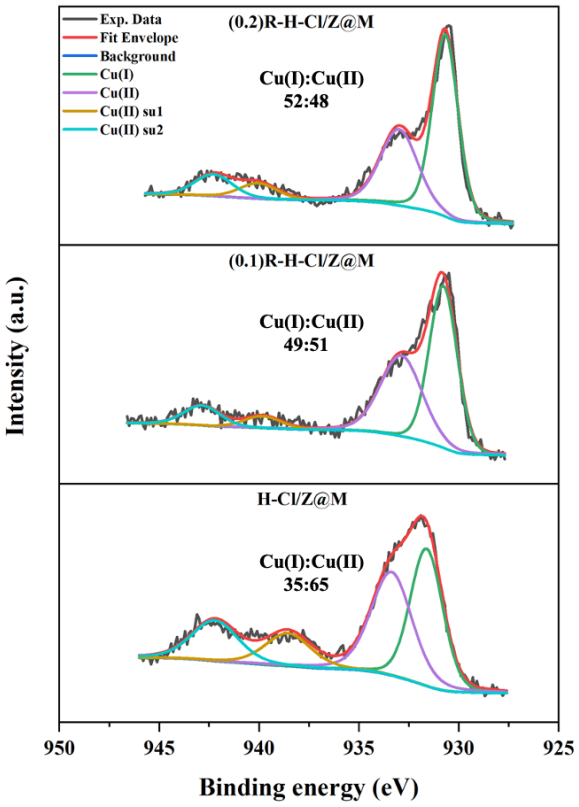

Figure 4-15 Cu $2p_{3/2}$ XPS spectrums of intact and mixed-valence composite adsorbents.

Successful synthesis of hierarchical HZSM-5 was confirmed using FTIR and XRD analysis (**Figure 4-16**). The FTIR spectrum of HZSM-5 exhibited a reduction in the relative intensity of bands at 430 and 550 cm^{-1}, which corresponds to the five-membered ring pentasil unit of ZSM-5, compared to parent ZSM-5. This decrease is attributed to the desilication process. However, as confirmed by the XRD analysis, the crystallinity of HZSM-5 was preserved. Additionally, a red

shift in the external asymmetric stretching of Si—O—Si bridge band from 1050 to 1065 cm^{-1} indicated ion-exchange process following the modification with NH_4Cl, where H^+ and Na^+ cations in the desilicated ZSM-5 framework were replaced by NH_4^+ ions [317]. The absence of the band at 1450 cm^{-1} for HZSM-5 shows the loss of extraframework cationic aluminum species (i.e., lewis acid sites) upon desilication and NH_4^+ ion-exchange reaction of ZSM-5 [291, 318, 319]. HZSM-5 exhibited a type IV adsorption isotherm, indicating the formation of uniform mesopores with an open geometry within a narrow range of pore sizes. This confirmed that the desilication process resulted in formation of mesopores and an increase in the BET surface area of HZSM-5 compared to ZSM-5 (**Figure 4-17, Table 4-8**). The composite adsorbent with HZSM-5 core displayed a type IV adsorption isotherm, indicating a pore geometry with a wide range of pore entrance sizes [55, 306].

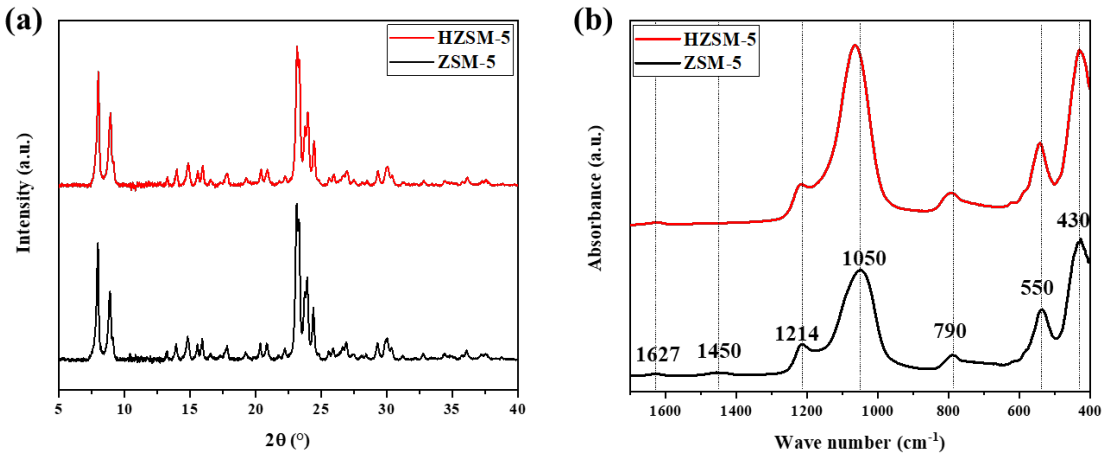

Figure 4-16 (a) XRD, and (b) FTIR spectra of ZSM-5 and hierarchical HZSM-5.

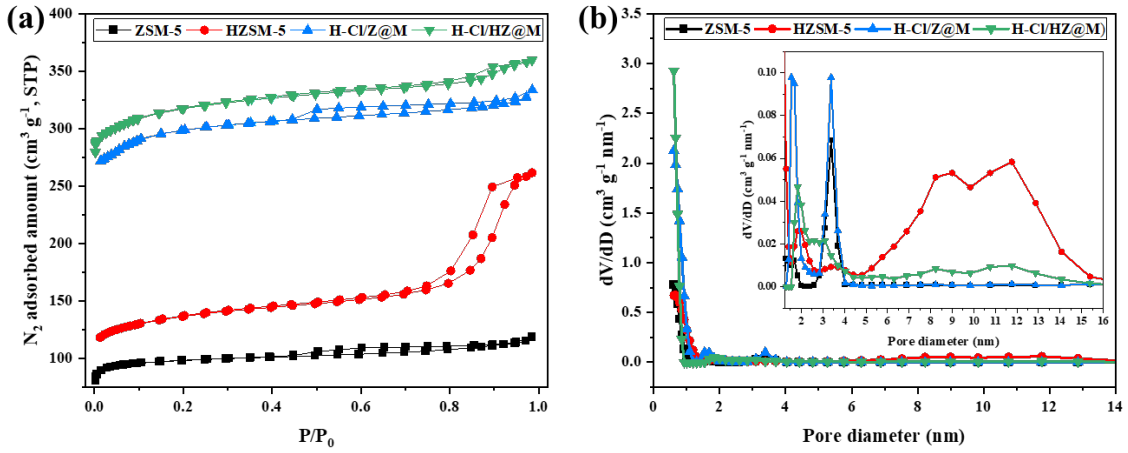

Figure 4-17 (a) N_2 adsorption isotherms, and (b) pore size distributions of ZSM-5, HZSM-5 and their corresponding core-shell structure.

Table 4-8 Structural properties of hierarchical HZSM-5 and the corresponding core-shell structure

Sample	S_{BET} (m^2 g^{-1})	V_{micro} (cm^3 g^{-1})	V_{meso} (cm^3 g^{-1})	Average pore size (nm)
HZSM-5	431 (± 11)	0.16 (± 0.01)	0.24 (± 0.02)	3.8
H-Cl/HZ@M	985 (± 25)	0.43 (± 0.02)	0.13 (± 0.01)	2.3

4.3.4 Single-component adsorption isotherms

Figure 4-18 illustrates the CO and CO_2 adsorption isotherms at 293 K. In general, composites show higher adsorption capacity compared to the parent adsorbents, except for the case where copper acetate was used as the copper source for formation of MOF-199. As mentioned earlier, high stability factor of Cu^{2+} with acetate anion prevents MOF shell formation, leading to pore blockage, loss of surface area, and a decrease in CO and CO_2 adsorption capacity. While the CO adsorption capacity at low pressures is comparable for all adsorbents, ZSM-5 exhibits a higher CO_2 adsorption capacity in the low-pressure range. This is due to strong electrostatic attraction of CO_2 molecules to NH_4^+ ions in the ZSM-5 framework, as well as the presence of strong Lewis

acid sites (aluminum extraframework cationic species) that act as electron acceptors, attracting electron-rich oxygen atoms of CO_2 [320]. These factors contribute to the higher affinity of composite adsorbents towards CO_2 at low pressures compared to MOF-199. Overall, the analysis results indicate 28 and 30% increase of CO and CO_2 adsorption capacity, respectively, for H-Cl/Z@M. These improvements are due to the structural advantages of H-Cl/Z@M over other composites and parent adsorbents (**Table 4-5** and **Figure 4-12**).

Figure 4-18c shows the equilibrium adsorption isotherm-estimated CO_2/CO selectivity for parent and composite adsorbents in an equimolar CO/CO_2 composition as a function of total bulk pressure. For the parents and the composite adsorbents, a decrease in selectivity is observed at lower pressures, followed by an increase as the pressure increases. This behavior can be explained by the smaller kinetic diameter, higher polarizability, and quadrupole moment of the CO_2 molecules compared to CO (**Table 4-1**) [321, 322]. CO_2 experiences stronger attractive forces to the surface of the adsorbents, leading to higher adsorption capacities, as shown in **Figure 4-18ab**. As the pressure increases, the active sites for CO_2 adsorption become limited, while the higher collision frequency of gas molecules with the adsorbent surface increases the likelihood of CO interactions with active sites. Furthermore, unlike CO_2, CO has non-zero dipole moment that can lead to dipole-dipole interactions with the adsorbent surface. These interactions become more noticeable with increasing of pressure, leading to a decrease in the CO_2/CO selectivity. The subsequent increase in the selectivity with the pressure is attributed to the strong interaction of CO_2 with adsorbent surface, driven by its large quadrupole moment [321-323]. This is further confirmed by the integral entropy of CO_2 adsorption which shows the change in structural arrangement of CO_2 to accommodate the increasing number of adsorbed molecules (**Figure 4-22**). The high affinity of the composite adsorbent towards CO_2 makes it a promising candidate for

production of high-purity CO from syngas which can be further utilized in production of a variety of chemicals [269, 273].

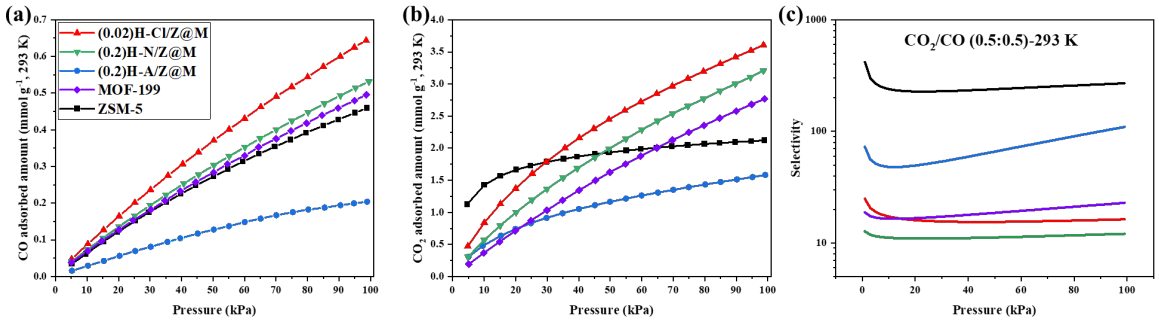

Figure 4-18(a) CO, (b) CO_2 adsorption isotherms, and (c) CO_2/CO selectivity of ZSM-5, MOF-199, and the corresponding composites at 293 K.

While upon reduction, the composite went through structural degradation (**Table 4-7**), the CO adsorption capacity significantly increased compared to the intact composite (**Figure 4-19a**). The enhanced CO adsorption capacity is due to presence of Cu(I) species within the MOF structure. Cu(I) is capable of forming the strong π-complexation bond with CO, leading to a higher CO adsorption [273]. The lower CO_2 uptake of the reduced composite at pressures below 60 kPa (**Figure 4-19b**), can be attributed to the loss of surface area and micropores during the reduction process. However, in the pressure range of 60 to 100 kPa, the comparable CO_2 uptake can be explained by the presence of the strong basic phase (i.e., Cu_2O) in the structure of mixed-valence MOF-199 [258, 286, 290] and the slightly acidic nature of CO_2 [258, 273]. The estimated CO_2/CO selectivity of the mixed-valence composite greatly decreased compared to intact composite (**Figure 4-19c**). This suggests that CO has stronger interaction with the reduced composite, resulting in a lower preference for CO_2 compared to CO (**Figure 4-21**).

The CO and CO_2 adsorption isotherms of hierarchical HZSM-5 exhibit higher adsorption capacities compared to ZSM-5 (**Figure 4-20**). This enhance performance is primarily due to presence of mesopores, and a larger surface area in hierarchical HZSM-5. However, the structural

modification of ZSM-5 led to the loss of certain active sites responsible for interacting with CO_2. This is evident from the higher adsorption capacity of ZSM-5 at lower pressure ranges when compared to HZSM-5. This can be explained by the loss of the Lewis and Brønsted acid sites, meaning the extraframework and framework cationic species, respectively [318], during the desilication and post NH_4^+ ion-exchange reaction calcination (**Figure 4-16**) [291, 319, 324]. The composite with hierarchical HZSM-5 core, showed a performance in adsorption of CO_2 and CO similar to that of HZSM-5 (**Figure 4-19ab**). The lower CO_2/CO selectivity of H-Cl/HZ@M compared to intact composite (**Figure 4-19c**) can be attributed to the stronger interaction between H-Cl/HZ@M and CO compared to H-Cl/Z@M, as indicated by the calculated isosteric heat of adsorption (**Figure 4-21**). This highlights the significance of materials selection and modification in composite materials for optimal performance gas adsorption applications.

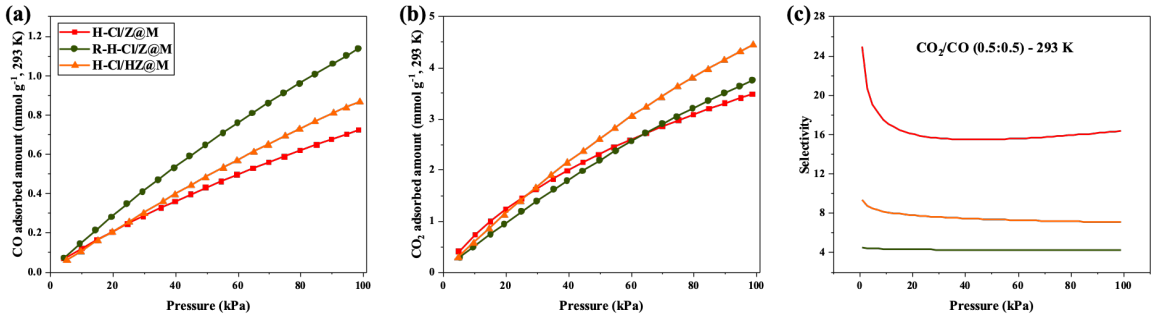

Figure 4-19 (a) CO, and (b) CO_2 adsorption isotherms, and (c) CO_2/CO selectivity of intact and structurally modulated composites at 293 K.

To estimate the isosteric heat of adsorption of CO and CO_2 on the parent, composite, and modulated composite adsorbents, single-component isotherms were measured at 293, 313, and 333 K (**Figure 4-17**). In general, these isotherms were fitted with LF and DSLF models, considering the energetic heterogeneity of adsorbent surfaces arising from the presence of different types and densities of adsorption sites for CO and CO_2. DSLF was considered for the composites since there are two different materials in the composite structure that have two distinct adsorption sites and

LF was considered for the parent adsorbents. The calculated values of isotherm fitting parameters along with their corresponding correlation coefficients (R^2), are summarized in **Table 4-9** and **Table 4-10**.

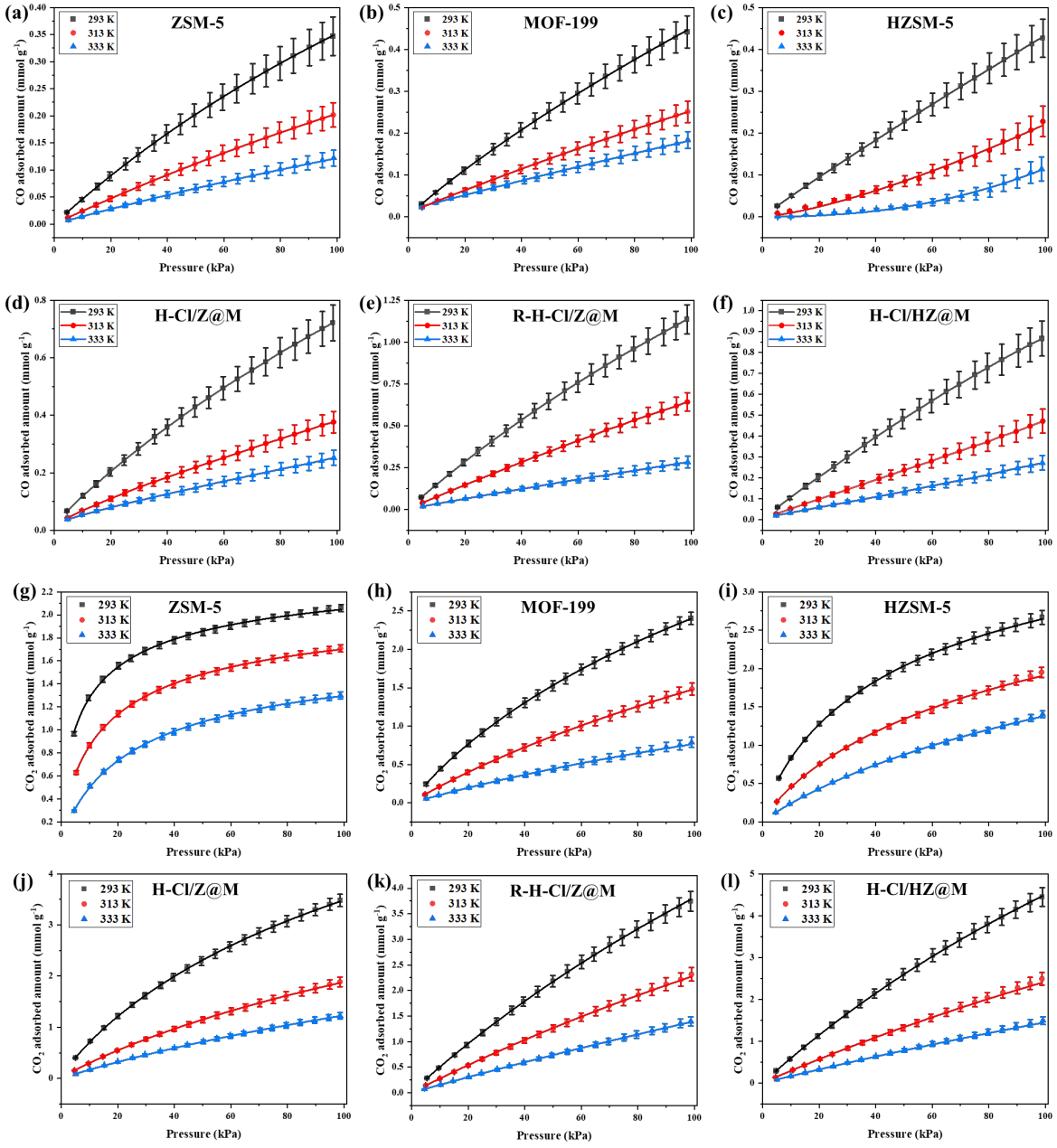

Figure 4-20 (a-f) CO and (g-l) CO_2 adsorption isotherms of parent, intact, and modulated composite adsorbents at 293, 313, and 333 K.

Table 4-9 LF isotherm parameters determined by non-linear regression.

Samples		CO				CO_2			
	T	k_S	n_S	qm	R^2	k_S	n_S	qm	R^2
ZSM-5	293	0.00362	1.00114	1.31829	0.99999	0.25000	0.59790	2.23779	0.99920
	313	0.00216	1.00403	1.13105	0.99993	0.12229	0.71388	2.02275	0.99971
	333	0.00145	0.99345	0.99849	0.99996	0.05765	0.81977	1.81624	0.99986
HZSM-5	293	0.00101	0.99446	4.19346	0.99989	0.03546	0.77816	4.75376	0.99988
	313	0.00003	1.39467	14.09240	0.99535	0.01459	0.76237	5.93146	0.99961
	333	0.00000	2.34886	6.88192	0.99159	0.00625	0.85583	5.75068	0.99982
MOF-199	293	0.00273	0.96063	1.93386	0.99996	0.00763	0.87390	6.74654	0.99997
	313	0.00050	0.87794	7.87736	0.99960	0.00333	0.90871	6.90813	0.99996
	333	0.00047	0.79907	9.86546	0.99688	0.00204	0.94879	5.69910	0.99994
H-Cl/Z@M	293	0.00232	0.83076	6.06884	0.99993	0.01093	0.84949	8.25103	0.99998
	313	0.00065	0.78036	14.82828	0.99916	0.00465	0.88122	8.95734	0.99994
	333	0.00067	0.72942	13.09736	0.99696	0.00332	0.95177	5.88088	0.99997
H-Cl/HZ@M	293	0.00233	1.00111	4.01911	0.99995	0.00394	1.02400	14.67838	0.99999
	313	0.00026	0.99582	17.86887	0.99953	0.00070	0.95438	47.00770	0.99996
	333	0.00021	0.98575	14.11124	0.99825	0.00057	0.98387	30.09572	0.99998
R-H-Cl/Z@M	293	0.00285	0.97119	4.10768	0.999997	0.00366	1.01639	13.38107	0.99996
	313	0.00126	0.98020	4.51074	0.99997	0.00146	0.96995	20.65860	0.99995
	333	0.00064	0.95879	5.64200	0.99994	0.00047	0.97784	35.05672	0.99997

Table 4-10 DSLF isotherm parameters determined by non-linear regression

gas	Samples	T	k_1	k_2	n_1	n_2	qm_1	qm_2	R^2
CO	ZSM-5	293	0.92268	0.00357	0.61793	1.00981	0.00110	1.28804	0.99999
		313	0.03545	0.00224	0.00192	1.00415	0.00026	1.09332	0.99992
		333	0.03244	0.00158	0.00071	0.98514	0.00018	0.95420	0.99989
	HZSM-5	293	0.07466	0.00125	1.52097	1.20208	0.01958	1.47334	0.99993
		313	0.03017	0.00006	0.02791	0.88639	0.00574	49.33344	0.92459
		333	0.01636	0.00013	0.05476	0.84422	0.00390	12.53293	0.73907
	MOF-199	293	0.02517	0.00283	0.27165	0.96088	0.00014	1.87107	0.99995
		313	0.66064	0.00220	0.14432	0.90987	0.00001	1.70683	0.99878
		333	0.00755	0.00686	0.86841	0.89985	0.36127	0.22205	0.98740
	H-Cl/Z@M	293	0.66357	0.00481	0.30693	0.91018	0.00099	2.38727	0.99955

		313	0.00937	0.00052	0.89743	0.35277	0.87862	0.00015	0.98815
		333	2.09589	0.00096	0.47934	0.70758	0.00303	9.93656	0.99582
	H-Cl/HZ@M	293	0.00370	0.00324	1.01179	1.09860	0.65176	1.67632	0.99924
		313	0.00652	0.00665	0.91798	0.92408	0.61280	0.66119	0.96245
		333	0.19922	0.00077	0.14658	1.00788	0.00209	3.63735	0.99773
	R-H-Cl/Z@M	293	0.00763	0.00456	0.59995	1.01257	0.00000	2.45280	0.99824
		313	0.00508	0.00348	0.92437	0.96664	0.01559	1.91841	0.99470
		333	0.83207	0.00074	0.43503	0.95926	0.00053	4.92628	0.99992
CO_2	ZSM-5	293	0.47628	0.24606	1.06688	0.59725	0.02135	2.22049	0.99921
		313	0.28379	0.12232	0.88047	0.71371	0.00054	2.02226	0.99971
		333	0.10301	0.05777	0.98613	0.78667	0.05659	1.82944	0.99977
	HZSM-5	293	0.15537	0.03546	0.42009	0.77817	0.00000	4.75371	0.99988
		313	0.04091	0.01583	0.55080	0.77116	0.00008	5.44527	0.99949
		333	0.00005	0.00625	0.00003	0.85584	0.00000	5.75062	0.99982
	MOF-199	293	0.09644	0.00762	0.72483	0.87466	0.00156	6.73029	0.99997
		313	0.02687	0.00338	0.16191	0.90969	0.00001	6.79708	0.99996
		333	0.00015	0.00204	0.00095	0.94878	0.00000	5.69988	0.99994
	H-Cl/Z@M	293	0.01108	0.01093	0.01165	0.84948	0.00062	8.25140	0.99998
		313	0.12594	0.00467	1.03270	0.88052	0.00028	8.95182	0.99994
		333	0.46990	0.00333	0.00835	0.95193	0.00016	5.86885	0.99997
	H-Cl/HZ@M	293	0.24751	0.00373	1.38444	1.05890	0.04113	13.52284	0.99999
		313	0.01562	0.00136	0.03450	0.99205	0.12396	21.49709	0.99991
		333	0.17059	0.00128	0.01488	1.02782	0.00016	11.78624	0.99988
	R-H-Cl/Z@M	293	0.20349	0.00250	0.94149	1.19798	0.22930	9.28179	0.99999
		313	0.00693	0.00695	0.96969	0.97510	2.78811	2.84429	0.97944
		333	0.87608	0.00072	0.31552	0.99196	0.00002	21.69530	0.99995

The calculated values of Q_{st} as a function of adsorbate loading for CO and CO_2 are plotted in **Figure 4-21**. The Q_{st} values for both CO and CO_2 on the intact composite (i.e., H-Cl/Z@M), fall within the range of Q_{st} values observed for parent adsorbents. This indicates that the adsorption behavior of CO and CO_2 on the intact composite is comparable to that of the individual parent adsorbents. Notably, the higher values of Q_{st} for CO_2 at zero coverage on parents and intact composite adsorbents signify a stronger interaction of CO_2 with the surface of these adsorbents, relative to CO. It should be noted that the obtained values of the Q_{st} for CO and CO_2 are comparable to previously reported values for MOF-199 (15—30 and 25—36 kJ/mol, respectively) [325-329] and ZSM-5 (27—52, and 30—85 kJ/mol, respectively) [134, 330-335]. The increasing values of the Q_{st} for MOF-199 and H-Cl/Z@M show that the lateral interactions of CO molecules are stronger than adsorbate-adsorbent interactions. More specifically, for the degassed adsorbents, the first CO molecules gets adsorbed into the micropores with narrowest accessible width with no or negligible adsorbate-adsorbate interactions contributing to the overall Q_{st}. Upon the completion of pore filling, there is a sharp increase in the values of Q_{st} which shows the adsorbate-adsorbate interactions. The broadness of the sharp increase depends on the amount and type of porosity present in the adsorbent [336]. The larger number of micropores in an adsorbent means more potential adsorption sites and therefore, a broader increase in the adsorbate-adsorbate contributed Q_{st} [336]. This is consistent with the pore size distribution of the MOF-199 and H-Cl/Z@M (**Figure 4-12**). The greater number of micropores in MOF-199 led to broader increase of Q_{st} compared to the intact composite.

In the case of HZSM-5, the value of Q_{st} for CO sharply decreases. This can be attributed to the different interaction sites available for CO adsorption on HZSM-5 including the cationic centers (i.e., Brønsted acidic sites (H^+) and Lewis acid sites (Al^{3+}, AlO^+, or Al-oxide)), the two present

OH groups (i.e., bridging Si(OH)Al, and terminal silanol groups), and the HZSM-5 framework (i.e., physisorption in the pores). Among these sites, the CO interaction with the terminal silanol group and the framework is comparatively weaker [337, 338]. Therefore, the sharp decrease of Q_{st} from the initially high value is the result of the varying energies associated with these different interaction sites. This behavior indicates the presence of significant energetic heterogeneity on the surface of HZSM-5 for CO interaction, which arises from ZSM-5 modification through desilication and ion-exchange reaction. Moreover, the calculated value of Q_{st} agrees well with the previously reported value (33.4 kJ/mol) [337].

It should be noted that the number of cationic adsorption sites in HZSM-5 is highly dependent on the calcination (i.e., dehydration) step of the synthesis process [339]. These same cationic centers that interact with CO are also responsible for CO_2 adsorption [330]. Unlike CO, the adsorption of CO_2 is not influenced by the electric field created by the surface cation charges due to its non-polarity. Instead, the strong interaction of CO_2 with the electric field gradient (quadrupole—adsorbent interaction) is driven by its high quadrupole moment compared to CO [340, 341]. However, in HZSM-5, this quadrupole—cation interaction is weak due to the very short distance (<1 Å) between the framework O atoms and the extra-framework H^+ cations in AlO^{-4} tetrahedrons [340, 342]. Additionally, smaller quadrupole—field gradient interaction values have been reported for CO_2 compared to CO over exposed aluminum sites [343]. This was attributed to the end-on approach of CO_2 to the surface site and its larger size of compared to CO leading to smaller field gradient [343].Therefore, HZSM-5 shows a minor effect of electric field gradient on the adsorption of gases with high quadrupole moment and polarizability, such as CO_2.

The higher CO interaction energy observed for the modulated composite adsorbent with HZSM-5 core (i.e., H-Cl/HZ@M) compared to the intact composite can be attributed to the CO interaction

with the hierarchical protonic core. This interaction explains the lower CO_2/CO selectivity of H-Cl/HZ@M compared to H-Cl/Z@M. Moreover, the estimated CO_2/CO selectivity for H-Cl/HZ@M (as shown in **Figure 4-19c**) is comparable to the reported values (ranging from 12 to 16.7) for HZSM-5 [340]. The low value of Q_{st} for CO_2 on H-Cl/HZ@M, in comparison with the intact composite, suggests a synergistic effect between HZSM-5 and MOF-199. This synergistic effect has altered the surface electronic properties of the composite adsorbent and influenced the adsorption behavior of CO_2.

The reduced composite adsorbent showed a higher value of Q_{st} for CO compared to intact composite adsorbent (**Figure 4-21a**). However, it should be noted that the intact composite offers a higher pore volume and surface area compared to the reduced composite (as indicated in **Table 4-7**). This suggests that the interaction between CO and the MOF primarily occurs through the electrostatic interactions with the open Cu sites. This observation is consistent with previous reports [326, 344]. On the other hand, both the open metal sites and micropores have a significant impact on CO_2 adsorption [344]. Furthermore, between CuO and Cu_2O, the former is preferred as an adsorption site for CO_2 due to its higher electronegativity [258, 273]. Accordingly, the lower value of Q_{st} for CO_2 can be explained by the reduced volume of micropores and the higher density of Cu_2O sites present in the reduced composite compared to intact one (**Figure 4-21b**).

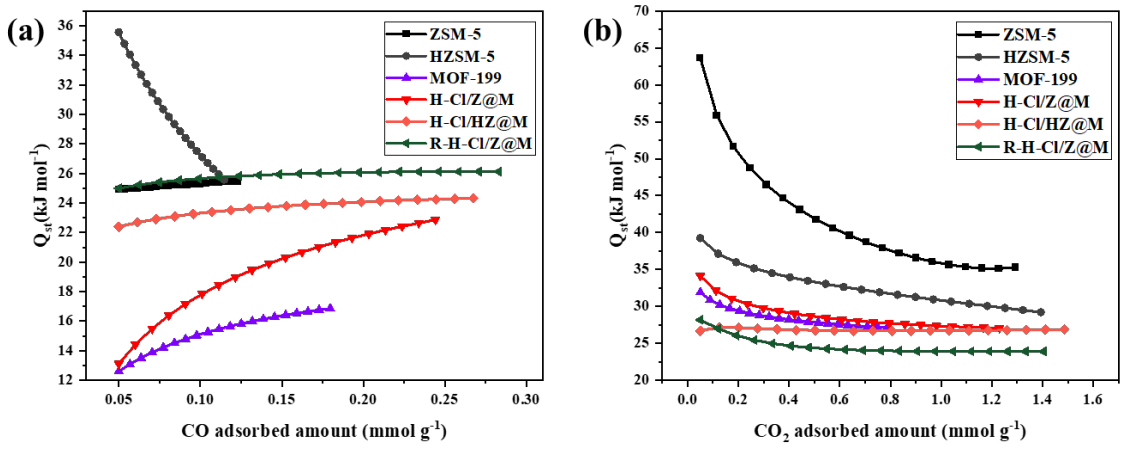

Figure 4-21 Estimated isosteric heat of adsorption for (a) CO, and (b) CO_2 over parent, intact, and modulated composite adsorbents.

Figure 4-22 shows the integral molar thermodynamic properties of adsorbed CO and CO_2 on parent, intact and modulated composite adsorbents. To capture the overall adsorption behavior of the adsorbents over the range of temperatures studied, we present these properties at the average temperature of 313 K. The integral properties at 293 and 333 K are presented in **Appendix A (Figure 7-1)**. ΔG is a measure of the work required to reach at equilibrium condition. The negative values of ΔG (**Figure 4-22ad**) indicate that the adsorption process for all adsorbents is spontaneous. As adsorption progresses and active sites become occupied, the ΔG values decrease. This is due to the higher isothermal work required to pack more molecules onto the remaining sites than the beginning stage of adsorption [299, 345-347]. It should be noted that the values and trends of ΔG depend on the adsorbent, adsorbate, and their interaction.

The value of ΔS show the overall balance between the vibration, rotation, and translation freedom of a guest molecule with respect to the adsorbent [190]. The negative sign shows that adsorption occurs from a state of randomness to an ordered state [346]. Over the entire pressure range, ΔS showed a decreasing trend with increasing pressure (**Figure 4-22be**). This is due to restricted movement of molecules as the number of available adsorption sites decreases. It is worth

mentioning that the high translational freedom of the molecules at low pressures contribute to the high entropy of adsorption [299]. MOF-199 and HZSM-5 exhibit the highest and the lowest degree of freedom for CO adsorption. Similarly, R-H-Cl/Z@M shows the highest degree of freedom for CO_2 adsorption. The efficiency of CO packing in the modulated composites is higher than the intact composite. For the mixed-valence composite, this can be explained by the electrostatic interaction of CO with Cu(I) sites. For the modulated composite with the HZSM-5 core, the higher efficiency can be explained by the quadrupole—field gradient interaction of CO [345]. On the other hand, the efficiency of CO_2 packing in the reduced composite is less than the intact composite due to similar interactions as CO, which are not favorable for CO_2 adsorption. The efficient packing of the CO_2 molecules in zeolites is facilitated by the quadrupole—field gradient interaction, which enhances the rotational freedom and improves the orientation of the molecules on the surface [299]. The increase of CO_2 packing efficiency with pressure in modulated composite with HZSM-5 core compared to the intact composite can be attributed to presence of mesopores that facilitates the accessibility of CO_2 molecules to the micropores. Furthermore, unlike micropores, the mesoropores of the HZSM-5 facilitate the transitional and rotational motions of CO_2 molecules, leading to more structure fluid or higher efficiency of packing [299]. For all samples, excluding ZSM-5 and R-H-Cl/Z@M, the values of ΔS show a complex behavior with a decreasing region up to CO_2 pressure range 20-30 kPa followed by a slight increase up to 100 kPa. The sharp decrease in the first region is attributed to the limited freedom of CO_2 molecules as the number of high-energy sites becomes minimal. The increasing region can be due to the structural rearrangement or changes in orientation of CO_2 molecules to accommodate the increasing number of adsorbed molecules. The increase in freedom of movement becomes more pronounced by the increase of temperature (**Figure 7-1**).

The value of ΔH represents the heat effect during the adsorption process. The negative values of ΔH (**Figure 4-22cf**) indicate that the adsorption of CO and CO_2 on all adsorbents is exothermic. This is consistent with the adsorption isotherms collected at different temperatures (see **Figure 4-20**). ΔH follows the same trend as ΔS (**Figure 4-22be**) indicating that more effective the packing leads to higher heat development. In general, ΔH values in the range 80 to 200 kJ/mol are indicative of chemical adsorption, while values below 20 kJ/mol correspond to physical adsorption [190]. The range between 20 to 80 kJ/mol represent a transition region where the nature of adsorption shows intermediate characteristics between physisorption and chemisorption. The ΔH values for CO and CO_2 adsorption on parent and composite adsorbents are below 80 kJ/mol. For both CO and CO_2, the ΔH values higher than 20 kJ/mol can be attributed to high polarizability and quadrupole moments of adsorbates, which enable them to interact with electric field or electric field gradient generated by surface charges [340, 341, 343]. In the case of the reduced composite, the higher ΔH value (**Figure 4-22c**) corresponds to the pi-complex bonding of CO with Cu(I) species in the MOF structure [190]. The ΔH value provides valuable information required for optimizing the design of adsorption processes. It should be noted that the high heat generation is not favorable in adiabatic adsorption processes, as it reduces the adsorption capacity.

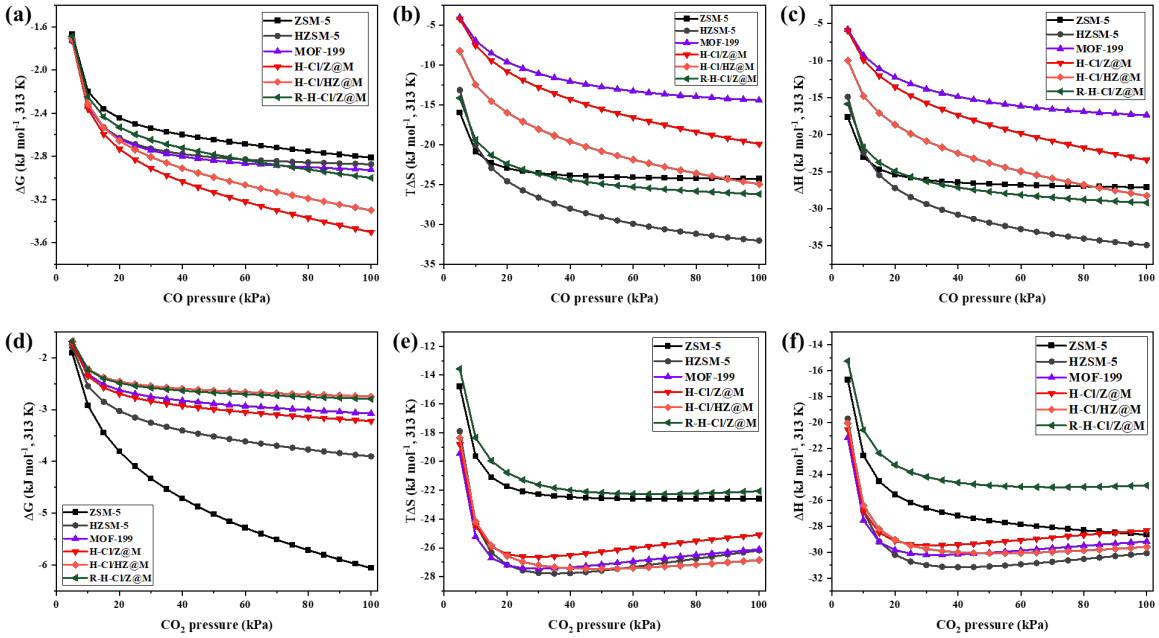

Figure 4-22 Integral molar thermodynamic properties of adsorbed phases of (a-c) CO and (d-f) CO_2 at 313 K.

4.4 Conclusion

In this study, we showed a facile synthesis method of ZSM-5@MOF-199 composites at room temperature through the formation of an HDS intermediate. The structural and chemical properties of the zeolite core and MOF shell were regulated using pre- and post-synthesis modifications, respectively. We evaluated the adsorption performance of the composites in separation of CO and CO_2 and characterized the structural and chemical properties of the adsorbents through the use of various techniques. It was shown that the formation of a MOF shell is highly dependent on the choice of the copper salt, for the copper salt's formation stability directly impacts the formation of an HDS intermediate. Among the used copper salts, copper chloride showed the fastest growth of the MOF, independent of ZnO loading. We optimized the structure of the composite through the choice of organic ligand solvent. We showed that the use of a stabilizing polar aprotic solvent, acetonitrile, led to better growth of the MOF layer by adjusting the solvent pH. The N_2 adsorption

isotherm data demonstrated the presence of mesopores and a larger surface area of composites than the parent adsorbents. As a result, the composite showed a higher adsorption capacity toward CO and CO_2. The composite showed structural degradation upon reduction of MOF-199 using $Na_2S_2O_3$. Upon reduction, CO adsorption performance greatly improved, which was attributed to the strong interaction of CO with Cu(I) ions through pi-complexation bonding. This finding was further confirmed using the isosteric heat of adsorption. The strength of the CO_2 interaction with reduced composite decreased, leading to a lower CO_2/CO selectivity. However, the structural degradation did not have an impact on overall CO_2 adsorption capacity. Modulation of the zeolite to protonic hierarchical ZSM-5 enhanced the structure of the composite by providing a greater frequency of mesopores and a higher surface area. As a result, the CO and CO_2 uptake increased by 20 and 28%, respectively. HZSM-5@MOF-199 showed better adsorption performance for CO capture and lower CO_2/CO selectivity compared to the intact composite. Furthermore, the isosteric heat of adsorption revealed a stronger interaction with CO than the intact composite, which was attributed to the interaction with HZSM-5 through cationic sites. It was shown that the decrease in CO_2/CO selectivity was due to the weaker quadrupole—field gradient interactions of CO_2 with the extra-framework H^+ cations and exposed aluminum sites of HZSM-5. Moreover, the CO_2 isosteric heat of adsorption revealed a synergistic effect between HZSM-5 and MOF-199 that altered the surface electronic properties of the composite adsorbent, thereby, affecting the adsorption performance of CO_2.

The integral thermodynamic properties of adsorption on parent and composites were calculated based on the LF and DSLF fitting parameters. The negative values of ΔG and ΔH expressed the spontaneousness and exothermicity of the adsorption on all adsorbents. The calculated values of integral enthalpy of adsorption were all below 80 kJ/mol expressing that the adsorbate-adsorbent

interaction was a mix of physisorption and electrostatic interactions such as quadrupole—field gradient and pi-complexation. The negative values of ΔS expressed the ordered arrangement of adsorbates on adsorbents. Efficient packing of CO was facilitated by electrostatic and quadrupole-field gradient interactions in the modulated composite. For CO_2 efficient packing relied on quadrupole-field gradient interaction and rotational freedom. The presence of HZSM-5 core in the composite increased the CO_2 packing efficiency due to presence of mesopores, which facilitate micropore accessibility, and transitional and rotational motions. ΔS values showed a complex behavior with CO_2 pressure, an initial decrease followed by a slight increase, indicating limited freedom followed by structural rearrangement of CO_2 molecules on the surface.

Chapter 5: Conclusions and future directions

In this dissertation, the adsorption-based separation of gases, with a particular focus on CO and CO_2 as a representative system, for environmental and energy production purpose was approached through design, synthesis, and optimization of copper-based adsorbents.

5.1 Conclusions

In chapter 2, we performed the surface modification of copper powder through chemical reaction with a copper containing solution at room temperature to form the Cu(I) active phase for interaction with CO. A structured analysis of was performed to assess the impact of solvent on structural properties and performance of the adsorbents. The results suggested that the difference in solvents properties and their interactions with copper ions significantly influence the growth and formation patterns of CuCl crystals. The adsorbents with solvent-regulated morphologies were tested using equilibrium and dynamic adsorption setups showing that they differed in their adsorption capacity, selectivity, and kinetics. Overall, the study showed the importance of choice of solvent for surface modification of adsorbent; however, the adsorbents suffered a low stability and adsorption capacity.

In chapter 3, we performed a two-step surface modification of copper oxide powder to form two Cu(I) active phase with different ligands. The first step was fast reduction of the copper oxide to form Cu(I) and Cu(0), followed by reaction with copper containing solvent to form CuCl on the surface. The influence of presence of two active sites with different ligands were assessed through surface energetic heterogeneity analysis. The adsorption data were fitted to different isotherm models revealing that the reduction step of surface modification resulted in a surface with enhanced energetic heterogeneity and average surface energy, while modification through solvent reaction led to a decreased in energetic heterogeneity but higher density of sites with lower energy. The

two-step modification approach led to very high stability of adsorbents under atmospheric condition by formation of a protective layer around the active adsorption sites that could be easily removed by heat treatment. The presence of two active adsorption sites on the surface of the adsorbent resulted in elevated CO adsorption capacity (higher than two times that of CuCl modified copper in chapter 2) and a highest ever reported CO/CO_2 selectivity. Overall, this study showed that introducing two active phases through chemical modification of surface enhanced the adsorption performance. However, the adsorbent suffers a low surface area and therefore, a low adsorption capacity compared to commercial adsorbents.

In chapter 4, we developed a zeolite@MOF composite adsorbent using a fast, room-temperature HDS-assisted method. ZSM-5 and MOF-199 were selected as the primary materials for this composite. ZSM-5 provided several desirable properties such as a high surface area, a micropore structure, and surface functionalities that facilitated interaction with adsorptive species. It also served as the foundation for forming the intermediate (Zn, Cu) HDS layer. The composite synthesis involved a three-step process. Firstly, we modified the zeolite surface with ZnO through wet impregnation technique. This step was crucial for subsequent surface chemical reaction. Secondly, we subjected the modified zeolite to a surface chemical reaction with a copper containing solvent, resulting in the formation of (Zn, Cu) hydroxy salt intermediate material. Finally, we performed a fast ion exchange reaction with organic linker containing solvent to incorporate BTC into the HDS lattices, thereby forming the MOF-199 shell. A comparative analysis was conducted to investigate the impact of copper ligand and organic linker solvent on formation and structural properties of the composites. The result indicated that the use of the chloride ligand and the polar aprotic solvent led to faster and structurally superior growth of MOF shell. We also employed pre- and post-synthesis modifications of the zeolite core and MOF shell

to regulate the structural and chemical properties of composite adsorbents. To evaluate the adsorption performance of the composites, we performed a comparative analysis of the parent adsorbents, intact, and modified composites. The results demonstrated that the intact composite exhibited an enhanced adsorption capacity due to structural improvement. Furthermore, the modified composites showed a higher CO adsorption capacity and selectivity, attributed to their specific structural properties and stronger CO interaction with adsorbent surface. The behavior of adsorption was studied through thermodynamic analysis, which shed light on the nature of adsorbate-adsorbent interactions and the arrangement of adsorbates on the adsorbent surface. Overall, this study showcased a facile and energy-efficient route for synthesis of highly versatile zeolite@MOF composite adsorbents while preserving the physical, chemical, structural properties of both constituents. This hybridization strategy introduces an innovative platform for formulating MOF materials, enabling their practical utilization as effective contractors for large-scale gas separation and purification applications.

5.2 Recommendation for future work

Throughout this study, we have emphasized on the need for improved stability, selectivity, and adsorption capacity of adsorbents to make them viable for practical applications. We have explored various synthesis and surface modification techniques to enhance the performance of adsorbent and address the challenges mentioned above. Moving forward, there are several directions proposed for future research.

1. Zeolite heat treatment: As previously mentioned, the heat treatment of zeolite has an impact on its structural properties and intensity of cationic sites on its surface. Therefore, a systematic approach into the effects of zeolite heat treatment on adsorption performance

would be beneficial. This would help understand how different heat treatment conditions affect the adsorption properties of zeolites and to optimize its performance accordingly.

2. Internal agent-assisted MOF growth: In this work, the formation of ZnO on the surface of the adsorbent through wet impregnation led to a loss of surface area and pore blockage. To minimize these drawbacks while achieving a good dispersion of ZnO, we propose modifying the adsorbent through an ion-exchange reaction with Zn to form Zn-ZSM-5. The Zn functionalities can act as internal agents to help in formation of HDS intermediate and MOF-199. A systematic study of the ion-exchange reaction with Zn can further enhance the structural properties, and consequently, the adsorption performance of the composite.
3. Investigation of the role of different organic linkers on the adsorption performance of composites: Organic linkers offer various structural properties and functionalities that can enhance the adsorption performance. A systematic study can reveal the feasibility of MOF formation by incorporation of organic linkers into the HDS lattice, exploring MOF growth kinetics, and determining the final structure of the composite. By understanding the effects of different organic linkers, we can optimize the composite design and enhance its adsorption capabilities.
4. Investigation of composite synergistic effects: In this study, CO_2 isosteric heat of adsorption revealed a synergistic effect by hybridization of HZSM-5 and MOF-199. This effect is attributed to the change in surface electronic properties. A better understanding of this synergistic effect can greatly impact the future development of more efficient adsorbents. To achieve this, an analysis of CO_2 adsorption sites and their corresponding

energy is required. In-situ FTIR analysis of CO_2 adsorption coupled with calorimetry would provide an ideal setup for investigating this phenomenon.

5. As mentioned in the first chapter of this dissertation, while equilibrium setups provide valuable information to identify the potential adsorbents, it is essential to test the performance of adsorbents using dynamic setups that replicate the practical operating processes such as PSA and TSA. Investigation of stability, selectivity, and adsorption capacity adsorbents under different gas mixtures and temperature, is crucial for practical application.

References

1. Evans, A., R. Luebke, and C. Petit, *The use of metal–organic frameworks for CO purification.* Journal of Materials Chemistry A, 2018. **6**(23): p. 10570-10594.
2. Lin, J.C.-T., L.G. Peeva, and A.G. Livingston. *Separation of pharmaceutical process-related impurities via an organic solvent nanofiltration membrane cascade*. in *AIChE 2006 Annual Meeting, San Francisco, CA, November 12–17, 2006*. 2006.
3. Yang, R.T., *Adsorbents : fundamentals and applications.* 2003.
4. Hassani, E., et al., *Carbonation, regeneration, and cycle stability of the mechanically activated Ca (OH) 2 sorbents for CO2 capture: an in situ X-ray diffraction study.* Industrial & Engineering Chemistry Research, 2020. **59**(25): p. 11402-11411.
5. Mozaffari, N., et al., *New insights into SnO2/Al2O3, Ni/Al2O3, and SnO2/Ni/Al2O3 composite films for CO adsorption: building a bridge between microstructures and adsorption properties.* The Journal of Physical Chemistry C, 2020. **124**(6): p. 3692-3701.
6. Cho, K., et al., *High CO adsorption capacity, and CO selectivity to CO2, N2, H2, and CH4 of CuCl/bayerite adsorbent.* Microporous and Mesoporous Materials, 2019. **277**: p. 142-148.
7. Ma, J., et al., *CO adsorption on activated carbon-supported Cu-based adsorbent prepared by a facile route.* Separation and purification technology, 2010. **76**(1): p. 89-93.
8. Yeom, C. and Y. Kim, *Mesoporous alumina with high capacity for carbon monoxide adsorption.* Korean Journal of Chemical Engineering, 2018. **35**(2): p. 587-593.
9. Kim, A.-R., et al., *Creating high CO/CO2 selectivity and large CO working capacity through facile loading of Cu (I) species into an iron-based mesoporous metal-organic framework.* Chemical Engineering Journal, 2018. **348**: p. 135-142.
10. Vo, T.K., et al., *Highly CO selective Cu (I)-doped MIL-100 (Fe) adsorbent with high CO/CO2 selectivity due to π complexation: Effects of Cu (I) loading and activation temperature.* Microporous and Mesoporous Materials, 2019. **274**: p. 17-24.
11. Xue, C., et al., *CO Adsorption Performance of CuCl/Activated Carbon by Simultaneous Reduction–Dispersion of Mixed Cu (II) Salts.* Materials, 2019. **12**(10): p. 1605.
12. Yin, Y., et al., *Cuprous/vanadium sites on MIL-101 for selective CO adsorption from gas mixtures with superior stability.* ACS Sustainable Chemistry & Engineering, 2019. **7**(13): p. 11284-11292.
13. Hou, S., et al., *Firing blast furnace gas without support fuel in steel mill boilers.* Energy Conversion and Management, 2011. **52**(7): p. 2758-2767.
14. Hogendoorn, J., W.P.M. van Swaaij, and G. Versteeg, *The absorption of carbon monoxide in COSORB solutions: absorption rate and capacity.* The Chemical Engineering Journal and the Biochemical Engineering Journal, 1995. **59**(3): p. 243-252.
15. Keller, A., R. Schendel, and C. DENVER, *The use of COSORB II to recover high purity carbon monoxide from a feed gas.* AIChE Summer Mtg., Denver, CO, 1988.
16. Gholap, R.V. and R.V. Chaudhari, *Absorption of carbon monoxide with reversible reaction in cualcl4-toluene-complex solutions.* The Canadian Journal of Chemical Engineering, 1992. **70**(3): p. 505-510.
17. Yang, R.T., *Adsorbents: fundamentals and applications*. 2003: John Wiley & Sons.
18. Kopecky, F., P. Kaclik, and T. Fazekas, *Laboratory manual for physical chemistry.* Farmaceutical faculty of Comenius University, Bratislava, 1996.
19. Ferrari, L., et al., *Interaction of cement model systems with superplasticizers investigated by atomic force microscopy, zeta potential, and adsorption measurements.* Journal of colloid and interface science, 2010. **347**(1): p. 15-24.
20. Nix, R. *Surface Science*. 2019; 34-37]. Available from: https://chem.libretexts.org/Bookshelves/Physical_and_Theoretical_Chemistry_Textbook_Maps/Book%3A_Surface_Science_(Nix)/2%3A_Adsorption_of_Molecules_on_Surfaces/2.4%3A_PE_Curves_and_Energetics_of_Adsorption.

21. Taylor, H.S. and A.T. Williamson, *Molecular and Activated Adsorption of Hydrogen on Manganous Oxide Surfaces.* Journal of the American Chemical Society, 1931. **53**(6): p. 2168-2180.
22. Humphrey, J.L., *Separation process technology*. 1997: McGraw-Hill (canada).
23. Gao, F., et al., *Selective CO adsorbent CuCl/AC prepared using CuCl 2 as a precursor by a facile method.* RSC advances, 2016. **6**(41): p. 34439-34446.
24. Sizirici, B. and I. Yildiz, *Adsorption capacity of iron oxide-coated gravel for landfill leachate: simultaneous study.* International Journal of Environmental Science and Technology, 2017. **14**(5): p. 1027-1036.
25. Bastos-Neto, M., et al., *Dynamic bed measurements of CO adsorption on microporous adsorbents at high pressures for hydrogen purification processes.* Separation and purification technology, 2011. **77**(2): p. 251-260.
26. Mozaffari, N., et al., *Investigation of carbon monoxide gas adsorption on the Al 2 O 3/Pd (NO 3) 2/zeolite composite film.* Journal of Theoretical and Applied Physics, 2020. **14**(1): p. 65-74.
27. Tantet, J., M. Eić, and R. Desai, *Breakthrough study of the adsorption and separation of sulfur dioxide from wet gas using hydrophobic zeolites.* Gas separation & purification, 1995. **9**(3): p. 213-220.
28. Murillo, R., et al., *Adsorption of phenanthrene on activated carbons: Breakthrough curve modeling.* Carbon, 2004. **42**(10): p. 2009-2017.
29. Park, J.-H., et al., *Adsorber dynamics and optimal design of layered beds for multicomponent gas adsorption.* Chemical Engineering Science, 1998. **53**(23): p. 3951-3963.
30. Garcia, S., et al., *Breakthrough adsorption study of a commercial activated carbon for pre-combustion CO2 capture.* Chemical Engineering Journal, 2011. **171**(2): p. 549-556.
31. Belmabkhout, Y., et al., *A complete experimental approach for synthesis gas separation studies using static gravimetric and column breakthrough experiments.* Adsorption, 2007. **13**(3-4): p. 341-349.
32. Kotoh, K., et al., *Breakthrough curve analysis of pressure swing adsorption for hydrogen isotope separation.* Fusion science and technology, 2008. **54**(2): p. 415-418.
33. Oh, K.-J., et al., *Breakthrough data analysis of adsorption of volatile organic compounds on granular activated carbon.* Korean Journal of Chemical Engineering, 2010. **27**(2): p. 632-638.
34. Regufe, M.J., et al., *Syngas purification by porous amino-functionalized titanium terephthalate MIL-125.* Energy & Fuels, 2015. **29**(7): p. 4654-4664.
35. Myers, A.L. and J.M. Prausnitz, *Thermodynamics of mixed-gas adsorption.* AIChE journal, 1965. **11**(1): p. 121-127.
36. Li, Y.-X., et al., *Incorporation of Cu (II) and its selective reduction to Cu (I) within confined spaces: efficient active sites for CO adsorption.* Journal of Materials Chemistry A, 2018. **6**(19): p. 8930-8939.
37. Bonjour, J., J.-B. Chalfen, and F. Meunier, *Temperature swing adsorption process with indirect cooling and heating.* Industrial & engineering chemistry research, 2002. **41**(23): p. 5802-5811.
38. Tlili, N., et al., *Electrical swing adsorption using new mixed matrix adsorbents for CO2 capture and recovery: experiments and modeling.* Industrial & engineering chemistry research, 2012. **51**(48): p. 15729-15737.
39. Nastaj, J., K. Witkiewicz, and F. Moskal, *Experimental studies on electrothermal regeneration of carbonaceous adsorbent in inductively heated column.* Chemical Engineering and Processing: Process Intensification, 2016. **110**: p. 1-8.
40. Moskal, F. and J. Nastaj, *Internal heat source capacity at inductive heating in desorption step of ETSA process.* International communications in heat and mass transfer, 2007. **34**(5): p. 579-586.
41. Hashisho, Z., M. Rood, and L. Botich, *Microwave-swing adsorption to capture and recover vapors from air streams with activated carbon fiber cloth.* Environmental science & technology, 2005. **39**(17): p. 6851-6859.
42. Keller, L., et al., *Electrical swing adsorption on functionalized hollow fibers.* Chemical Engineering Journal, 2019. **371**: p. 107-117.

43. Giraudet, S., B. Boulinguiez, and P. Le Cloirec, *Adsorption and electrothermal desorption of volatile organic compounds and siloxanes onto an activated carbon fiber cloth for biogas purification.* Energy & fuels, 2014. **28**(6): p. 3924-3932.
44. Grande, C.A., R.P. Ribeiro, and A.E. Rodrigues, *Challenges of electric swing adsorption for CO2 capture.* ChemSusChem, 2010. **3**(8): p. 892-898.
45. Ribeiro, R., C. Grande, and A. Rodrigues, *Activated carbon honeycomb monolith–Zeolite 13X hybrid system to capture CO2 from flue gases employing Electric Swing Adsorption.* Chemical Engineering Science, 2013. **104**: p. 304-318.
46. An, H. and B. Feng, *Desorption of CO2 from activated carbon fibre–phenolic resin composite by electrothermal effect.* International Journal of Greenhouse Gas Control, 2010. **4**(1): p. 57-63.
47. Ribeiro, R., C. Grande, and A. Rodrigues, *Electrothermal performance of an activated carbon honeycomb monolith.* Chemical Engineering Research and Design, 2012. **90**(11): p. 2013-2022.
48. Regufe, M.J., et al., *New hybrid composite honeycomb monolith with 13X zeolite and activated carbon for CO 2 capture.* Adsorption, 2018. **24**(3): p. 249-265.
49. Sevanthi, R., et al., *Electrical current stimulated desorption of carbon dioxide adsorbed on graphene based structures.* RSC advances, 2016. **6**(49): p. 43401-43407.
50. Lillia, S., et al., *A comprehensive modeling of the hybrid temperature electric swing adsorption process for CO2 capture.* International Journal of Greenhouse Gas Control, 2018. **74**: p. 155-173.
51. Yang, S.-I., et al., *Hydrogen separation by multi-bed pressure swing adsorption of synthesis gas.* Adsorption, 2008. **14**(4): p. 583-590.
52. Delgado, J.A., et al., *Adsorption and diffusion of H2, CO, CH4, and CO2 in BPL activated carbon and 13X zeolite: evaluation of performance in pressure swing adsorption hydrogen purification by simulation.* Industrial & Engineering Chemistry Research, 2014. **53**(40): p. 15414-15426.
53. Cavenati, S., C.A. Grande, and A.E. Rodrigues, *Upgrade of methane from landfill gas by pressure swing adsorption.* Energy & fuels, 2005. **19**(6): p. 2545-2555.
54. Kim, M.-B., et al., *Kinetic separation of landfill gas by a two-bed pressure swing adsorption process packed with carbon molecular sieve: nonisothermal operation.* Industrial & engineering chemistry research, 2006. **45**(14): p. 5050-5058.
55. Al-Naddaf, Q., H. Thakkar, and F. Rezaei, *Novel Zeolite-5A@ MOF-74 Composite Adsorbents with Core–Shell Structure for H2 Purification.* ACS applied materials & interfaces, 2018. **10**(35): p. 29656-29666.
56. Agueda, V.I., et al., *Adsorption and diffusion of H2, N2, CO, CH4 and CO2 in UTSA-16 metal-organic framework extrudates.* Chemical Engineering Science, 2015. **124**: p. 159-169.
57. Sircar, S., *Air fractionation by adsorption.* Separation Science and Technology, 1988. **23**(14-15): p. 2379-2396.
58. Sircar, S., *Pressure swing adsorption.* Industrial & engineering chemistry research, 2002. **41**(6): p. 1389-1392.
59. Whysall, M. and L.J.M. Wagemans, *Very large-scale pressure swing adsorption processes*. 2001, Google Patents.
60. Relvas, F., et al., *Single-stage pressure swing adsorption for producing fuel cell grade hydrogen.* Industrial & Engineering Chemistry Research, 2018. **57**(14): p. 5106-5118.
61. Sircar, S. and T. Golden, *Purification of hydrogen by pressure swing adsorption.* Separation Science and Technology, 2000. **35**(5): p. 667-687.
62. Xiao, P., et al., *Capture of CO 2 from flue gas streams with zeolite 13X by vacuum-pressure swing adsorption.* Adsorption, 2008. **14**(4-5): p. 575-582.
63. Liu, Z., et al., *Multi-bed vacuum pressure swing adsorption for carbon dioxide capture from flue gas.* Separation and Purification Technology, 2011. **81**(3): p. 307-317.
64. Gao, F., et al., *Adsorption separation of CO from syngas with CuCl@ AC adsorbent by a VPSA process.* RSC advances, 2018. **8**(69): p. 39362-39370.
65. Fubini, B., *Adsorption calorimetry in surface chemistry.* Thermochimica Acta, 1988. **135**: p. 19-29.

66. Dunne, J., et al., *Calorimetric heats of adsorption and adsorption isotherms. 1. O2, N2, Ar, CO2, CH4, C2H6, and SF6 on silicalite.* Langmuir, 1996. **12**(24): p. 5888-5895.
67. Cardona-Martinez, N. and J. Dumesic, *Applications of adsorption microcalorimetry to the study of heterogeneous catalysis*, in *Advances in catalysis*. 1992, Elsevier. p. 149-244.
68. Piper, J., J. Morrison, and C. Peters, *The adsorption of carbon monoxide on graphite.* Molecular Physics, 1984. **53**(6): p. 1463-1480.
69. Gao, F., et al., *Ethylene/ethane separation by CuCl/AC adsorbent prepared using CuCl 2 as a precursor.* Adsorption, 2016. **22**(7): p. 1013-1022.
70. Gao, F., et al., *Adsorptive separation of ethylene/ethane mixtures with CuCl@ HY adsorbent: equilibrium and reversibility.* Journal of Porous Materials, 2017. **24**(3): p. 713-719.
71. Piper, J., et al., *Heats and entropies of adsorption of N 2 on grafoil at 79.3 K.* Journal of the Chemical Society, Faraday Transactions 1: Physical Chemistry in Condensed Phases, 1983. **79**(12): p. 2863-2874.
72. Garrone, E., et al., *Thermodynamic and spectroscopic characterization of heterogeneity among adsorption sites: carbon monoxide on anatase at ambient temperature.* Langmuir, 1989. **5**(4): p. 892-899.
73. Bolis, V., et al., *Temkin-type model for the description of induced heterogeneity: CO adsorption on group 4 transition metal dioxides.* Langmuir, 1993. **9**(6): p. 1521-1528.
74. Jaroniec, M., *Adsorption on heterogeneous surfaces: The exponential equation for the overall adsorption isotherm.* Surface Science, 1975. **50**(2): p. 553-564.
75. Moussavi, G., et al., *The investigation of mechanism, kinetic and isotherm of ammonia and humic acid co-adsorption onto natural zeolite.* Chemical Engineering Journal, 2011. **171**(3): p. 1159-1169.
76. Yang, C.-h., *Statistical mechanical study on the Freundlich isotherm equation.* Journal of colloid and interface science, 1998. **208**(2): p. 379-387.
77. Xing, B. and J.J. Pignatello, *SORPTION | Organic Chemicals.* Encyclopedia of Soils in the Environment, 2005: p. 537-548.
78. Boparai, H.K., M. Joseph, and D.M. O'Carroll, *Kinetics and thermodynamics of cadmium ion removal by adsorption onto nano zerovalent iron particles.* Journal of hazardous materials, 2011. **186**(1): p. 458-465.
79. Jung, K.-D. and O.-S. Joo, *Study on CO adsorption on in-situ brass formed Cu/ZnO.* BULLETIN-KOREAN CHEMICAL SOCIETY, 2002. **23**(12): p. 1765-1768.
80. Kumar, K.V., et al., *Characterization of the adsorption site energies and heterogeneous surfaces of porous materials.* Journal of Materials Chemistry A, 2019. **7**(17): p. 10104-10137.
81. Kinniburgh, D.G., *General purpose adsorption isotherms.* Environmental science & technology, 1986. **20**(9): p. 895-904.
82. Ayawei, N., et al., *Synthesis, characterization and application of Mg/Al layered double hydroxide for the degradation of congo red in aqueous solution.* Open Journal of Physical Chemistry, 2015. **5**(03): p. 56.
83. Bloch, E.D., et al., *Reversible CO binding enables tunable CO/H2 and CO/N2 separations in metal–organic frameworks with exposed divalent metal cations.* Journal of the American Chemical Society, 2014. **136**(30): p. 10752-10761.
84. Sanford, C. and S. Ross, *Homotattic surface—a suggested new word.* The Journal of Physical Chemistry, 1954. **58**(3): p. 288-288.
85. Klotz, I.M. and D.L. Hunston, *Properties of graphical representations of multiple classes of binding sites.* Biochemistry, 1971. **10**(16): p. 3065-3069.
86. Tzabar, N. and H. ter Brake, *Adsorption isotherms and Sips models of nitrogen, methane, ethane, and propane on commercial activated carbons and polyvinylidene chloride.* Adsorption, 2016. **22**(7): p. 901-914.
87. Ayawei, N., A.N. Ebelegi, and D. Wankasi, *Modelling and interpretation of adsorption isotherms.* Journal of Chemistry, 2017. **2017**.

88. Kumara, N., et al., *Equilibrium isotherm studies of adsorption of pigments extracted from kuduk-kuduk (Melastoma malabathricum L.) pulp onto TiO2 nanoparticles.* Journal of Chemistry, 2014. **2014**.
89. Bae, Y.-S., et al., *Separation of CO2 from CH4 using mixed-ligand metal− organic frameworks.* Langmuir, 2008. **24**(16): p. 8592-8598.
90. McDonald, T.M., et al., *Capture of carbon dioxide from air and flue gas in the alkylamine-appended metal–organic framework mmen-Mg2 (dobpdc).* Journal of the American Chemical Society, 2012. **134**(16): p. 7056-7065.
91. Wu, X., et al., *Microwave synthesis and characterization of MOF-74 (M= Ni, Mg) for gas separation.* Microporous and mesoporous materials, 2013. **180**: p. 114-122.
92. Peng, J., et al., *A supported Cu (I)@ MIL-100 (Fe) adsorbent with high CO adsorption capacity and CO/N2 selectivity.* Chemical Engineering Journal, 2015. **270**: p. 282-289.
93. Abedini, H., A. Shariati, and M.R. Khosravi-Nikou, *Adsorption of propane and propylene on M-MOF-74 (M= Cu, Co): Equilibrium and kinetic study.* Chemical Engineering Research and Design, 2020. **153**: p. 96-106.
94. Kim, A.-R., et al., *Facile loading of Cu (I) in MIL-100 (Fe) through redox-active Fe (II) sites and remarkable propylene/propane separation performance.* Chemical Engineering Journal, 2018. **331**: p. 777-784.
95. Chen, Y., et al., *A new MOF-505@ GO composite with high selectivity for CO2/CH4 and CO2/N2 separation.* Chemical Engineering Journal, 2017. **308**: p. 1065-1072.
96. Terzyk, A.P., et al., *Developing the solution analogue of the Toth adsorption isotherm equation.* Journal of colloid and interface science, 2003. **266**(2): p. 473-476.
97. Kumar, K.V., et al., *A site energy distribution function from Toth isotherm for adsorption of gases on heterogeneous surfaces.* Physical Chemistry Chemical Physics, 2011. **13**(13): p. 5753-5759.
98. Sreńscek-Nazzal, J., et al., *Comparison of optimized isotherm models and error functions for carbon dioxide adsorption on activated carbon.* Journal of Chemical & Engineering Data, 2015. **60**(11): p. 3148-3158.
99. Gun'ko, V., *Competitive adsorption.* Theoretical and Experimental Chemistry, 2007. **43**(3): p. 139-183.
100. Kapoor, A., J. Ritter, and R.T. Yang, *An extended Langmuir model for adsorption of gas mixtures on heterogeneous surfaces.* Langmuir, 1990. **6**(3): p. 660-664.
101. Choy, K.K., J.F. Porter, and G. McKay, *Langmuir isotherm models applied to the multicomponent sorption of acid dyes from effluent onto activated carbon.* Journal of Chemical & Engineering Data, 2000. **45**(4): p. 575-584.
102. Couble, J. and D. Bianchi, *Experimental microkinetic approach of the CO/H2 reaction on Pt/Al2O3 using the Temkin formalism. 1. Competitive chemisorption between adsorbed CO and hydrogen species in the absence of reaction.* Journal of catalysis, 2017. **352**: p. 672-685.
103. Couble, J. and D. Bianchi, *Experimental microkinetic approach of the CO/H2 reaction on Pt/Al2O3 using the Temkin formalism. 2. Coverages of the adsorbed CO and hydrogen species during the reaction and rate of the CH4 production.* Journal of catalysis, 2017. **352**: p. 686-698.
104. Patel, H., *Fixed-bed column adsorption study: a comprehensive review.* Applied Water Science, 2019. **9**(3): p. 45.
105. Negrea, A., et al., *Estimation on Fixed-Bed Column Parameters of Breakthrough Behaviors for Gold Recovery by Adsorption onto Modified/Functionalized Amberlite XAD7.* International Journal of Environmental Research and Public Health, 2020. **17**(18): p. 6868.
106. Yoro, K.O., et al., *Modelling and Experimental Study of the CO2 adsorption behaviour of polyaspartamide as an adsorbent during Post-combustion CO2 capture.* Energy Procedia, 2017. **114**: p. 1643-1664.
107. Han, R., et al., *Adsorption of methylene blue by phoenix tree leaf powder in a fixed-bed column: experiments and prediction of breakthrough curves.* Desalination, 2009. **245**(1-3): p. 284-297.

108. Długosz, O. and M. Banach, *Sorption of Ag+ and Cu2+ by vermiculite in a fixed-bed column: Design, process optimization and dynamics investigations.* Applied Sciences, 2018. **8**(11): p. 2221.
109. Pérez-Marín, A., et al., *Removal of cadmium from aqueous solutions by adsorption onto orange waste.* Journal of hazardous materials, 2007. **139**(1): p. 122-131.
110. Nascimento, T.A., et al., *Preparation and characterization of a composite based on polyaniline, polypyrrole and cigarette filters: adsorption studies and kinetics of phenylbutazone in aqueous media.* RSC advances, 2016. **6**(69): p. 64450-64459.
111. Ho, Y. and G. McKay, *A comparison of chemisorption kinetic models applied to pollutant removal on various sorbents.* Process safety and environmental protection, 1998. **76**(4): p. 332-340.
112. Rudzinski, W. and W. Plazinski, *Kinetics of solute adsorption at solid/solution interfaces: a theoretical development of the empirical pseudo-first and pseudo-second order kinetic rate equations, based on applying the statistical rate theory of interfacial transport.* The Journal of Physical Chemistry B, 2006. **110**(33): p. 16514-16525.
113. Wu, F.-C., et al., *Characteristics of pseudo-second-order kinetic model for liquid-phase adsorption: a mini-review.* Chemical Engineering Journal, 2009. **151**(1-3): p. 1-9.
114. Xiao, Y., J. Azaiez, and J.M. Hill, *Erroneous application of pseudo-second-order adsorption kinetics model: ignored assumptions and spurious correlations.* Industrial & Engineering Chemistry Research, 2018. **57**(7): p. 2705-2709.
115. Wu, F.-C., R.-L. Tseng, and R.-S. Juang, *Characteristics of Elovich equation used for the analysis of adsorption kinetics in dye-chitosan systems.* Chemical Engineering Journal, 2009. **150**(2-3): p. 366-373.
116. Ho, Y.-S., *Review of second-order models for adsorption systems.* Journal of hazardous materials, 2006. **136**(3): p. 681-689.
117. Sparks, D.L., *Environmental soil chemistry*. 2003: Elsevier.
118. Gamboa Mutuberría, I., J. Guil, and R. Paniego, *Adsorption of CO, H2, and O2 on Co3O4.* Berichte der Bunsengesellschaft für physikalische Chemie, 1993. **97**(1): p. 77-84.
119. Stanislaus, A., M. Evans, and R. Mann, *Kinetics of adsorption of carbon monoxide on alumina.* The Journal of Physical Chemistry, 1972. **76**(17): p. 2349-2352.
120. Aly, Z., et al., *Removal of aluminium from aqueous solutions using PAN-based adsorbents: characterisation, kinetics, equilibrium and thermodynamic studies.* Environmental Science and Pollution Research, 2014. **21**(5): p. 3972-3986.
121. Wu, F.-C., R.-L. Tseng, and R.-S. Juang, *Initial behavior of intraparticle diffusion model used in the description of adsorption kinetics.* Chemical engineering journal, 2009. **153**(1-3): p. 1-8.
122. Britt, D., D. Tranchemontagne, and O.M. Yaghi, *Metal-organic frameworks with high capacity and selectivity for harmful gases.* Proceedings of the National Academy of Sciences, 2008. **105**(33): p. 11623-11627.
123. Ford, R., *Carbon monoxide adsorption on the transition metals*, in *Advances in Catalysis*. 1970, Elsevier. p. 51-150.
124. Kundappaden, I. and R. Chatanathodi, *A DFT study of CO adsorption on pt (111) using van der Waals functionals.* Surface Science, 2019. **681**: p. 143-148.
125. Khan, N.A. and S.H. Jhung, *Adsorptive removal and separation of chemicals with metal-organic frameworks: Contribution of π-complexation.* Journal of hazardous materials, 2017. **325**: p. 198-213.
126. Ehrlich, G., *Low-Temperature Chemisorption. II. Flash Desorption of Carbon Monoxide.* The Journal of Chemical Physics, 1961. **34**(1): p. 39-46.
127. Föhlisch, A., et al., *How carbon monoxide adsorbs in different sites.* Physical review letters, 2000. **85**(15): p. 3309.
128. Zeinalipour-Yazdi, C.D., A.L. Cooksy, and A.M. Efstathiou, *CO adsorption on transition metal clusters: trends from density functional theory.* Surface science, 2008. **602**(10): p. 1858-1862.
129. Bagus, P.S., C.J. Nelin, and C.W. Bauschlicher Jr, *Bonding of CO to metal surfaces: a new interpretation.* Physical Review B, 1983. **28**(10): p. 5423.

130. Morterra, C., et al., *An infrared spectroscopic characterization of the coordinative adsorption of carbon monoxide on TiO2.* Spectrochimica Acta Part A: Molecular Spectroscopy, 1987. **43**(12): p. 1577-1581.
131. Bolis, V., et al., *Induced heterogeneity at the surface of group 4 dioxides as revealed by CO adsorption at room temperature.* Journal of the Chemical Society, Faraday Transactions, 1992. **88**(3): p. 391-398.
132. Bolis, V., et al., *Development and suppression of surface acidity on monoclinic zirconia: a spectroscopic and calorimetric investigation.* Langmuir, 1990. **6**(3): p. 695-701.
133. Mino, L., et al., *CO adsorption on anatase nanocrystals: a combined experimental and periodic DFT study.* The Journal of Physical Chemistry C, 2011. **115**(15): p. 7694-7700.
134. Garrone, E., et al., *Thermodynamics of CO adsorption on the zeolite Na-ZSM-5 A combined microcalorimetric and FTIR spectroscopic study.* Physical Chemistry Chemical Physics, 1999. **1**(4): p. 513-518.
135. Nachtigall, P., et al., *Computational and FTIR spectroscopic studies on carbon monoxide and dinitrogen adsorption on a high-silica H-FER zeolite.* Physical Chemistry Chemical Physics, 2009. **11**(5): p. 791-802.
136. Rubeš, M., et al., *Temperature dependence of carbon monoxide adsorption on a high-silica H-FER zeolite.* The Journal of Physical Chemistry C, 2018. **122**(45): p. 26088-26095.
137. Unger, K., *Structure of porous adsorbents.* Angewandte Chemie International Edition in English, 1972. **11**(4): p. 267-278.
138. Čejka, J., *Organized mesoporous alumina: synthesis, structure and potential in catalysis.* Applied Catalysis A: General, 2003. **254**(2): p. 327-338.
139. Rouquerol, J., et al., *Adsorption by powders and porous solids: principles, methodology and applications*. 2013: Academic press.
140. Santacesaria, E., D. Gelosa, and S. Carrà, *Basic behavior of alumina in the presence of strong acids.* Industrial & Engineering Chemistry Product Research and Development, 1977. **16**(1): p. 45-47.
141. Park, Y.S., et al., *Attrition characteristics of alumina catalyst for fluidized bed incinerator.* Korean Journal of Chemical Engineering, 2000. **17**(3): p. 284-287.
142. Samain, L., et al., *Structural analysis of highly porous γ-Al2O3.* Journal of Solid State Chemistry, 2014. **217**: p. 1-8.
143. Hu, C., et al., *Synthesis, characterization, and application of mesoporous alumina prepared from pseudo-boehmite as precursor.* Chemical Physics Letters, 2020. **742**: p. 137130.
144. Kim, Y., B. Lee, and J. Yi, *Synthesis of mesoporous γ-alumina through pre-and post-hydrolysis methods.* Korean Journal of Chemical Engineering, 2002. **19**(5): p. 908-910.
145. Cho, K., et al., *Synthesis of CuCl/Boehmite adsorbents that exhibit high CO selectivity in CO/CO2 separation.* Journal of hazardous materials, 2018. **344**: p. 857-864.
146. Yin, Y., et al., *Constructing a confined space in silica nanopores: an ideal platform for the formation and dispersion of cuprous sites.* Journal of Materials Chemistry A, 2014. **2**(10): p. 3399-3406.
147. Zhu, Q., et al., *Highly Porous Carbon Xerogels Doped with Cuprous Chloride for Effective CO Adsorption.* ACS omega, 2019. **4**(4): p. 6138-6143.
148. Auerbach, S.M., K.A. Carrado, and P.K. Dutta, *Handbook of zeolite science and technology*. 2003: CRC press.
149. Qin, L. and H.-G. Zheng, *Structures and applications of metal–organic frameworks featuring metal clusters.* CrystEngComm, 2017. **19**(5): p. 745-757.
150. Rosi, N.L., et al., *Rod packings and metal− organic frameworks constructed from rod-shaped secondary building units.* Journal of the American Chemical Society, 2005. **127**(5): p. 1504-1518.
151. Furukawa, H., et al., *The chemistry and applications of metal-organic frameworks.* Science, 2013. **341**(6149).
152. Liao, Y., et al., *Tuning ethylene gas adsorption via metal node modulation: Cu-MOF-74 for a high ethylene deliverable capacity.* Chemical Communications, 2017. **53**(67): p. 9376-9379.

153. Zhang, S., et al., *MOF-derived CoN/NC@ SiO2 yolk-shell nanoreactor with dual active sites for highly efficient catalytic advanced oxidation processes.* Chemical Engineering Journal, 2020. **381**: p. 122670.
154. Liu, G., et al., *MOF derived in-situ carbon-encapsulated Fe3O4@ C to mediate polysulfides redox for ultrastable Lithium-sulfur batteries.* Chemical Engineering Journal, 2020. **381**: p. 122652.
155. Jin, M., et al., *Spindle-Like MOF Derived TiO2@ NC–NCNTs Composite with Modulating Defect Site and Graphitization Nanoconfined Pt NPs as Superior Bifunctional Fuel Cell Electrocatalysts.* ACS Sustainable Chemistry & Engineering, 2020. **8**(4): p. 1933-1942.
156. Rashti, A., et al., *Electrophoretic Deposition of Nickel Cobaltite/Polyaniline/rGO Composite Electrode for High-Performance All-Solid-State Asymmetric Supercapacitors.* Energy & Fuels, 2020. **34**(5): p. 6448-6461.
157. Rashti, A., et al., *Tuning MOF-Derived Co3O4/NiCo2O4 Nanostructures for High-Performance Energy Storage.* ACS Applied Energy Materials, 2021. **4**(2): p. 1537–1547.
158. Xie, Y., et al., *Zeolites modified by CuCl for separating CO from gas mixtures containing CO 2.* Adsorption, 1997. **3**(1): p. 27-32.
159. Férey, G., et al., *A chromium terephthalate-based solid with unusually large pore volumes and surface area.* Science, 2005. **309**(5743): p. 2040-2042.
160. Munusamy, K., et al., *Sorption of carbon dioxide, methane, nitrogen and carbon monoxide on MIL-101 (Cr): volumetric measurements and dynamic adsorption studies.* Chemical engineering journal, 2012. **195**: p. 359-368.
161. Saha, D. and S. Deng, *Adsorption equilibria and kinetics of carbon monoxide on zeolite 5A, 13X, MOF-5, and MOF-177.* Journal of Chemical & Engineering Data, 2009. **54**(8): p. 2245-2250.
162. Adhoum, N. and L. Monser, *Removal of cyanide from aqueous solution using impregnated activated carbon.* Chemical Engineering and Processing: Process Intensification, 2002. **41**(1): p. 17-21.
163. Pevida, C., et al., *Surface modification of activated carbons for CO2 capture.* Applied Surface Science, 2008. **254**(22): p. 7165-7172.
164. Choi, S., et al., *Modification of the Mg/DOBDC MOF with amines to enhance CO2 adsorption from ultradilute gases.* The journal of physical chemistry letters, 2012. **3**(9): p. 1136-1141.
165. Ahmadi, Z., et al., *Application of lasers in the synthesis and processing of two-dimensional quantum materials.* Journal of Laser Applications, 2019. **31**(3): p. 031202.
166. Zhang, D., et al., *Carbon-encapsulated metal/metal carbide/metal oxide core–shell nanostructures generated by laser ablation of metals in organic solvents.* ACS Applied Nano Materials, 2018. **2**(1): p. 28-39.
167. Lam, D.V., et al., *Laser Synthesis of MOF-Derived Ni@ Carbon for High-Performance Pseudocapacitors.* ACS Applied Materials & Interfaces, 2020.
168. Zhang, X., et al., *Comparison of adsorption mechanisms for cadmium removal by modified zeolites and sands coated with Zn-layered double hydroxides.* Chemical Engineering Journal, 2020. **380**: p. 122578.
169. Fatah, N., et al., *Favored hydrogenation of linear carbon monoxide over cobalt loaded on fibrous silica KCC-1.* International Journal of Hydrogen Energy, 2020. **45**(16): p. 9522-9534.
170. Ahmadi, Z., et al., *Self-limiting laser crystallization and direct writing of 2D materials.* International Journal of Extreme Manufacturing, 2019. **1**(1): p. 015001.
171. Yang, R. and E. Kikkinides, *New sorbents for olefin/paraffin separations by adsorption via π-complexation.* AIChE Journal, 1995. **41**(3): p. 509-517.
172. Cheng, L.S. and R.T. Yang, *Monolayer cuprous chloride dispersed on pillared clays for olefin-paraffin separations by π-complexation.* Adsorption, 1995. **1**(1): p. 61-75.
173. Hirai, H., K. Wada, and M. Komiyama, *Active carbon-supported copper (I) chloride as solid adsorbent for carbon monoxide.* Bulletin of the Chemical Society of Japan, 1986. **59**(7): p. 2217-2223.

174. Yoon, J.W., et al., *Highly selective adsorption of CO over CO2 in a Cu (I)-chelated porous organic polymer.* Journal of hazardous materials, 2018. **341**: p. 321-327.
175. Wang, Y., R.T. Yang, and J.M. Heinzel, *Desulfurization of jet fuel by π-complexation adsorption with metal halides supported on MCM-41 and SBA-15 mesoporous materials.* Chemical Engineering Science, 2008. **63**(2): p. 356-365.
176. Hernández-Maldonado, A.J. and R.T. Yang, *Desulfurization of commercial liquid fuels by selective adsorption via π-complexation with Cu (I)− Y zeolite.* Industrial & engineering chemistry research, 2003. **42**(13): p. 3103-3110.
177. Li, H., et al., *Palladium nanoparticles confined in the cages of MIL-101: an efficient catalyst for the one-pot indole synthesis in water.* ACS Catalysis, 2011. **1**(11): p. 1604-1612.
178. Wang, Y., R.T. Yang, and J.M. Heinzel, *Desulfurization of jet fuel JP-5 light fraction by MCM-41 and SBA-15 supported cuprous oxide for fuel cell applications.* Industrial & Engineering Chemistry Research, 2009. **48**(1): p. 142-147.
179. Kou, J., et al., *Facile fabrication of cuprous oxide-based adsorbents for deep desulfurization.* ACS Sustainable Chemistry & Engineering, 2015. **3**(12): p. 3053-3061.
180. Wang, Y. and Y. Lin, *Sol-gel synthesis and gas adsorption properties of CuCl modified mesoporous alumina.* Journal of sol-gel science and technology, 1998. **11**(2): p. 185-195.
181. Aijaz, A., et al., *Immobilizing highly catalytically active Pt nanoparticles inside the pores of metal–organic framework: a double solvents approach.* Journal of the American Chemical Society, 2012. **134**(34): p. 13926-13929.
182. Chang, G., et al., *Fabrication of cuprous nanoparticles in MIL-101: an efficient adsorbent for the separation of olefin–paraffin mixtures.* RSC advances, 2014. **4**(39): p. 20230-20233.
183. Khan, N.A. and S.H. Jhung, *Low-temperature loading of Cu+ species over porous metal-organic frameworks (MOFs) and adsorptive desulfurization with Cu+-loaded MOFs.* Journal of hazardous materials, 2012. **237**: p. 180-185.
184. Khan, N.A. and S.H. Jhung, *Remarkable adsorption capacity of CuCl2-loaded porous vanadium benzenedicarboxylate for benzothiophene.* Angewandte Chemie International Edition, 2012. **51**(5): p. 1198-1201.
185. Horcajada, P., et al., *Synthesis and catalytic properties of MIL-100 (Fe), an iron (III) carboxylate with large pores.* Chemical Communications, 2007(27): p. 2820-2822.
186. Xie, Y., et al., *Highly regenerable mussel-inspired Fe3O4@ polydopamine-Ag core–shell microspheres as catalyst and adsorbent for methylene blue removal.* ACS applied materials & interfaces, 2014. **6**(11): p. 8845-8852.
187. Liu, R., et al., *Core–shell Fe3O4 polydopamine nanoparticles serve multipurpose as drug carrier, catalyst support and carbon adsorbent.* ACS applied materials & interfaces, 2013. **5**(18): p. 9167-9171.
188. Jiang, W.-J., et al., *Fabrication of supported cuprous sites at low temperatures: an efficient, controllable strategy using vapor-induced reduction.* Journal of the American Chemical Society, 2013. **135**(22): p. 8137-8140.
189. Ahmed, I. and S.H. Jhung, *Adsorptive denitrogenation of model fuel with CuCl-loaded metal–organic frameworks (MOFs).* Chemical Engineering Journal, 2014. **251**: p. 35-42.
190. Gao, F., Y. Wang, and S. Wang, *Selective adsorption of CO on CuCl/Y adsorbent prepared using CuCl2 as precursor: Equilibrium and thermodynamics.* Chemical Engineering Journal, 2016. **290**: p. 418-427.
191. Park, Y., et al., *Adsorption equilibria and kinetics of six pure gases on pelletized zeolite 13X up to 1.0 MPa: CO2, CO, N2, CH4, Ar and H2.* Chemical Engineering Journal, 2016. **292**: p. 348-365.
192. Rakić, V., et al., *Competitive adsorption of N2O and CO on CuZSM-5, FeZSM-5, CoZSM-5 and bimetallic forms of ZSM-5 zeolite.* Catalysis today, 2005. **110**(3-4): p. 272-280.
193. Yin, Y., et al., *Modification of metal organic framework HKUST-1 with CuCl for selective separation of CO/H 2 and CO/N 2.* Journal of Porous Materials, 2018. **25**(5): p. 1513-1519.

194. Yin, Y., et al., *Cuprous/Vanadium Sites on MIL-101 for Selective CO Adsorption from Gas Mixtures with Superior Stability.* ACS Sustainable Chemistry & Engineering, 2019.
195. Wang, Y., et al., *CuAlCl4 doped MIL-101 as a high capacity CO adsorbent with selectivity over N2.* Frontiers of Chemical Science and Engineering, 2014. **8**(3): p. 340-345.
196. Sethia, G., R.S. Somani, and H.C. Bajaj, *Adsorption of carbon monoxide, methane and nitrogen on alkaline earth metal ion exchanged zeolite-X: structure, cation position and adsorption relationship.* RSC advances, 2015. **5**(17): p. 12773-12781.
197. DeCoste, J.B. and G.W. Peterson, *Metal–organic frameworks for air purification of toxic chemicals.* Chemical reviews, 2014. **114**(11): p. 5695-5727.
198. Bae, Y.S. and R.Q. Snurr, *Development and evaluation of porous materials for carbon dioxide separation and capture.* Angewandte Chemie International Edition, 2011. **50**(49): p. 11586-11596.
199. Subramanian, R.S., *Flow through packed beds and fluidized beds.* URL: http://www. pdfdrive. com/flow-through-packed-bedsand-fluidized-beds-clarkson-university-e1826488. html (Accessed 21 February 2017), 2004.
200. Xubiao Luo, F.D., *Nanomaterials for the Removal of Pollutants and Resource Reutilization*, in *Nanomaterials for the Removal of Pollutants and Resource Reutilization*, X.L.F. Deng, Editor. 2019, Elsevier. p. 312.
201. Zhang, Z., et al., *Enhancement of CO2 adsorption on high surface area activated carbon modified by N2, H2 and ammonia.* Chemical Engineering Journal, 2010. **160**(2): p. 571-577.
202. Plaza, M., et al., *Evaluation of ammonia modified and conventionally activated biomass based carbons as CO2 adsorbents in postcombustion conditions.* Separation and purification technology, 2011. **80**(1): p. 96-104.
203. Wang, J., et al., *Preparation and CO2 adsorption of amine modified Mg–Al LDH via exfoliation route.* Chemical Engineering Science, 2012. **68**(1): p. 424-431.
204. Stevens, L., et al., *Preparation and CO2 adsorption of diamine modified montmorillonite via exfoliation grafting route.* Chemical Engineering Journal, 2013. **215**: p. 699-708.
205. Shafeeyan, M.S., et al., *Modeling of carbon dioxide adsorption onto ammonia-modified activated carbon: kinetic analysis and breakthrough behavior.* Energy & Fuels, 2015. **29**(10): p. 6565-6577.
206. Miao, Z., et al., *Cation-induced fast growth of ultrathin cuprous chloride nanoplatelets.* CrystEngComm, 2016. **18**(19): p. 3340-3342.
207. Molinder, R., et al., *In situ X-ray diffraction of CaO based CO 2 sorbents.* Energy & Environmental Science, 2012. **5**(10): p. 8958-8969.
208. *NOVAWin & NOVAWin-P version 10.0+*, in *Characterizing Porous Materials and Powders*. 2008, Quantachrome instruments. p. 100.
209. Raganati, F., et al., *Kinetic study and breakthrough analysis of the hybrid physical/chemical CO2 adsorption/desorption behavior of a magnetite-based sorbent.* Chemical Engineering Journal, 2019. **372**: p. 526-535.
210. Feyzbar-Khalkhali-Nejad, F., et al., *Adsorption-based CO removal: principles and materials.* Journal of Environmental Chemical Engineering, 2021: p. 105317.
211. Keller, A., R. Schendel, and C. DENVER. *The use of COSORB II to recover high purity carbon monoxide from a feed gas*. in *Kinetics Technology International Corporation, California, AICHE Summer Meeting*. 1988.
212. Sujan, A.R., et al., *Poly (glycidyl amine)-Loaded SBA-15 Sorbents for CO2 Capture from Dilute and Ultradilute Gas Mixtures.* ACS Applied Polymer Materials, 2019. **1**(11): p. 3137-3147.
213. Sujan, A.R., et al., *Direct CO2 capture from air using poly (ethylenimine)-loaded polymer/silica fiber sorbents.* ACS Sustainable Chemistry & Engineering, 2019. **7**(5): p. 5264-5273.
214. Kang, P.-C., et al., *Room-Temperature Hydrogen Adsorption via Spillover in Pt Nanoparticle-Decorated UiO-66 Nanoparticles: Implications for Hydrogen Storage.* ACS Applied Nano Materials, 2021. **4**(10): p. 11269-11280.
215. Relvas, F., et al., *Single-stage pressure swing adsorption for producing fuel cell grade hydrogen.* Industrial & Engineering Chemistry Research, 2018. **57**(14): p. 5106-5118.

216. Xiang, C., et al., *Tracking internal electron shuttle using X-ray spectroscopies in La/Zr hydroxide for reconciliation of charge-transfer interaction and coordination toward phosphate.* ACS applied materials & interfaces, 2019. **11**(27): p. 24699-24706.
217. Xiong, Y., et al., *Construction of Dual-Active-Site Copper Catalyst Containing both Cu□ N3 and Cu□ N4 Sites.* Small, 2021. **17**(8): p. 2006834.
218. Liu, H., et al., *Dual active site tandem catalysis of metal hydroxyl oxides and single atoms for boosting oxygen evolution reaction.* Applied Catalysis B: Environmental, 2021: p. 120451.
219. Zhang, Z., et al., *Tuning the dual-active sites of ZIF-67 derived porous nanomaterials for boosting oxygen catalysis and rechargeable Zn-air batteries.* Nano Research, 2021. **14**(7): p. 2353-2362.
220. Liu, N., et al., *Auδ−–Ov–Ti3+ interfacial site: catalytic active center toward low-temperature water gas shift reaction.* ACS Catalysis, 2019. **9**(4): p. 2707-2717.
221. Fu, J., Y. Yang, and J.-S. Hu, *Dual-Sites Tandem Catalysts for C–N Bond Formation via Electrocatalytic Coupling of CO2 and Nitrogenous Small Molecules.* ACS Materials Letters, 2021. **3**(10): p. 1468-1476.
222. Xue, C., et al., *Effects of pore size distribution of activated carbon (AC) on CuCl dispersion and CO adsorption for CuCl/AC adsorbent.* Chemical Engineering Journal, 2019. **375**: p. 122049.
223. Klopman, G., *Chemical reactivity and the concept of charge-and frontier-controlled reactions.* Journal of the American Chemical Society, 1968. **90**(2): p. 223-234.
224. Tamon, H., K. Kitamura, and M. Okazaki, *Adsorption of carbon monoxide on activated carbon impregnated with metal halide.* AIChE Journal, 1996. **42**(2): p. 422-430.
225. Chen, S., et al., *Probing surface structures of CeO2, TiO2, and Cu2O nanocrystals with CO and CO2 chemisorption.* The Journal of Physical Chemistry C, 2016. **120**(38): p. 21472-21485.
226. Wei, B., et al., *Cu2O–CuO hollow nanospheres as a heterogeneous catalyst for synergetic oxidation of CO.* The Journal of Physical Chemistry C, 2018. **122**(34): p. 19524-19531.
227. Rudzinski, W. and D.H. Everett, *Adsorption of gases on heterogeneous surfaces*. 2012: Academic Press.
228. Yan, B., C.H. Niu, and R. Feng, *Site Energy Distribution and X-ray Analyses of Nickel Loaded on Heterogeneous Adsorbents.* Industrial & Engineering Chemistry Research, 2017. **56**(29): p. 8283-8291.
229. He, J., et al., *Analysis of 17α-ethinylestradiol and bisphenol A adsorption on anthracite surfaces by site energy distribution.* Chemosphere, 2019. **216**: p. 59-68.
230. Kumar, K.V., et al., *Site energy distribution function for the sips isotherm by the condensation approximation method and its application to characterization of porous materials.* Journal of Chemical & Engineering Data, 2011. **56**(5): p. 2218-2224.
231. Ozawa, S., S. Kusumi, and Y. Ogino, *Physical adsorption of gases at high pressure. IV. An improvement of the Dubinin—Astakhov adsorption equation.* Journal of Colloid and Interface Science, 1976. **56**(1): p. 83-91.
232. Wjihi, S., et al., *Advanced interpretation of CO2 adsorption thermodynamics onto porous solids by statistical physics formalism.* Chemical Engineering Journal, 2021. **406**: p. 126669.
233. Hust, J.G. and R.B. Stewart, *Thermodynamic Property Values for Gaseous and Liquid Carbon Monoxide from 70 to 3000 K with Pressures to 300 Atmospheres*. Vol. 202. 1963: US Department of Commerce, National Bureau of Standards.
234. Carter, M.C., J.E. Kilduff, and W.J. Weber, *Site energy distribution analysis of preloaded adsorbents.* Environmental Science & Technology, 1995. **29**(7): p. 1773-1780.
235. Kim, J.Y., et al., *Reduction of CuO and Cu2O with H2: H embedding and kinetic effects in the formation of suboxides.* Journal of the American Chemical Society, 2003. **125**(35): p. 10684-10692.
236. Zhang, F., et al., *A green method for preparing CuCl nanocrystal in deep eutectic solvent.* Australian Journal of Chemistry, 2012. **66**(2): p. 237-240.
237. Lutterotti, L., *Maud: a Rietveld analysis program designed for the internet and experiment integration.* Acta Crystallographica Section A, 2000. **56**(s1): p. s54.

238. Hassani, E., et al., *Ca2CuO3: A high temperature CO2 sorbent with rapid regeneration kinetics.* Journal of Environmental Chemical Engineering, 2022: p. 107334.
239. Walton, K.S. and D.S. Sholl, *Predicting multicomponent adsorption: 50 years of the ideal adsorbed solution theory.* AIChE Journal, 2015. **61**(9): p. 2757-2762.
240. Khalili, S., B. Khoshandam, and M. Jahanshahi, *A comparative study of CO 2 and CH 4 adsorption using activated carbon prepared from pine cone by phosphoric acid activation.* Korean Journal of Chemical Engineering, 2016. **33**(10): p. 2943-2952.
241. Abdelnaby, M.M., et al., *A microporous organic copolymer for selective CO2 capture under humid conditions.* ACS Sustainable Chemistry & Engineering, 2019. **7**(16): p. 13941-13948.
242. Lawson, S. and F. Rezaei, *Effects of Process Parameters on CO2/H2 Separation Performance of 3D-Printed MOF-74 Monoliths.* ACS Sustainable Chemistry & Engineering, 2021. **9**(32): p. 10902-10912.
243. Khoramzadeh, E., M. Mofarahi, and C.-H. Lee, *Equilibrium adsorption study of CO2 and N2 on synthesized zeolites 13X, 4A, 5A, and Beta.* Journal of Chemical & Engineering Data, 2019. **64**(12): p. 5648-5664.
244. Serna-Guerrero, R. and A. Sayari, *Modeling adsorption of CO2 on amine-functionalized mesoporous silica. 2: Kinetics and breakthrough curves.* Chemical Engineering Journal, 2010. **161**(1-2): p. 182-190.
245. Wang, X., L. Chen, and Q. Guo, *Development of hybrid amine-functionalized MCM-41 sorbents for CO2 capture.* Chemical Engineering Journal, 2015. **260**: p. 573-581.
246. Li, Z., et al., *Adsorption behaviors of near-critical carbon dioxide on organic-rich shales: Modeling, multifractality, and kinetics.* Chemical Engineering Journal, 2022. **428**: p. 132526.
247. Liu, Y. and X. Yu, *Carbon dioxide adsorption properties and adsorption/desorption kinetics of amine-functionalized KIT-6.* Applied energy, 2018. **211**: p. 1080-1088.
248. Benedict, J.B. and P. Coppens, *Kinetics of the single-crystal to single-crystal two-photon photodimerization of α-trans-cinnamic acid to α-truxillic acid.* The Journal of Physical Chemistry A, 2009. **113**(13): p. 3116-3120.
249. Cychosz, K.A., et al., *Recent advances in the textural characterization of hierarchically structured nanoporous materials.* Chemical Society Reviews, 2017. **46**(2): p. 389-414.
250. Badillo-Avila, M., et al., *Fast rate oxidation to Cu2O, at room temperature, of metallic copper films produced by the argon-plasma bombardment of CuO films.* Materials Chemistry and Physics, 2019. **236**: p. 121759.
251. Platzman, I., et al., *Oxidation of polycrystalline copper thin films at ambient conditions.* The Journal of Physical Chemistry C, 2008. **112**(4): p. 1101-1108.
252. Rai, B., *Optical transmittance of thin copper films in the visible region.* physica status solidi (a), 1987. **99**(1): p. K35-K39.
253. Ho, C., et al., *High-temperature stability of Au/Pd/Cu and Au/Pd (P)/Cu surface finishes.* Applied Surface Science, 2018. **434**: p. 1353-1360.
254. Tanvir, N.B., et al., *Investigation of CO2 reaction with copper oxide nanoparticles for room temperature gas sensing.* Journal of Materials Chemistry A, 2016. **4**(14): p. 5294-5302.
255. Yang, Y., et al., *Spontaneous Symmetry-Breaking in the Corrosion Transformation of Ancient Bronzes.* Minerals, 2020. **10**(8): p. 656.
256. Lee, S., et al., *Copper oxide reduction through vacuum annealing.* Applied Surface Science, 2003. **206**(1-4): p. 102-109.
257. Popp, N., et al., *Porous imine-based networks with protonated imine linkages for carbon dioxide separation from mixtures with nitrogen and methane.* Journal of Materials Chemistry A, 2015. **3**(36): p. 18492-18504.
258. Isahak, W.N.R.W., et al., *Adsorption–desorption of CO2 on different type of copper oxides surfaces: Physical and chemical attractions studies.* Journal of CO2 Utilization, 2013. **2**: p. 8-15.

259. Vo, T.K., et al., *Cost-effective and eco-friendly synthesis of MIL-101 (Cr) from waste hexavalent chromium and its application for carbon monoxide separation.* Journal of Industrial and Engineering Chemistry, 2019. **80**: p. 345-351.
260. Vo, T.K., et al., *A novel approach to prepare Cu (I) Zn@ MIL-100 (Fe) adsorbent with high CO adsorption capacity, CO/CO2 selectivity and stability via controlled host–guest redox reaction.* Chemical Engineering Journal, 2021. **404**: p. 126492.
261. Vo, T.K., J. Kim, and D.T. Quang, *Chelating Cu-N within Cu+-incorporated MIL-101 (Cr)-NH2 framework for enhanced CO adsorption and CO/CO2 selectivity.* Colloids and Surfaces A: Physicochemical and Engineering Aspects, 2022. **635**: p. 128076.
262. Sing, K.S.W., *Reporting physisorption data for gas/solid systems with special reference to the determination of surface area and porosity (Recommendations 1984).* Pure and Applied Chemistry, 1985. **57**(4): p. 603-619.
263. Prasetyo, I. and D. Do, *Adsorption kinetics of light paraffins in AC by a constant molar flow-rate method.* AIChE journal, 1999. **45**(9): p. 1892-1900.
264. He, H., et al., *Structure design of a hyperbranched polyamine adsorbent for CO 2 adsorption.* Green Chemistry, 2016. **18**(21): p. 5859-5869.
265. Avgouropoulos, G. and T. Ioannides, *TPD and TPSR study of CO interaction with CuO–CeO2 catalysts.* Journal of Molecular Catalysis A: Chemical, 2008. **296**(1-2): p. 47-53.
266. Luo, J., et al., *Insight into the chemical adsorption properties of CO molecules supported on Au or Cu and hybridized Au–CuO nanoparticles.* Nanoscale, 2017. **9**(39): p. 15033-15043.
267. Mukherjee, S., et al., *Nanocellulose-reinforced organo-inorganic nanocomposite for synergistic and affordable defluoridation of water and an evaluation of its sustainability metrics.* ACS Sustainable Chemistry & Engineering, 2019. **8**(1): p. 139-147.
268. Jiménez-González, C., D.J. Constable, and C.S. Ponder, *Evaluating the "Greenness" of chemical processes and products in the pharmaceutical industry—a green metrics primer.* Chemical Society Reviews, 2012. **41**(4): p. 1485-1498.
269. Feyzbar-Khalkhali-Nejad, F., et al., *Adsorption-based CO removal: Principles and materials.* Journal of Environmental Chemical Engineering, 2021. **9**(4): p. 105317.
270. Hassani, E., et al., *Ca2CuO3: A high temperature CO2 sorbent with rapid regeneration kinetics.* Journal of Environmental Chemical Engineering, 2022. **10**(2): p. 107334.
271. Hassani, E., et al., *Solid-state decomposition of Ca2CuO3 enhances its CO2 reactivity and cycle stability.* Fuel, 2023. **332**: p. 126160.
272. Taghavi Kouzehkanan, S.M., et al., *Calcium-Based Sorbent Carbonation at Low Temperature via Reactive Milling under CO2.* Inorganics, 2023. **11**(5): p. 200.
273. Feyzbar-Khalkhali-Nejad, F., et al., *A highly stable CuO-derived adsorbent with dual Cu (I) sites for selective CO adsorption.* Separation and Purification Technology, 2022. **290**: p. 120906.
274. Zhu, G., et al., *Synthesis of zeolite@ metal–organic framework core–shell particles as bifunctional catalysts.* RSC advances, 2014. **4**(58): p. 30673-30676.
275. Herm, Z.R., et al., *Metal− organic frameworks as adsorbents for hydrogen purification and precombustion carbon dioxide capture.* Journal of the American Chemical Society, 2011. **133**(15): p. 5664-5667.
276. He, Y., et al., *A microporous metal–organic framework assembled from an aromatic tetracarboxylate for H 2 purification.* Journal of Materials Chemistry A, 2013. **1**(7): p. 2543-2551.
277. Qingyuan, Y., et al., *Molecular simulation of CO2/H2 mixture separation in metal-organic frameworks: Effect of catenation and electrostatic interactions.* Chinese Journal of Chemical Engineering, 2009. **17**(5): p. 781-790.
278. Huang, W., et al., *Preparation and adsorption performance of GrO@ Cu-BTC for separation of CO2/CH4.* Industrial & Engineering Chemistry Research, 2014. **53**(27): p. 11176-11184.
279. Tate, K.L., et al., *Zeolite adsorbent-MOF layered nanovalves for CH 4 storage.* Adsorption, 2017. **23**: p. 19-24.

280. Zhao, J., et al., *Facile conversion of hydroxy double salts to metal–organic frameworks using metal oxide particles and atomic layer deposition thin-film templates.* Journal of the American Chemical Society, 2015. **137**(43): p. 13756-13759.
281. Meyn, M., K. Beneke, and G. Lagaly, *Anion-exchange reactions of hydroxy double salts.* Inorganic Chemistry, 1993. **32**(7): p. 1209-1215.
282. Crawford, S.E., et al., *Rapid, selective, ambient growth and optimization of copper benzene-1, 3, 5-tricarboxylate (Cu–BTC) metal–organic framework thin films on a conductive metal oxide.* Crystal Growth & Design, 2018. **18**(5): p. 2924-2931.
283. Hadjiivanov, K., H. Knözinger, and M. Mihaylov, *FTIR study of CO adsorption on Ni− ZSM-5.* The Journal of Physical Chemistry B, 2002. **106**(10): p. 2618-2624.
284. Czaja, A.U., N. Trukhan, and U. Müller, *Industrial applications of metal–organic frameworks.* Chemical Society Reviews, 2009. **38**(5): p. 1284-1293.
285. Xue, C., Q. Yang, and C. Zhong, *Effects of the side pockets on gas separation in metal-organic framework Cu-BTC: a molecular simulation study.* Molecular Simulation, 2009. **35**(15): p. 1249-1255.
286. Szanyi, J., et al., *Well-studied Cu–BTC still serves surprises: Evidence for facile Cu 2+/Cu+ interchange.* Physical Chemistry Chemical Physics, 2012. **14**(13): p. 4383-4390.
287. Marx, S., W. Kleist, and A. Baiker, *Synthesis, structural properties, and catalytic behavior of Cu-BTC and mixed-linker Cu-BTC-PyDC in the oxidation of benzene derivatives.* Journal of catalysis, 2011. **281**(1): p. 76-87.
288. Ferreira, A.F., et al., *Suitability of Cu-BTC extrudates for propane–propylene separation by adsorption processes.* Chemical engineering journal, 2011. **167**(1): p. 1-12.
289. Ghazvini, M.F., et al., *Investigation of the MOF adsorbents and the gas adsorptive separation mechanisms.* Journal of Environmental Chemical Engineering, 2021. **9**(1): p. 104790.
290. Ahmed, A., et al., *Cu (i) Cu (ii) BTC, a microporous mixed-valence MOF via reduction of HKUST-1.* RSC advances, 2016. **6**(11): p. 8902-8905.
291. Dauda, I.B., et al., *Highly selective hierarchical ZnO/ZSM-5 catalysts for propane aromatization.* ACS omega, 2020. **5**(6): p. 2725-2733.
292. Oseke, G.G., et al., *Highly selective and stable Zn–Fe/ZSM-5 catalyst for aromatization of propane.* Applied Petrochemical Research, 2020. **10**: p. 55-65.
293. Tan, X., et al., *Restructuring of Cu2O to Cu2O@ Cu-metal–organic frameworks for selective electrochemical reduction of CO2.* ACS Applied Materials & Interfaces, 2019. **11**(10): p. 9904-9910.
294. Chen, Y., et al., *Structure–Property–Energetics Relationship of Organosulfide Capture Using Cu (I)/Cu (II)-BTC Edited by Valence Engineering.* Industrial & Engineering Chemistry Research, 2020. **60**(1): p. 371-377.
295. Lutterotti, L., *Maud: a Rietveld analysis program designed for the internet and experiment integration.* Acta Crystallogr. A, 2000. **56**(s1): p. 54.
296. Caldwell, S.J., et al., *Carbon dioxide separation from nitrogen/hydrogen mixtures over activated carbon beads: adsorption isotherms and breakthrough studies.* Energy & Fuels, 2015. **29**(6): p. 3796-3807.
297. Goel, C., H. Bhunia, and P.K. Bajpai, *Prediction of binary gas adsorption of CO2/N2 and thermodynamic studies on nitrogen enriched nanostructured carbon adsorbents.* Journal of Chemical & Engineering Data, 2017. **62**(1): p. 214-225.
298. Sochard, S., N. Fernandes, and J.M. Reneaume, *Modeling of adsorption isotherm of a binary mixture with real adsorbed solution theory and nonrandom two-liquid model.* AIChE journal, 2010. **56**(12): p. 3109-3119.
299. Ridha, F.N. and P.A. Webley, *Entropic effects and isosteric heats of nitrogen and carbon dioxide adsorption on chabazite zeolites.* Microporous and mesoporous materials, 2010. **132**(1-2): p. 22-30.

300. Jesudoss, S., et al., *Retraction: Anti-cancer activity of hierarchical ZSM-5 zeolites synthesized from rice-based waste materials.* RSC advances, 2022. **12**(37): p. 24139-24139.
301. Pelicano, C.M., N.J. Rapadas, and E. Magdaluyo Jr. *X-ray peak profile analysis of zinc oxide nanoparticles formed by simple precipitation method*. in *AIP Conference Proceedings*. 2017. AIP Publishing LLC.
302. Cardiel, A.C., K.J. McDonald, and K.-S. Choi, *Electrochemical growth of copper hydroxy double salt films and their conversion to nanostructured p-type CuO photocathodes.* Langmuir, 2017. **33**(37): p. 9262-9270.
303. Xin, C., et al., *Effect of various alkaline agents on the size and morphology of nano-sized HKUST-1 for CO 2 adsorption.* RSC Advances, 2015. **5**(35): p. 27901-27911.
304. Zacher, D., et al., *Nanocrystals of [Cu 3 (btc) 2](HKUST-1): a combined time-resolved light scattering and scanning electron microscopy study.* Chemical communications, 2009(9): p. 1031-1033.
305. Powell, K.J., et al., *Chemical speciation of environmentally significant metals with inorganic ligands Part 2: The Cu2+-OH-, Cl-, CO32-, SO42-, and PO43-systems (IUPAC Technical Report).* Pure and Applied Chemistry, 2007. **79**(5): p. 895-950.
306. Cychosz, K.A. and M. Thommes, *Progress in the physisorption characterization of nanoporous gas storage materials.* Engineering, 2018. **4**(4): p. 559-566.
307. Thommes, M., et al., *Physisorption of gases, with special reference to the evaluation of surface area and pore size distribution (IUPAC Technical Report).* Pure and applied chemistry, 2015. **87**(9-10): p. 1051-1069.
308. Ameloot, R., et al., *Direct patterning of oriented metal–organic framework crystals via control over crystallization kinetics in clear precursor solutions.* Advanced materials, 2010. **22**(24): p. 2685-2688.
309. Zhuang, J.L., et al., *Rapid room-temperature synthesis of metal–organic framework HKUST-1 crystals in bulk and as oriented and patterned thin films.* Advanced functional materials, 2011. **21**(8): p. 1442-1447.
310. Gascon, J., S. Aguado, and F. Kapteijn, *Manufacture of dense coatings of Cu3 (BTC) 2 (HKUST-1) on α-alumina.* Microporous and Mesoporous Materials, 2008. **113**(1-3): p. 132-138.
311. Khan, N.A. and S.-H. Jhung, *Facile syntheses of metal-organic framework Cu 3 (BTC) 2 (H 2 O) 3 under ultrasound.* Bulletin of the Korean Chemical Society, 2009. **30**(12): p. 2921-2926.
312. Khoshhal, S., et al., *Study of the temperature and solvent content effects on the structure of Cu–BTC metal organic framework for hydrogen storage.* RSC Advances, 2015. **5**(31): p. 24758-24768.
313. Majano, G. and J. Pérez-Ramírez, *Room Temperature Synthesis and Size Control of HKUST-1.* Helvetica Chimica Acta, 2012. **95**(11): p. 2278-2286.
314. Chen, H., et al., *Boosting photocatalytic performance in mixed-valence MIL-53 (Fe) by changing FeII/FeIII ratio.* ACS Applied Materials & Interfaces, 2019. **11**(32): p. 28791-28800.
315. Vitillo, J.G., et al., *Role of exposed metal sites in hydrogen storage in MOFs.* Journal of the American Chemical Society, 2008. **130**(26): p. 8386-8396.
316. Wang, D., et al., *Manipulating oxidation states of copper within Cu-BTC using Na2S2O3 as a new strategy for enhanced adsorption of sulfide.* Industrial & Engineering Chemistry Research, 2019. **58**(42): p. 19503-19510.
317. Othman, I., et al., *Synthesis and modification of ZSM-5 with manganese and lanthanum and their effects on decolorization of indigo carmine dye.* Applied Catalysis A: General, 2006. **299**: p. 95-102.
318. Huang, J., et al., *Characterization and acidic properties of aluminum-exchanged zeolites X and Y.* The Journal of Physical Chemistry C, 2008. **112**(10): p. 3811-3818.
319. Radosavljević-Mihajlović, A.S., et al., *Physicochemical and structural characteristics of HEU-type zeolitic tuff treated by hydrochloric acid.* Journal of the Serbian Chemical Society, 2004. **69**(4): p. 273-282.

320. Costa Hernandez, A.N., *Gas-phase adsorption in dealuminated natural clinoptilolite and liquid-phase adsorption in commercial DAY zeolite and modified ammonium Y zeolite*. 2013, Universidad del Turabo (Puerto Rico): United States -- Puerto Rico. p. 147.
321. Wang, W. and D. Yuan, *Mesoporous carbon originated from non-permanent porous MOFs for gas storage and CO2/CH4 separation.* Scientific Reports, 2014. **4**(1): p. 5711.
322. Yan, X., et al., *Extremely enhanced CO2 uptake by HKUST-1 metal–organic framework via a simple chemical treatment.* Microporous and mesoporous materials, 2014. **183**: p. 69-73.
323. Zhang, Z., Z. Li, and J. Li, *Computational study of adsorption and separation of CO2, CH4, and N2 by an rht-type metal–organic framework.* Langmuir, 2012. **28**(33): p. 12122-12133.
324. Choi, H.J. and S.B. Hong, *Effect of framework Si/Al ratio on the mechanism of CO2 adsorption on the small-pore zeolite gismondine.* Chemical Engineering Journal, 2022. **433**: p. 133800.
325. Rubeš, M., et al., *Combined theoretical and experimental investigation of CO adsorption on coordinatively unsaturated sites in CuBTC MOF.* ChemPhysChem, 2012. **13**(2): p. 488-495.
326. Karra, J.R. and K.S. Walton, *Effect of open metal sites on adsorption of polar and nonpolar molecules in metal− organic framework Cu-BTC.* Langmuir, 2008. **24**(16): p. 8620-8626.
327. Kim, J., H.-Y. Cho, and W.-S. Ahn, *Synthesis and adsorption/catalytic properties of the metal organic framework CuBTC.* Catalysis Surveys from Asia, 2012. **16**: p. 106-119.
328. Du, Z., et al., *Comparative analysis of calculation method of adsorption isosteric heat: Case study of CO2 capture using MOFs.* Microporous and Mesoporous Materials, 2020. **298**: p. 110053.
329. Grajciar, L., et al., *Understanding CO2 adsorption in CuBTC MOF: comparing combined DFT–ab initio calculations with microcalorimetry experiments.* The Journal of Physical Chemistry C, 2011. **115**(36): p. 17925-17933.
330. Wilson, S.M. and F.H. Tezel, *CO2 and CO adsorption equilibrium on ZSM-5 for different SiO2/Al2O3 ratios.* Separation Science and Technology, 2019. **54**(5): p. 722-730.
331. Choudhary, V. and S. Mayadevi, *Adsorption of methane, ethane, ethylene, and carbon dioxide on high silica pentasil zeolites and zeolite-like materials using gas chromatography pulse technique.* Separation science and Technology, 1993. **28**(13-14): p. 2197-2209.
332. Harlick, P. and F. Tezel, *Adsorption of carbon dioxide, methane and nitrogen: pure and binary mixture adsorption for ZSM-5 with SiO2/Al2O3 ratio of 280.* Separation and purification technology, 2003. **33**(2): p. 199-210.
333. Harlick, P. and F. Tezel, *Adsorption of carbon dioxide, methane, and nitrogen: pure and binary mixture adsorption by ZSM-5 with SiO2/Al2O3 ratio of 30.* Separation science and technology, 2002. **37**(1): p. 33-60.
334. Fang, H., et al., *A strong test of atomically detailed models of molecular adsorption in zeolites using multilaboratory experimental data for CO2 adsorption in ammonium ZSM-5.* The Journal of Physical Chemistry Letters, 2019. **11**(2): p. 471-477.
335. Newsome, D., et al., *Adsorption of CO 2 and N 2 in Na–ZSM-5: effects of Na+ and Al content studied by Grand Canonical Monte Carlo simulations and experiments.* Adsorption, 2014. **20**: p. 157-171.
336. Madani, S.H., et al., *Analysis of adsorbate–adsorbate and adsorbate–adsorbent interactions to decode isosteric heats of gas adsorption.* ChemPhysChem, 2015. **16**(18): p. 3797-3805.
337. Szanyi, J. and M.T. Paffett, *The adsorption of carbon monoxide on H-ZSM-5 and hydrothermally treated H-ZSM-5.* Microporous materials, 1996. **7**(4): p. 201-218.
338. Zecchina, A., et al., *Silicalite characterization. 2. IR spectroscopy of the interaction of carbon monoxide with internal and external hydroxyl groups.* The Journal of Physical Chemistry, 1992. **96**(12): p. 4991-4997.
339. Lunsford, J.H., *A study of surface interactions on γ-alumina, silica-alumina, and silica-magnesia using the EPR spectra of adsorbed nitric oxide.* Journal of Catalysis, 1969. **14**(4): p. 379-385.
340. Kim, M.H., et al., *Adsorption of CO 2 and CO on H-zeolites with different framework topologies and chemical compositions and a correlation to probing protonic sites using NH 3 adsorption.* Journal of Porous Materials, 2016. **23**: p. 291-299.

341. Schoonheydt, R.A., et al., *The framework basicity of zeolites.* Journal of Materials Chemistry, 2012. **22**(36): p. 18705-18717.
342. Vitale, G., et al., *A neutron diffraction study of the acid form of zeolite Y and its complex with benzene.* Journal of the Chemical Society, Chemical Communications, 1995(22): p. 2253-2254.
343. Huang, Y.-Y., *Quadrupole interaction of carbon dioxide on silica-alumina surface.* The Journal of Physical Chemistry, 1973. **77**(1): p. 103-106.
344. Karra, J.R. and K.S. Walton, *Molecular simulations and experimental studies of CO2, CO, and N2 adsorption in metal− organic frameworks.* The Journal of Physical Chemistry C, 2010. **114**(37): p. 15735-15740.
345. Deng, H., et al., *Adsorption equilibrium for sulfur dioxide, nitric oxide, carbon dioxide, nitrogen on 13X and 5A zeolites.* Chemical Engineering Journal, 2012. **188**: p. 77-85.
346. Zhou, X., et al., *Thermodynamics for the adsorption of SO2, NO and CO2 from flue gas on activated carbon fiber.* Chemical Engineering Journal, 2012. **200**: p. 399-404.
347. Yi, H., et al., *Adsorption separation of CO2, CH4, and N2 on microwave activated carbon.* Chemical Engineering Journal, 2013. **215**: p. 635-642.

Appendix A

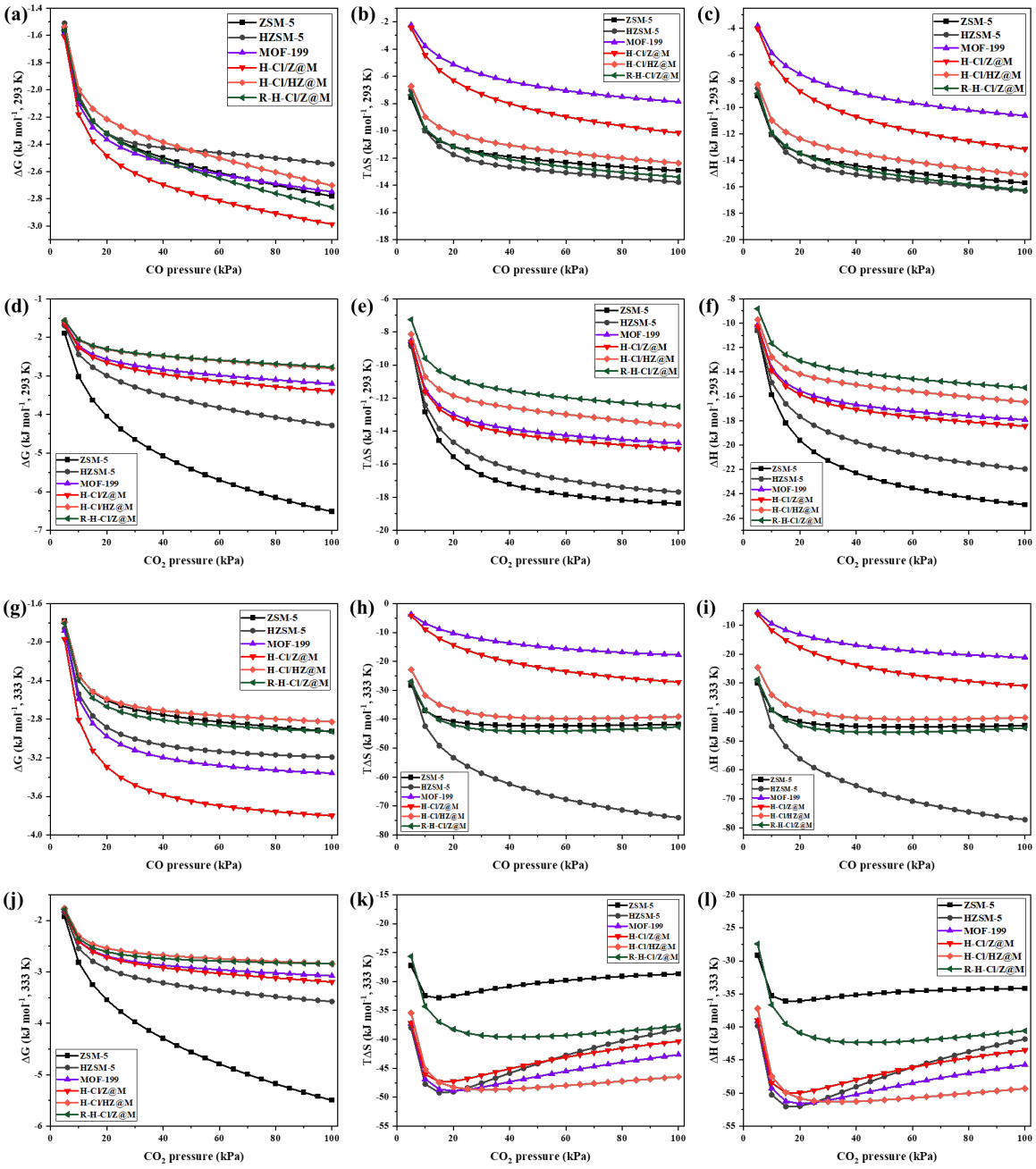

Figure 7-1 Thermodynamic properties of CO and CO_2 adsorption at (a-f) 293 K, and (g-l) 333 K.